INFORMATION TO USERS

This manuscript has been reproduced from the microfilm master. UMI films the text directly from the original or copy submitted. Thus, some thesis and dissertation copies are in typewriter face, while others may be from any type of computer printer.

The quality of this reproduction is dependent upon the quality of the copy submitted. Broken or indistinct print, colored or poor quality illustrations and photographs, print bleedthrough, substandard margins, and improper alignment can adversely affect reproduction.

In the unlikely event that the author did not send UMI a complete manuscript and there are missing pages, these will be noted. Also, if unauthorized copyright material had to be removed, a note will indicate the deletion.

Oversize materials (e.g., maps, drawings, charts) are reproduced by sectioning the original, beginning at the upper left-hand corner and continuing from left to right in equal sections with small overlaps.

Photographs included in the original manuscript have been reproduced xerographically in this copy. Higher quality 6" x 9" black and white photographic prints are available for any photographs or illustrations appearing in this copy for an additional charge. Contact UMI directly to order.

Bell & Howell Information and Learning
300 North Zeeb Road, Ann Arbor, MI 48106-1346 USA

UMI®
800-521-0600

Trace element partitioning between amphibole and basaltic melt

Claude Dalpé

Earth and Planetary Sciences

McGill University, Montreal

December 1997

A thesis submitted to the Faculty of Graduate Studies and Research in partial fulfilment of the requirements of the degree of Ph.D.

Abstract

The effects of composition, pressure and oxygen fugacity on partition coefficients between amphibole and hydrous basaltic melt were studied at 1.5 to 2.5 GPa and 1000 to 1130 °C. Partition coefficients (D_i = concentration of element *i* in amphibole / concentration of *i* in melt) of large-ion-lithophile elements (LILE: Rb, Sr, Ba), high-field-strength elements (HFSE: Y, Zr, Nb, Ta, Hf), and rare-earth elements (REE: La to Lu) were determined between amphiboles and coexisting quenched melts created by partial crystallization of seven different starting compositions in a piston-cylinder high-pressure apparatus. Trace elements were analyzed by laser-ablation microprobe inductively coupled plasma - mass spectrometer (LAM-ICP-MS). The effects of pressure, temperature and oxygen fugacity on the partition coefficients are minor, but statistically measurable. Amphibole composition affects partitioning of these trace elements by a maximum factor of 3.5 in the range of pressures and temperatures studied within an oxygen fugacity range of 2 orders of magnitude above and below nickel-nickel oxide buffer. Experiments specifically investigating the role of Ti demonstrate that a positive correlation exists between amphibole $^{VI}Ti^{4+}$ content and D_{Ba}, D_{Sr}, D_{Ta}, D_{Zr}, D_{La}, D_{Ce},, D_{Pr}, and D_{Nd}. Increasing pressure from 1.5 GPa to 2.2 or 2.5 GPa (depending upon composition) increases D_{LILE}, but decreases D_{HFSE} and D_{REE}. Raising the oxygen fugacity at 1.5 or 2.5 GPa by 3 orders of magnitude increases D_{Rb}, D_{Ba}, D_{La}, and D_{Nd}, whereas D_{Ti}, D_{Hf}, and D_{Zr} decrease; however, the maximum difference between partition coefficients measured at low and high oxygen fugacities is only a factor of 1.7. All of the effects of composition, pressure, and oxygen fugacity reflect the control of crystal chemistry

on the partitioning of trace elements between amphibole and basaltic melt. No effects of melt composition were discerned in this study. The measured partition coefficients were used to investigate trace element compositions of primary melts formed from an amphibole-bearing peridotite. This modeling demonstrates that changes in either the oxygen fugacity or pressure of melting can exert a significant effect on Rb/HFSE ratios in the melts and thus help explain the wide variations of these ratios sometimes observed in basaltic rock suites.

Sommaire

Les effets de la composition, de la pression et de la fugacité d'oxygène sur les coefficients de partage entre l'amphibole et son liquide hydraté de composition basaltique ont été étudiés à différentes pressions (1.5 à 2.5 GPa) et températures (1000 à 1130 °C). Les coefficients de partage (D_i = concentration d'un élément *i* dans l'amphibole / concentration du même élément *i* dans le liquide) pour les éléments lithophiles à grand rayon ionique (LILE: Rb, Sr, Ba), les éléments à champ de force élevé (HFSE: Ti, Y, Zr, Nb, Ta, Hf) et pour les éléments des terres rares (REE: La à Lu) ont été mesurés sur des produits d'expériences provenant de fusion partielle entre une amphibole et son liquide basaltique à l'état solide pour sept compositions différentes. Les éléments traces ont été analysés à l'aide d'une microsonde par ablation au laser intégrée à un plasma à couplage inductif avec spectromètre de masse (LAM-ICP-MS). Les effets de la pression, de la température et de la fugacité d'oxygène sur les coefficients de partage sont minimes mais statistiquement distincts. La composition affecte les coefficients de partage des éléments traces pouvant atteindre une variation maximale d'un facteur de 3.5 pour les différentes pressions et températures étudiées aux diverses conditions d'état d'oxydation variant de deux ordres de grandeur de part et d'autre du tampon nickel-oxyde de nickel. Les expériences sur l'effet du titane démontrent une relation positive entre $^{VI}Ti^{4+}$ de l'amphibole et D_{Ba}, D_{Sr}, D_{Ta}, D_{Zr}, D_{La}, D_{Ce}, D_{Pr}, ainsi que D_{Nd}. L'augmentation de la pression allant de 1.5 GPa à 2.2 ou 2.5 GPa (selon la composition) fait augmenter D_{LILE}, mais fait diminuer D_{HFSE} ainsi que D_{REE}. L'élévation de la fugacité d'oxygène par 3 ordres de grandeur à 1.5 GPa ou à 2.5 GPa fait augmenter D_{Rb}, D_{Ba}, D_{La}, ainsi que D_{Nd}, alors que D_{Ti},

D_{Hf} et D_{Zr} diminuent. Par contre, l'étude démontre que la variation maximale atteinte entre les coefficients de partage mesurés à base et à haute fugacité d'oxygène est d'un facteur de 1.7 seulement. Tous ces effets de composition, de pression, et de fugacité d'oxygène sur le partage des éléments traces entre l'amphibole et le liquide basaltique reflètent plutôt un contrôle chimique dans la structure cristalline de l'amphibole. Aucun effet de la composition du liquide basaltique n'à été décelé dans cette étude. Les coefficients de partage mesurés ont été utilisés pour une modélisation afin de déterminer la composition en éléments traces d'un liquide primaire provenant d'une péridotite contenant de l'amphibole. Ce modèle permet d'expliquer les variations des rapports Rb/HFSE observés à l'occasion dans les roches basaltiques alcalines par des changements de pressions et de fugacité d'oxygène.

Acknowledgements

First, I would like to thank my advisor Don R. Baker for his professional relationship and the scientific discussions which I had with him during my studies at McGill. I thank him for his great patience concerning the thousands of questions related to experiments, analytical techniques, and geochemistry which I asked him during classes, laboratories, meetings, dinners, short courses, and our traditional "Friday meeting". I also thank him for having the great confidence in me to send me to the National Synchrotron Light Source (NSLS) at Brookhaven National Laboratory (BNL; N.Y., U.S.A.) to learn and use the synchrotron X-ray-fluorescence microprobe (SXRFM). I also thank him for giving me the great opportunity to complete the analyses by laser-ablation microprobe ICP-MS at l'Université de Montréal (Que., Can.).

I thank Steve R. Sutton (BNL; N.Y., U.S.A.) for providing beamtime at the NSLS on X26A, for helping me on data acquisition and data reduction, and for his co-authorship in Dalpé *et al.* 1995. Mark Rivers, Saša Bajt and Pat Nuessle (BNL; N.Y., U.S.A.) are thanked for providing technical assistance with SXRFM on X26A.

Gilles Gauthier and Amira Khoury (both at Université de Montréal) are thanked for providing technical support on the laser-ablation microprobe with inductively coupled plasma - mass spectrometer (LAM-ICP-MS).

Glenn Poirier (McGill University) is thanked for providing technical support on the electron-microprobe analysis (EMPA).

I thank Don Francis for discussions on partition coefficients and modelling, and for

providing the use of his large dataset on mafic volcanic rocks from the northern Canadian Cordillera (some of which were unpublished). I thank him for graciously providing the HF13 rock powder and its bulk composition.

I thank Hatten S. Yoder Jr. (Geophysical Laboratory, Carnegie Institution of Washington, Wash. D.C., U.S.A.) who graciously supplied K1921 and FM10 rock samples.

John Adam and Trevor H. Green (both at Macquarie University, N.S.W, Aus.) are thanked for exchanging data before publication and unpublished data on amphibole / melt partitioning.

Postgraduate students Pierre Hudon, Rob A. Marr, Souad Guernina, Leyla Hoosain (Earth and Planetary Sciences, McGill University), and a visiting scientist Lilli Freda (Dipartimento di Scienze della Terra, Università degli Studi "La Sapienza", P.le Aldo Moro, Roma), all attached to the high pressure and high temperature, laboratory are thanked for providing helpful discussions during the "Friday meeting" and acting as a critical audience during preliminary oral presentations before meetings.

I thank Trevor H. Green, Robert F. Martin, D. Günther, L. Forsythe, George Jenner, John Stix, and Henry Longerich for their constructive comments, which greatly improved the Dalpé *et al.* (1995) manuscript. Furthermore, I thank Robert F. Martin for stimulating my interest in crystal chemistry during his graduate course.

I thank David Hanna (Pro-Dean; McGill University), Don R. Baker (Supervisor and internal member; McGill University), Clément Gariépy (External member, GÉOTOP; Université du Québec à Montréal), Trevor H. Green (External member, GEMOC; Macquarie University, Aus.), Alfonso Mucci (Deputy, McGill University), Jeanne Paquette and Don

Francis (both from McGill University) for their constructive comments about the thesis during my oral examination .

Finally, I wish to thank all the members of my family and, in particular my wife Martine Germain and my three daughters Isabelle L. Dalpé, Amélia Dalpé, and Allyson Dalpé for supporting me during my research, for their great comprehension, and for their love of life.

This research was supported by NSERC and FCAR scholarships to C. Dalpé, NSERC grant OGP89662 and FCAR Nouveau Chercheur Grant to D.R. Baker, and DOE DE#-FG02-92ER14244, NASA NAG9-106, NSF EAR89-15699 grants to S.R. Sutton.

Table of contents

Preface concerning the faculty regulations

Candidates have the option of including, as part of the thesis, the text of one or more papers submitted or to be submitted for publication, or the clearly-duplicated text of one or more published papers. These texts must be bound as an integral part of the thesis.

If this option is chosen, connecting texts that provide logical bridges between the different papers are mandatory. The thesis must be written in such a way that it is more than a mere collection of manuscripts; in other words, results of a series of papers must be integrated.

The thesis must still conform to all other requirements of the "Guidelines for Thesis Preparation". The thesis must include: A Table of Contents, an abstract in English and French, an introduction which clearly states the rationale and objectives of the study, a review of the literature, a final conclusion and summary, and thorough bibliography or reference list.

Additional material must be provided where appropriate (e.g., in appendices) and in sufficient detail to allow a clear and precise judgement to be made of the importance and originality of the research reported in the thesis.

In the case of manuscripts co-authored by the candidate and others, the candidate is required to make an explicit statement in the thesis as to who contributed to such work and to what extent. Supervisors must attest to the accuracy of such statements at the doctoral oral defense. Since the task of the examiners is made more difficult in these cases, it is in the candidate's interest to make perfectly clear the responsibilities of all authors and the co-authored papers.

Preface concerning the thesis

The thesis is subdivided in seven different chapters.

Chapter 1 presents a general introduction of the study concerning the goals and objectives, methodology used, and a review of the literature on partition coefficients between amphibole and melt using different bulk compositions.

In Chapter 2, I discuss two microbeam instruments useful for the analysis of experimental run products. This chapter was published in Canadian Mineralogist by Dalpé *et al.* (1995). The contribution of both co-authors (Don R. Baker and Steve R. Sutton) was different regarding correction of the paper or scientific contribution. Professor Don R. Baker corrected the versions which I gave him and suggested during this process sometimes to expand on a subject or sometime to cut parts, paragraphs, sentences, or words. Dr. Steve Sutton rewrote parts of two sections in the paper (*i.e.*, "Synchrotron X-ray-fluorescence microprobe" in 2.5.1. and "Computation of element concentrations and their precision and accuracy" in 2.5.1.1.) and suggested some modifications to the paper concerning the comparison of both instruments. Furthermore, one of his main contribution to this study was to give me the possibility of using the SXRFM by sharing his own beamtime on X26A at BNL in order to perform trace element analyses. He also modified a version of the program NRLXRF for the computation of trace element concentrations. The different technical parts of the paper and most of the writing (including figures and tables) were done by the first author.

In Chapter 3, I investigate how different natural mafic compositions from alkalic to sub-alkalic can modify the partition coefficients between amphibole and melt. I show that

crystal chemistry controls partitioning instead of melt composition. Furthermore, a thermodynamic model (Blundy and Wood 1994) is used to indirectly establish the variations of the amphibole lattice-site parameters among the different bulk compositions.

In Chapter 4, I evaluate the effects of pressure and oxygen fugacity on partition coefficients. Again, the variations of the amphibole lattice-site parameters were used in order to evaluate their effects on partitioning.

In Chapter 5, I evaluate if titanium significantly affects partition coefficients between amphibole and melt. The addition of titanium results in increasing compatibility of some trace elements.

In Chapter 6, I evaluate the role of amphibole in the petrogenetic evolution of an alkaline magmatic basaltic rock series formed at different pressures and oxygen fugacities.

In Chapter 7, I present a general conclusion of the study.

Chapter 1

General introduction

1.1 Goals and objectives

The goal of this thesis is to report the results of an investigation of trace element partitioning between calcic amphibole and basaltic melt. Calcic amphiboles, mainly pargasite and kaersutite, are frequently found in primary alkali-olivine basaltic magmas, basanites, and nephelinites; additionally these amphiboles are also found in mantle xenoliths and alpine peridotites. Their occurrence suggests that they are essential hydrous phases in subcrustal environments. Many previous studies demonstrated that amphibole is a major host of minor and trace elements. Because of their enrichment in alkalies and incompatible trace elements, amphiboles provide an appropriate source for alkaline magmatism. Other studies, however, disagree and suggest that some phenocrystic amphiboles are petrogenetically unrelated to the rocks in which they are found (*e.g.*, accidental xenocrysts). The importance of amphibole in alkaline magmatism can be assessed by modelling the trace element evolution of alkaline suites using partition coefficients between mineral phases and melts. Unfortunately, few data are available for trace element partitioning between amphibole and basaltic melt at subcrustal conditions.

The objectives of this research are to investigate experimentally the partitioning of trace elements (Rb, Sr, Ba, Y, Zr, Nb, Hf, U, Th, Ta, La, Ce, Pr, Nd, Sm, Eu, Gd, Tb, Dy, Ho, Er, Tm, Yb, Lu) between amphibole and melt under controlled conditions of (1) pressure and temperature, (2) melt composition, (3) oxygen fugacity, and (4) titanium content. This

experimental study covers a range of pressure and temperature corresponding to upper mantle conditions, between 1.5 to 2.5 GPa (~45 - 75 km depth) and 1000 to 1125 °C.

1.2 Methodology

1.2.1. Starting compositions

In order to investigate the role of bulk composition on partitioning, experiments were performed with different bulk compositions initially in various states (*i.e.*, powdered crystals, powdered rocks, powdered glasses). For the powdered crystals, two natural calcic amphiboles were utilized. These crystals were handpicked from a Monteregian lamprophyre dike (*i.e.*, pargasite; Quebec, Can.) and from a Hoover Dam lamprophyre dike (*i.e.*, kaersutite; Arizona, U.S.A.). The three different powdered rocks consist of an olivine-normative nephelinite from a Tertiary intrusion at Mount Llangorse (British Columbia, Can.), an olivine tholeiite from the 1921 lava flow of Kilauea (Hawaii, U.S.A.), and an alkali basalt lava flow from the north of Keauhou (Hawaii, U.S.A.). Two Ti-doped glasses originating from the pargasite crystal and the olivine-normative nephelinite bulk rock were used to investigate the effects of Ti on trace element partitioning. A third powdered glass of pargasitic composition was formed by melting of the pargasite crystals.

1.2.2. Experimental equipment

The experiments were performed in a high-pressure piston-cylinder apparatus at the Department of Earth and Planetary Sciences at McGill University (Que., Can.). The starting compositions were encased in graphite capsules with measured amounts of deionized water and sealed inside noble metal alloy outer capsules. Some experiments were performed without the graphite capsules in order to investigate the effect of variation in oxygen fugacity on partition coefficients.

1.2.3. Analytical techniques

The identification of the different phases in the run products was performed under an optical microscope. From a total of 190 experiments, 79 of them were selected for major and minor element determinations of each phase in the run products by electron microprobe analysis at the Department of Earth and Planetary Sciences at McGill University (*i.e.*, Si, Ti, Al, Fe, Mn, Mg, Ca, Na, K). From the 79 run products, 13 of them were subsequently selected and analyzed for different trace elements by laser-ablation microprobe ICP-MS at the Département de Géologie de l'Université de Montréal (Que., Can.) (*i.e.*, Rb, Sr, Ba, Y, Zr, Nb, Ta, Hf, U, Th, La, Ce, Pr, Nd, Sm, Eu, Gd, Tb, Dy, Ho, Er, Tm, Yb, Lu). In order to cross-check our analytical results from the laser-ablation microprobe, one experiment was selected and analyzed by synchrotron X-ray-fluorescence microprobe at the National Synchrotron Light Source of Brookhaven National Laboratory (N.Y., U.S.A.) for the most abundant trace elements (*i.e.*, Rb, Sr, Y, Zr, Nb).

1.2.4. Chemical classifications used for run products

We used major and minor element concentrations determined by the electron microprobe to classify the different phases obtained in each run product. For the amphibole, I used the nomenclature of Leake *et al.* (1997) according to the diagram Ti *vs.* Mg/(Mg+Fe^{2+}) on a basis of 23 atoms of oxygen per formula unit. However, at the time that I submitted the paper on "Synchrotron X-ray-fluorescence and laser-ablation ICP-MS microprobes: Useful instruments for analysis of experimental run-products" by Dalpé *et al.* (1995; see Chapter 1), I used the nomenclature of Leake (1978). The proportion of ferric- and ferrous-iron was calculated using the empirical estimation of Schumacher (1997). For the mica, I used the nomenclature of Mitchell (1995) according to the diagram Mg - Al - (Fe^{2+}+Fe^{3+}) on a basis of 22 atoms of oxygen per formula unit based on Deer *et al.*'s (1992) recommendations. For the pyroxene, I used the nomenclature of Morimoto (1989) according to the diagram Ca - Mg - (Fe^{2+}+Fe^{3+}+Mn) on a basis of 6 atoms of oxygen per formula unit. Olivines were classified according to their atomic proportion of 100 Mg/(Mg+Fe^{2+}+Fe^{3+}+Mn) on a basis of 4 atoms of oxygen per formula unit (Deer *et al.* 1992). Glasses were classified according to the diagram K_2O+Na_2O *vs.* SiO_2 (in wt.%) from Miyashiro (1978) and Cox *et al.* (1979). The classification of alkalic and sub-alkalic basalts in terms of K_2O *vs.* SiO_2 (in wt.%) and Na_2O *vs.* SiO_2 (in wt.%) was done according to Middlemost (1975). The classification of tholeiitic and high-alumina or calc-alkaline basalts in term of alkali index [*i.e.*, (Na_2O+K_2O) / ((SiO_2-43)×0.17)] *vs.* SiO_2 (in wt.%) was done following Middlemost (1975). The weight percentages of normative minerals were calculated using Prof. D. Francis's program (Francis,

pers. comm.) specifically designed for basaltic rock compositions.

1.3 Review of the literature concerning partition coefficients between experimentally produced amphibole and silicate melt

This review of the literature is basically focused on the study of partition coefficients between experimentally produced amphibole and silicate melt at upper mantle conditions. A brief summary on those results regarding the physical and chemical aspects that may influence partitioning are reported here (*i.e.*, bulk composition, crystal composition, melt composition, pressure, and oxygen fugacity).

Drake and Holloway (1977) reported preliminary values of Sm partitioning measured between amphibole and intermediate melt in experiments performed at 0.5 and 1.2 GPa, 900 and 925 °C using a natural andesite and a radioactive tracer of ^{151}Sm-spiked material. Using the β-track autoradiography technique, they showed that increasing the pressure increases D_{Sm} for similar temperatures. However, their D_{Sm} values are higher by approximately a factor of 2 compared to those measured in experimental amphibole/basaltic melt pairs (see Irving 1978).

Mysen (1978a) studied the partition coefficient of Ni measured between Ti-Fe-K-free calcic amphibole (pargasite) and a "haplobasaltic melt" in experiments performed at 1.5 GPa and 1000 °C using a mixture of oxides ($Ab_{41}An_{41}Fo_{16}Q_2$) and ^{63}Ni-spiked material. He focused his study on the concentration limit of Henry's law behaviour of nickel during

partitioning between pargasite and haplobasaltic melt using the β-track autoradiography technique. Based on four experiments performed at the same pressure and temperature, he observed constant partitioning of Ni up to 300 ppm in the pargasite (*i.e.*, Henry's law was obeyed). At concentrations above 300 ppm Ni in the pargasite D_{Ni} was found to decrease (*i.e.*, beyond the Henry's law range). Based on these results, he showed that pargasite has a very limited range of Ni concentration where Henry's law appears to be obeyed.

Mysen (1978b) studied partition coefficients of Ce, Sm, and Tm between Ti-Fe-K-free calcic amphibole (pargasite) crystallized from a "haplobasaltic melt" in an experiment performed at 1.5 GPa and 1000 °C using a synthetic mixture of oxides ($Ab_{41}An_{41}Fo_{16}Q_2$) and radioactive tracers of ^{141}Ce, ^{151}Sm, ^{171}Tm. He focused his study on the concentration limit of Henry's law behaviour of the rare-earth elements between pargasite and haplobasaltic melt using the β-track autoradiography technique. Based on four ^{151}Sm-doped experiments at the same pressure and temperature, he observed constant partitioning of Sm up to 1.5 ppm in the pargasite (*i.e.*, Henry's law was obeyed). At concentrations above 1.5 ppm D_{Sm} was found to decrease (*i.e.*, Sm in pargasite was beyond the Henry's law range). However, the results of his experiments in the Henry's law range yield D_{Ce}, D_{Sm}, and D_{Tm} which grossly different (*i.e.*, lower by a factor of 10 or more) than those previously reported by Irving (1978). Furthermore, the pargasite has a very limited range of Sm concentration in which Henry's law appears to be obeyed.

F.A. Frey [unpublished data; reported by Irving (1978)] measured partition coefficients of La, Ce, Nd, Sm, Eu, Yb, and Lu between separated pargasite and basaltic melt

obtained from an experiment conducted by J.R. Holloway on H_2O-saturated, undoped 1921 Kilauea olivine tholeiite performed at 0.5 GPa and 1000 °C. The measured partition coefficients are comparable to those measured between three natural kaersutite-ferrokaersutite and basaltic host rock pairs (see Irving 1978).

Nicholls and Harris (1980) reported partition coefficients of La, Sm, Ho, and Yb measured between calcic amphibole (Ti-rich pargasite) and basaltic-to-andesitic melts using synthetic glass spiked with La-, Sm-, Ho-, and Yb-oxides at 1.0 GPa and 1020 °C. The doping concentration of each individual rare-earth was 1000 ppm, permitting the use of an electron microprobe for the analyses of the calcic amphibole/silicate melt pairs. They showed that partition coefficients of the rare-earth elements, D_{REE}, for andesitic systems are higher than those for the basaltic systems by a factor of 3 and followed sub-parallel patterns. Based on the amphibole run products, they observed a lower D_{REE} for the lighter REE as Na/(Na+Ca) of the amphibole increases.

Green and Pearson (1985a) reported partition coefficients of Sr, La, Sm, Ho, and Lu measured between calcic amphibole (Ti-rich pargasite and kaersutite) and basaltic to andesitic melts for experiments performed at 0.75 to 2.0 GPa, 900 to 1050 °C under two different oxygen fugacities (fO_2). For their experiments, they used three natural rock powders (andesite, tholeiite, and K-rich tholeiite) spiked with a rare-earth oxide bearing glass at the ~0.5 wt.% level permitting the use of an electron microprobe for run product analysis. They recognize a clear bulk composition and temperature effect on partitioning while pressure and oxygen fugacity effects appear to be subordinate.

Adam *et al.* (1993) reported partition coefficients of Rb, Sr, Ba, Y, Ti, Zr, Nb, and Ta measured between calcic amphibole (Ti-rich pargasite) and basaltic-to-andesitic melts for different pressures (1.0 to 3.0 GPa) and temperatures (875 to 1100 °C). They used nepheline basanite and tholeiitic basaltic andesite rock powders spiked with a Nb-Ta-enriched glass at the ~5 wt.% level, and they added various amounts of volatile components, between 1 to 10 wt.% of H_2O, F, Cl. The Nb-Ta-doped glass allows the analysis of the individual run products by proton microprobe. Within a pressure range of 1.0 GPa (between 1.0 to 2.0 GPa) and within a relatively small range of temperature (between 1000 to 1050 °C), they observed that partition coefficients for the high-field-strength elements, D_{HFSE}, are relatively insensitive. However, partition coefficients for the HFSE and other incompatible elements (excepting Rb) increase as the SiO_2 concentration in the melt phase increases. Furthermore, the effects of F on partition coefficients for incompatible elements were found to be important in melts containing low concentrations of Al_2O_3, FeO, MgO, and CaO (*e.g.*, felsic magmas).

Adam and Green (1994) reported partition coefficients of Ti, Sr, La, Sm, Ho, and Lu between calcic amphibole (Ti-rich pargasite) and basaltic melt for different pressures (0.5 to 2.0 GPa) and temperatures (1000 to 1100 °C). They used nephelinite basanite rock powder spiked in rare-earths (La, Sm, Ho, Lu) and Sr at the ~0.5 wt.% level. They observed that partition coefficients of Ti, Sr, Sm, Ho, and Lu decrease with increasing pressure from 0.5 to 2.0 GPa. The variations in partition coefficients with pressure can be explained by modifications of the major element compositions of the amphibole (*i.e.*, crystal-chemical control). As pressure increases, the amphibole shows an enrichment in SiO_2 and Na_2O and

a depletion in Al^{IV}/Al^{VI}, Ti, Sr, and REE, thus reducing partitioning. Partition coefficients for Ti, Sm, and Ho are relatively insensitive to a temperature range of 50 °C at the same pressure. Increasing the oxygen fugacity from a low value (*i.e.*, between Ni-NiO and magnetite-wüstite buffers) to a higher value (*i.e.*, hematite-magnetite buffer) does not affect partition coefficients.

Brenan *et al.* (1995) measured partition coefficients of a series of elements (Ti, Rb, Sr, Zr, Nb, Ba, Hf, Ta, Ce, Nd, Sm, Yb, Pb, Th, U) between Fe-free and K-free calcic amphibole (Ti-rich pargasite) and andesitic melt obtained from a series of experiments performed at 1.5 GPa and 1000 °C. They used a synthetic andesitic glass spiked with trace elements (Rb, Ba, Sr, U, Th, Pb, Nb, Ta, Hf, Zr, Ce, Nd, Sm, and Yb) added as dilute nitrate solutions for ion microprobe analyses. Based on three concentration levels of trace elements (except for Ti, Ta, and the REE), they observed constant partition coefficients between amphibole and silicate melt for a range of ~1 to >100 ppm using identical pressure and temperature conditions. Using their partition coefficients values and those from Adam *et al.* (1993), they applied the elastic strain theory of Blundy and Wood (1994) to predict amphibole/melt partition coefficients at conditions of pressures, temperatures, and compositions different than those used in their study. They were able to reproduce the measured partition coefficients from previous studies to within 45 %.

Dalpé *et al.* (1995) measured partition coefficients of a series of elements (Ti, K, Rb, Sr, Y, Zr, Nb, Ba, Hf, Ta, La, Ce, Nd, Sm, Eu) between calcic amphibole (Ti-rich pargasite) and basanitic glass for an experiment performed at 1.5 GPa and 1100 °C. They were able

to use natural kaersutite megacrysts as starting material due to the low lower limit of detection of both the synchrotron x-ray fluorescence microprobe and the laser-ablation microprobe inductively-coupled plasma mass spectrometer. They measured similar values of D_{Sr} and D_{Y}, and identical values of D_{Zr} between Ti-rich pargasite and basanitic melt using both instruments. They mentioned that the relatively low partition coefficients for the rare-earth elements (*i.e.*, La, Ce, Nd, Sm, Eu) measured between their Ti-rich pargasite and basanitic melt might reflect an amphibole composition effect (*e.g.*, titanium content in the *M*1,2,3 octahedral sites).

LaTourrette *et al.* (1995) reported partition coefficients for a series of elements (Si, Ti, Al, Fe, Mn, Mg, Ca, Na, K, Rb, Ba, Pb, Th, U, Nb, La, Ce, Pr, Sr, Nd, F, Hf, Zr, Gd, Li, Be, Ho, Y, Er, Tm, Lu) between calcic amphibole (Ti-rich pargasite) and a basaltic melt at 1.5 GPa and 1092 °C using a natural basanite enriched with a premelted glass spiked in trace element oxides or carbonates. The doping concentrations ranged from 50 to 1250 ppm. Trace element concentration in run products were analyzed by ion microprobe. They showed the ability to model partition coefficients using the elastic strain theory model of Blundy and Wood (1994) and demonstrated an important relationship between trace element partitioning and the macroscopic properties of the amphibole.

Fujinawa and Green (1997) reported partition coefficients of Zr, Hf, and Ti between calcic amphibole (Ti-rich pargasite) and basaltic-to-andesitic glasses performed at different pressures (0.5 to 3.0 GPa) and temperatures (900 to 1100 °C) using a natural basanite and andesite spiked with trace element oxides. The doping concentrations of Zr and Hf range

from 500 to 5000 ppm whereas Ti is at the natural level, permitting the use of the electron microprobe for the analyses of the run products. They showed that Henry's law behaviour is obeyed for Hf concentration levels ranging from 500 to 5000 ppm and their results are consistent with those results of D_{Zr} and D_{Hf} from Dalpé *et al.* (1995) using natural abundances. They observed that D_{Hf}, D_{Zr} and D_{Ti} between amphibole and silicate melt decrease with increasing pressure from 0.5 to 2.5 GPa. They mentioned that the decrease in partitioning is more pronounced between 0.5 and 1.5 GPa then between 1.5 to 2.5 GPa. Similarly to the Adam and Green (1994) study, they correlated the variations of D_{Hf}, D_{Zr}, and D_{Ti} as function of pressure with the crystal-chemical control by the amphibole. They illustrated that as pressure increases, K in the *A* site increases whereas Al^{IV}/Al^{VI} decreases.

Klein *et al.* (1997) studied the partition coefficients of Nb, Ta, Zr, Hf, La, Ce, Nd, Sm, Eu, Gd, Dy, Er, Yb, and Lu between amphibole and quartz-dioritic-to-tonalitic melts performed at a pressure of 1.0 GPa and temperatures of 800, 850, and 900 °C. They used a natural quartz-diorite rock doped with a variety of elements for electron microprobe analyses at the 0.5 wt.% level. Furthermore, they performed an undoped experiment in order to check for Henry's law behaviour. In this case, run products were analyzed by an ion microprobe. They demonstrated the applicability of the Henry's law behaviour for trace element concentrations ranging from few ppm up to the 0.5 wt.% of doping level. Based on their experimental results, they showed that partition coefficients between amphibole and silicate melt are negatively correlated with the degree of polymerization of the melt expressed as the ratio of nonbridging oxygens to the number of tetrahedral cations (NBO/T).

Furthermore, partitioning of trace elements are negatively correlated to run temperatures (*i.e.*, partition coefficients decrease as temperature increases).

Chapter 2

Synchrotron X-ray-fluorescence and laser-ablation ICP-MS microprobes: Useful instruments for analysis of experimental run products

(Published in Canadian Mineralogist by Dalpé *et al.* 1995)

2.1 Introduction

Trace elements provide a powerful tool for the investigation of the petrogenesis of igneous rocks. Using trace-element concentrations in a suite of rock samples, one can construct an inverse model that not only constrains the mechanisms responsible for the genesis of the suite but also can provide information on the source region (*e.g.*, Allègre *et al.* 1977, Allègre and Minster 1978, Hofmann 1986). These models depend upon accurately characterized partition coefficients (D) between minerals and melts. Most of these partition coefficients are based upon analyses of natural phenocrysts and their enclosing glassy matrix. However, because partition coefficients are sensitive to pressure, temperature, mineral, and melt compositions (including volatile content and oxygen fugacity), they are best measured in minerals and quenched glasses synthesized in the laboratory under controlled conditions.

Electron-microprobe analysis (EMPA) can be used to measure partition coefficients of major and minor elements in glasses and crystals from experimental run-products, but EMPA cannot be used for trace elements (<100 ppm). Furthermore, because of the small size of experimental run products, minerals and quenched glasses only rarely can be separated by magnetic or density techniques for traditional analytical techniques used on natural rocks and minerals (Watson *et al.* 1987). To determine partition coefficients accurately in experimental

run-products, they must be analyzed *in situ* for trace elements using a microbeam technique.

Two microbeam instruments, the synchrotron X-ray fluorescence microprobe (SXRFM) and the laser-ablation microprobe inductively coupled plasma mass spectrometer (LAM-ICP-MS), recently have been used to measure partition coefficients between crystals and glasses in experimental run-products (Dalpé *et al.* 1992, Dalpé and Baker 1994a, -b, Jenner *et al.* 1994, Skulski *et al.* 1994). Both instruments are rapid and have a lower limit of detection (LLD) near, or below, 5 ppm. These instruments also have been applied to other studies requiring *in situ* analysis (Sutton *et al.* 1987, Jackson *et al.* 1992, Pearce *et al.* 1992, Federowich *et al.* 1993, Feng *et al.* 1993, Feng 1994). In addition, other microbeam instruments have been used for *in situ* analysis as discussed by Hawthorne (1993) and Green (1994).

These two instruments are based on different principles and have different analytical characteristics, such as sensitivity, stability, interference, and beam size (Gordon 1982, Bos *et al.* 1984, Jones *et al.* 1984, Sutton *et al.* 1986, Lu *et al.* 1989, Jarvis *et al.* 1992, Jarvis and Williams 1993, Perkins *et al.* 1993). Synchrotron radiation is intense, white light of X-ray wavelengths, $\geq$105 times more brilliant than that of conventional X-ray tubes, emitted from electrons circling a synchrotron ring. As the specimen is excited by synchrotron X-ray radiation, the SXRFM measures the energies and intensities of X-rays emitted by the sample using either an energy-dispersive or wavelength-dispersive detector. Quantification of the elemental concentrations based on the XRF spectrum is relatively straightforward because the physics of photon interactions with matter is well understood. The SXRFM provides

nondestructive trace element analysis of geological specimens with a LLD of 1-10 ppm for a spot size of 10 μm depending on the element and the matrix analyzed (Sutton *et al.* 1986, Bajt *et al.* 1992).

The recent refinement of the laser-ablation technique for ICP-MS analysis allows microsampling and rapid analysis of materials as different as silicate glass, pressed pellets of rocks, minerals, alloys, and ceramics (Jarvis *et al.* 1992). The LAM-ICP-MS ablates a small volume of the sample, some of which is converted into an aerosol and is carried out of the sample cell by argon gas to the inductively coupled plasma (ICP) unit. Inside the ICP, the sample is volatilized, atomized, and ionized; the resulting material undergoes supersonic expansion and is introduced into a quadrupole mass spectrometer (Jarvis *et al.* 1992). Ions are separated from one another by difference in kinetic energies related to their specific mass, and the abundance of selected stable isotopes of trace elements is detected with a Channeltron electron multiplier (Jarvis *et al.* 1992). Advantages of laser-ablation ICP-MS analysis include low LLD, 2 ppm down to hundreds of ppb, speed of analysis, and the ease of sample preparation.

In this paper, we compare these two microprobe techniques in terms of their ability to accurately and precisely analyze two different in-house basaltic glass standards. Then we apply the techniques developed to measure partition coefficients of Rb, Sr, Y, Zr, and Nb between a Ti-rich calcic amphibole and a Ti-rich basanitic quenched glass produced from natural starting materials at 1.5 GPa and 1100 °C. These techniques are also applicable to the analysis of other solid experimental run products and small samples of silicate.

2.2 Preparation of in-house standard materials

Two natural materials were used for optimization of analytical techniques and as in-house standards for analysis of run products. The first material, P-MT, was made from pargasite megacrysts from a lamprophyre dike of Cretaceous age located in the eastern part of the Island of Montréal, Québec (Canada; donated by G. Pouliot). The second material, HF13, is an olivine nephelinite from a Tertiary intrusion located in the Mount Llangorse alkaline volcanic field of northern British Columbia (Canada; Francis and Ludden 1995; donated by D. Francis).

The pargasite megacrysts are euhedral with lengths up to 5 cm. They contain veins of white material along some cleavage surfaces; we presume this material consists of calcite + zeolite + anorthoclase, which has been noted in similar megacrysts (Campbell and Schenk 1950, Wallace 1977). Pargasite megacrysts were first coarsely crushed in a steel percussion mortar, and clean chips, free of the white material were handpicked. These chips were ground to a powder (<500 μm) in an agate mortar. The olivine nephelinite was received as powder (<140 μm) prepared in a tungsten carbide ball mill. Contamination in W, Co, Sc, Ta, and possibly Nb is well known for this type of mill (Hickson and Juras 1986).

Powders of each material were melted four times at 1400 °C in an Fe-treated Pt crucible at 1 atmosphere under a controlled oxygen fugacity equal to that of the Fe_2SiO_4-Fe_3O_4-SiO_2 (FMQ) buffer. The duration of each melting was three hours. Controlled oxygen fugacity was used to prevent the crystallization of opaque phases during melting, which is

essential to make a homogeneous glass. After each melting, we obtained a clear brown glass free of crystalline material; this glass was crushed using a steel percussion mortar (to <2 mm in size) and cleaned with a magnet to remove any steel filings from the mortar. After the final melting, the glass was removed from the crucible and crushed into chips up to 3 mm across and magnetically cleaned.

2.3 Analysis of the in-house standard glasses for major and minor elements

These reference glasses were analyzed for major and minor elements with a JEOL 8900 electron microprobe operated at an accelerating potential of 15 kV with a beam current of 10 nA; for each element, counting times were 25 s on the peak and 10 s on each background position. The beam size was chosen to be the same diameter as the beam size of the SXRFM (*i.e.*, 10 μm). Albite (Na), diopside (Si, Ca, Mg), andradite (Fe), orthoclase (K, Al), and pyrophanite (Mn, Ti) were used as standards. We have checked the homogeneity of the synthesized glasses by analyzing different chips of glass (3-4 mm in size) from the top, middle, and bottom of the crucible (Table 2.1). Boyd's homogeneity index was used to characterize the homogeneity in major elements of both glasses (Boyd and Finger 1975). On the basis of the standard deviation expected from counting statistics, σ_e, and the standard deviation associated with data measured on the sample, σ, Boyd and Finger (1975) suggested that a sigma ratio σ/σ_e in excess of 2-3 for a major element "is highly suggestive of the presence of an inhomogeneity" in the material. All major elements from the three subsamples

Table 2.1. Homogeneity test using Boyd's index calculated from top, middle, and bottom chips inside the crucible for P-MT and HF13 glasses

P-MT Glass

	Top			Middle			Bottom		
n	10		Boyd's index[a]	10		Boyd's index	10		Boyd's index
SiO_2	40.64	(0.19)	1.32	40.47	(0.12)	0.82	40.16	(0.14)	0.97
TiO_2	3.82	(0.04)	0.91	3.82	(0.03)	0.68	3.80	(0.05)	1.19
Al_2O_3	14.81	(0.10)	1.17	14.79	(0.07)	0.80	14.71	(0.06)	0.69
Fe_2O_3[b]	1.53			1.57			1.58		
FeO[b]	7.24			7.40			7.46		
FeO_t[c]	8.62	(0.15)	1.30	8.81	(0.10)	0.87	8.88	(0.09)	0.79
MnO	0.08	(0.03)	2.81	0.08	(0.03)	3.08	0.10	(0.02)	2.16
MgO	14.44	(0.11)	1.16	14.52	(0.05)	0.55	14.46	(0.06)	0.66
CaO	12.30	(0.06)	0.78	12.34	(0.06)	0.67	12.36	(0.05)	0.61
Na_2O	1.92	(0.03)	0.80	1.92	(0.03)	0.80	1.91	(0.03)	0.83
K_2O	2.31	(0.03)	0.93	2.28	(0.03)	1.01	2.28	(0.03)	1.03
P_2O_5	0.04	(0.02)	n.d.	0.04	(0.02)	n.d.	0.04	(0.02)	n.d.
Total	98.98[d]			99.07			98.70		

Table 2.1. (continued)

HF13 Glass

	Top			Middle			Bottom		
n	10		Boyd's index	10		Boyd's index	10		Boyd's index
SiO_2	41.24	(0.21)	1.43	41.43	(0.11)	0.74	41.64	(0.17)	1.12
TiO_2	2.45	(0.03)	0.96	2.47	(0.03)	1.04	2.45	(0.02)	0.76
Al_2O_3	11.61	(0.06)	0.86	11.63	(0.05)	0.73	11.49	(0.10)	1.37
Fe_2O_3[b]	2.32			2.31			2.30		
FeO[b]	10.17			10.16			10.11		
FeO_t[c]	12.26	(0.14)	0.96	12.24	(0.23)	1.57	12.18	(0.17)	1.19
MnO	0.24	(0.02)	1.34	0.22	(0.03)	1.68	0.23	(0.03)	1.66
MgO	11.36	(0.04)	0.56	11.37	(0.05)	0.65	11.34	(0.08)	0.97
CaO	11.01	(0.07)	0.90	11.02	(0.07)	0.91	11.04	(0.06)	0.82
Na_2O	5.12	(0.04)	0.63	5.13	(0.06)	0.98	5.11	(0.04)	0.71
K_2O	2.02	(0.03)	0.90	2.00	(0.03)	0.89	2.01	(0.02)	0.76
P_2O_5	1.46	(0.03)	n.d.	1.46	(0.03)	n.d.	1.46	(0.03)	n.d.
Total	98.77[d]			98.97			98.95		

Concentrations are in weight percent (wt.%).

Values in parentheses are based on one standard deviation from multiple analyses (1σ).

Abbreviation denotes: n.d.-Not determined.

[a] Boyd's index is calculated using the relationship σ / σ_e where σ is the measured standard deviation from electron probe in the sample and σ_e is expressed by the following equation: $\sigma_e = C / R * [(R * c) / (C * t) + (R * c^2) / (T * C^2)]^{1/2}$ where: C = concentration of an element in the standard; c = concentration of an element in the sample; R = counting rates on the standard (= N / T); N = total counts on the standard; T = counting time on the standard; t = counting time on the sample (Boyd and Finger 1975). [b] Fe_2O_3 and FeO proportions are calculated using total iron from the electron probe at T = 1400°C, P = 1 atm, and fO_2 = FMQ (Kress and Carmichael 1991). [c] Total iron is calculated as FeO from electron probe. [d] Totals are calculated using FeO_t.

of P-MT glass have sigma ratios less than 1.5, with a maximum of 1.32 calculated for Si at the top position (Table 2.1). Because manganese is not a major element, high values were calculated in all three positions, and Boyd's homogeneity test could not be applied. Major elements in HF13 glass samples displayed sigma ratios less than 2 with a maximum of 1.57 for FeO_t in the middle subsample. Here too, the test for manganese could not be applied. These low values of the sigma ratio indicate that P-MT and HF13 glasses are homogeneous in major elements.

2.4 Analysis of in-house standard glasses by solution ICP-MS techniques

Two grams of each glass (mixtures from the top, middle, and bottom of the crucible) were ground to a powder (<245 μm) in agate mortar, split into 1-gram aliquots, and sent to two different laboratories (Memorial University of Newfoundland and Université de Montréal) for analysis by solution ICP-MS techniques. Table 2.2a shows the concentrations of major and minor elements measured by electron microprobe, and Table 2.2b shows the concentrations of trace elements measured by solution ICP-MS techniques. The solution ICP-MS analyses performed at Memorial University of Newfoundland used the method of standard addition to correct for matrix effects (Jenner *et al.* 1990, Longerich *et al.* 1990); at the Université de Montréal a matrix-matched external standardization calibration method and non-linear response drift-corrections were used (Cheatham *et al.* 1993). The composition of the original HF13 bulk rock before melting, analyzed by three different techniques, also is

Table 2.2a. In-house glass standard compositions (major and minor elements)

Ref. Glass comp.	P-MT Glass Pargasitic		HF13 Glass ol-normative nephelinitic	
n	30		30	
SiO_2	40.43	(0.25)	41.44	(0.24)
TiO_2	3.81	(0.04)	2.46	(0.03)
Al_2O_3	14.77	(0.09)	11.58	(0.10)
$Fe_2O_3^a$	1.56		2.31	
FeO^a	7.37		10.15	
FeO_t^b	8.77	(0.16)	12.23	(0.18)
MnO	0.09	(0.03)	0.23	(0.03)
MgO	14.48	(0.09)	11.36	(0.06)
CaO	12.34	(0.06)	11.02	(0.07)
Na_2O	1.92	(0.03)	5.12	(0.05)
K_2O	2.29	(0.03)	2.01	(0.03)
P_2O_5	0.04	(0.02)	1.46	(0.03)
Total	98.94[c]		98.91	

Concentrations are in weight percent (wt.%).

[a] Fe_2O_3 and FeO proportions are calculated using total iron from the electron probe at T= 1400 °C, P= 1 atm, and fO_2= FMQ (Kress and Carmichael 1991). [b] Total iron is calculated as FeO from electron probe. [c] Totals are calculated using FeO_t.

Table 2.2b. In-house glass standard compositions (trace elements)

Ref. Glass comp.	P-MT Glass pargasitic				HF13 Glass ol-normative nephelinitic			
	sol. ICP-MS[a]				sol. ICP-MS		XRF+ICP[b] Before melting	
	UM[c]		MU[d]		UM[c]	MU[d]		
n	3		4		2	1	3	
Li	n.d.		2.7	(0.5)	n.d.	12.40	n.d.	
Rb	16.2	(0.31)	16.9	(0.5)	29.0	28.4	29.72	(0.45)
Sr	461.7	(13.4)	474.6	(5.20)	1532	1485	1498	(37.6)
Y	12.00	(0.32)	9.73	(0.25)	30.46	23.89	27.40	(2.28)
Zr	53.08	(1.95)	52.35	(1.46)	301.9	292.7	299.9	(13.9)
Nb	13.25	(0.89)	16.62	(0.38)	103.6	114.6	90.78	(7.28)
Ba	360.4	(12.7)	365.9	(8.90)	320.9	337.1	391.4	(62.4)
Hf	2.14	(0.12)	2.35	(0.12)	6.05	6.54	5.99	(0.25)
Ta	0.96	(0.07)	1.02	(0.06)	5.79	5.87	4.68	(0.05)
Pb	3.83	(0.17)	4.50	(1.06)	0.61	0.45	n.d.	
Th	0.17	(0.01)	0.21	(0.04)	9.13	9.21	9.61	(1.34)
U	0.05	(0.002)	0.06	(0.01)	2.84	2.81	2.47	(0.25)

Table 2.2b. (continued)

Ref. Glass comp.	P-MT Glass pargasitic				HF13 Glass ol-normative nephelinitic			
	sol. ICP-MS[a]				sol. ICP-MS		XRF+ICP[b] Before melting	
	UM[c]		MU[d]		UM[c]	MU[d]		
n	3		4		2	1	3	
La	5.77	(0.21)	5.78	(0.06)	82.82	83.73	77.87	(1.19)
Ce	17.01	(0.75)	18.07	(0.21)	159.18	167.76	139	(11)
Pr	3.11	(0.11)	2.89	(0.04)	20.03	18.67	n.d.	
Nd	14.53	(0.53)	15.31	(0.40)	73.35	76.91	67.17	(3.16)
Sm	3.74	(0.15)	3.91	(0.23)	14.06	14.42	13.85	(0.25)
Eu	1.29	(0.05)	1.36	(0.06)	4.48	4.49	4.08	(0.13)
Gd	3.41	(0.16)	4.40	(0.31)	11.31	11.76	10.88[e]	
Tb	0.48	(0.03)	0.52	(0.04)	1.53	1.47	1.40	(0.08)
Dy	2.53	(0.14)	2.62	(0.12)	6.97	7.04	6.71[e]	
Ho	0.43	(0.02)	0.45	(0.01)	1.06	1.11	1.18	(0.13)
Er	1.08	(0.03)	1.05	(0.06)	2.72	2.45	n.d.	
Tm	0.13	(0.01)	0.12	(0.01)	0.30	0.27	0.27[e]	
Yb	0.73	(0.05)	0.68	(0.01)	1.61	1.38	1.47	(0.02)
Lu	0.10	(0.004)	0.09	(0.01)	0.20	0.18	0.20	(0.01)

Concentrations are in parts per million (ppm).

Abbreviation denotes: n.d.-not determined.

[a] Analyzed by solution inductively coupled plasma mass spectrometry at respectively laboratories show in table. [b] Analyzed by X-ray fluorescence, solution ICP-MS, and irradiation neutron activation (INA) at McGill University and the Université de Montréal before melting the bulk powder to make standard (D. Francis, pers. comm. 1994). Concentrations of trace elements are recalculated on anhydrous basis. [c] Analyses done at the Laboratoire Ultratrace du Département de Géologie de l'Université de Montréal by G. Gauthier and A. Khoury. [d] Analyses done at the Department of Earth Sciences, Memorial University of Newfoundland by S.E. Jackson. [e] Single analysis.

Values in parentheses are based on one standard deviation from multiple analyses (1σ). Sample chips from both glasses are available upon request to the first author.

listed in Table 2.2b. This composition was recalculated on an anhydrous basis for comparison with the actual glass composition after melting. At the two-sigma level for most elements, no systematic difference appears between the original composition and the results of solution-mode ICP-MS analyses of the HF13 glass after melting (Table 2.2b). The only exceptions are Ta, La, and Eu whose concentrations are higher than those reported in the original bulk-rock analysis. Comparison of the results of different ICP-MS analyses of in-house glass standards from both laboratories demonstrate that they are in very good agreement for the majority of elements, with the exception of Y, Nb, Ba, Pr, Nd, and Yb (Table 2.2b). The concentrations of Nb, Ba, Nd are systematically higher, and those of Y, Pr, Yb, lower, for glasses analyzed at Memorial University of Newfoundland compared to those analyzed at Université de Montréal. Both laboratories use different methods to establish the concentration of those elements. Calibration curves for Y at Université de Montréal are based upon the average values of Y in the standards BIR-1, BHVO-1, JB-1, and BR (Govindaraju 1989), whereas at Memorial University of Newfoundland, a pure Y-metal is use for calibration. The Y concentrations obtained by Memorial University of Newfoundland on different international reference materials are reported to be 20% lower than values previously suggested (G. Jenner, pers. comm., 1995). So without any evidence to the contrary, and knowing that both laboratories can reproduce compositions of basaltic reference standards with excellent accuracy using different calibration procedures (typically better than ±5%; Jenner *et al.* 1990, Cheatham *et al.* 1993), we decided to use the average trace-element concentrations for Rb, Sr, Y, Zr, Nb, Ba, La, Ce, Nd, Sm, Eu, Hf, and Ta determined from

the two solution-mode ICP-MS analyses as the working values for the in-house standard glasses HF13 and P-MT (Table 2.3). In any case, discrepancies between the different values for Y, Nb, Ba, Pr, Nd, and Yb concentrations will not affect the conclusions of this study.

2.5 Microbeam trace-element analysis

2.5.1. Synchrotron X-ray-fluorescence microprobe

SXRFM analyses were performed on beam line X26A at the National Synchrotron Light Source at Brookhaven National Laboratory (Upton, New York, U.S.A.). The synchrotron storage ring was operated at 2584 MeV with an electron current in the range of 110 to 202 mA. Figure 2.1 shows a schematic view of the X26A beam line and includes the major devices used during analyses. The X radiation from the synchrotron is reduced to a 10-μm beam by a series of collimators (slits) and a final pinhole. The beam intensity is measured in a He-filled ion chamber upstream of the pinhole, and the X-ray fluorescence from the sample is detected by a Si(Li) energy-dispersion spectrometer (EDS) (150 eV resolution at Mn$K\alpha$) positioned at 90° to the incident beam (Bos *et al.* 1984, Lu *et al.* 1989, Sutton *et al.* 1986). Between the detector and the sample, an aluminum filter either 85 or 170 μm thick (depending upon the sample's composition) is positioned to suppress the intense *K* fluorescence lines of major elements, principally Ca and Fe in our samples. Counting dead-time for the EDS detector was maintained in the range of 20 to 30%. Concentrations of trace elements were measured on the same areas previously analyzed by electron microprobe

Table 2.3. Levels of different trace elements as determined by SXRF and laser-ablation ICP-MS microprobes

P-MT Glass

	Working values[a]	SXRFM				
		Top		Middle		LLD[b]
n		5		5		10
Rb	16.6	16.0	(0.89)	13.6	(0.49)	2.05
Sr	469	449	(10.9)	359	(3.41)	2.30
Y	10.7	10.6	(0.49)	9.40	(0.80)	2.22
Zr	52.7	42.4	(1.50)	29.2	(0.98)	3.67
Nb	15.2	12.4	(1.02)	10.2	(1.17)	3.59
		LAM-ICP-MS[c]				
		Top		Middle		LLD
n		5		5		10
Rb	16.6	16.7	(0.21)	20.08	(0.53)	0.71
Sr	469	451	(1.94)	456	(2.42)	0.81
Y	10.7	9.24	(0.32)	9.75	(0.26)	0.86
Zr	52.7	52.4	(0.72)	53.3	(1.19)	1.09
Nb	15.2	13.9	(0.18)	14.3	(0.29)	0.72
Ba	363	407	(1.11)	417	(3.71)	0.12
La	5.78	5.78	(0.14)	5.93	(0.12)	0.18
Ce	17.7	18.9	(0.32)	19.3	(0.15)	0.11
Nd	14.9	15.8	(0.37)	16.2	(0.20)	0.10
Sm	3.82	4.44	(0.28)	4.27	(0.35)	0.37
Eu	1.33	1.29	(0.09)	1.35	(0.08)	0.09
Hf	2.26	2.49	(0.21)	2.32	(0.07)	0.09
Ta	1.0	1.06	(0.07)	1.14	(0.05)	0.10

Table 2.3. (continued)

HF-13 Glass

	Working values[a]	SXRFM				
		Top		Middle		LLD[b]
n		5		5		10
Rb	28.8	33.0	(0.89)	28.6	(1.02)	1.74
Sr	1516	1718	(9.80)	1432	(65.2)	1.95
Y	28.3	27.4	(0.80)	23.8	(1.72)	2.37
Zr	299	290	(5.31)	229	(14.4)	2.92
Nb	107	92.6	(2.06)	74.6	(3.88)	3.52
		LAM-ICP-MS[c]				
		Top		Middle		LLD
n		5		5		10
Rb	28.8	33.6	(0.51)	31.0	(0.61)	0.65
Sr	1516	1506	(5.28)	1506	(2.45)	0.65
Y	28.3	25.4	(0.41)	25.3	(0.47)	0.77
Zr	299	316	(2.91)	320	(3.11)	0.90
Nb	107	101	(0.64)	101	(1.06)	0.66
Ba	326	344	(3.83)	347	(2.28)	0.12
La	83.1	87.3	(0.44)	88.3	(0.84)	0.19
Ce	162	171	(0.65)	170	(1.17)	0.11
Nd	74.2	80.6	(0.85)	79.8	(1.43)	0.10
Sm	14.2	14.2	(0.85)	16.0	(0.45)	0.36
Eu	4.5	4.41	(0.08)	4.60	(0.08)	0.09
Hf	6.2	6.86	(0.18)	7.06	(0.22)	0.09
Ta	5.8	6.02	(0.10)	6.38	(0.05)	0.09

[a] Working values are based on average of solution ICP-MS analyses. [b] Lower Limit of Detection are based on 10 different analyses from spots (SXRFM) or grids (LAM-ICP-MS).

[c] Analytical masses used are listed in Table 2.4.

Values in parentheses are based on one standard deviation from multiple analyses (1σ).

Figure 2.1. Schematic view of the X26A beam line at the National Synchrotron Light Source, Brookhaven National Laboratory. The X radiation is emitted from the divergent electrons along their trajectory inside the ring, passes through a series of collimators (slits) and pinhole before exciting the specimen 9 m downstream. The sample is mounted vertically and at 45° to the incident X-ray beam. The fluorescence and scattered X-rays from the specimen are detected with a Si(Li) EDS detector mounted at 90° to the incident beam.

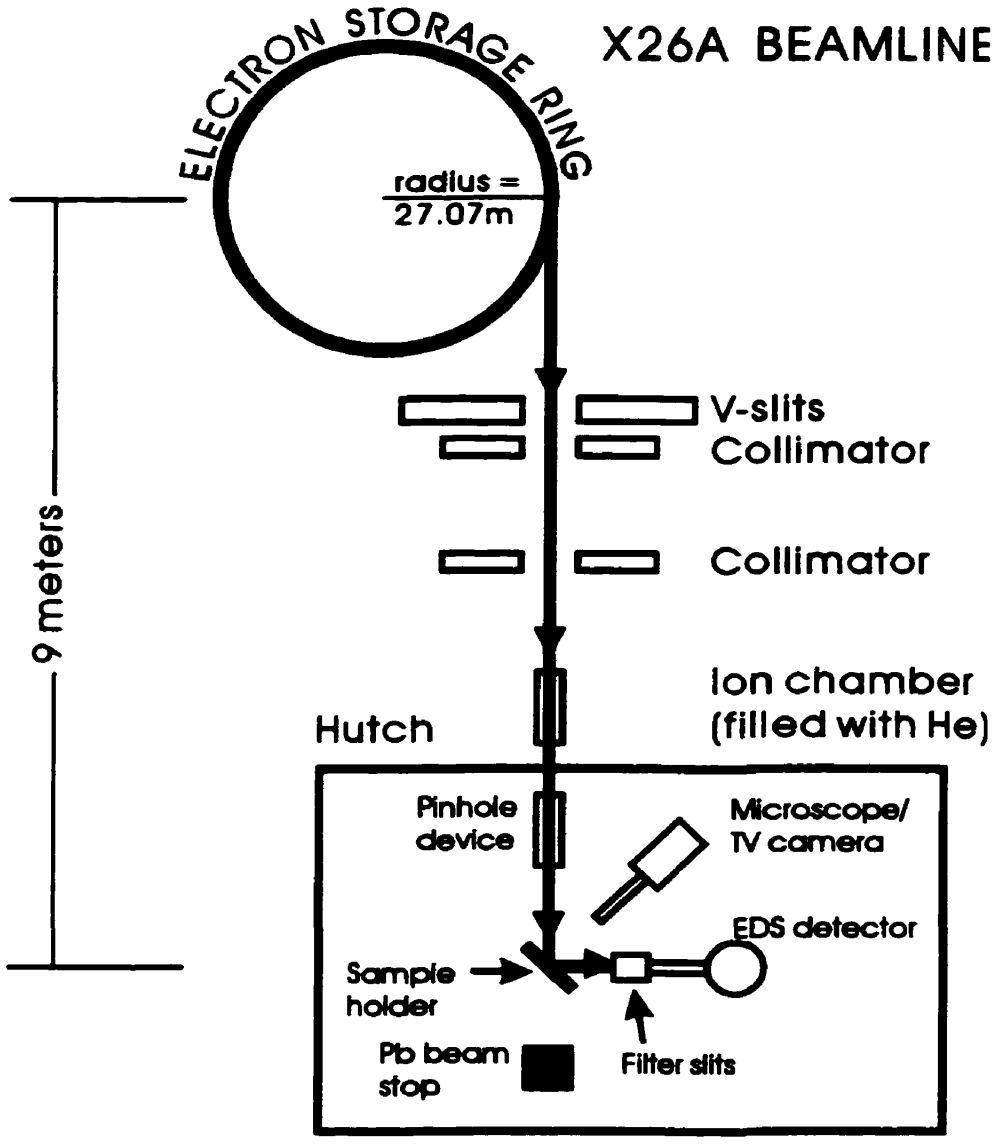
X26A BEAMLINE
ELECTRON STORAGE RING
radius =
27.07m
9 meters
V-slits
Collimator
Collimator
Ion chamber
(filled with He)
Hutch
Pinhole
device
Microscope/
TV camera
EDS detector
Sample
holder
Pb beam
stop
Filter slits

(position located at ±10 μm to the previously analyzed area on the basis of back-scattered electron images). Live time was selected to be 300 s for analyses, yielding a real acquisition time of 390 s. The energy window of the measured spectra was between 2 and 20 keV.

2.5.1.1. Computation of element concentrations and their precision and accuracy

Typical SXRFM spectra of P-MT and HF13 are shown in Figure 2.2. The net areas under the peak in each spectrum were obtained by fitting and subtracting a polynomial background, then fitting Gaussians functions to the residual. Trace-element concentrations are based on an internal standard analysis technique using a modified version of the program NRLXRF (Sutton *et al.* 1987, Bajt *et al.* 1992). This program calculates concentrations of trace elements with corrections for filters (incident beam and detector filters), major-element composition, self absorption, secondary fluorescence, and the specimen's density and thickness. The thickness of each specimen at the point of analysis was measured with a NIKON binocular microscope at 100X and corrected with the material's mean index of refraction to yield the true thickness. The index of refraction of the glasses was measured using immersion oils. Glass densities were calculated using the model of Bottinga *et al.* (1982). Indices of refraction and densities of crystalline phases were estimated using values from Deer *et al.* (1985) for minerals of similar composition. A trace element's concentration is determined by a comparison of the area of trace element's $K\alpha$ peak with the area of the $K\alpha$ peak of an element whose concentration in the sample is known. The internal standard used was iron, previously determined by EMPA at the same point analyzed by SXRFM. The areas

Figure 2.2. Synchrotron X-ray-fluorescence microprobe (SXRFM) spectra showing counts *vs.* X-ray energy. The labeled peaks refer to the principal *K*-energy fluorescence lines. (a) Top subsample of P-MT glass. (b) Top subsample of HF13 glass.

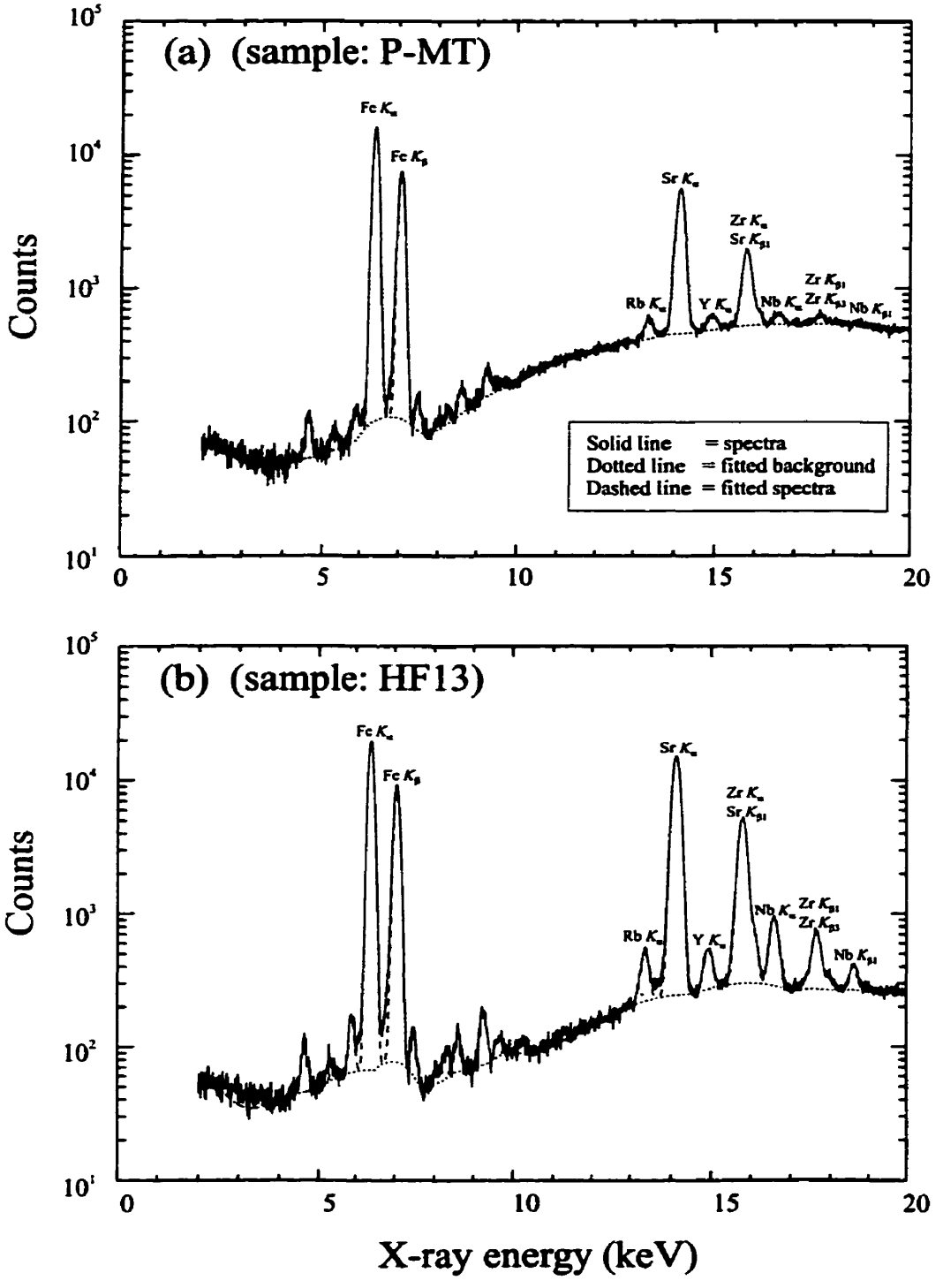
(a) (sample: P-MT)
Fe K_α
Fe K_β
Sr K_α
Zr K_α
Sr $K_{\beta 1}$
Rb K_α
Y K_α
Nb K_α
Zr $K_{\beta 1}$
Zr $K_{\beta 3}$
Nb $K_{\beta 1}$
Solid line = spectra
Dotted line = fitted background
Dashed line = fitted spectra
(b) (sample: HF13)
Counts
X-ray energy (keV)

of the Fe$K\alpha$ peak and trace element-$K\alpha$ peak were combined with the concentration of iron in the specimen to determine the concentration of a trace element using the relation:

$$C_i = S_i \times \frac{I_i}{I_{Fe}} \times C_{Fe}$$

in which, C_i is the concentration of a trace element i, S_i is detection sensitivity (ppm/count) for an element i relative to that for Fe calculated by the NRLXRF program, I_i represents the integrated counts from element i ($K\alpha$ peak), I_{Fe} stands for the integrated counts from the Fe$K\alpha$ peak, and C_{Fe} is the Fe content of the specimen (expressed as the weight fraction of the element; Sutton *et al.* 1987, Lu *et al.* 1989).

We calculated the effects of errors in thickness, density, and iron content of the specimen on the measured concentrations of the trace elements. An error of ±10% relative on either the thickness or the density of a specimen produces a maximum error of ±7% relative in the trace-element concentrations; an error of ±10% relative in the iron concentration results in a maximum error of ±10% relative in the trace-element concentrations. Other potential, systematic errors associated with the SXRFM include uncertainties in the thickness and composition of the filters used between the specimen and the detector (Lu *et al.* 1989). As we show below, by careful analysis, we can analyze trace elements using SXRFM to accuracies within ±20% relative of the accepted values, at concentrations in the ppm range.

2.5.2. Laser-ablation microprobe - inductively coupled plasma - mass spectrometry

LAM-ICP-MS analyses were performed with a Fisons PQ2+ ICP-MS mass spectrometer equipped with a laser microprobe at Université de Montréal. The laser is of the Nd:YAG type, operating at a wavelength of 1064 nm. This laser can be used in two modes: Q-switched and "free-running". In the Q-switched mode, laser radiation does not exit the laser cavity until the radiation reaches a critical level of power, which produces a high-power, short-duration pulse (Jarvis *et al.* 1992, Williams and Jarvis 1993). In the free-running mode, all laser radiation exits the laser cavity; this radiation is of lower power than radiation in the Q-switched mode, but is emitted as a relatively long sequence of pulses (Jarvis *et al.* 1992). The Q-switched mode is used routinely at our facility because it is practically impossible to ablate clear glass samples (*e.g.*, NIST-612 standard) using the free-running mode owing to lower overall efficiencies in ablation (Federowich *et al.* 1993).

However, for the analysis of small samples, the free-running mode has the advantage of minimizing damage to the sample. We have measured the ablation rates for both Q-switched and free-running modes on HF13, P-MT and NIST-612 glasses with a laser blank voltage of 945 V and a repetition rate of 4 Hz. In the present study, the ablation rate of the free-running mode is ~80 μm/min, whereas in Q-switched mode, the ablation rate is 25% greater, ~100 μm/min. Furthermore, diameters of the ablation craters are smaller for the free-running than the Q-switched mode, 34 μm and 62 μm, respectively. The same response in crater diameter between both modes was observed by Williams and Jarvis (1993). Thus the free-running mode is better suited for the analysis of small samples than the Q-switched mode.

However, the free-running mode must be used with a colored sample and results in minimum limits of detection that are a factor of 10 to 100 times greater than in the Q-switched mode (discussed below).

The specimen was ablated inside a silica-glass sample cell under a microscope, with the laser in the free-running mode at a 945 V blank voltage and repetition frequency of 4 Hz. The parameters used for the free-running mode analysis are listed in Table 2.4. To minimize damage, the specimen was rastered during ablation and analysis. Each analysis results from a 2 x 10 matrix of ablation holes, which corresponds to a volume of 50 x 150 x 80 (L x W x D) μm^3 (Fig. 2.3). This mode results in relatively little damage to the anhydrous and hydrous samples, but cannot be used where elements have abundances below ~0.1 ppm (Table 2.3). The ablated material from the sample cell was transferred to the ICP-MS torch *via* a polyurethane tube of 3 mm (i.d.) on a distance of approximately 1.5 m by a continuously flowing stream of Ar gas at atmospheric pressure.

2.5.2.1. Protocol used during the LAM-ICP-MS analyses

The protocol followed during the analyses begins with a gas blank to establish the instrument's background levels, three analyses of our HF13 in-house glass standard for external calibration, another gas blank, and then five unknowns. For our purpose, we repeated that protocol twice to analyze a total of 10 unknowns in 1.5 h. Prior to data collection for every analysis of the in-house standard and unknowns, the sample was ablated with the laser for 1.25 s at each of the 20 points of the grid (Fig. 2.3a); this procedure

Table 2.4. Laser microprobe and ICP-MS (operating conditions)

Laser Microprobe	
laser mode	free-running
voltage	945 V
repetition rate	4 Hz/4 shots
grid parameters	matrix of 2 x 10 ablation holes (increment of 20 μm along x-axis and 15 μm along y-axis)
total shots per grid	80
element menu	17 elements including ^{44}Ca as internal standard
size of sampling grid	50 x 150 x 80 (L x W x D) μm^3
uptake	one full grid (25 s/grid)
focus condition	on sample surface
ICP-MS	
extraction lens	-188 to -202 V
collector lens	1.36 to 3.4 V
nebulizer flow rate	1.144 to 1.192 L/m
cooling gas	13.50 to 13.75 L/m
auxiliary gas	0.800 to 0.825 L/m
mass resolution	0.8 at 10 % peak height
acquisition mode	peak jumping
measuring point/peak	3 points separated by 1/200 AMU[a]
dwell-time per point	10.24 ms/pt
acquisition time	45 s
numbers of repeats	3 (total time = 135 s)
completed sweep	65
total time/mass	1.997 s/mass
analytical masses	^{44}Ca, ^{85}Rb, ^{88}Sr, ^{89}Y, ^{90}Zr, ^{93}Nb, ^{137}Ba, ^{139}La, ^{140}Ce, ^{141}Pr, ^{146}Nd, ^{147}Sm, ^{151}Eu, ^{178}Hf, ^{181}Ta, ^{232}Th, ^{238}U

[a] Atomic mass unit.

Figure 2.3. Physical characteristics of the laser-ablation rastered grid. (a) Schematic view of the ablation-grid pattern. (b) Back-scattered electron images of anhydrous glass (HF13) showing top view of rastered grid produced in free-running mode at operating conditions shown in Table 2.4 (scale bar: 100 μm).

(a)

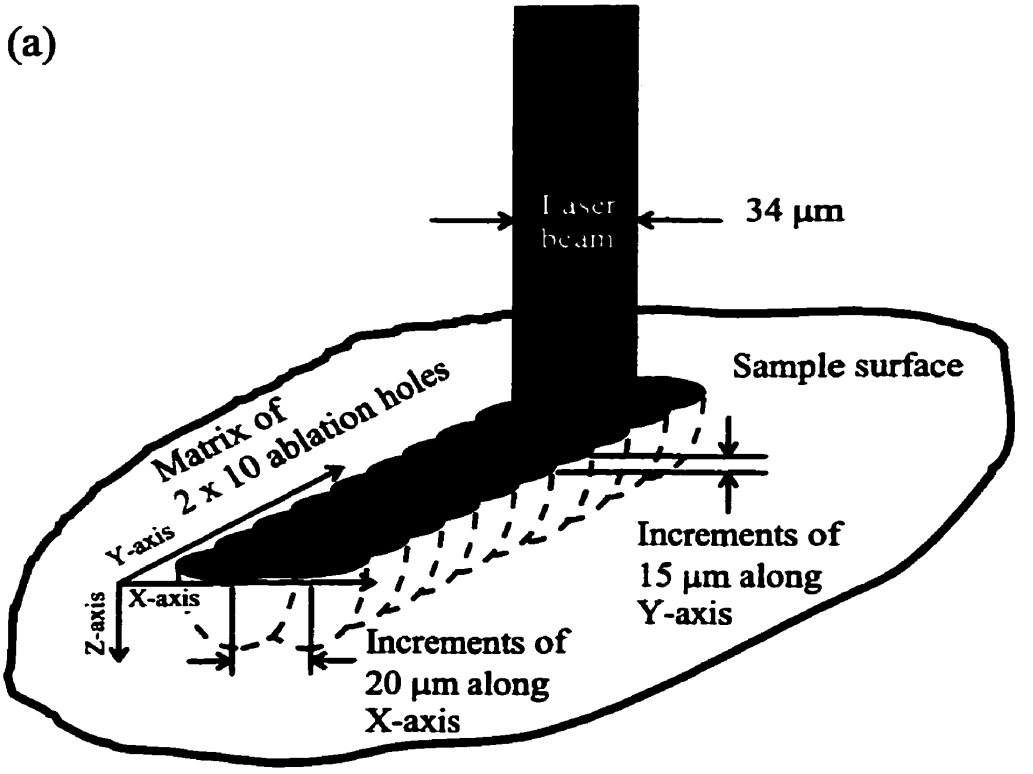
Laser beam
34 µm
Sample surface
Matrix of 2 x 10 ablation holes
Y-axis
X-axis
Z-axis
Increments of 15 µm along Y-axis
Increments of 20 µm along X-axis

(b)

removed the sample's surface (to a depth of ~34 μm) and any contaminants adhering to it. Between each analysis, a pause of 1 min served to flush the gas line between the sample cell and the ICP-MS unit, and also to allow the mass spectrometer to stabilize at background levels.

The acquisition time for one complete analysis was fixed at three repetitions of 45 s each on the same grid for a total time of 135 s (Table 2.4). In this way, each analysis represents ~22 laser shots in each of the 20 holes made in the 2 x 10 grid. For a typical menu of 17 isotopes, the total time spent on each mass during one complete analysis is approximately 2 s. The internal standard used was ^{44}Ca because it successfully reproduces trace-element concentrations of P-MT and HF13 glasses within a relative difference of ±15% compared to the solution-mode results obtained on the HF13 in-house glass standard.

2.5.2.2. Computation of element concentrations and their precision and accuracy

Trace-element concentrations were calculated from the measured count-rates for each isotope by comparing the average background-corrected ablation values of the specimen to an in-house basaltic glass standard (HF13). As mentioned previously, basaltic glass was used instead of NIST glasses because the Nd:YAG laser does not inductively couple with transparent glasses in the free-running mode at the conditions used (Table 2.4).
Concentrations were calculated with the relation:

$$C_{elem,unk} = \frac{\left[\frac{Cps_{isotope}}{Cps_{Ca}}\right]_{unk}}{\left[\frac{Cps_{isotope}}{Cps_{Ca}}\right]_{stand}} \times \frac{CaO_{unk}}{CaO_{stand}} \times C_{elem,stand}$$

where $C_{elem,\,unk}$ stands for the calculated concentration of a particular element in the unknown sample (in oxide wt.%, ppm, ppb, *etc.*), $Cps_{isotope}$ is the background-corrected counts per second of a particular isotope, Cps_{Ca} represents the background-corrected counts per second of the internal standard reference isotope, ^{44}Ca, *unk* is the unknown sample, *stand* is the in-house standard sample, CaO_{unk} is the CaO content in the unknown sample analyzed by EMPA or other analytical techniques (in oxide wt.%), CaO_{stand} is the CaO content in the in-house standard sample analyzed by EMPA or other analytical techniques (in oxide wt.%), and $C_{elem.stand}$ is the concentration of the element in the in-house standard analyzed previously by EMPA or other analytical techniques (in oxide wt.%, ppm, ppb, *etc.*).

An error of ± 10% relative in the Ca concentration measured by the EMPA on both materials (*i.e.*, CaO determined in unknown and in-house standard) results in a maximum error of ± 20% relative for all the elements analyzed with the LAM-ICP-MS using the above formula. This error is similar to that for the SXRFM. Other variables associated with the instrument and the specimen will affect both precision and accuracy: focusing below the surface of the specimen, differences in total abundance of rare-earth elements (REE) between the standard and specimen, thermal fractionation between the internal isotope and the isotopes monitored during ablation, irregular rate of sampling during the ablation owing to physical weakness (*e.g.*, internal fracture in glass due to quench, fluid inclusions and cleavage in

crystals), and differential characteristics in the absorption of infrared light between the standard and specimen (*e.g.*, Moenke-Blankenburg 1989, Jackson *et al.* 1992, Jarvis *et al.* 1992, Fedorowich *et al.* 1993, Feng *et al.* 1993, Jarvis and Williams 1993, Williams and Jarvis 1993, Feng 1994, Jenner *et al.* 1994). Also, instrumental drift of the ICP-MS instrument can affect precision and accuracy of analysis. This drift is corrected by using an external standard for calibration (in our case HF13 glass as mentioned in the above protocol).

2.6 Proof of homogeneity of in-house standards at the trace-element level using EMPA, SXRF, and LAM-ICP-MS

Trace-element homogeneity of both in-house standards has been investigated by EMPA, SXRFM, and LAM-ICP-MS. The EMPA was operated at an accelerating potential of 25 kV with a beam current of 50 nA and a beam diameter of 10 μm. The first test was to analyze subsamples of HF13 for Sr (concentration in HF13: 1516 ppm). The amount of Sr in P-MT standard (469 ppm; see Table 2.3) is too low to give reliable counting-statistics by EMPA. The Sr$L\alpha$ line was counted for 100 s, and backgrounds on both sides for 50 s. Based on four line-profiles of 10 points each, located randomly on HF13 subsamples, the relative standard deviation (RSD: standard deviation/average) based on 40 analyses is 3.9%. The similarity of the theoretical RSD based upon counting statistics (*i.e.*, $\sqrt{N_{\text{net counts}}}/N_{\text{net counts}} = 4.43\%$) with the measured RSD suggests the sample is homogeneous in Sr.

Other tests were performed for Rb, Sr, Y, Zr, and Nb using SXRFM and LAM-ICP-

MS and Ba, La, Ce, Nd, Sm, Eu, Hf, and Ta using LAM-ICP-MS. The RSD determined on the P-MT in-house standard using both microbeam instruments is close to or less than 10% with the exception of Zr and Nb, as obtained by SXRFM, which display an RSD maximum of 19% (Fig. 2.4a). For the HF13 in-house standard, the RSD values of all elements are close to, or below, 12% for both instruments (Fig. 2.4b). However, the RSD calculated on both in-house standards for Rb, Sm, Eu, Hf, and Ta by LAM-ICP-MS are higher than that for Sr, Y, Zr, Nb, Ba, La, Ce, and Nd. One hypothesis is that these elements do not behave in a similar manner to the internal standard (in our case, ^{44}Ca) during the ablation and ionization (Williams and Jarvis 1993). The RSD values for both in-house standards have a similar pattern and similar relative values for each instrument. The low values of RSD calculated for both in-house standards show that they are homogeneous in Rb, Sr, Y, Zr, Nb, Ba, La, Ce, Nd, Sm, Eu, Hf, and Ta using the different microprobe techniques and suggest that they are probably homogeneous in other trace elements.

The upper portions of Figure 2.4 show the measured concentrations of Rb, Sr, Y, Zr, Nb, Ba, La, Ce, Nd, Sm, Eu, Hf, and Ta in P-MT and HF13 using SXRFM and LAM-ICP-MS results compared to solution-mode ICP-MS analyses of the glasses (Table 2.3). For LAM-ICP-MS analyses, HF13 was used for calibration. These plots are based on average values from ten-point, SXRFM, and ten-grid, LAM-ICP-MS analyses from top and middle subsamples of each glass. With the exception of Zr, trace-element concentrations in P-MT can be reproduced to within ±20% by SXRFM and within ±15% by LAM-ICP-MS (Fig. 2.4a). The concentration of Zr determined by SXRFM has a large difference relative to the

Figure 2.4. SXRFM and LAM-ICP-MS results on both in-house standards. The concentration of each element is normalized to solution-mode ICP-MS values in Table 2.3. (a) P-MT standard. (b) HF13 standard. Abbreviations denote: average value based on top and middle subsamples performed by laser-ablation microprobe ICP-MS (LAM-ICP-MS); average value based on top and middle subsamples performed by synchrotron X-ray-fluorescence microprobe (SXRFM). The error bars reflect ±1 standard deviation of ten-point (SXRFM) or ten-grid (LAM-ICP-MS) analyses. Standard deviations smaller than symbol size are not shown in this and subsequent figures. The relative standard deviation (RSD in %) is calculated from the net counts and based on ten analyses, including top and middle subsamples.

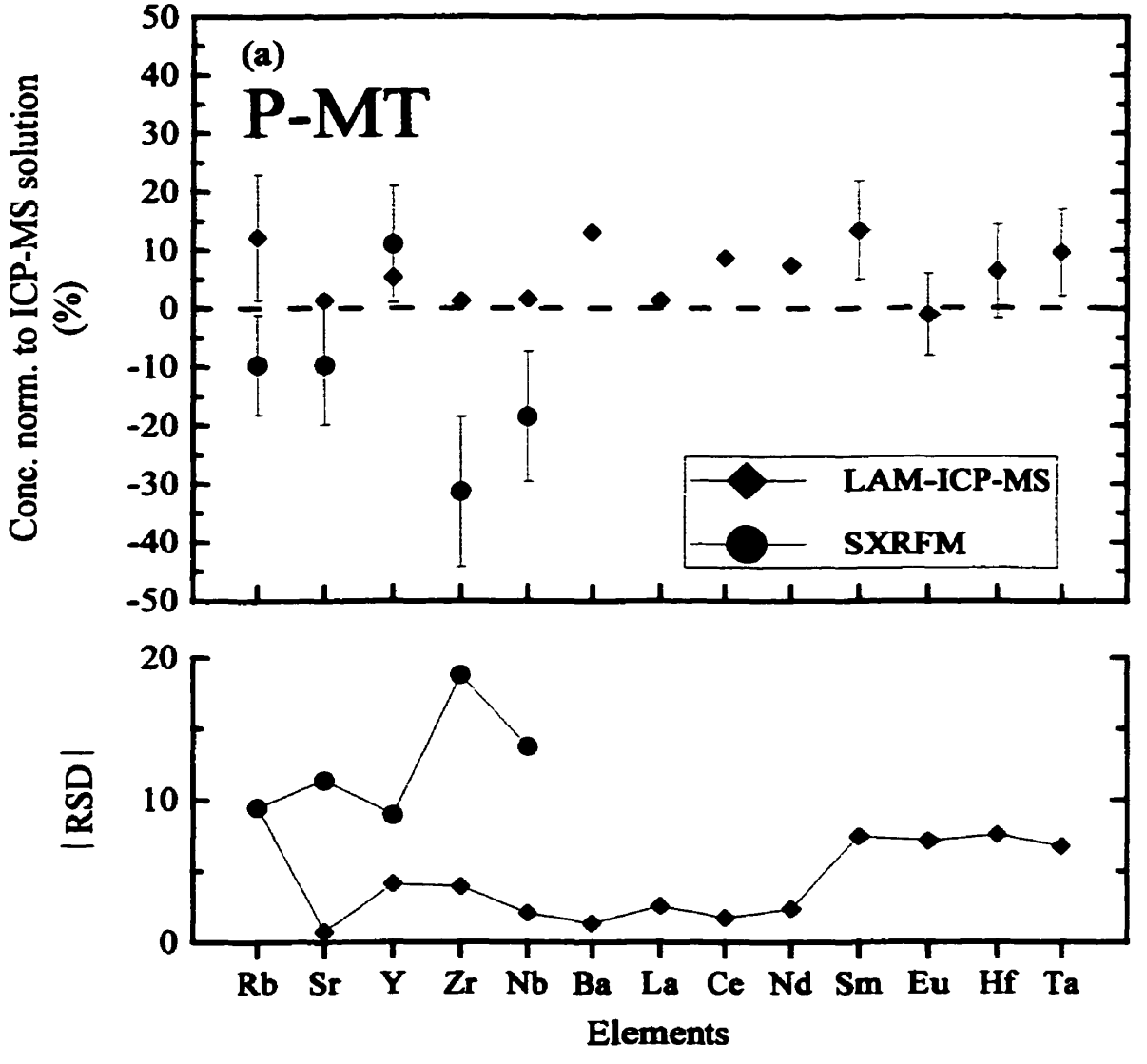
(a)
P-MT
Conc. norm. to ICP-MS solution (%)
50
40
30
20
10
0
-10
-20
-30
-40
-50
LAM-ICP-MS
SXRFM
|RSD|
20
10
0
Rb
Sr
Y
Zr
Nb
Ba
La
Ce
Nd
Sm
Eu
Hf
Ta
Elements

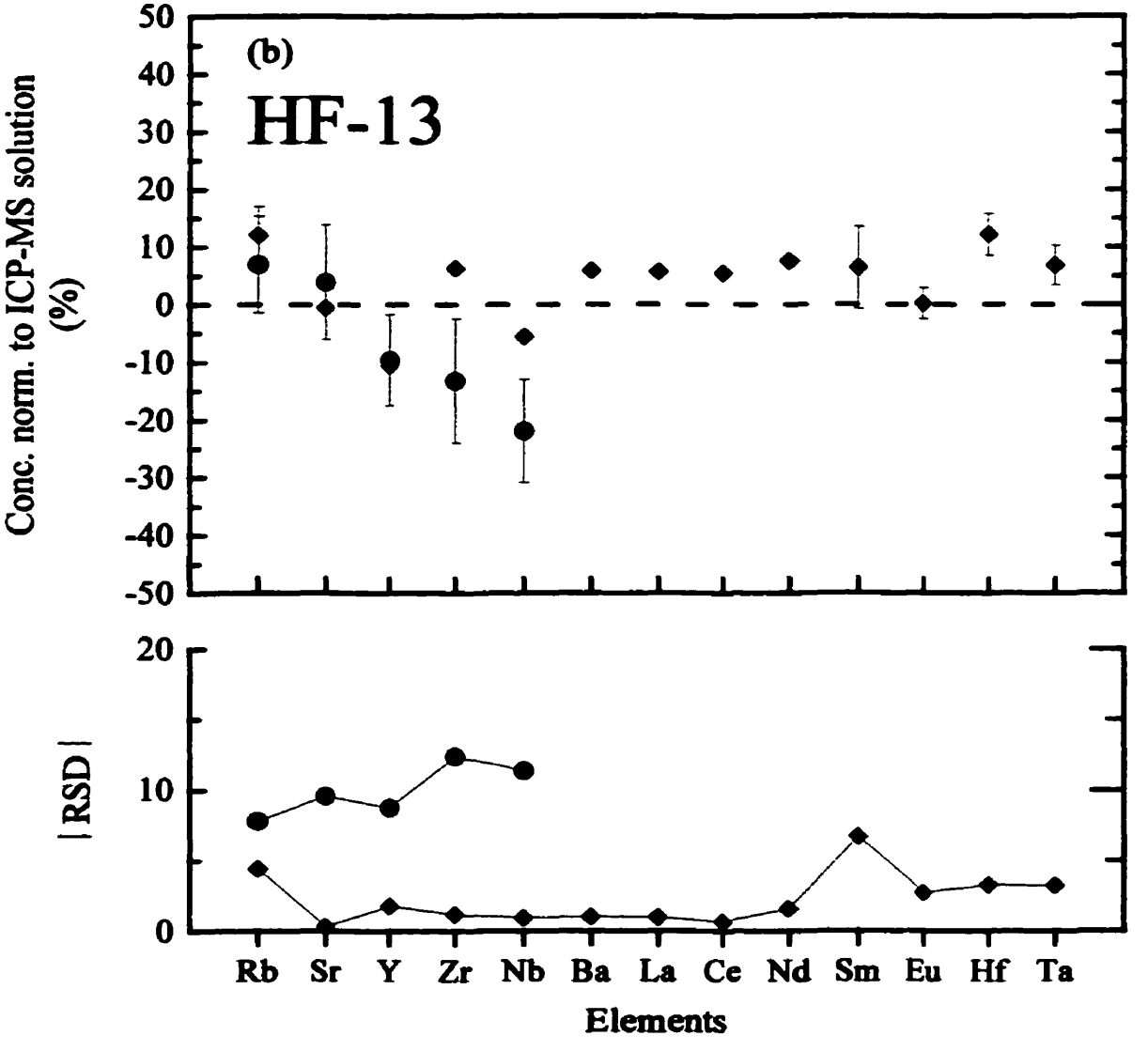
(b)
HF-13
Conc. norm. to ICP-MS solution (%)
50
40
30
20
10
0
-10
-20
-30
-40
-50
|RSD|
20
10
0
Rb
Sr
Y
Zr
Nb
Ba
La
Ce
Nd
Sm
Eu
Hf
Ta
Elements

working value (>30%). This correlates with the high RSD calculated previously (RSD of Zr: 19%), and may be explained by imperfect peak-fitting. We know that in the high-energy range of the spectra (*e.g.*, 14.5 keV to 17 keV), there exists a zone where many peaks overlap. A better peak-fitting routine will improve the results for these elements, but the present results are still acceptable. The trace-element concentrations of HF13 can be reproduced well by the SXRFM technique with a relative error of ±20% based on average values (Fig. 2.4b), with the exception of Nb determined by SXRFM, which shows a larger discrepancy, ~20%. Again, better peak-fitting should improve the results. Overall, the SXRFM results are very good and compare favourably with systematic errors previously reported for this instrument, ±20% relative (Lu *et al.* 1989). The accuracies associated with concentrations of Rb, Sr, Y, Zr, Nb, Ba, La, Ce, Nd, Sm, Eu, Hf, and Ta by LAM-ICP-MS on the HF13 glass are similar to those on P-MT glass (±10 to 15%). In general, the LAM-ICP-MS gives better reproducibility than SXRFM for Sr, Y, Zr, and Nb. The LAM-ICP-MS has poor precision for Rb, Sm, Eu, Hf, and Ta, resulting in large standard deviations on multiple analysis (Fig. 2.4). Lack of matrix matching in major, minor and trace elements, variation in ablation coupling-absorption, physical features, *etc.*, cannot explain these differences for those elements because of the similarity of the in-house standard and the unknown (Jackson *et* al. 1992, Williams and Jarvis 1993). Furthermore, the Rb, Sm, Eu, Hf, and Ta isotopes determined by LAM-ICP-MS and solution ICP-MS are the same (*i.e.*, ^{85}Rb, ^{147}Sm, ^{151}Eu, ^{178}Hf, ^{181}Ta), and there is no evidence of any interferences.

2.7 Sensitivity and detection limits of SXRFM and LAM-ICP-MS techniques

The sensitivities of SXRFM and LAM-ICP-MS were tested using both in-house standard glasses. The purpose of this test was to verify the linear response of the SXRFM and LAM-ICP-MS to changes in the concentrations of different trace elements in our in-house glasses. Also, this test was done for the LAM-ICP-MS to determine the possibility of calibrating with a single in-house standard (in our case, HF13) for quantitative analysis of our experimental run products for a suite of trace elements. We define the sensitivity by the relation:

$$S_i = \frac{\left(Counts_{net-i}\right)}{\left(T_{live} \times Abund_i\right)}$$

where S_i is the sensitivity of a particular element i, $Counts_{net,\,i}$ are the background-corrected counts for element i ($K\alpha$ or isotope peaks for SXRFM and LAM-ICP-MS, respectively), T_{live} is the live time spent during acquisition for the element i (values of 390 s and 1.997 s were used for the SXRFM and the LAM-ICP-MS analysis, respectively), and $Abund_i$ is the relative abundance of the isotope i analyzed with the LAM-ICP-MS [for SXRFM, this variable equals one for all the elements; abundance values taken from De Bièvre and Barnes (1985)].

The sensitivity behaves linearly for both instruments to 30 ppm for Rb, 1600 ppm for Sr, 30 ppm for Y, 300 ppm for Zr, and 120 ppm for Nb (the maximum concentrations of these elements in our in-house standards). However, a larger scatter at low count-rates has

been found for all elements in P-MT glass analyzed by SXRFM compared to LAM-ICP-MS results. This reflects the lower sensitivity of the SXRFM with a small beam-spot at low concentrations, or the higher background-levels of the SXRFM compared to the LAM-ICP-MS. The overall sensitivity of the LAM-ICP-MS is about 1.5 to 2 orders of magnitude (*i.e.*, $10^{1.5}$ to 10^{2}, respectively) greater than the SXRFM for Rb, Sr, Y, Zr, and Nb.

The lower limit of detection for both instruments can be calculated following Bos *et al.* (1984) with the relation:

$$LLD = 3.29 \times f \times Conc_i \times Abund_i \times \frac{\left(N_{blg-i}\right)^{1/2}}{N_{net\ peak-i}}$$

where *LLD* is the lower limit of detection, 3.29 is a constant [defined previously by Currie 1968; Eq. (5b)], f is the correction factor for low background-counts ($1 \leq f \leq \sqrt{2}$; a value of $\sqrt{2}$ was used for both instruments considering the propagation of the errors between the background and peak; Currie 1968), $Conc_i$ is the concentration of the element i (ppm), $Abund_i$ is the relative abundance of the isotope i quantified with the LAM-ICP-MS [for SXRFM, this variable equals one for all elements; abundance values taken from De Bièvre and Barnes (1985)], N_{blg-i} is the total number of background counts of element i ($K\alpha$ or isotope peaks for SXRFM and LAM-ICP-MS, respectively), and $N_{net\text{-}peak\text{-}i}$ is the total background-corrected counts of the peak of element i ($K\alpha$ or the isotope peaks for SXRFM and LAM-ICP-MS, respectively).

This formula was used to calculate LLD values for SXRFM analysis and could be

used for any analytical instrument (Currie 1968). However, it seems in general to overestimate the LLD calculated for LAM-ICP-MS by an average factor of 1.7 for Rb, Sr, Y, Zr, Nb, Ba, La, Ce, Nd, Sm, Eu, Hf, and Ta if compared to the relation (H. Longerich, pers. comm., 1995):

$$LLD = 3 \times Conc_i \times Abund_i \times \frac{Std_{blg-i}}{C_{net\ peak-i}}$$

where Std_{blg-i} is the standard deviation of the total background counts (or cps) of the element i ($K\alpha$ or isotope peaks for SXRFM and LAM-ICP-MS, respectively), $C_{net\ peak-i}$ stands for the background-corrected counts (or cps) of the element i ($K\alpha$ or isotope peaks for SXRFM and LAM-ICP-MS, respectively).

Typical lower limits of detection for Rb, Sr, Y, Zr, and Nb have been calculated for both glasses and are listed in Table 2.3 using the relation of Bos *et al.* (1984). The overall lower limits of detection for elements determined by SXRFM and LAM-ICP-MS are on the order of 5.5 ppm and 2 ppm or less, respectively, and are assumed to be the most conservative LLD values that could be determined for LAM-ICP-MS (Table 2.3). Those results are of the same order of magnitude as those reported in previous studies (Sutton *et al.* 1986, Bajt *et al.* 1992, Jackson *et al.* 1992, Williams and Jarvis 1993).

2.8 Partition coefficients from run products using SXRFM and LAM-ICP-MS data

Kaersutite megacrysts from Hoover Dam, Arizona (U.S.A.), were ground (<500 μm) and used as starting materials. Mixtures of this kaersutite powder + 10 wt.% deionized water were enclosed in graphite capsules and then sealed inside $Ag_{50}Pd_{50}$ capsules. Experiments were performed in a piston-cylinder apparatus with a NaCl-pyrex assembly 1.91 cm in diameter (Baker 1993, Fig. 8.10). Temperature was measured with type-D thermocouples, and no corrections were applied for the effect of pressure on EMF. Experiments were performed by bringing the pressure and temperature of the assembly to 1.5 GPa, 1200°C for 1 h to totally melt the amphibole. The samples then were isobarically cooled at a rate of 10°C/min to 1100°C, and that temperature was maintained for 100 h before quenching. Our previous experiments have shown that constant partition-coefficients seem to be reached within 10 h, but long-duration experiments result in larger crystals that are easier to analyze (Dalpé *et al.* 1992). Run products were inspected optically under oil, and chips of quenched glass + crystals were mounted in epoxy for analysis by EMPA, SXRFM and LAM-ICP-MS.

Run products consist of prisms of calcic amphibole (up to 1 mm along their longest axis; modal proportion: 85%) and hydrated Ti-rich quenched glass (modal proportion: 15%). The calcic amphibole is Ti-rich pargasite based on the classification of Leake (1978), and has a higher Mg_t number [*i.e.*, $Mg\#_t = Mg/(Mg+Fe_{total}) = 85$] compared to that in other experimental studies [*e.g.*, Nicholls and Harris (1980): average $Mg\#_t = 72$; Green and Pearson (1985a): average $Mg\#_t = 70$; Adam *et al.* (1993): average $Mg\#_t = 77$; Adam and Green

(1994): average $Mg\#_t = 77$; J. Adam (pers. comm., 1994): $Mg\#_t = 72$]. The crystal chemistry of our pargasite shows the same amount of calcium in the *M*(4) site [$^{VIII}Ca_{M(4)}$, normalized on a basis of 23 atoms of oxygen per formula unit (apfu)], but a higher proportion of titanium in the *M*(1,2,3) octahedral sites ($^{VI}Ti_{M(1,2,3)}$ 0.47 apfu) compared to that found in other studies [Philpotts and Schnetzler (1970): ^{VI}Ti 0.41; Nicholls and Harris (1980): ^{VI}Ti 0.27; Green and Pearson (1985a): ^{VI}Ti 0.40; Adam *et al.* (1993): ^{VI}Ti 0.23; Adam and Green (1994): ^{VI}Ti 0.23; J. Adam (pers. comm., 1994): ^{VI}Ti 0.25]. The composition of the quenched glass is listed in Table 2.5. It has an $Mg\#_t$ of 65, and contains 7 wt.% normative Ne. It is a Ti-rich basanitic glass based on the classification of Yoder and Tilley (1962).

Line traverses were performed by EMPA across the pargasite and quenched glass to evaluate their homogeneity in major and trace elements (Fig. 2.5). The EMPA was operated at the accelerating potential of 15 kV with a beam current of 50 nA and a beam diameter of 10 μm. The Mg profile shows two flat patterns, one from core to rim in the pargasite crystal and a second located about 100 μm away from the rim (referred to the quenched glass) (Fig. 2.5a). RSD factors of 1.3 and 12.6% were calculated for the two phases, respectively. Some peaks and troughs along the crystal profile are related to fractures made during the polishing and to cleavage in the thin crystal. As we cross from the rim of the crystal to the quenched glass, a rapid drop is observed in Mg, which then gradually increases to a plateau (beyond 100 μm). That pattern is attributed to modification of the melt during quenching (referred as quench-modified glass). The Sr profile shows two flat patterns also separated by a quench-modified region (Fig. 2.5b). Sr in the quench-modified glass shows a profile reverse from that

Table 2.5. Composition of pargasite and quenched Ti-rich basanitic melt from run products at 1.5 GPa, 1100°C

Major elements (in wt.%) determined by EMPA[a]:

	Pargasite		Ti-rich hydrous basanitic quenched melt	
n	18		17	
SiO_2	41.13	(0.42)	38.82	(1.14)
TiO_2	4.33	(0.21)	5.67	(0.26)
Al_2O_3	14.03	(0.43)	13.90	(0.87)
FeO	5.08	(0.25)	7.11	(0.58)
MnO	0.07	(0.02)	0.18	(0.03)
MgO	16.70	(0.19)	6.82	(1.72)
CaO	11.37	(0.37)	11.26	(0.85)
Na_2O	2.19	(0.12)	1.70	(0.28)
K_2O	1.36	(0.38)	1.07	(0.43)
Total	96.26		86.51	

Trace elements (in ppm) determined by[b]:

	SXRFM Pargasite	LAM-ICP-MS[c] Pargasite	SXRFM Quenched melt	LAM-ICP-MS[c] Quenched melt
n	5	5	9	5
Rb	*B-LLD*[d]	2.02 (0.34)	9.78 (1.69)	9.19 (0.91)
Sr	311 (41.4)	334 (4.76)	958 (82.8)	889 (2.71)
Y	8.80 (1.17)	9.61 (0.76)	35.9 (4.43)	28.8 (0.74)
Zr	13.0 (7.26)	15.7 (1.18)	109 (9.96)	127 (1.43)
Nb	*B-LLD*	3.19 (0.37)	54.7 (5.89)	63.7 (1.40)
Ba		115 (2.95)		415 (7.46)
La		0.62 (0.08)		16.0 (0.25)
Ce		4.01 (0.13)		60.1 (0.82)
Nd		5.91 (0.27)		41.5 (0.79)
Sm		2.06 (0.80)		11 (0.98)
Eu		1.20 (0.07)		3.42 (0.08)
Hf		1.38 (0.20)		4.16 (0.16)
Ta		0.27 (0.06)		3.67 (0.09)

Table 2.5. (continued)

Partition coefficients determined by:

	EMPA	SXRFM	LAM-ICP-MS
Ti	0.76 (0.05)		
K	1.27 (0.62)		
Rb		D_{max}= 0.21[e]	0.22 (0.04)[f]
Sr		0.32 (0.04)[f]	0.38 (0.01)
Y		0.25 (0.04)	0.33 (0.03)
Zr		0.12 (0.07)	0.12 (0.01)
Nb		D_{max}= 0.07[e]	0.05 (0.01)
Ba			0.28 (0.01)
La			0.04 (0.00)
Ce			0.07 (0.00)
Nd			0.14 (0.01)
Sm			0.19 (0.08)
Eu			0.35 (0.02)
Hf			0.33 (0.01)
Ta			0.07 (0.02)

[a] Operating conditions used: see section 2.3. [b] Operating conditions used: see section 2.5. [c] Analytical masses used are listed in Table 2.4. [d] B-LLD = concentration Below the Lower Limit of Detection. [e] D_{max} is obtained from: highest LLD of the element$_i$ / conc. of the element$_i$ in quenched melt (see Table 2.3 for LLD values). [f] Values in parentheses are based on one standard deviation from the relationship: $S.D. = [(C_m^2 \times S.D._{gl}^2 / C_{gl}^4) + (S.D._m^2 / C_{gl}^2)]^{0.5}$ where: C is the concentration; m is the mineral; gl is the glass (Adam *et al.* 1993).

Values in parentheses are based on one standard deviation from multiple analyses (1σ).

Figure 2.5. Line traverse showing results of background-corrected qualitative analyses by EPMA on K-HD-08 run products. (a) Mg. (b) Sr. Abbreviations denote: pargasite crystal (PC); quench-modified glass close to rim (QMG); quenched glass located at >100 μm from rim position (QG).

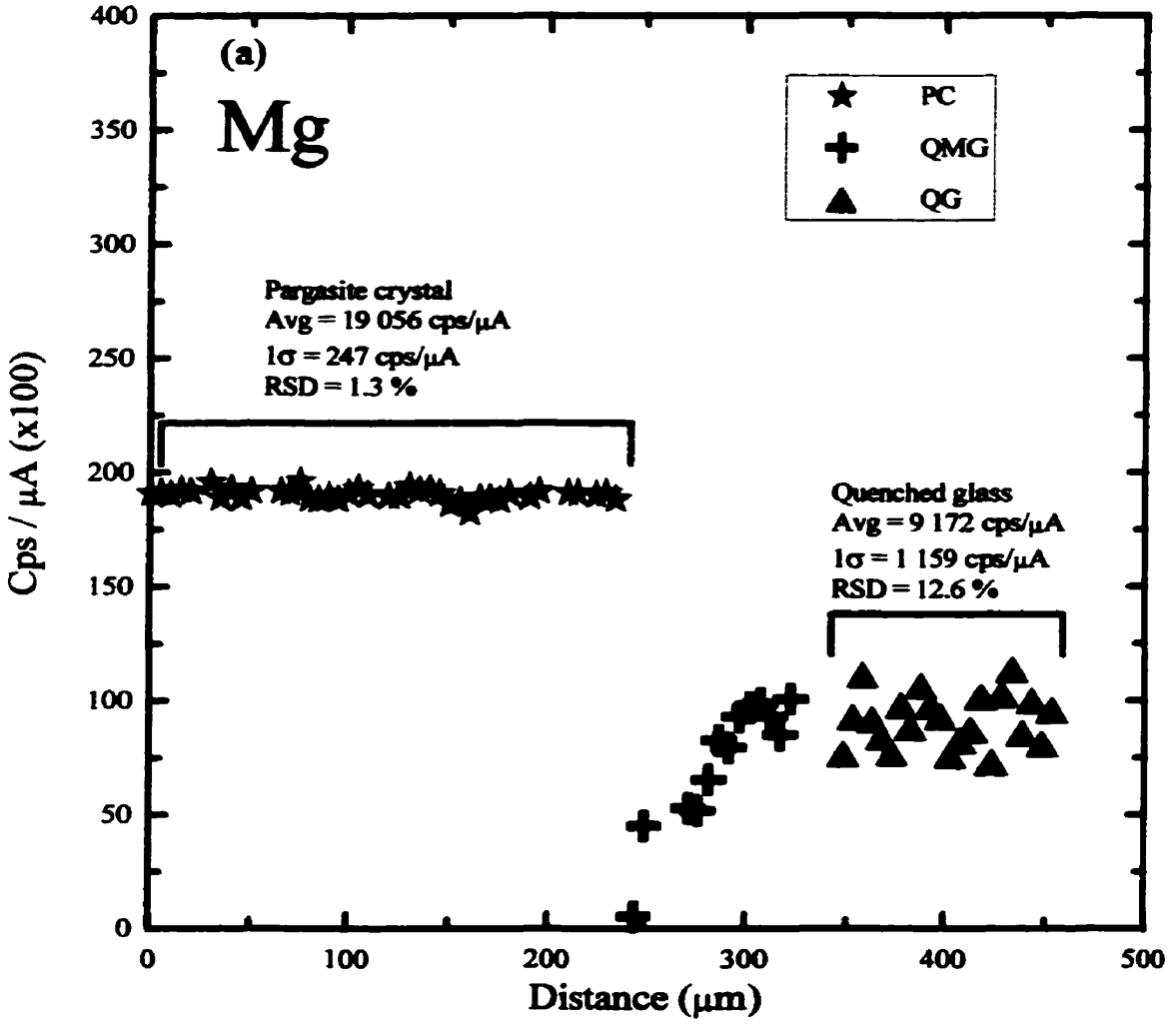
(a)
Mg
PC
QMG
QG
Pargasite crystal
Avg = 19 056 cps/μA
1σ = 247 cps/μA
RSD = 1.3 %
Quenched glass
Avg = 9 172 cps/μA
1σ = 1 159 cps/μA
RSD = 12.6 %
Cps / μA (x100)
Distance (μm)
0
50
100
150
200
250
300
350
400
0
100
200
300
400
500

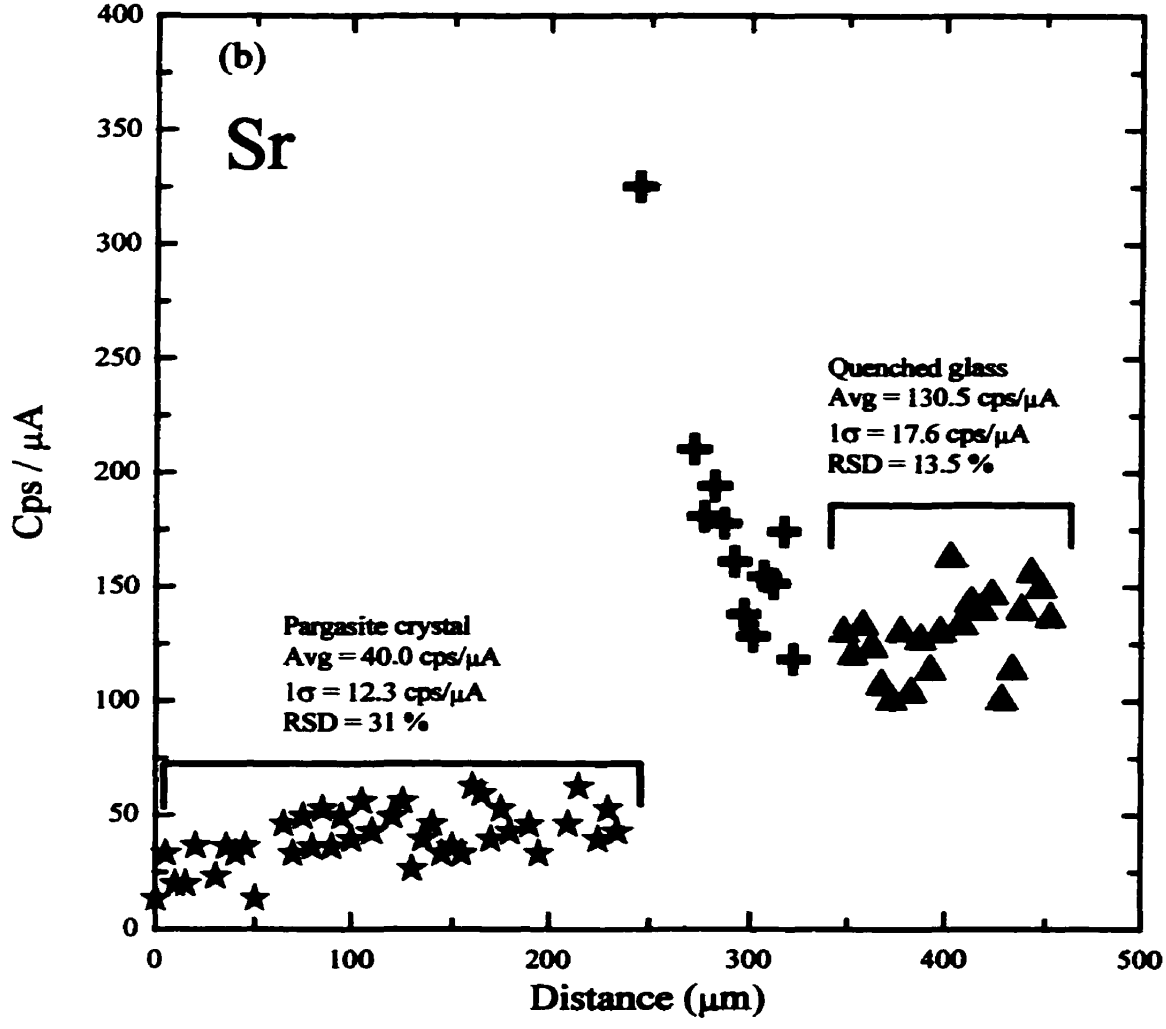
(b)
Sr
Cps / μA
Distance (μm)
Quenched glass
Avg = 130.5 cps/μA
1σ = 17.6 cps/μA
RSD = 13.5 %
Pargasite crystal
Avg = 40.0 cps/μA
1σ = 12.3 cps/μA
RSD = 31 %
0
50
100
150
200
250
300
350
400
0
100
200
300
400
500

of Mg because Sr is incompatible and Mg compatible (Fig. 2.5). The calculated RSD values for Sr are 31 and 13.5% for pargasite crystal and quenched glass, respectively. The high RSD calculated for Sr in the pargasite is not due to inhomogeneity, but reflects low net counts and physical features such as the fractures in the crystal. The RSD calculated in the quench glass for Sr and Mg are similar (<15%) and indicate homogeneity in both cases.

Concentrations of major, minor and trace elements were measured using the procedures previously described in the pargasite and quenched glass with the EMPA, SXRFM and LAM-ICP-MS (Table 2.5). Within one standard deviation, there is agreement for Sr, Y, and Zr in pargasite, as documented by both SXRFM and LAM-ICP-MS (Table 2.5). However, the concentrations of Rb and Nb are below the lower limit of detection for the SXRFM (<3 and 5.5 ppm, respectively; Table 2.3).

For the quenched glass, we report data collected 100 μm beyond the zone of quench-modified glass (Fig. 2.5). This is possible owing to large area of quenched glass found in this run products (glass area of 400 x 700 μm). The level of concentration of Rb, Sr, Y, Zr, and Nb determined by SXRFM in the quenched glass lies within, or close to, one standard deviation of LAM-ICP-MS values (Table 2.5) and invariably within two standard deviations.

Partition coefficients (*i.e.*, $D = C_i^{crystal} / C_i^{melt}$) of selected trace elements were calculated based on SXRFM (Sr, Y, Zr) and LAM-ICP-MS (Rb, Sr, Y, Zr, Nb, Ba, La, Ce, Nd, Sm, Eu, Hf, Ta) data on pargasite and quenched Ti-rich basanitic glass (Table 2.5). The partition coefficients D_{Sr}, D_{Zr}, and D_Y measured by SXRFM between the crystal and the quenched glass are within two standard deviations of values derived from the LAM-ICP-MS

data (Table 2.5).

The partition coefficients D_{Ba}, D_{Rb}, D_{Ta}, D_{Nb}, D_{La}, D_{Sr}, D_{Zr}, and D_{Y} measured by both techniques agree well with previous experimental results, with the exception of D_{Sm}, which is lower than the value measured by Nicholls and Harris (1980), Green and Pearson (1985a), Adam *et al.* (1993), Adam and Green (1994), J. Adam (pers. comm., 1994) (Fig. 2.6a). Our new values for D_{Ce}, D_{Nd}, D_{Hf}, and D_{Eu} determined from LAM-ICP-MS data agree well with the interpolated fields that are formed by previous experimental studies (Fig. 2.6a). In general, our partition coefficients are lower than partition coefficients measured between natural pargasite and coexisting matrix (Higuchi and Nagasawa 1969, Philpotts and Schnetzler 1970, Nagasawa 1973, Sun and Hanson 1976, Irving and Price 1981, Liotard *et al.* 1983, Lemarchand *et al.* 1987) (Fig. 2.6b). Such discrepancies between natural and experimental studies are well documented and may suggest disequilibrium in the case of natural pairs (Green and Pearson 1985a, Beattie 1994).

Partition coefficients for the REE determined in this study are low compared to those documented in most other studies (Fig. 2.6a). The glass compositions of these earlier experimental studies range from basanitic to tholeiitic and do not demonstrate any obvious effects of composition on the partition coefficients. However, it is possible that slight differences in amphibole composition (perhaps differences in $^{VI}Ti_{M(1,2,3)}$ in the pargasite run-products as mentioned previously) have a significant effect on the partition coefficients of trivalent elements. Adam and Green (1994) noted that for amphibole and clinopyroxene,

Figure 2.6. Partition coefficients determined by SXRFM and LAM-ICP-MS between pargasite and Ti-rich basanitic quenched melt. (a) Experimental run-products. Symbols denote: SXRFM (circle); LAM-ICP-MS (diamond); other experimental results [sources: Nicholls and Harris (1980), Green and Pearson (1985a), Adam *et al.* (1993), Adam and Green (1994), J. Adam (pers. comm., 1994)]. The error bars shown reflect one standard deviation from the relationship: $S.D. = [(C_m^2 \times S.D._{gl}^2 / C_{gl}^4) + (S.D._m^2 / C_{gl}^2)]^{0.5}$, where C represents concentration, m stands for mineral, and gl stands for glass (Adam *et al.* 1993). (b) Natural pairs showing minimum and maximum partition-coefficients between pargasite and host rocks [sources: Higuchi and Nagasawa (1969), Phipotts and Schnetzler (1970), Nagasawa (1973), Sun and Hanson (1976), Irving and Price (1981), Liotard *et al.* (1983), and Lemarchand *et al.* (1987)].

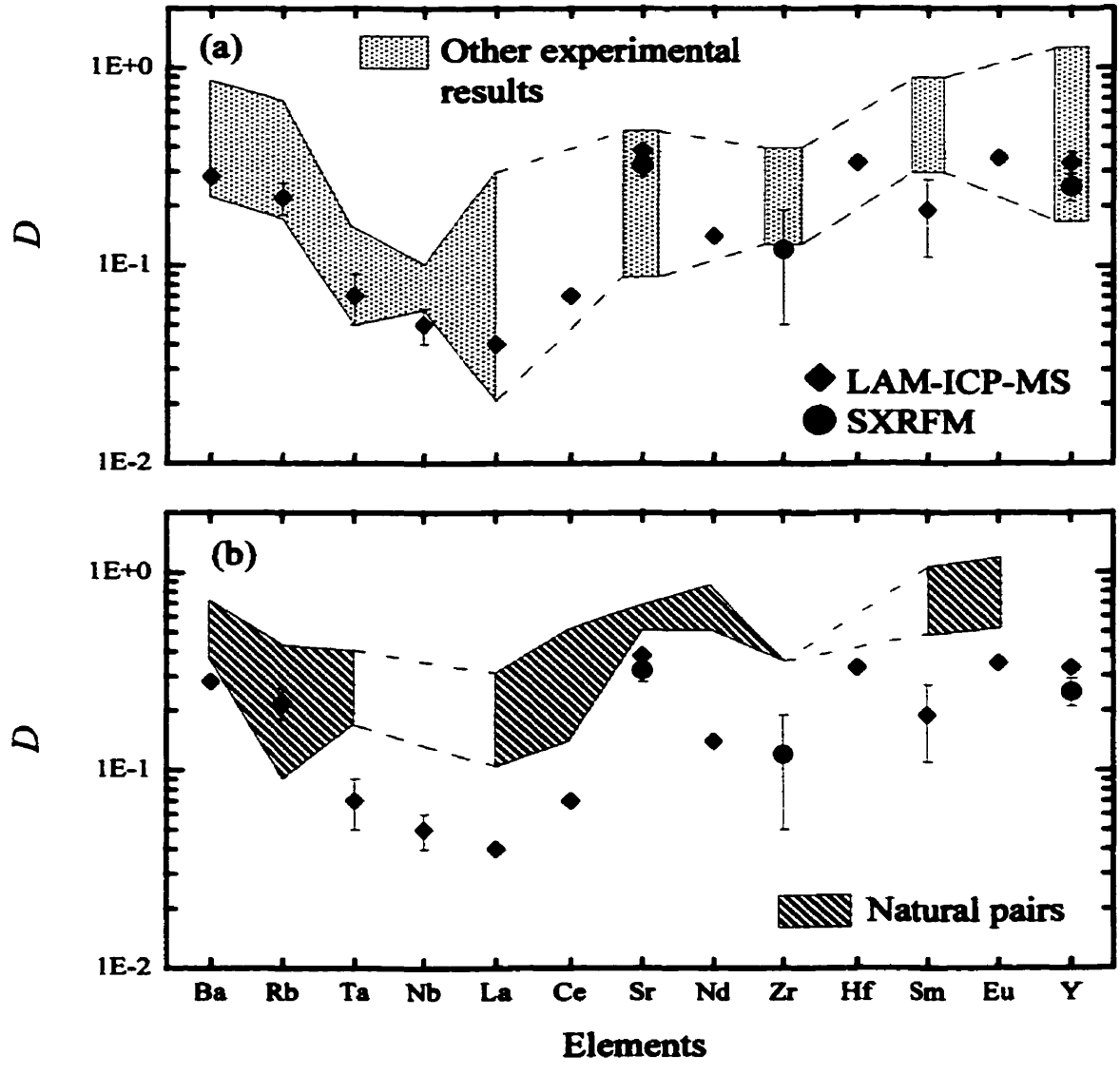
(a)
Other experimental results
LAM-ICP-MS
SXRFM
(b)
Natural pairs
D
1E+0
1E-1
1E-2
Ba
Rb
Ta
Nb
La
Ce
Sr
Nd
Zr
Hf
Sm
Eu
Y
Elements

there is a linear relationship between partition coefficients for Ti and the REE; as D_{Ti} increases, D values for the REE increase at constant pressure and temperature. The low partition coefficients for Ti and REE measured in this study are qualitatively consistent with the results of Adam and Green (1994). However, the influence of the structure of pargasite and the quantitative relationships between REE partition coefficients and Ti cannot be established more firmly without more experiments.

2.9 Comparison of SXRFM and LAM-ICP-MS, and conclusions

The two analytical techniques are reliable and convenient techniques for quantitative determination of the level of concentration of trace elements. The SXRFM offers the possibility of analyzing silicates for all elements between chlorine and molybdenum using $K\alpha$ lines (2.822 to 20 keV) at a very small spatial resolution (on the order of tens of μm) without specimen damage. The LAM-ICP-MS offers the possibility of analyzing a larger suite of elements (*e.g.*, from mass ^{7}Li to ^{238}U) at lower limits of detection than the SXRFM, but damages the sample during analysis.

The overall lower limit of detection for Rb, Sr, Y, Zr, and Nb is on the order of 5.5 ppm and 2 ppm, respectively, for SXRFM and LAM-ICP-MS techniques, the techniques can reproduce the concentrations of these elements within ± 20% and ± 15% of the accepted values, respectively. However, the LAM-ICP-MS data reveal irregular precision in the Rb, Sm, Eu, Hf, and Ta concentrations, which we attribute to the different behaviours of Rb, Sm,

Eu, Hf, and Ta relative to the internal standard, ^{44}Ca, during ablation. Furthermore, the larger area sampled by the LAM-ICP-MS limits this instrument to use on specimens that are homogenous at the scale of hundreds of μm. Future development of LAM-ICP-MS should allow a significant decrease in this size.

Both instruments were used to measure the partition coefficients (*i.e.*, $D = C_i^{crystal} / C_i^{melt}$) between pargasite and a Ti-rich basanitic quenched melt on the same run products. Similar values of D_{Sr} and D_Y, and identical value of D_{Zr}, were measured by both instruments. Also, these D values, together with D_{Be}, D_{Rb}, D_{Ta}, D_{Nb}, D_{La} measured by LAM-ICP-MS, agree well with published results of experimental studies. New values of D_{Ce}, D_{Nd}, D_{Hf}, and D_{Eu} from experimental results in a basaltic system are reported here for the first time.

Chapter 3

Experimental investigation on partitioning of LILE, HFSE, and REE between calcic amphibole and basaltic melt: I- The effect of melt composition and the role of crystal chemistry

3.1 Introduction

The presence of amphibole in upper mantle samples (Best 1974, Dawson and Smith 1982) and its great capacity to host incompatible elements such as K (Oxburgh 1964, Griffin and Murthy 1969), Ba, Rb, Sr (Basu and Murthy 1977), Nb, and Ta (O'Reilly *et al.* 1991, Ionov and Hofmann 1995) relative to other lherzolite minerals suggests its importance in controlling the trace element distribution in the upper mantle and in basaltic melts. Since the study of Oxburgh (1964) demonstrating that amphibole could account for a large proportion of upper mantle source regions for basalts, various petrologic studies recognized that amphibole is responsible for controlling the chemical evolution of primary melts of the alkaline rock series (*e.g.*, Francis and Ludden 1995). Amphibole also represents a "fingerprint" of modal mantle metasomatism (Francis 1976a, -b, Wass and Roger 1980, Wilkinson and Le Maître 1987, Vannucci *et al.* 1995), irrespective of whether that metasomatism is by hydrous fluids or by hydrous magmas (Basu and Murthy 1977). However, to investigate the details of models, or even constrain mantle and melt compositions during partial melting, accurate measurements of the partition coefficients (D) between amphibole and melt are necessary. Because partition coefficients are sensitive to pressure, temperature, and compositions of minerals and melts (McKay 1989) they are best measured in minerals and quenched glasses

synthesized in the laboratory under controlled conditions (*e.g.*, Green and Pearson 1985a).

Even if amphibole is a good repository phase for incompatible elements, their concentrations in synthetic amphiboles from experiments using natural basaltic rocks are quite low (ppb's to ppm's). With such low concentrations in amphibole, the determination of partition coefficients between amphibole and glass by some microbeam techniques is only possible by spiking natural basaltic rock powders with different trace elements of interest using enriched glass, carbonate, or reagent grade oxide material (Green and Pearson 1985a, Adam *et al.* 1993, Adam and Green 1994, LaTourrette *et al.* 1995, Fujinawa and Green 1997), or by using a hand made synthetic glass spiked with 'Specpure' oxides for different trace elements (Nicholls and Harris 1980). The "spiking" experimental method allows analysis of run products by electron or proton-induced X-ray emission (PIXE) microprobes. However one important aspect to verify when using a doping technique is the adherence to Henry's law. Henry's law implies that the partition coefficient of an element i (D_i) should be constant for a range of concentration because the activity coefficient of the doping trace element in each phase remains constant (Navrotsky 1978). In order to test the applicability of Henry's law, some studies performed experiments at identical run conditions with different doping concentrations of a selected element [*e.g.*, hundreds to thousands of ppm] and compared the constancy of the calculated partition coefficient (*e.g.*, Nicholls and Harris 1980, Fujinawa and Green 1997). Other studies compared their partition coefficients with studies on natural mineral/groundmass pairs or with other experimental studies using natural bulk compositions without doping (Green and Pearson 1985a, Adam *et al.* 1993, Adam and Green

1994, LaTourrette *et al.* 1995). Watson (1985) discussed the applicability of Henry's law in synthetic experiments in detail and suggested that doped experiments significantly above natural concentrations should not be discredited. Furthermore, his arguments attempt to demonstrate that non-Henry's law behaviour might occur at very low concentrations which are not generally observed in nature (Watson 1985).

However, large discrepancies have been observed between element ratios analyzed in amphibole or glass in doped experiments compared to element ratios in natural systems (*e.g.*, Nb/Ta, Zr/Nb, Rb/K, La/K). These ratios are very useful for modelling natural systems (*e.g.*, Francis and Ludden 1995, Green 1995). Furthermore, previous experiments only studied the partitioning of the spiked elements which in most cases encompassed different groups of incompatible elements. Thus there is a need for experimental measurements of partitioning for a large suite of elements such as the large-ion-lithophile elements (D_{LILE}), the high-field-strength elements (D_{HFSE}), and the rare-earth elements (D_{REE}) to resolve the appropriate ratios at values close to upper mantle levels. Because mantle amphiboles are mainly associated with alkalic magma series (Best 1974, Dawson and Smith 1982), most recent experimental studies on amphibole partitioning used basanitic compositions (Adam *et al.* 1993, Adam and Green 1994, LaTourrette *et al.* 1995), or alkali basalt compositions (Nicholls and Harris 1980). However, tholeiitic compositions were used by Green and Pearson (1985a) in their experiments. Unfortunately, no complete data set of partition coefficients exists between amphibole and a variety of melt compositions applicable to petrogenesis in the upper mantle.

Chapter 3

In this study, I report on a series of experiments at high pressures (1.5-2.5 GPa) and high temperatures (1000-1130 °C) using a relatively large range of natural mafic compositions from alkalic to sub-alkalic to establish if bulk composition can influence trace element partitioning between amphibole and melt (olivine-normative nephelinite, alkali basalt, olivine-normative tholeiite, and two natural amphiboles, pargasite and kaersutite). Two oxygen buffers (-2 and +1.7 log units from the nickel-nickel oxide buffer) were used to evaluate if the Fe^{3+}/Fe^{2+} ratio affects partitioning using the alkali basalt and the pargasitic compositions (Chapter 4). Two of these mafic compositions were doped with titanium to evaluate if titanium significantly affects partitioning (Chapter 5). Analysis of run products without spiking was possible due to the recent improvement of the laser ablation microprobe inductively coupled plasma mass spectrometer (LAM-ICP-MS) (Jenner *et al.* 1993, Dalpé and Baker 1994a, -b, Dalpé *et al.* 1995). For each experiment, a consistent data-set of 29 elements including 23 trace elements were determined by electron microprobe and LAM-ICP-MS analysis. These data were used to calculate amphibole-melt partitioning. The LAM-ICP-MS provided accurate measurements of a large suite of trace elements (*e.g.*, LILE, HFSE, REE); it is rapid and has a lower limit of detection (LLD) on the order of 1 ppm, or below. Such large data-sets of partition coefficients were used to establish indirectly the physical characteristics of the cation sites in the amphibole structure using Blundy and Wood's (1994) model to investigate the effect of pressure and oxygen fugacity (Chapter 4), and the bulk titanium (Chapter 5) content on trace element partitioning.

Chapter 3

3.2 Experimental techniques

3.2.1. Starting material

Different starting materials of basaltic composition were used to investigate the role of composition on trace element partition coefficients between calcic amphibole and melt. The materials used in this study were: two calcic amphiboles (kaersutite and pargasite megacrysts), olivine nephelinite, alkali basalt and olivine tholeiite (Table 3.1). The kaersutite, K-HD, was from a lamprophyre dike of Pleistocene age located near Hoover Dam, Arizona (U.S.A.; Damon *et al.* 1967, Campbell and Schenk 1950). The pargasite, P-MT, was sampled from a lamprophyre dike of Cretaceous age located in the eastern part of the Island of Montréal, Québec (Canada; donated by G. Pouliot). The olivine nephelinite, HF13, was from a Tertiary intrusion located in the Mount Llangorse alkaline volcanic field of northern British Columbia (Canada; Francis and Ludden 1995; donated by D. Francis). The olivine tholeiite, K1921, was from 1.4 miles south of Volcano Observatory at Kilauea, Hawaii (U.S.A.; Yoder and Tilley 1962). The alkali basalt, FM10, was from north of Keauhou, Hawaii (U.S.A.; Yoder and Tilley 1962). Both of these Hawaiian basalts were graciously donated by H. S. Yoder.

The kaersutite megacrysts K-HD were euhedral and measured up to 10 cm along their longest axes (Campbell and Schenk 1950). The pargasite megacrysts P-MT were also euhedral with lengths as long as 5 cm. Both megacrysts contained veins of white material along some cleavage surfaces; this material probably consisted of calcite + zeolite +

Table 3.1. Starting materials (major and minor elements in wt%)

Bulk samples								
Ref. comp.	K-HD kaersutite		P-MT pargasite		HF13[a] ol-normative nephelinite	K1921[b] ol-normative tholeiite		FM10[b] Alk.-basalt	
n	39		25		1	29		30	
SiO_2	39.37	(0.24)	39.19	(0.35)	40.07	49.89	(0.21)	47.37	(0.19)
TiO_2	5.72	(0.10)	3.61	(0.08)	2.37	2.62	(0.05)	2.25	(0.05)
Al_2O_3	14.02	(0.19)	14.46	(0.24)	11.43	12.62	(0.08)	14.58	(0.12)
Fe_2O_3	nd		nd		4.88	1.53[c]		1.69[c]	
FeO	nd		nd		8.91	8.29[c]		9.20[c]	
FeO_t[c]	9.34	(0.30)	9.11	(0.19)	nd	9.67	(0.24)	10.72	(0.19)
MnO	0.11	(0.03)	0.08	(0.02)	0.23	0.17	(0.02)	0.18	(0.02)
MgO	13.26	(0.20)	14.33	(0.09)	10.91	10.48	(0.09)	9.93	(0.11)
CaO	10.99	(0.19)	11.89	(0.09)	10.69	10.80	(0.07)	10.33	(0.09)
Na_2O	2.35	(0.05)	1.90	(0.04)	4.95	2.16	(0.04)	2.80	(0.05)
K_2O	1.89	(0.09)	2.22	(0.06)	1.86	0.52	(0.02)	0.90	(0.03)
P_2O_5	blld		blld		1.42	0.25	(0.03)	0.26	(0.03)
LOI	nd		nd		0.75	nd		nd	
Total	97.08		96.79		98.47	99.18[b]		99.32[b]	

Table 3.1. (continued)

	Glass samples				Ti-doped glasses			
Ref. comp.	P-MTg[c] pargasitic		HF13g[c] ol-normative nephelinitic		P-MTg$_{Ti}$[d]		HF13g$_{Ti}$[d]	
n	30		30		30		29	
SiO_2	40.43	(0.25)	41.44	(0.24)	42.55	(0.13)	45.74	(0.14)
TiO_2	3.81	(0.04)	2.46	(0.03)	5.87	(0.07)	4.06	(0.06)
Al_2O_3	14.77	(0.09)	11.58	(0.10)	15.85	(0.07)	12.77	(0.04)
Fe_2O_3	1.56[f]		2.31[f]		0.77[f]		1.48[f]	
FeO	7.37[f]		10.15[f]		3.79[f]		7.33[f]	
FeO_t[g]	8.77	(0.16)	12.23	(0.18)	4.48	(0.20)	8.66	(0.10)
MnO	0.09	(0.03)	0.23	(0.03)	0.09	(0.02)	0.24	(0.02)
MgO	14.48	(0.09)	11.36	(0.06)	15.05	(0.11)	12.31	(0.10)
CaO	12.34	(0.06)	11.02	(0.07)	12.75	(0.09)	11.93	(0.08)
Na_2O	1.92	(0.03)	5.12	(0.05)	1.32	(0.05)	2.38	(0.04)
K_2O	2.29	(0.03)	2.01	(0.03)	1.40	(0.05)	0.96	(0.02)
P_2O_5	0.04	(0.02)	1.46	(0.03)	blld		0.32	(0.03)
LOI	nd		nd		nd		nd	
Total	98.94[h]		98.91[h]		99.40[h]		99.37[h]	

Abbreviations: n-number of analyses, nd-not determined, blld-concentration below the lower limit of detection. [a] Analysis taken from Francis and Ludden (1995). [b] Sample analyses were done on glass formed by melting the bulk powder at T = 1300 °C under controlled oxygen fugacity (FMQ) in a 1 atm furnace for 4 h. [c] Analyses taken from Dalpé *et al.* (1995). [d] See text for details. [e] Fe_2O_3 and FeO proportions are calculated using total iron from the electron microprobe at T = 1300 °C, P = 1 atm, and fO_2 = FMQ (Kress and Carmichael 1991). [f] Fe_2O_3 and FeO proportions are calculated using total iron from the electron microprobe at T = 1400 °C, P = 1 atm, and fO_2 = FMQ (Kress and Carmichael 1991). [g] Total iron as FeO. [h] Totals are calculated using FeO_t.

Values in parentheses are based on one standard deviation from multiple analyses (1σ).

anorthoclase, which was noted by Campbell and Schenk (1950). The kaersutite and pargasite megacrysts were first coarsely crushed in a steel percussion mortar then clean chips free of the white material were handpicked. These chips were ground into a powder (<500 μm) in an agate mortar. The olivine nephelinite was received as powder (<140 μm) prepared in a tungsten carbide ball mill. The alkali basalt and the olivine tholeiite were received as rock samples (Yoder, pers. comm., 1994). Both were ground in a tungsten carbide ball mill to a fine powder (<140 μm). This grinding apparatus almost certainly contaminated the samples with W, Co, Sc, Ta, and possibly, Nb (Hickson and Juras 1986).

Two compositions were used as starting materials in both crystalline and glassy phases. The P-MT and HF13 bulk powders were melted four times at 1400 °C, 1 atm in an Fe-treated Pt crucible at the Fe_2SiO_4-Fe_3O_4-SiO_2 (FMQ) oxygen fugacity buffer. To minimize iron loss to the Pt crucible I dedicated one Pt crucible to melting only basaltic material which was cleaned with BDH® Analar grade hydrofluoric acid 48 % (HF) between each glass synthesis. Samples were melted for four hours each time. Between fusions samples were crushed in a steel percussion mortar, cleaned of steel fragments with a magnet, and coarsely ground in an agate mortar and pestle. The final glasses were homogeneous and free of oxide minerals (Dalpé *et al.* 1995). In order to investigate the possible effect of Ti on the partition coefficients, aliquots of these two glasses were doped with TiO_2 (anatase; Baker analyzed reagent, lot no. 25592) and mixed for 45 min in an agate mortar under ethanol. The Ti-enriched P-MT glass, P-MTg_{Ti}, and the Ti-enriched HF13 glass, HF13g_{Ti}, each contained approximatly 50 % more TiO_2 than their initial compositions. The mixed powders were dried

and melted for 4 hours at 1400 °C in an Fe-pretreated large Pt capsule (i.d. = 4.7 mm) at 1 atm and at FMQ buffer. To minimize iron loss the new Pt capsules were pretreated by melting the initial rock or glass powders for four hours at the same conditions as used for the preparation of the Ti-doped glasses. The capsule used to synthesize $HF13g_{Ti}$ was treated with HF13, and the capsule for $P\text{-}MTg_{Ti}$ was treated with P-MTg. Between Fe treatment and glass synthesis, the Pt capsules were cleaned with BDH® Analar grade hydrofluoric acid 48 % (HF). These clear brown glasses, free of crystalline material, were crushed in an agate mortar under ethanol (< 200 μm in size) and dried (Table 3.1). They were stored at room temperature in hermetic vials.

3.2.2. Details of the experimental procedure

3.2.2.1. Piston-cylinder assemblies and techniques

Experiments were performed in a piston-cylinder apparatus (Boyd and England 1960) with NaCl-Pyrex® furnace assemblies. Experiments at 1.5 GPa were performed with a 1.91 cm assembly (see Hudon *et al.* 1994, fig. 1) and those at and above 2.0 GPa were performed using a 1.27 cm assembly (Dunn 1993). A pressure correction of - 12.5 % was applied for the 1.91 cm diameter furnace assembly based on pressure calibration with the NaCl melting curve (Bohlen 1984). No pressure correction was used for the 1.27 cm furnace assembly based upon the same calibration.

Temperature was measured with $W_{95}Re_5/W_{26}Re_{74}$ (type-C) thermocouples, and no corrections were applied for the effect of pressure on the electromotive force (EMF).

Experiments were performed in different ways for the 1.91 and 1.27 cm assemblies. For the 1.91 cm assembly, I used a modified "hot piston-out" technique. For 1.5 GPa experiments, pressure and temperature were simultaneously increased to 1.7 GPa and 1200 °C (or 1225 °C depending upon bulk material), respectively. After reaching 1.7 GPa, 1200 °C (or 1225 °C), pressure was decreased slowly to 1.5 GPa. The samples were held at these conditions for 1 h to form a melt then isobarically cooled at 1 to 10 °C/min to the desired run temperature. For the 1.27 cm assembly, I used another modification of the "hot piston-out" technique. Pressure was initially increased to 0.2 GPa over the run pressure (*e.g.*, 2.4 and 2.7 for the 2.2 and 2.5 GPa run pressures, respectively). The samples then were isobarically heated to 1200 °C for 1 h to totally melt the starting materials. Preliminary experiments at 1200 °C (or 1225 °C) for the different starting materials (*i.e.*, crystals and bulk rocks) were found to be long enough to ensure the total melting of the hydrated materials after 1 h (Dalpé *et al.* 1992). During experiments, I used the same initial procedure (*i.e.*, 1 h at 1200 or 1225 °C) for the glass *vs.* crystal or bulk rock starting materials in order to maintain the same pressure and temperature paths. After reaching the melting point of the starting materials, the pressure was maintained at the +0.2 GPa run pressure. The samples then were cooled at 10 °C/min and pressure was allowed to fall to the desired run conditions. At the final run temperature, a little adjustment (± 5 %) of the final pressure was needed for some runs. During all experiments pressure was maintained within 0.05 GPa of the desired value. Quenching of all experiments was done by cutting off the power resulting in cooling rates of ~200 °C/s for the first four seconds.

3.2.2.2. Oxygen fugacities in experiments

Two different capsule assemblies were used to create low and high oxygen fugacity conditions. The low oxygen fugacity experiments were approximately 2 log units below the Nickel-Nickel Oxide buffer (NNO-2). The high oxygen fugacity experiments were approximately 1.7 log units above NNO (NNO+1.7). For low oxygen fugacity experiments, mixtures of the starting materials (~ 12 mg of powder) + 8-12 wt.% deionized water were enclosed in graphite capsules (O.D. = 2.60, I.D. = 2.10, and length = 2.90 mm) and covered with a graphite lid. These graphite capsules were inserted into a noble metal capsule of $Ag_{50}Pd_{50}$ (or $Au_{75}Pd_{25}$; both with O.D. = 3.00, I.D. = 2.70, and length = 9.00 mm) which was carefully packed with graphite powder at the bottom and top of the graphite capsule. The outer capsule was crimped and welded in a water bath to eliminate water loss. The oxygen fugacity was determined in an experiment at 1.5 GPa, 1100 °C for 20 h using $Ag_{50}Pd_{50}$ as the outer container with a starting material of iron oxide (FeO; V. T. Baker analyzed reagent, Lot #785176) + 10 wt.% deionized water. X-ray powder diffraction of the run products demonstrated that the oxygen fugacity was in the wüstite field (FeO), which corresponds to at least 2 log units below the nickel-nickel oxide buffer (*i.e.*, NNO-2). For all experiments performed using this assembly, the estimated Fe^{3+}/Fe^{2+} ratio was assumed to be 0. The second assembly used a single container to produce the high oxygen fugacity. Mixtures of starting materials (~ 20 mg) + ~ 10 wt.% deionized water were enclosed in $Au_{75}Pd_{25}$ (O.D. = 3.00, I.D. = 2.70, and length = 9.00 mm) and welded closed without water loss. The oxygen fugacity inside this assembly was determined to be + 1.7 log units above the nickel-nickel

oxide buffer (*i.e.*, NNO+1.7) at 1.5 GPa, 1220°C using P-MTg as the starting material (*i.e.*, P-MTg powder + 10 wt.% deionized water). The value was calculated using analyses of the run products, which consisted of olivine + quenched glass, and assuming a Fe^{2+}-Mg exchange coefficient between olivine and melt of 0.30 (*i.e.*, $K_D^{Fe2+/Mg} = (Fe^{2+}/Mg)_{Olivine} / (Fe^{2+}/Mg)_{Liquid} = 0.30$; Roeder and Emslie 1970). In such a case, the estimated Fe^{3+}/Fe^{2+} ratio in the melt calculated for this assembly was 0.6. Combining this measurement with the Kress and Carmichael (1991) relationship between fO_2 and the Fe^{3+}/Fe^{2+} yields an oxygen fugacity of NNO+1.7. Using a similar NaCl-pyrex assembly, Kawamoto and Hirose (1994) estimated an oxygen fugacity of about 1.3 log units above nickel-nickel oxide (*i.e.*, NNO+1.3) for an experiment at 0.5 GPa, 1100 °C using $Au_{75}Pd_{25}$.

3.2.2.3. Discussion on iron-loss to the different alloy containers

The estimated iron-loss for the double capsules with $Ag_{50}Pd_{50}$ alloy outer capsules (*i.e.*, $Ag_{50}Pd_{50}$ + graphite inner capsule + graphite powder in both ends) was calculated by mass-balance to be less than 14 relative % for run conditions at 1020-1130 °C, at 1.5 GPa, for all experimental durations (*i.e.*, 24 to 100 h). However, the estimated iron-loss to $Au_{75}Pd_{25}$ alloy (*i.e.*, $Au_{75}Pd_{25}$ + graphite inner capsule + graphite powder in both ends) calculated by the same technique was very high ~ 55 relative %, resulting in a zoned amphibole in the experiment for run conditions at 1050 °C and at 1.5 GPa after 72 h. However, only one experiment was performed with this double $Au_{75}Pd_{25}$ assembly. For the single capsule the estimated iron-loss to the $Au_{75}Pd_{25}$ container calculated by mass-balance

was less than 10 relative % for run conditions at 1000-1075 °C and at 1.5-2.5 GPa for various durations (*i.e.*, 24 to 100 h). Kawamoto and Hirose (1994) calculated an iron-loss to $Au_{75}Pd_{25}$ less than 4 relative % after 24 h at 1225-1400 °C and 0.5-1.5 GPa. The iron-loss from the charge to the $Au_{75}Pd_{25}$ container depends on the iron activity in the Au-Pd-Fe alloy which depends on the oxygen fugacity and temperature of the run. The present results indicate that at more reducing conditions (*i.e.*, NNO-2), $Au_{75}Pd_{25}$ with a graphite inner capsule produced a higher degree of iron-loss, approximately four times that of experiments in which $Ag_{50}Pd_{50}$ was used as the outer capsule.

3.2.3. Preparation of run products

After each experiment, different parts of the run products were mounted in oil for optical microscopy to determine the presence of amphibole and glass. After this verification a fraction of the run products were mounted in epoxy resin then polished using a final 0.30 μm pure alumina powder for electron microprobe and laser-ablation microprobe analyses. There was no attempt to preserve any spatial relationship of the run products during mounting and polishing for the analysis. As discussed below, multiple analyses of major, minor, and trace elements of amphibole crystals demonstrated that they are homogenous in each experiments.

3.3 Analyses of experiments

3.3.1. Major and minor element analyses

Major and minor elements were analyzed with a JEOL 8900 electron-microprobe at the Department of Earth and Planetary Sciences, McGill University. The electron-microprobe operated at an accelerating potential of 15 kV with a beam current of 10 nA; for each element, counting times were 25 s on the peak and 10 s on each background position. For both phases (*i.e.* crystal and glass) I used a defocussed beam with a diameter of 10 μm. The beam was defocussed because the texture found in most of our hydrous basaltic glass run products showed 1-5 μm anhedral to euhedral crystals formed during quenching. Albite (Na), diopside (Si, Ca, Mg), andradite (Fe), orthoclase (K, Al), and pyrophanite (Mn, Ti) were used as standards for both minerals and glass.

3.3.2. Trace element analyses

LAM-ICP-MS analyses were performed with a Fisons VG PQII+ ICP-MS mass spectrometer equipped with a Fisons VG laser microprobe at Laboratoire Ultratrace, Département de Géologie, Université de Montréal. The laser is a Nd:YAG operating at a wavelength of 1064 nm. All analyses were performed with the laser in free-running mode at a blank voltage of 610 V and repetition frequency of 4 Hz. The specimens were ablated inside a silica-glass sample cell with a high magnification lens (40x) that produces a laser beam of approximately 34 μm in diameter in the free-running mode. The free-running mode

has the advantage of generating a smaller beam size with less penetration and less specimen damage than the Q-switched mode (Dalpé *et al.* 1995). The parameters used for analysis in the free-running mode are listed in Table 3.2. To minimize damage, the specimen was rastered under the laser beam during ablation. Each analysis was from a 2 × 10 matrix (*i.e.*, large grid), or from a 1 × 5 matrix (*i.e.*, small grid) of ablation holes which corresponded to a volume of 50 × 150 × 80 or 35 × 90 × 20 (L × W × D μm^3), respectively (see Dalpé *et al.* 1995; Fig. 3). The small grid was used for K1921 run products because amphiboles were too small to be analyzed using the large grid (amphibole crystals less than ~250 μm along their longest axis). This analysis technique resulted in relatively little damage to the samples, but could not be used where elements had abundances below ~0.03 ppm (see lower limit of detection in Table 3.2). The ablated material from the sample cell was transferred to the ICP-MS torch *via* a polyurethane tube of 3 mm (I.D.) over a distance of approximately 1.5 m by a continuously flowing stream of Ar gas at atmospheric pressure.

3.3.2.1. Protocol used during the LAM-ICP-MS analyses

The protocol followed during the analyses began with a gas blank measurement to establish the instrument's background levels, three analyses of an in-house glass calibration standard (Dalpé *et al.* 1995), another gas blank, and then five unknowns. I repeated this protocol twice to analyze a total of 10 unknowns in 1.5 h. Prior to data collection for every analysis the sample was ablated for 1.25 s at each of the 20 points of the large grid or each of the 5 points of the small grid; this procedure removed the sample surface to a depth of ~34

Table 3.2. Laser microprobe and ICP-MS: operating conditions.

Laser microprobe

laser mode	free-running	
voltage	610 V	
repetition rate	4 Hz/4 shots	
grid parameters[a]	Large grid matrix of 2 × 10 ablation holes (increments of 20 μm along x-axis and 15 μm along y-axis)	Small grid matrix of 1 × 5 ablation holes (increments of 0 μm along x-axis and 10 μm along y-axis)
total shots per grid	80	20
size of sampling grid (L × W × D) μm^3	50 × 150 × 80	35 × 90 × 50
uptake	one full grid (25 s/grid)	one full grid (≈7 s/grid)
focus condition	sample surface	idem

ICP-MS

extraction lens	-188 to -202 V		
collector lens	1.36 to 3.4 V		
nebulizer flow rate	1.144 to 1.192 l/m		
cooling gas	13.50 to 13.75 l/m		
auxiliary gas	0.800 to 0.825 l/m		
mass resolution	0.8 at 10 % peak height		
acquisition mode	peak jumping		
measuring point/peak	3 pts/peak separated by 1/200 atomic mass unit		
dwell-time/point	10.24 ms/pt		
acquisition menu	A	B	C
acquisition time[b]	45 s	45 s	45 s
numbers of repeats	3	3	3
completed sweep[b]	65	157	157
total time/mass[b]	1.997 s/mass	4.823 s/mass	4.823 s/mass
analytical masses[b] (lower limit of detection - unit in ppm)[c]			
	^{44}Ca, ^{85}Rb (0.5), ^{88}Sr (0.6), ^{89}Y (0.5), ^{90}Zr (1.3) ^{93}Nb (0.6), ^{137}Ba (0.1) ^{139}La (.09), ^{140}Ce (.06), ^{141}Pr (.07), ^{146}Nd (.08), ^{147}Sm (.03), ^{151}Eu (.04), ^{178}Hf (.15), ^{181}Ta (.03), ^{232}Th (.08), ^{238}U (0.04)	^{44}Ca, ^{151}Eu (.04), ^{159}Tb (.07), ^{160}Gd (.04), ^{163}Dy (.06) ^{165}Ho (.07), ^{166}Er (.14)	^{44}Ca, ^{166}Er (0.14), ^{169}Tm (0.06), ^{172}Yb (.08), ^{175}Lu (.04) ^{232}Th (.08), ^{238}U (.04)

Table 3.2. (continued)

[a] Two different grids used in this study for large and small amphibole run products (see text). [b] The numbers mentioned under the acquisition time, completed sweep, total time/mass, and (lower limit of detection) are based on the large grid parameters (*i.e.*, 2 × 10 matrix). The calculated parameters for the small grid (*i.e.*, 1 × 5 matrix) are: acquisition time (20 s); completed sweep (28 for menu A and 69 for menus B and C); total time/mass (0.86 s/mass for menu A and 2.12 s/mass for menus B and C); lower limit of detection [Rb (0.13), Sr (0.53), Y (0.58), Zr (1.0), Nb (0.43), Ba (0.08), La (0.09), Ce (0.09), Pr (0.07), Nd (0.07), Sm (0.06), Eu (0.05), Hf (0.15), Ta (0.07), Th (0.13), U (0.08) ppm]. [c] The lower limit of detection (*i.e.*, lld) are calculated using Longerich's equation based on pargasitic glass composition as opposed to Bos *et al.*'s (1984) equation used in Chapter 2 (*i.e.*, P-MTg; see Dalpé *et al.* 1995). The operating conditions from this Table are different than those mentioned in Table 2.4 due the replacement of the Spectron SL-400 Nd:YAG 500 mJ pulsed laser (1064 nm at a pulse of 15 ns) by a Spectron SL-282 Nd:YAG 350 mJ pulsed laser (1064 nm at a pulse width of 5 ns) in 1994.

μm and any contaminants adhering to it. Between each analysis a pause of one minute served to flush the gas line between the sample cell and the ICP-MS unit of any residual material and to allow the mass spectrometer to stabilize at background levels.

Because the concentrations of heavy-rare-earth elements (HREE), Th, and U in amphibole run products were very low, three element menus were used to optimize counting statistics. The LILE (Rb, Sr, Ba) + HFSE (Y, Zr, Nb, Ta, Hf, U, Th) + light-rare-earth elements (LREE: La, Ce, Pr, Nd, Sm, Eu) were grouped together to form the first element menu, the middle-rare-earth element (MREE: Eu, Tb, Gd, Dy, Ho, Er) formed the second group, and HREE (Er, Tm, Yb, Lu) + Th and U formed the third group. In the three menus, ^{44}Ca was used as the internal standard and replicate isotopes were used to monitor reproducibility between different acquisition element menus (*e.g.*, Eu, Er, Th, U). For the large grid (*i.e.*, 2 × 10 matrix), the acquisition time for one complete analysis was fixed at three repetitions of 45 s for a total time of 135 s (Table 3.2). The total time spent on each mass during one complete analysis was between approximately 2 to 5 s for the 17 or 7 isotopes in the different element menus, respectively. However for the small grid (*i.e.*, 1 × 5 matrix), the acquisition time for one complete analysis was fixed at three repetitions of 20 s for a total time of 60 s (Table 3.2). The total time spent on each mass during one complete analysis was between approximately 0.9 to 2 s for the 17 or 7 isotopes in the different element menus, respectively.

3.4 Run products

3.4.1. General observations

The experimental conditions and run products are listed in Table 3.3. For all the starting materials used in this study, large amphiboles (~400-1000 μm along their longest axis) were relatively easy to crystallize by simply adding water to the different bulk compositions. However, technical problems occurred in run K1921-15 (tholeiite composition) and in run P-MT-34 (pargasite composition). For K1921-15 run, amphiboles were too small to be analyzed by the large grid matrix normally used on the laser (crystals formed ~250 μm along their longest axis). In such cases, the small grid was used on the laser ablation microprobe to complete the analyses of all the different trace elements (Table 3.2). A zoned amphibole was observed in P-MT-34 run due to the significant iron-loss to the container as mentioned previously. This particular run will be discussed below.

Based upon back-scattered electron images, it seems that amphiboles finished crystallizing after olivine or clinopyroxene. In general, I observed that amphiboles enclosed anhedral to euhedral olivine and clinopyroxene crystals (*e.g.*, Fig. 3.1). Similar relationships were observed in another experimental study (Brenan *et al.* 1995) and in xenoliths found in alkaline rocks (Francis 1976b). Two exceptions in this sequence were observed using the kaersutite composition (*i.e.*, K-HD-08 run) and using the alkali basalt composition (*i.e.*, FM10-02 run). In these experiments, amphibole was the liquidus phase (K-HD-08) or shared the liquidus with mica (FM10-02). Merrill and Wyllie (1975; see Fig. 1) observed the same

Table 3.3. Experimental conditions and run products.

sm	run#	T (°C)	P (GPa)	fO_2[a]	H_2O[b] (wt.%)	Time (h)	Modes[c] am	mi	ol	cpx[1]	cpx[2]	ilm	gl
P-MT	27	1100	1.5	low	10.0	100	62	9	tr	11	-	-	18
P-MT	34[d]	1050	2.5	low	9.65	72	20	8	-	16	-	-	56
P-MTg	12	1100	1.5	low	8.0	24	48	5	tr	7	-	-	40
P-MTg	43	1050	1.5	high	10.0	24	24	3	8	2	-	-	63
P-MTg	41	1075	2.5	high	10.1	24	8	10	3	14	-	-	65
$P\text{-}MTg_{Ti}$	31	1130	1.5	low	10.3	200	15	-	10	4	-	-	71
K-HD	08	1100	1.5	low	9.5	100	65	-	-	-	-	-	35
HF13	38	1020	1.5	low	9.96	72	52	-	-	1	-	-	47
$HF13g_{Ti}$	03	1040	1.5	low	9.7	100	42	-	-	4	-	-	54
K1921	15	1020	1.5	low	12.0	24	17	-	-	25	8	1	49
FM10	02	1040	1.5	low	10.4	24	21	6	-	-	-	-	73
FM10	23	1000	1.5	high	10.1	100	27	-	-	14	-	-	59
FM10	25	1000	2.2	high	10.0	100	48	-	-	13	-	1	38

Abbreviations: sm-starting material, run#-run number, am-amphibole, mi-mica, ol-olivine, cpx[1]-Ca-rich clinopyroxene, cpx[2]-Ca-poor clinopyroxene, ilm-ilmenite, gl-glass. [a] Low oxygen fugacity buffer using the graphite inner capsule with $Ag_{50}Pd_{50}$ or $Au_{75}Pd_{25}$ and high oxygen fugacity buffer using a single capsule of $Au_{75}Pd_{25}$ alloy; the log fO_2 determined inside these containers were found to be NNO+1.7 and NNO-2.0, respectively (see text). [b] Total weight percent of deionized water added to the starting materials (see text). [c] Modes are calculated by least-square mass-balance using SiO_2, TiO_2, Al_2O_3, FeO, MgO, CaO, Na_2O, and K_2O from electron microprobe analyses. [d] Zoned amphibole was observed for this run (see text). None of these run products appeared water saturated.

Figure 3.1. Back-scattered electron images showing typical run products. (a) HF13-38; (b) P-MTg$_{Ti}$-31. Figures (c) and (d) show the ablation grid produced by the LAM-ICP-MS analyses for both HF13-38 and P-MTg$_{Ti}$-31 run products, respectively (grid dimensions: 50 × 150 μm^2, Table 3.2). Letters denote: Am-amphibole, Cpx-clinopyroxene, Ol-olivine. In both run products amphibole surrounds clinopyroxene (lighter zone) and olivine (darker zone); better observation on (b) and (d). Note at the bottom of (a) and (c) the penetration of liquid into cracks in the graphite capsule. Scale bar: 100 μm.

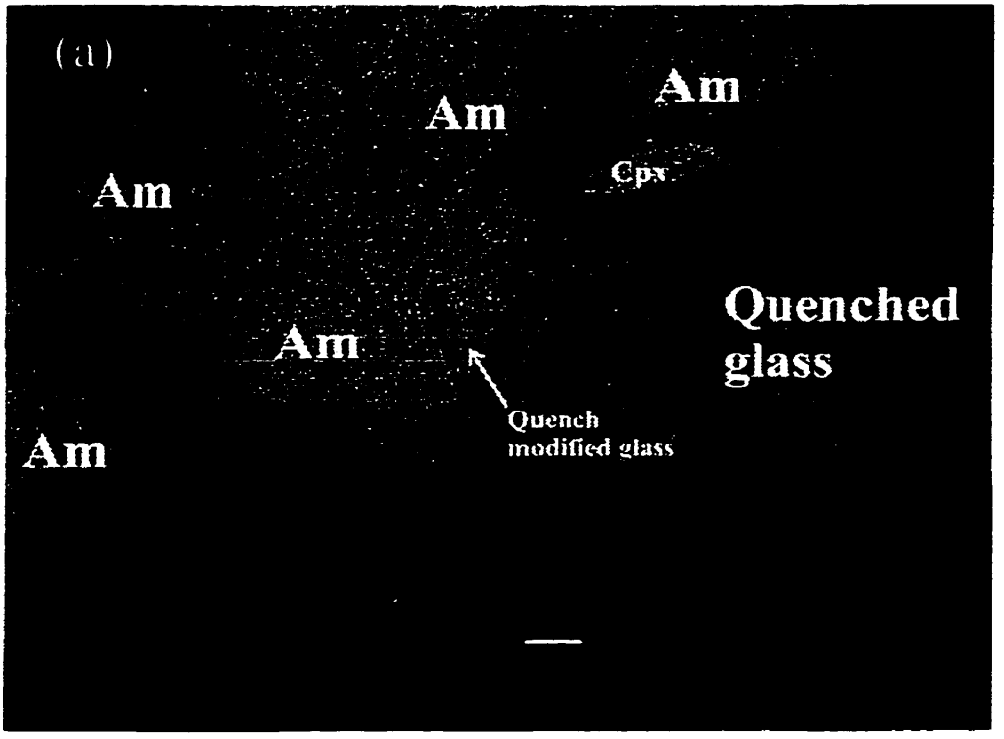
(a)
Am
Am
Am
Cpx
Quenched glass
Am
Am
Quench modified glass

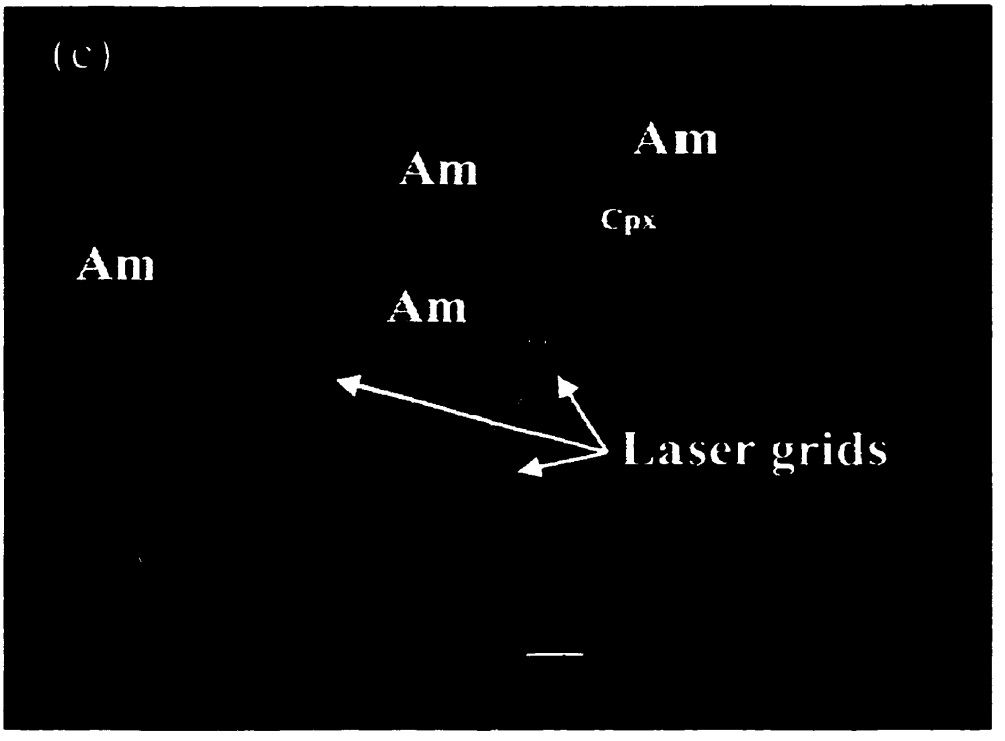
(c)
Am
Am
Cpx
Am
Am
Laser grids

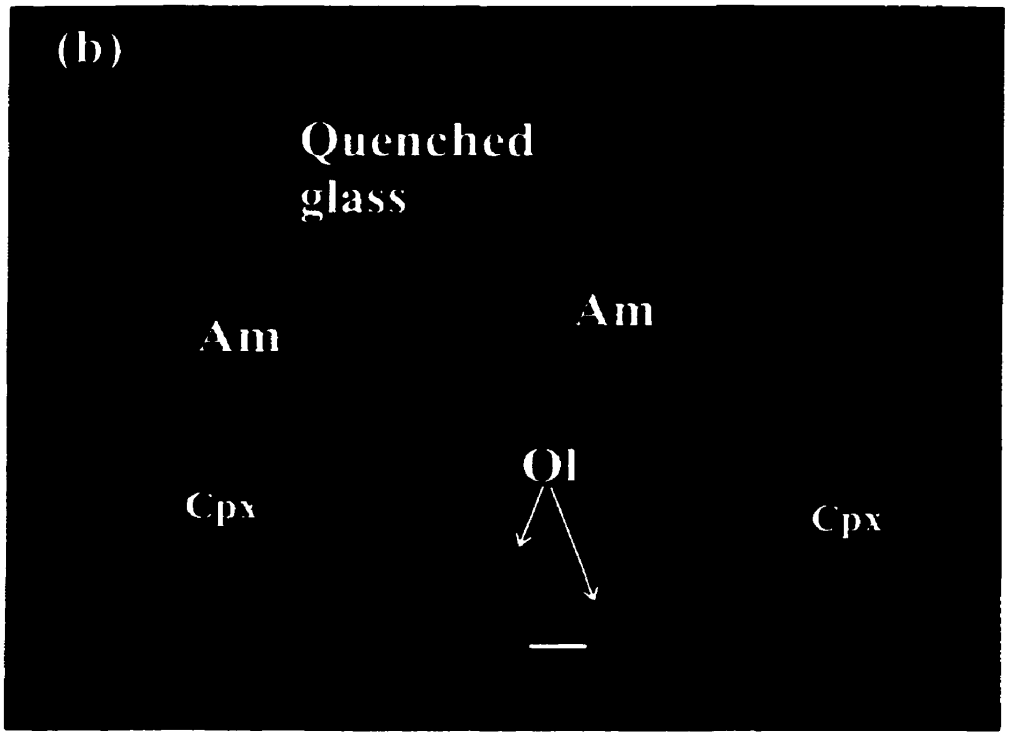
(b)
Quenched glass
Am
Am
Ol
Cpx
Cpx

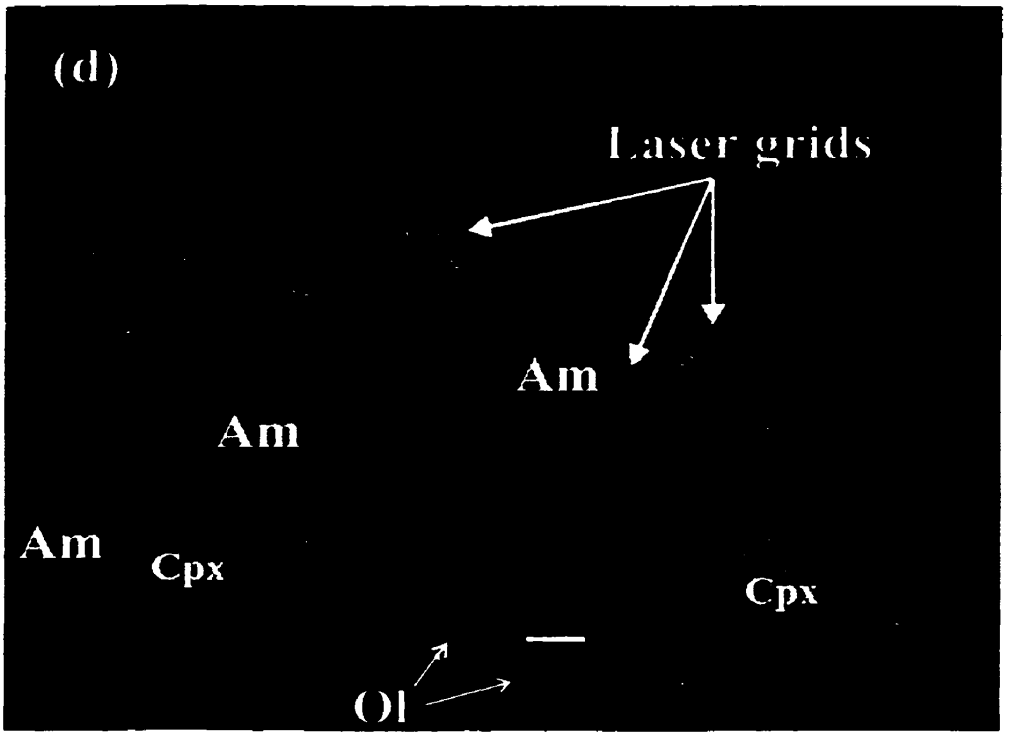
(d)
Laser grids
Am
Am
Am
Cpx
Cpx
Ol

run products (*i.e.*, amphibole + melt) as in our K-HD-08 experiment using a kaersutite megacryst plus excess water at 1100 °C, 1.5 GPa, and at an oxygen fugacity below the nickel-nickel oxide buffer (*i.e.*, $fO_2 < NNO$).

3.4.1.1. Amphibole

The major and trace element analyses of amphiboles are listed in Table 3.4. All the amphiboles from this study are classified as calcic amphibole using Leake *et al.*'s (1997) classification. The estimated Fe^{3+}/Fe^{2+} ratio of each amphibole run product was determined using the empirical model of Schumacher (1997). Based on the six different stoichiometric constraints of Schumacher (1997; see his Fig. A-1), amphiboles from experiments P-MT-27, P-MT-34, P-MTg-12, P-MTg$_{Ti}$-31, K-HD-08, HF13-38, HF13g$_{Ti}$-03, K1921-15, and FM10-02 performed at the low oxygen fugacity (*i.e.*, NNO-2) and amphiboles from experiments FM10-23 and FM10-25 performed at the high oxygen fugacity (*i.e.*, NNO+1.7) satisfied individually the six stoichiometric limits using total iron as ferrous iron in their structural formula (*i.e.*, $Si \leq 8$, $\sum Al \geq 8$, $\sum Mn \geq 13$, $\sum Ca \leq 15$, $\sum Na \geq 15$, and $\sum K \leq 16$ atoms per formula unit, referred hereafter as apfu; Schumacher 1997). For these amphiboles, acceptable formulae are shown in Table 3.5. However, amphiboles which crystallized from experiments P-MTg-41 and P-MTg-43 violated at least one of the stoichiometric limits when I considered total iron as ferrous iron in their structural formula (*e.g.*, $Si \leq 8$, $\sum Ca \leq 15$, and $\sum K \leq 16$; Schumacher 1997). In such cases, Fe^{3+} may be present in their structural formula. The

Table 3.4. Amphibole compositions in experiments

sm	P-MT		P-MT[a]		P-MT[a]		P-MTg		P-MTg	
run#	27		34a		34b		12		41	
n	30		25		12		30		34	
(wt.%)										
SiO_2	40.65	(0.64)	41.28	(0.52)	42.59	(0.38)	40.23	(0.60)	40.90	(0.53)
TiO_2	3.56	(0.16)	2.13	(0.11)	2.12	(0.05)	3.78	(0.22)	1.79	(0.15)
Al_2O_3	15.46	(0.56)	16.05	(0.67)	15.43	(0.41)	16.18	(0.40)	15.93	(0.29)
FeO	4.98	(0.20)	5.03	(0.46)	2.50	(0.08)	5.15	(0.30)	4.67	(0.15)
MnO	blld		blld		blld		blld		blld	
MgO	16.29	(0.37)	16.99	(0.26)	18.50	(0.16)	16.27	(0.24)	17.27	(0.31)
CaO	11.86	(0.18)	11.21	(0.30)	11.69	(0.08)	12.08	(0.25)	12.23	(0.19)
Na_2O	2.13	(0.18)	2.14	(0.17)	1.91	(0.04)	1.86	(0.09)	1.80	(0.10)
K_2O	1.83	(0.25)	2.22	(0.24)	2.54	(0.05)	2.21	(0.12)	2.77	(0.08)
Total	96.76		97.05		97.27		97.76		97.36	
(ppm)										
n[c]	6-12		2-6		1		3-13		1-4	
Rb	5.16	(1.25)	4.19	(0.35)	nd		5.16	(1.23)	6.73	(0.003)
Sr	336.8	(16.4)	214.8	(20.0)	nd		343.0	(14.9)	277.7	(3.6)
Y	6.81	(0.47)	4.89	(0.26)	nd		6.77	(0.50)	4.97	(0.16)
Zr	15.1	(1.5)	5.13	(0.44)	nd		16.4	(1.2)	5.67	(0.04)
Nb	2.78	(0.33)	blld		nd		3.08	(0.51)	blld	
Ba	180.2	(26.2)	108.5	(7.1)	nd		175.6	(27.8)	182.0	(3.7)
Hf	1.05	(0.17)	0.39	(0.03)	nd		1.06	(0.16)	0.19[d]	
Ta	0.17	(0.06)	0.05	(0.01)	nd		0.28	(0.03)	0.04[d]	
Th	blld		blld		nd		blld		blld	
U	blld		blld		nd		blld		blld	
La	1.58	(0.31)	0.39	(0.02)	nd		0.92	(0.16)	0.59	(0.09)
Ce	6.74	(1.09)	1.97	(0.18)	nd		4.27	(0.52)	2.88	(0.01)
Pr	1.39	(0.14)	0.55	(0.06)	nd		0.99	(0.12)	0.68	(0.02)
Nd	7.48	(0.65)	3.39	(0.28)	nd		6.16	(0.27)	4.57	(0.14)
Sm	2.18	(0.24)	1.30	(0.16)	nd		1.91	(0.28)	1.41	(0.03)
Eu	0.88	(0.19)	0.74	(0.13)	1.10		0.89	(0.08)	0.56	(0.09)
Gd	2.00	(0.50)	1.60	(0.28)	1.78		2.47	(0.16)	1.73	(0.07)
Tb	0.30	(0.08)	0.24	(0.01)	0.26		0.33	(0.04)	0.26	(0.01)
Dy	1.43	(0.37)	1.23	(0.12)	1.18		1.73	(0.12)	1.18	(0.03)
Ho	0.22	(0.06)	0.25	(0.004)	0.21		0.29	(0.04)	0.19	(0.01)
Er	0.59	(0.16)	0.51	(0.07)	0.67		0.78	(0.07)	0.47	(0.04)
Tm	blld		blld		nd		0.10	(0.01)	blld	
Yb	0.40	(0.13)	0.34	(0.10)	nd		0.47	(0.05)	0.24	(0.06)
Lu	blld		blld		nd		0.09	(0.01)	0.05	(0.01)

Table 3.4. (continued)

sm	P-MTg		P-MTg$_{Ti}$		K-HD[b]		HF13		HF13g$_{Ti}$	
run#	43		31		08		38		03	
n	30		45		18		40		32	
(wt.%)										
SiO_2	40.23	(0.59)	40.29	(0.46)	41.13	(0.42)	43.51	(0.41)	43.65	(0.56)
TiO_2	3.19	(0.23)	4.97	(0.16)	4.33	(0.21)	2.66	(0.13)	3.94	(0.33)
Al_2O_3	15.41	(0.50)	15.63	(0.35)	14.03	(0.43)	11.59	(0.49)	11.88	(0.48)
FeO	5.79	(0.57)	2.28	(0.06)	5.08	(0.25)	8.35	(0.42)	6.91	(0.47)
MnO	blld		blld		blld		0.13	(0.02)	0.12	(0.02)
MgO	16.40	(0.55)	17.28	(0.32)	16.70	(0.19)	15.43	(0.28)	16.58	(0.33)
CaO	12.50	(0.11)	12.24	(0.12)	11.37	(0.37)	10.63	(0.43)	10.50	(0.32)
Na_2O	1.86	(0.08)	1.97	(0.06)	2.19	(0.12)	3.06	(0.12)	3.07	(0.09)
K_2O	2.38	(0.12)	2.02	(0.06)	1.36	(0.38)	1.35	(0.12)	1.48	(0.12)
Total	97.76		96.68		96.19		96.71		98.13	
(ppm)										
n[c]	3-7		2-5		2-7		2-4		2-5	
Rb	6.22	(1.33)	5.58	(0.31)	1.98	(0.33)	5.29	(0.27)	5.21	(0.06)
Sr	379.6	(28.9)	366.2	(14.4)	329.8	(4.6)	363.9	(9.0)	447.7	(9.6)
Y	6.90	(0.41)	7.15	(0.35)	11.0	(0.8)	9.77	(0.23)	12.1	(0.2)
Zr	20.8	(0.70)	22.1	(3.2)	15.1	(1.1)	82.1	(0.2)	104.1	(3.7)
Nb	2.91	(1.02)	5.90	(0.66)	3.35	(0.39)	21.1	(0.5)	18.4	(0.8)
Ba	250.2	(28.3)	194.9	(10.1)	107.8	(2.8)	51.8	(2.1)	86.7	(4.2)
Hf	1.22	(0.07)	1.15	(0.39)	1.26	(0.19)	3.12	(0.12)	3.22	(0.29)
Ta	0.26	(0.06)	0.50	(0.10)	0.26	(0.05)	1.45	(0.05)	1.40	(0.09)
Th	blld		blld		blld		blld		blld	
U	blld		blld		blld		blld		blld	
La	1.44	(0.33)	5.01	(0.64)	0.60	(0.07)	5.57	(0.20)	8.73	(0.18)
Ce	6.51	(0.94)	16.0	(2.3)	3.75	(0.12)	20.6	(0.8)	26.5	(0.1)
Pr	1.39	(0.19)	2.20	(0.27)	0.90	(0.06)	3.32	(0.05)	4.37	(0.01)
Nd	8.04	(0.69)	10.6	(0.4)	5.51	(0.25)	17.3	(0.7)	21.77	(0.03)
Sm	2.53	(0.16)	1.97	(0.48)	1.95	(0.76)	4.81	(0.15)	4.37	(0.24)
Eu	0.97	(0.05)	0.93	(0.09)	1.13	(0.08)	1.77	(0.05)	1.90	(0.09)
Gd	2.56	(0.06)	2.26	(0.17)	3.35	(0.14)	4.47	(0.18)	4.80	(0.27)
Tb	0.34	(0.02)	0.29	(0.03)	0.51	(0.03)	0.60	(0.01)	0.65	(0.01)
Dy	1.66	(0.03)	1.40	(0.16)	2.80	(0.08)	2.87	(0.004)	3.15	(0.03)
Ho	0.29	(0.01)	0.23	(0.004)	0.44	(0.05)	0.42	(0.02)	0.49	(0.02)
Er	0.72	(0.08)	0.70	(0.02)	1.26	(0.03)	1.00	(0.04)	1.07	(0.08)
Tm	0.08	(0.01)	0.14	(0.01)	0.12	(0.01)	0.12	(0.01)	0.09	(0.01)
Yb	0.51	(0.01)	0.81	(0.03)	0.83	(0.11)	0.56	(0.01)	0.46	(0.05)
Lu	0.06	(0.01)	blld		0.08	(0.01)	0.06	(0.02)	0.07	(0.02)

Table 3.4. (continued)

sm	K1921		FM10		FM10		FM10	
run#	15		02		23		25	
n	18		27		22		19	
(wt.%)								
SiO_2	41.57	(0.87)	43.42	(0.49)	42.25	(0.27)	41.60	(0.45)
TiO_2	2.96	(0.23)	2.59	(0.17)	2.17	(0.09)	1.66	(0.03)
Al_2O_3	14.57	(0.39)	11.89	(0.53)	13.72	(0.33)	14.54	(0.20)
FeO	11.14	(0.29)	8.06	(0.37)	8.80	(0.32)	11.94	(0.33)
MnO	0.14	(0.02)	0.12	(0.02)	0.11	(0.03)	0.15	(0.02)
MgO	13.87	(0.25)	16.73	(0.35)	15.95	(0.31)	13.59	(0.31)
CaO	10.11	(0.13)	10.67	(0.35)	10.75	(0.19)	10.11	(0.11)
Na_2O	2.57	(0.08)	3.05	(0.10)	2.74	(0.06)	2.77	(0.05)
K_2O	0.55	(0.04)	1.15	(0.12)	1.06	(0.06)	1.08	(0.04)
Total	97.48		97.68		97.55		97.44	
(ppm)								
n[c]	3-4		6-12		6-12		2-8	
Rb	3.21	(0.26)	5.48	(1.28)	6.23	(0.62)	8.69	(0.66)
Sr	214.4	(12.9)	430.9	(24.5)	216.4	(13.0)	201.9	(7.1)
Y	21.3	(1.7)	11.5	(1.6)	12.5	(0.6)	14.6	(0.4)
Zr	44.8	(2.2)	85.0	(13.2)	22.3	(3.4)	19.1	(1.7)
Nb	5.47	(0.20)	18.8	(1.4)	3.20	(0.46)	3.15	(0.94)
Ba	51.0	(3.2)	57.6	(3.4)	114.8	(11.7)	107.0	(7.2)
Hf	1.72	(0.22)	2.82	(0.56)	0.86	(0.14)	0.76	(0.09)
Ta	1.07	(0.09)	1.29	(0.08)	0.67	(0.08)	0.57	(0.16)
Th	blld		blld		blld		blld	
U	blld		blld		blld		blld	
La	2.51	(0.40)	6.97	(0.80)	2.02	(0.48)	1.90	(0.31)
Ce	10.6	(0.3)	24.4	(2.0)	7.76	(1.11)	8.03	(0.74)
Pr	2.03	(0.17)	4.13	(0.33)	1.45	(0.10)	1.58	(0.14)
Nd	11.3	(1.0)	20.3	(1.7)	8.39	(0.97)	8.33	(0.48)
Sm	4.88	(1.13)	5.55	(0.92)	2.34	(0.29)	2.71	(0.23)
Eu	1.38	(0.28)	1.86	(0.23)	1.01	(0.11)	1.04	(0.16)
Gd	3.91	(0.29)	4.75	(0.24)	2.93	(0.25)	3.36	(0.29)
Tb	nd		0.65	(0.05)	0.47	(0.03)	0.51	(0.02)
Dy	3.47	(1.01)	2.86	(0.17)	2.65	(0.14)	2.87	(0.24)
Ho	0.66	(0.14)	0.43	(0.02)	0.50	(0.02)	0.53	(0.03)
Er	2.36	(0.28)	1.10	(0.32)	1.28	(0.13)	1.63	(0.18)
Tm	0.27	(0.02)	0.14	(0.03)	0.12	(0.01)	0.23	(0.03)
Yb	1.62	(0.24)	0.72	(0.26)	0.77	(0.03)	1.34	(0.10)
Lu	0.20	(0.05)	0.06	(0.01)	0.12	(0.02)	0.17	(0.01)

Abbreviations: sm-starting material (see Table 3.1), run#-run number (see Table 3.3), n-number of analyses, blld-concentration below the lower limit of detection, nd-not determined. [a] Zoned amphibole observed in run products (see text). [b] Major elements were taken from Dalpé *et al.* (1995) and trace elements were reanalyzed by LAM-ICP-MS. [c] Number of analyses vary as function of the different acquisition menus and replicate isotopes. [d] Single analysis. Values in parentheses are based on one standard deviation from multiple analyses (1σ).

Table 3.5. Formulae of amphibole

sm	P-MT	P-MT[a]	P-MT[a]	P-MTg	P-MTg	P-MTg	P-MTg$_{Ti}$	K-HD
run#	27	34a	34b	12	41	43	31	08
T	1100	1050	1050	1100	1075	1050	1130	1100
P	1.5	2.5	2.5	1.5	2.5	1.5	1.5	1.5
fO_2	low	low	low	low	high	high	low	low
(apfu)								
T(1,2)								
Si	5.903	5.965	6.073	5.803	5.885	5.803	5.804	5.991
Al	2.097	2.035	1.927	2.197	2.115	2.197	2.196	2.009
$\sum$	8.000	8.000	8.000	8.000	8.000	8.000	8.000	8.000
M(1,2,3)								
Al	0.550	0.698	0.666	0.553	0.587	0.450	0.457	0.400
Ti	0.389	0.231	0.227	0.410	0.194	0.355	0.538	0.474
Fe^{3+}[b]	0.000	0.000	0.000	0.000	0.266	0.138	0.000	0.000
Mg	3.526	3.660	3.932	3.498	3.704	3.520	3.711	3.627
Fe^{2+}	0.535	0.411	0.175	0.539	0.249	0.537	0.275	0.499
Mn	bild	bild	bild	bild	bild	bild	bild	bild
$\sum$	5.000	5.000	5.000	5.000	5.000	5.000	4.981	5.000
M(4)								
Fe^{2+}	0.070	0.197	0.124	0.082	0.047	0.028	0.000	0.120
Mn	bild	bild	bild	bild	bild	bild	bild	bild
Ca	1.845	1.735	1.785	1.867	1.885	1.940	1.889	1.774
Na	0.085	0.068	0.091	0.051	0.068	0.032	0.111	0.106
$\sum$	2.000	2.000	2.000	2.000	2.000	2.000	2.000	2.000
A								
Na	0.515	0.532	0.435	0.470	0.434	0.484	0.439	0.513
K	0.339	0.409	0.463	0.406	0.508	0.447	0.371	0.253
$\sum$	0.854	0.941	0.898	0.876	0.943	0.931	0.810	0.766
Total	15.854	15.941	15.898	15.876	15.943	15.931	15.791	15.766
Mg#	85.4	85.8	92.9	84.9	92.6	86.2	93.1	85.4
$Mg\#_t$	85.4	85.8	92.9	84.9	86.8	83.3	93.1	85.4
$Fe^{3+/2+}$	0.00	0.00	0.00	0.00	0.899	0.244	0.00	0.00
C/CN	0.755	0.743	0.772	0.782	0.790	0.790	0.774	0.741

Table 3.5. (continued)

sm	HF13	HF13g_{Ti}	K1921	FM10	FM10	FM10
run#	38	03	15	02	23	25
T	1020	1040	1020	1040	1000	1000
P	1.5	1.5	1.5	1.5	1.5	2.2
fO_2	low	low	low	low	high	high
(apfu)						
T(1,2)						
Si	6.381	6.275	6.085	6.294	6.146	6.134
Al	1.619	1.725	1.915	1.706	1.854	1.866
$\sum$	8.000	8.000	8.000	8.000	8.000	8.000
M(1,2,3)						
Al	0.385	0.288	0.598	0.326	0.499	0.661
Ti	0.293	0.426	0.326	0.282	0.237	0.184
Fe^{3+} [b]	0.000	0.000	0.000	0.000	0.000	0.000
Mg	3.374	3.553	3.026	3.616	3.459	2.987
Fe^{2+}	0.948	0.733	1.050	0.776	0.805	1.168
Mn	0.000	0.000	0.000	0.000	0.000	0.000
$\sum$	5.000	5.000	5.000	5.000	5.000	5.000
M(4)						
Fe^{2+}	0.076	0.097	0.315	0.201	0.266	0.305
Mn	0.016	0.015	0.017	0.015	0.013	0.019
Ca	1.670	1.617	1.585	1.657	1.676	1.597
Na	0.238	0.271	0.083	0.127	0.045	0.079
$\sum$	2.000	2.000	2.000	2.000	2.000	2.000
A						
Na	0.632	0.585	0.646	0.730	0.728	0.713
K	0.253	0.271	0.103	0.213	0.197	0.203
$\sum$	0.885	0.856	0.749	0.943	0.925	0.916
Total	15.885	15.856	15.749	15.943	15.925	15916
Mg#	76.7	81.1	68.9	78.7	76.4	67.0
$Mg\#_t$	76.7	81.1	68.9	78.7	76.4	67.0
$Fe^{3+/2+}$	0.00	0.00	0.00	0.00	0.00	0.00
C/CN	0.657	0.654	0.685	0.659	0.684	0.668

Abbreviations: sm-starting material (see Table 3.1), run#-run number (see Table 3.3), T-run temperature in °C, P-run pressure in GPa, fO_2-oxygen fugacity maintained during experiment (see text), apfu-atoms per formula unit (based on 23 atoms of oxygen; Leake *et al.* 1997), Mg#-Mg number = [100Mg/(Mg + Fe^{2+})], $Mg\#_t$ -Mg number$_t$ = [100Mg/(Mg + Fe^{3+} + Fe^{2+})], $Fe^{3+/2+}$-calculated Fe^{3+}/Fe^{2+} ratio, C/CN-calculated Ca/(Ca+Na) ratio.

[a] Zoned amphibole (see Table 3.4). [b] Fe^{3+} was calculated by the empirical estimation of Schumacher (1997) using electron microprobe analyses (see text).

Fe^{3+}/Fe^{2+} ratio reported for P-MTg-41 and P-MTg-43 in Table 3.5 resulted from the average of the normalization-factors that were obtained for the minimum and the maximum amount of ferric iron in the structural formulae applied to each amphibole (Schumacher 1997). For this empirical procedure of ferric iron estimation, I assumed that each amphibole must contain exactly two anions (OH, F, Cl) in their structural formula (*i.e.*, calculations have been done on the basis of 23 atoms of oxygen per formula unit). However, even if trace amounts of F and Cl were present in our amphiboles, their concentrations do not affect the ferric iron estimation (Schumacher 1997). I checked the homogeneity of the synthesized amphibole in all experiments by performing line traverses across them and calculating the relative standard deviation from the multiple analyses [*i.e.*, Relative Standard Deviation = RSD = 100 (standard deviation/average)]. The average RSD calculated from different analyses in amphibole run products gave: SiO_2 (1.23 %), TiO_2 (5.4 %), Al_2O_3 (3.0 %), FeO (4.5 %), MgO (1.9 %), CaO (2.0 %), Na_2O (3.8 %), and K_2O (8.0 %), respectively. These average RSD values were all less than 10 % suggesting homogeneity in major elements.

3.4.1.1.1. Equilibrium aspect of amphibole run products

Our experiments demonstrate that constant partitioning between amphibole and liquid seems to be reached within 20 h. Figure 3.2 shows the variation of partition coefficient (*i.e.*, D_i = *concentration*$_{element\text{-}i}$ *in amphibole / concentration*$_{element\text{-}i}$ *in liquid*) for Sr and Y as a function of the duration of the experiments (Dalpé *et al.* 1992; see Appendix 1). As shown

Figure 3.2. Variation of partition coefficient (D) as a function of the run duration. (a) Sr; (b) Y. The analyses of P-MT-05 (1 h), P-MT-09 (10 h), P-MT-10 (10 h), and P-MT-20 (20 h) runs were performed by synchrotron X-ray-fluorescence microprobe (SXRFM) on beamline X26A at the National Synchrotron Light Source at Brookhaven National Laboratory (Upton, New York) (Dalpé *et al.* 1992, Dalpé *et al.* 1995) while P-MT-27 was performed by LAM-ICP-MS. Each run on this figure was performed in a piston-cylinder using the double capsules (*i.e.*, Pt or $Ag_{50}Pd_{50}$ + graphite inner capsule) at 1.5 GPa, 1100 °C. Note that both P-MT-09 and P-MT-10 had the same run duration, 10 h, but were plotted apart for better clarity. Standard deviations smaller than the symbol size are not shown in this and subsequent figures.

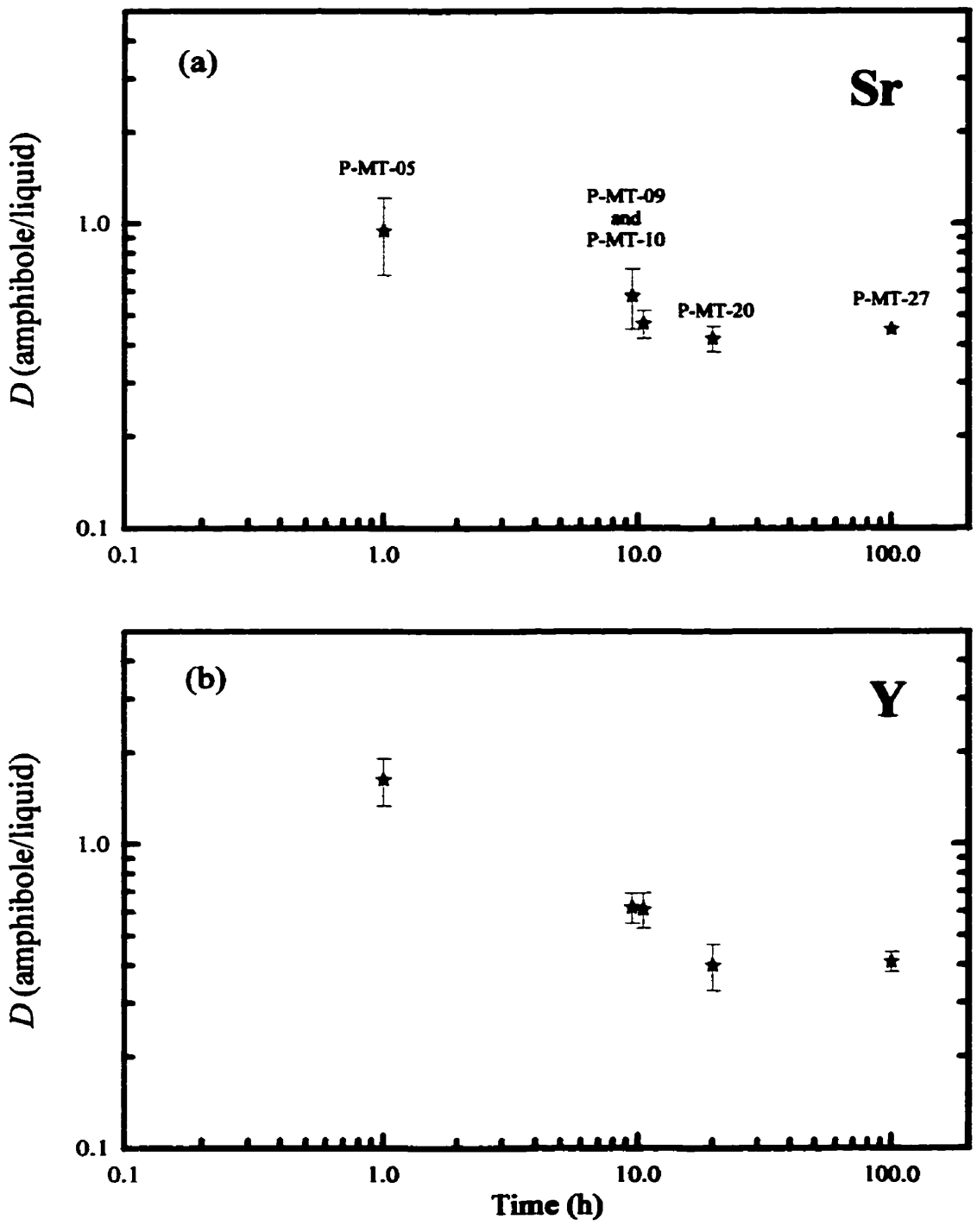
(a)
Sr
P-MT-05
P-MT-09
and
P-MT-10
P-MT-20
P-MT-27
D (amphibole/liquid)
1.0
0.1
0.1
1.0
10.0
100.0
(b)
Y
D (amphibole/liquid)
1.0
0.1
0.1
1.0
10.0
100.0
Time (h)

in this figure, constant partition coefficients are reached within 20 h based on one standard deviation or within 10 h based on two standard deviations.

The experiments P-MT-05, P-MT-09, P-MT-10, and P-MT-20 are not listed in Table 3.3 and subsequent Tables due to their non-equilibrium nature (P-MT-05) or the incapacity to analyse the amphibole run products by LAM-ICP-MS due to their small size (P-MT-09, P-MT-10, P-MT-20). Knowing that the 10-20 h run duration was the minimum time to reach equilibrium between amphibole and melt, the experiments in this study were all greater or equal than 24 h duration. Homogeneous compositions of the amphibole run products suggests equilibrium was attained in all experiments (Table 3.4). However, an additional tool to estimate if equilibrium was attained during experiments is the Fe^{2+}-Mg exchange coefficient between amphibole and melt [*i.e.*, $K_D = (Fe^{2+}/Mg)_{am} / (Fe^{2+}/Mg)_{melt}$]. Unfortunately, the Fe^{2+}-Mg exchange coefficient for amphibole and other hydrous phases is not well calibrated, leaving a doubt as to the acceptable range of equilibrium values (LaTourrette *et al.* 1995). Furthermore, because the Fe^{3+}/Fe^{2+} ratio in amphiboles is not well constrained and the estimated ratio resulting from the empirical model represents an average value between minimum and maximum amounts of the ferric iron content in the structural formulae (Schumacher 1997), I preferred the $\sum$Fe-Mg exchange coefficient instead [*i.e.*, $K_D^{\Sigma Fe/Mg} = (\sum Fe/Mg)_{am} / (\sum Fe/Mg)_{glass}$, where $\sum Fe = Fe^{2+} + Fe^{3+}$ in cation units]. The $K_D^{\Sigma Fe/Mg}$ is not sensitive to the empirical method used to estimate the Fe^{3+}/Fe^{2+} ratio in amphibole, or in melt, unlike the Fe^{2+}-Mg exchange coefficient.

The $K_D^{\Sigma Fe/Mg}$ values of the run products showed a variation between 0.33 to 0.40 with the exception of P-MT-27 run which had a low $K_D^{\Sigma Fe/Mg}$ value (0.28) and the P-MT-34 experiment which had a zoned amphibole (P-MT-34a and P-MT-34b; Table 3.4), yielding high $K_D^{\Sigma Fe/Mg}$ values for both zones (1.0 and 0.47, respectively). These exceptions will be discussed below. The $K_D^{\Sigma Fe/Mg}$ values obtained for most of our experiments were similar to the range reported by Sisson and Grove (1993) and LaTourrette *et al.* (1995) (*i.e.*, 0.30 to 0.38). However, LaTourrette *et al.* (1995) mentioned that the low $K_D^{\Sigma Fe/Mg}$ reported by Jakobsson and Holloway (1986) (*i.e.*, $K_D^{\Sigma Fe/Mg}$ ~0.23 to ~0.29) could be due to the more reducing conditions of their experiments (*i.e.*, iron-wüstite). This argument does not explain the range of $K_D^{\Sigma Fe/Mg}$ values (*i.e.*, 0.26-0.42) that I calculated from Adam *et al.* (1993) and Adam and Green's (1994) experiments buffered at more oxidized conditions (*i.e.*, wüstite-magnetite and magnetite-hematite).

The low $K_D^{\Sigma Fe/Mg}$ obtained for the P-MT-27 run could be explained by a dominant number of analyses performed in the glass close to the crystal rims. Figure 3.1b shows a darker zone in the glass surrounding the crystal rims. This darker zone is common for all our run products and its width varies between 10 to 100 μm from crystal rims depending on the melt composition, glass proportion, and the amount of water (*e.g.*, see Fig. 3.1a where this zone is very thin). It was observed on the back-scattered electron images and attributed to a modification of the melt during quenching, reflecting a lower magnesium and iron content (referred as quench-modified glass, Dalpé *et al.* 1995). For all experiments, I observed

beyond this quench-modified glass (*i.e.*, > 50 to 100 μm away from the crystal rims), a clear glass or a glass with tiny crystallized minerals showing a spinifex texture (*i.e.*, 1-5 μm anhedral to euhedral quenched crystals; both referred to as quenched glass). However in the P-MT-27 run, the modal proportion of the melt was relatively low (*i.e.*, 18 %; Table 3.3) and in such cases the quench-modified glass occupied a large proportion of the sample. Results of $K_D^{\Sigma Fe/Mg}$ values calculated from different spots in the quench-modified glass (*i.e.*, < 100 μm to the crystal rim) and in the quenched glass (*i.e.*, beyond 100 μm of the crystal rim for this run product) had a range between 0.21 and 0.32, respectively (using a constant value of $\sum Fe/Mg^{amphibole} = 0.172$; Table 3.5). The upper limit value of $K_D^{\Sigma Fe/Mg}$ from the P-MT-27 run was very close to the lowest value obtained from the other runs as mentioned earlier (*i.e.*, 0.33). I believe that the trace element analyses of the quenched glass and of the quench-modified glass from the P-MT-27 run products are consistent with the other run products and reliable because during LAM-ICP-MS analyses: (1) calcium concentrations (^{44}Ca) used as the internal standard and previously analyzed in both glass phases (*i.e.*, quench-modified glass and quenched glass) were practically identical based on electron microprobe precision (*i.e.*, average from both glass phases is 12.89 ±0.72 wt.% CaO; Table 3.6); (2) trace element concentrations were calculated using grid analyses done in both glass phases, giving an average value for the different trace elements; and (3) the RSD values attached to the trace elements had the same range as those measured on other quenched glasses where analyses were performed more than 100 μm away from the crystal rim (Table 3.6).

Table 3.6. Quenched glass compositions in experiments

sm	P-MT		P-MT		P-MTg		P-MTg		P-MTg	
run#	27		34		12		41		43	
n	18		10		26		18		16	
(wt.%)										
SiO_2	37.11	(1.43)	34.14	(2.98)	36.59	(1.70)	34.18	(1.83)	37.98	(1.70)
TiO_2	4.07	(0.15)	4.15	(0.40)	3.86	(0.19)	4.46	(0.46)	4.81	(0.19)
Al_2O_3	14.34	(0.66)	14.10	(1.33)	16.75	(2.31)	14.75	(1.20)	15.36	(0.67)
FeO	8.51	(0.43)	3.28	(0.34)	8.55	(0.79)	8.35	(0.66)	8.54	(0.28)
MnO	0.15	(0.03)	0.08	(0.02)	0.13	(0.03)	0.10	(0.02)	0.14	(0.02)
MgO	7.67	(0.90)	11.33	(2.81)	9.35	(1.73)	10.24	(1.23)	8.67	(0.34)
CaO	12.89	(0.72)	10.04	(2.24)	12.44	(1.37)	11.34	(1.24)	12.63	(0.62)
Na_2O	1.55	(0.28)	1.22	(0.39)	1.62	(0.26)	1.56	(0.13)	1.45	(0.21)
K_2O	1.21	(0.24)	1.23	(0.44)	1.39	(0.44)	1.26	(0.26)	1.40	(0.18)
P_2O_5	0.14	(0.05)	blld		0.07	(0.02)	0.04	(0.01)	0.05	(0.02)
Total	87.64		79.59		90.75		86.27		91.03	
$Fe^{3+/2+}$	0		0		0		0.6		0.6	
$Mg\#_t$	61.6		86.0		66.1		68.7		64.4	
(ppm)										
n[b]	3-12		2-6		2-9		6-12		2-10	
Rb	16.1	(0.8)	6.65	(0.57)	15.5	(2.0)	6.46	(1.07)	11.6	(1.2)
Sr	745.1	(16.9)	486.5	(14.8)	661.2	(13.3)	555.5	(18.5)	660.4	(3.3)
Y	16.6	(0.3)	11.2	(0.2)	14.8	(0.5)	13.2	(0.3)	17.1	(0.6)
Zr	96.8	(2.3)	57.3	(2.6)	88.3	(3.1)	70.7	(5.8)	99.1	(3.8)
Nb	34.3	(0.4)	15.1	(1.5)	29.8	(1.1)	20.5	(0.7)	35.0	(1.1)
Ba	428.1	(11.1)	255.8	(4.0)	371.6	(3.5)	253.3	(14.4)	346.6	(4.3)
Hf	3.31	(0.29)	2.16	(0.15)	3.02	(0.25)	2.77	(0.13)	3.53	(0.12)
Ta	2.10	(0.04)	1.11	(0.07)	1.89	(0.08)	1.39	(0.12)	2.26	(0.09)
Th	0.50	(0.05)	0.16	(0.03)	0.37	(0.05)	0.26	(0.03)	0.43	(0.02)
U	0.15	(0.04)	0.09	(0.01)	0.11	(0.01)	0.07	(0.01)	0.11	(0.01)
La	27.1	(1.6)	11.8	(0.4)	11.8	(0.7)	7.79	(0.17)	12.9	(0.3)
Ce	66.7	(3.3)	25.6	(1.4)	35.6	(0.9)	23.9	(0.7)	37.3	(0.8)
Pr	9.13	(0.28)	4.26	(0.17)	5.63	(0.24)	4.06	(0.14)	6.06	(0.13)
Nd	36.3	(0.5)	18.9	(0.5)	25.5	(0.7)	19.6	(0.7)	27.3	(0.6)
Sm	6.41	(0.23)	4.42	(0.20)	6.12	(0.49)	4.61	(0.26)	6.09	(0.09)
Eu	2.06	(0.38)	2.68	(0.04)	2.04	(0.07)	1.65	(0.06)	2.13	(0.05)
Gd	4.38	(0.86)	3.73	(0.13)	5.20	(0.29)	4.42	(0.08)	5.68	(0.10)
Tb	0.60	(0.12)	0.51	(0.01)	0.72	(0.03)	0.61	(0.05)	0.77	(0.01)
Dy	2.88	(0.65)	2.73	(0.08)	3.55	(0.14)	3.14	(0.18)	3.96	(0.12)
Ho	0.49	(0.12)	0.46	(0.01)	0.61	(0.01)	0.55	(0.04)	0.69	(0.03)
Er	1.41	(0.32)	1.14	(0.05)	1.61	(0.11)	1.41	(0.08)	1.81	(0.06)
Tm	0.20	(0.03)	0.14	(0.01)	0.19	(0.02)	0.18	(0.01)	0.24	(0.01)
Yb	1.26	(0.09)	0.86	(0.01)	1.09	(0.01)	1.02	(0.07)	1.48	(0.02)
Lu	0.15	(0.03)	0.10	(0.01)	0.18	(0.02)	0.11	(0.01)	0.16	(0.01)

Table 3.6. (continued)

sm	P-MTg$_{ri}$		K-HD[a]		HF13		HF13g$_{ri}$		K1921	
run#	31		08		38		03		15	
n	18		17		16		30		34	
(wt.%)										
SiO_2	37.82	(0.13)	38.82	(1.14)	36.67	(0.32)	35.56	(0.94)	47.53	(0.61)
TiO_2	6.87	(0.10)	5.67	(0.26)	2.22	(0.03)	3.37	(0.10)	2.08	(0.08)
Al_2O_3	15.83	(0.07)	13.90	(0.87)	11.51	(0.15)	12.34	(0.16)	16.21	(0.22)
FeO	3.40	(0.04)	7.11	(0.58)	9.30	(0.15)	6.50	(0.17)	8.34	(0.31)
MnO	0.11	(0.02)	0.18	(0.03)	0.28	(0.02)	0.26	(0.02)	0.15	(0.02)
MgO	8.39	(0.06)	6.82	(1.72)	5.98	(0.10)	6.22	(0.25)	3.86	(0.26)
CaO	12.18	(0.09)	11.26	(0.85)	10.60	(0.33)	9.48	(0.50)	7.67	(0.15)
Na_2O	2.03	(0.13)	1.70	(0.28)	4.00	(0.51)	6.26	(0.55)	1.29	(0.48)
K_2O	1.38	(0.05)	1.07	(0.43)	2.22	(0.17)	2.22	(0.20)	0.75	(0.04)
P_2O_5	0.17	(0.02)	nd		2.80	(0.10)	2.65	(0.15)	0.48	(0.04)
Total	88.17		86.51		85.60		84.86		88.37	
$Fe^{3+/2+}$	0		0		0		0		0	
$Mg\#_t$	81.5		63.1		53.4		63.0		45.2	
(ppm)										
n[b]	3-9		5-10		3-5		2-4		2-15	
Rb	12.5	(0.3)	9.18	(0.91)	32.7	(1.0)	36.1	(0.9)	15.2	(1.8)
Sr	643.7	(4.1)	896.8	(2.7)	2332	(6)	2277	(11)	520.6	(40.1)
Y	15.1	(0.3)	33.4	(0.7)	38.9	(0.5)	36.3	(0.4)	27.0	(2.0)
Zr	90.8	(1.5)	124.4	(1.4)	422.9	(1.2)	426.1	(8.7)	218.9	(22.9)
Nb	29.8	(0.4)	68.3	(1.5)	167.6	(1.6)	156.5	(1.9)	30.5	(4.4)
Ba	331.2	(4.2)	396.9	(7.1)	458.2	(3.2)	477.2	(1.5)	185.6	(17.8)
Hf	3.25	(0.49)	3.91	(0.15)	7.65	(0.07)	7.00	(0.42)	5.46	(0.85)
Ta	1.89	(0.22)	3.60	(0.08)	9.18	(0.03)	7.77	(0.02)	6.49	(1.17)
Th	0.33	(0.10)	0.21	(0.02)	14.4	(0.8)	14.7	(1.0)	1.83	(0.21)
U	blld		0.53	(0.02)	4.66	(0.28)	4.41	(0.18)	0.75	(0.10)
La	24.5	(0.4)	15.7	(0.2)	137.5	(0.3)	131.0	(1.3)	22.1	(2.4)
Ce	70.6	(0.8)	57.3	(0.8)	260.7	(1.3)	242.8	(4.0)	54.8	(5.5)
Pr	8.15	(0.15)	8.81	(0.11)	30.3	(0.1)	28.7	(0.3)	7.41	(0.70)
Nd	33.0	(1.1)	39.6	(0.7)	110.7	(0.2)	105.8	(1.3)	32.0	(3.3)
Sm	5.49	(0.34)	10.6	(0.9)	19.6	(0.1)	18.5	(0.3)	7.64	(1.03)
Eu	2.07	(0.19)	3.43	(0.09)	6.84	(0.19)	6.59	(0.13)	2.62	(0.34)
Gd	5.44	(0.44)	9.31	(0.22)	15.4	(0.4)	14.7	(0.6)	6.53	(0.21)
Tb	0.79	(0.09)	1.36	(0.01)	1.97	(0.10)	1.93	(0.09)	nd	
Dy	3.66	(0.32)	7.04	(0.07)	9.21	(0.37)	9.02	(0.35)	5.24	(0.003)
Ho	0.59	(0.07)	1.27	(0.02)	1.40	(0.05)	1.49	(0.11)	1.03	(0.5)
Er	1.71	(0.16)	3.56	(0.03)	3.51	(0.13)	3.57	(0.24)	2.71	(0.16)
Tm	0.27	(0.03)	0.45	(0.02)	0.40	(0.02)	0.43	(0.05)	0.34	(0.06)
Yb	1.52	(0.07)	2.44	(0.03)	2.31	(0.10)	2.25	(0.07)	2.50	(0.21)
Lu	0.10	(0.003)	0.32	(0.01)	0.26	(0.02)	0.32	(0.03)	0.37	(0.11)

Table 3.6. (continued)

sm	FM10		FM10		FM10	
run#	02		23		25	
n	20		14		17	
(wt.%)						
SiO_2	35.92	(1.77)	45.30	(1.78)	47.07	(2.25)
TiO_2	2.15	(0.17)	2.25	(0.12)	1.65	(0.13)
Al_2O_3	11.64	(0.90)	16.49	(1.04)	16.37	(1.05)
FeO	10.45	(0.39)	9.47	(0.89)	8.46	(1.97)
MnO	0.25	(0.03)	0.18	(0.03)	0.18	(0.04)
MgO	7.14	(0.41)	6.08	(1.17)	3.29	(1.17)
CaO	11.06	(1.19)	7.52	(0.81)	7.14	(0.97)
Na_2O	3.56	(0.77)	1.70	(0.43)	1.35	(0.60)
K_2O	1.63	(0.20)	0.87	(0.27)	0.77	(0.25)
P_2O_5	2.25	(0.33)	0.26	(0.09)	0.51	(0.12)
Total	86.06		90.11		86.79	
$Fe^{3+/2+}$	0		0.6		0.6	
$Mg\#_t$	54.9		53.4		40.8	
(ppm)						
n[b]	4-11		2-8		3-8	
Rb	25.7	(1.2)	26.6	(2.5)	32.7	(2.1)
Sr	1924	(129)	493.6	(18.7)	682.2	(33.3)
Y	33.2	(1.9)	19.9	(0.5)	24.4	(0.9)
Zr	352.9	(17.3)	142.6	(4.1)	216.6	(9.2)
Nb	136.2	(9.6)	31.6	(0.3)	47.9	(1.7)
Ba	353.4	(21.0)	339.5	(8.2)	463.2	(17.7)
Hf	6.79	(0.27)	3.27	(0.37)	5.11	(0.30)
Ta	7.13	(0.43)	5.56	(0.38)	8.61	(0.30)
Th	12.4	(0.8)	1.93	(0.15)	3.19	(0.30)
U	4.06	(0.34)	0.63	(0.07)	1.04	(0.03)
La	112.9	(8.0)	20.4	(0.3)	32.7	(2.1)
Ce	216.7	(15.8)	47.3	(1.0)	70.9	(4.0)
Pr	25.3	(1.9)	5.73	(0.13)	8.72	(0.69)
Nd	93.7	(6.0)	23.5	(0.8)	34.3	(1.4)
Sm	17.5	(1.1)	4.57	(0.70)	6.54	(0.34)
Eu	5.89	(0.38)	1.72	(0.09)	2.34	(0.23)
Gd	14.4	(0.9)	4.88	(0.31)	5.67	(0.23)
Tb	1.97	(0.08)	0.72	(0.06)	0.89	(0.01)
Dy	8.80	(0.22)	3.90	(0.07)	4.53	(0.46)
Ho	1.34	(0.11)	0.74	(0.03)	0.84	(0.02)
Er	3.28	(0.21)	2.12	(0.13)	2.62	(0.16)
Tm	0.37	(0.02)	0.23	(0.004)	0.41	(0.02)
Yb	2.08	(0.32)	1.71	(0.07)	2.45	(0.30)
Lu	0.19	(0.02)	0.28	(0.004)	0.32	(0.02)

Table 3.6. (continued)

Abbreviations: sm-starting material (see Table 3.1), run#-run number (see Table 3.3), n-number of analyses, nd-not determined, blld-concentration below the lower limit of detection, $Fe^{3+/2+}$-Fe^{3+}/Fe^{2+} ratio in cation units were calculated from the respective oxygen fugacitites maintained during experiments (see text), $Mg\#_t$-Mg number$_t$ = [100Mg/(Mg + Fe^{2+} + Fe^{3+})] using the respective Fe^{3+}/Fe^{2+} ratio mentioned in Table. [a]Major elements were taken from Dalpé *et al.* (1995) and trace elements were reanalyzed by LAM-ICP-MS. [b] Number of analyses vary as function of the different acquisition menus and replicate isotopes. Values in parentheses are based on one standard deviation from multiple analyses (1σ).

3.4.1.1.2. Zoned amphibole

As mentioned previously, a zoned amphibole was observed in the P-MT-34 run. Based on back-scattered electron images and electron microprobe analyses, all the amphiboles from this run product showed an Fe-rich core surrounded by a 10 to 50 μm thick zone along the rim of an Fe-poor composition (*i.e.*, P-MT-34a and P-MT-34b, respectively; Table 3.4). The longest axis of the amphibole crystals observed in the run product were ~1000 μm including both zones [i.e, the Fe-rich (core) and Fe-poor (rim) zones]. However, it is important to note the homogeneity in major elements for both zones and in trace elements for the Fe-rich zone based on their RSD's (Table 3.4). Due to the small size of the Fe-poor zone, I was limited to performing a single analysis in this zone by LAM-ICP-MS (*i.e.*, the MREE: Eu, Gd, Tb, Dy, Ho, Er; see Table 3.4). The level of MREE concentrations between the Fe-rich and the Fe-poor zones agree to within one standard deviation for Gd and Dy (P-MT-34a and P-MT-34b). However I am convinced that the level of concentration of Eu Tb, Ho, and Er determined in both zones would lie within, or close to, two standard deviations if it had been possible to perform more than one analysis in the Fe-poor zone (*i.e.*, P-MT-34b).

In the quenched glass, the large standard deviations attached to SiO_2, MgO, and CaO suggest inhomogeneity at the scale of the electron microprobe (the electron beam used was 10 μm; Table 3.6). Results of $K_D^{\Sigma Fe/Mg}$ values calculated from different spots in the quenched glass were between 0.76-1.5 and 0.35-0.69 using a fixed value of $\sum Fe/Mg^{amphibole}$ at 0.166 or 0.076 for P-MT-34a and P-MT-34b, respectively (Table 3.5). As discussed below, the Fe-

rich and Fe-poor amphiboles had high contents of ^{VI}Al in the $M(1,2,3)$ octahedral sites compared to all other amphibole run products (Table 3.5). In calcic amphiboles, ^{VI}Al and ^{VI}Mg are strongly ordered in the $M(2)$ site, but $^{VI}Fe^{2+}$ prefers the $M(1)$ and $M(3)$ sites over the $M(2)$ site (Hawthorne 1983). Increasing pressure increases the aluminum in the amphibole structure (Hammarstrom and Zen 1986) resulting in a displacement of ^{VI}Mg from the $M(2)$ site by ^{VI}Al substitution causing a higher Fe^{2+}/Mg ratio in the equilibrium amphibole (Robinson *et al.* 1982). However, the high $K_D^{\Sigma Fe/Mg}$ obtained for both compositions (Fe-rich and Fe-poor) can also be attributed to iron-loss to the outer container (*i.e.*, $Au_{75}Pd_{25}$) as mentioned previously (~ 55 relative %). Such high iron-loss from the charge to the outer container results in a decrease of the $\sum Fe/Mg_{liquid}$ which will affect the $\sum Fe/Mg_{amphibole}$ due to equilibrium between amphibole and liquid. This new equilibrium will eventually force the amphibole to lose iron to the liquid resulting in a Fe-poor zone surrounding the Fe-rich crystal core. The iron-loss from the charge to the container may have occurred at the end of the experiment, leaving a zoned amphibole which did not have enough time to reequilibrate its Fe-Mg values with the evolved liquid. Despite the fact that $K_D^{\Sigma Fe/Mg}$ ratios associated with both zones suggest a non-equilibrium state for this particular run product, I believe that useful constraints on the effect of pressure, oxygen fugacity and crystal chemical controls on trace element partitioning can still be extracted from this experiment due to: (1) the trace element concentrations (MREE) between both zones were within, or close to, two standard deviations; (2) both zones were homogeneous in major elements; (3) the RSD values attached

to the trace elements in the Fe-rich zone had the same range as those measured on other amphibole run products; (4) the *D* values associated with the MREE from both zones are within one standard deviation of each other (discussed below).

3.4.1.1.3. The crystal chemistry of amphibole

Figure 3.3 shows a diagram of Ti against $100Mg/(Mg+Fe^{2+})$ which demonstrates that most experimentally produced amphiboles occupy the pargasite field composition, typical of amphiboles found in xenoliths hosted by alkaline basaltic rocks (Dawson and Smith 1982). In this study, the only composition that produced kaersutite in the final amphibole run products was the P-MTg_{Ti} starting material (*i.e.*, P-MTg_{Ti}-31 run; Table 3.1). Note that all amphiboles in previous experimental studies using modified basaltic compositions (Nicholls and Harris 1980, Adam *et al.* 1993, Adam and Green 1994, LaTourrette *et al.* 1995, Fujinawa and Green 1997) or natural kaersutite crystals (Dalpé *et al.* 1995) are also classified as pargasite with the exception of a kaersutite obtained by Green and Pearson (1985a; run# 998) which was produced by using a modified tholeiite.

For comparison with our P-MT starting material, I plot on Figure 3.3 the pargasite phenocryst compositions sampled from an olivine-free nepheline basalt (Gunn 1972) and another sample from a lamprophyre dike (Philpotts and Schnetzler 1970). These phenocrysts came from the same alkaline intrusive complexes of Montreal (Quebec, Canada) as P-MT but from different outcrops. The composition of our pargasite megacryst agrees in titanium

Figure 3.3. Sub-classification of calcic amphiboles (experimental and natural) occurring in basaltic and ultramafic compositions. All amphiboles are calculated on a basis of 23 atoms of oxygen per formula unit [*i.e.*, 23(O) apfu; Leake *et al.* 1997]. Abbreviations denote: Nicholls and Harris (1980) [NH (80)]; Green and Pearson (1985a) [GP (85a)]; Adam *et al.* (1993) and Adam and Green (1994) [AGS (93) and AG (94)]; Dalpé *et al.* (1995) [DBS (95)]; LaTourrette *et al.* (1995) [LHH (95)]; Fujinawa and Green (1997) [FG (97)]. Letters and numbers denote: kaersutite phenocryst from Hoover Dam lamprophyre dike (*K* = K-HD; Table 3.1); pargasite megacryst from Monteregian lamprophyre dike (*P* = P-MT; Table 3.1); pargasite phenocryst from Monteregian olivine-free nephelinite basalt [1, source: Gunn (1972, sample MT0008)]; pargasite phenocryst from Monteregian lamprophyre dike [2, source: Philpotts and Schnetzler (1970, sample GSFC 29)]; kaersutite phenocryst from Hoover Dam lamprophyre dike [3, source: Campbell and Schenk (1950)]; pargasite from "Alpine" peridotites (A), interstitial pargasite in spinel peridotite xenoliths (I), megacryst kaersutite (M), poikilitic kaersutite in Ti-augite pyroxenites (P), vein kaersutite (V), source: Wilkinson and Le Maître (1987). The dashed lines show the effect of Ti-doping on amphibole compositions (see text). The solid lines show the effect of pressure on the amphibole compositions (see text).

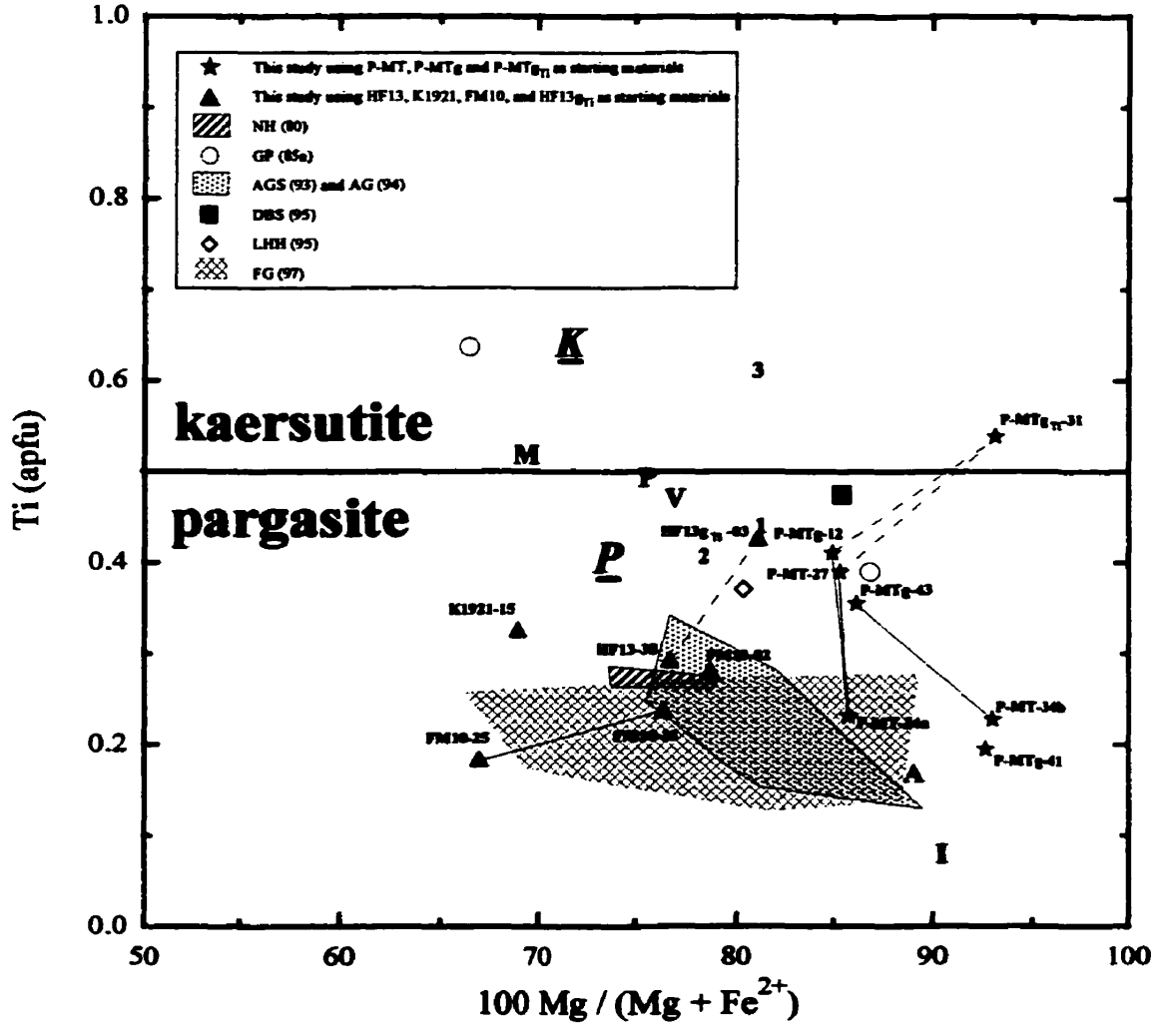
This study using P-MT, P-MTg and P-MTTi as starting materials
This study using HF13, K1921, FM10, and HF13Ti as starting materials
NH (80)
GP (85a)
AGS (93) and AG (94)
DBS (95)
LHH (95)
FG (97)
kaersutite
pargasite
K
P
M
P
V
3
2
1
A
I
P-MTTi-31
P-MTg-12
P-MT-27
P-MTg-43
P-MT-34b
P-MTg-41
K1921-15
FM10-25
HF13-30
0.0
0.2
0.4
0.6
0.8
1.0
50
60
70
80
90
100
Ti (apfu)
100 Mg / (Mg + Fe2+)

content but does not agree in Mg# compared to phenocrysts reported by Philpotts and Schnetzler (1970) and Gunn (1972) (Fig. 3.3). Such a difference in Mg# could be explained by the impurity component associated with the pargasite sample (*e.g.*, Gunn 1972, see Table 2, sample MT0008 has 95 % purity) or by the measured or estimated proportion of Fe^{3+} in the amphibole (discussed below for our samples). For comparison with our kaersutite starting material (*i.e.*, K-HD; Fig. 3.3), I added a kaersutite phenocryst composition analyzed by Campbell and Schenk (1950) where both materials came from the same alkaline intrusive complexes at Hoover Dam (Arizona, U.S.A.), but from different outcrops. Based on the electron microprobe precision, there is practically no significant difference in titanium content between both samples. However, this is not the case for the Mg#. Our partition coefficients will be compared to those of natural crystal/matrix pairs below. Also shown for comparison are average compositions of some natural calcic amphiboles associated with upper mantle rocks such as interstitial pargasite in spinel peridotite xenoliths, poikilitic kaersutite (*i.e.*, Ti-rich pargasite) in Ti-augite pyroxenites, vein kaersutite in peridotites, megacryst kaersutite, and pargasite from 'alpine' peridotites (Wilkinson and Le Maître 1987).

The crystal chemistry of our calcic amphiboles showed two distinct groups based on the distribution of ^{IV}Si and ^{IV}Al into the $T(1,2)$ tetrahedral sites, ^{VI}Ti into the $M(1,2,3)$ octahedral sites, ^{VIII}Ca into the $M4$ site, K/(K+Na) ratio, Ca/(Ca+Na) ratio, and on their Mg# values (Table 3.5). Table 3.7 shows the principal characteristics of both groups based on their crystal chemistry. The first group [gr. (1)] of amphiboles included those which crystallized

Table 3.7. Principal characteristics of amphibole run products based on their crystal chemistry (this study)

sm group		natural rocks (1)	natural crystals (2)
structural site	*cation*	*empirical limit (apfu)*	
T(1,2)	Si	> 6.000	< 6.000
	Al	< 2.000	> 2.000
M(1,2,3)	Ti	< 0.350	> 0.350
M(4)	Ca	< 1.740	> 1.740
Ratios[a]:	K/(Na + K)	< 0.290	> 0.290
	Ca/(Ca + Na)	<0.735	>0.735
	Mg#[b]	< 82	> 82

Abbreviations: sm-starting material, apfu-atoms per formula unit. [a] Ratios were obtained using the total number of atoms per formula unit (see Table 3.5). [b] Mg# = $Mg/(Mg+Fe^{2+})$ from the structural formula.

from natural bulk rock materials and had a high ^{IV}Si content (*i.e.*, > 6.000 apfu), low ^{IV}Al, ^{VI}Ti, and ^{VIII}Ca contents (*i.e.*, < 2.000, < 0.350, < 1.740 apfu, respectively), low K/(K+Na) and Ca/(Ca+Na) ratios (*i.e.*, < 0.290 and 0.735, respectively), and low Mg# (*i.e.*, < 82), independent of pressure and temperature conditions (*e.g.*, HF13-38, K1921-15, FM10-02, FM10-23, FM10-25; Fig. 3.3 and Table 3.5). The distinction of Ca/(Ca+Na) against K/(K+Na) for both groups can be observed in Figure 3.4. One exception to this group was the HF13g_{Ti}-03 run which had a higher ^{VI}Ti content than the 0.350 apfu limit (*i.e.*, 0.426 apfu), resulting from its Ti-doping (Table 3.5). In general, the crystal chemistry of amphibole from previous experimental studies using modified basaltic rock compositions (*i.e.*, Nicholls and Harris 1980, Adam *et al.* 1993, Adam and Green 1994, LaTourrette *et al.* 1995, Fujinawa and Green 1997) agrees well based on their ^{IV}Si, ^{IV}Al, ^{VI}Ti, and Ca/(Ca+Na) ratio while the Mg# limits and the K/(K + Na) ratio showed some discrepancies about our limits (see Figs. 3.3 and 3.4). The second group [gr. (2)] of calcic amphiboles included those which crystallized from natural bulk amphibole materials (*i.e.*, pargasite or kaersutite) and had a low ^{IV}Si content (*i.e.*, < 6.000 apfu), high ^{IV}Al, ^{VI}Ti, and ^{VIII}Ca contents (*i.e.*, > 2.000, > 0.350, > 1.740 apfu, respectively), high K/(K + Na) and Ca/(Ca+Na) ratios (*i.e.*, > 0.290 and 0.735, respectively), and a high Mg# (*i.e.*, > 82; P-MT-27, P-MTg-12, P-MTg-43, P-MTg_{Ti}-31, K-HD-08; Figs. 3.3, 3.4 and Table 3.5). However in this second group, the amphiboles that crystallized from higher pressure runs (*i.e.*, P-MT-34a, P-MT-34b, and P-MTg-41, all at 2.5 GPa) showed a similar content in ^{VI}Ti as in the first group (*i.e.*, < 0.350 apfu) but maintained

Figure 3.4. Variation of Ca/(Ca+Na) against K/(K+Na) in experimentally produced amphibole from this and previous studies using basaltic compositions. Symbols and fields as in Fig. 3.3. The dashed line shows the empirical limit between experimentally produced amphiboles using basaltic rocks (< 0.735 Ca/(Ca+Na)) or natural amphiboles (> 0.735 Ca/(Ca+Na)) as starting materials (see text).

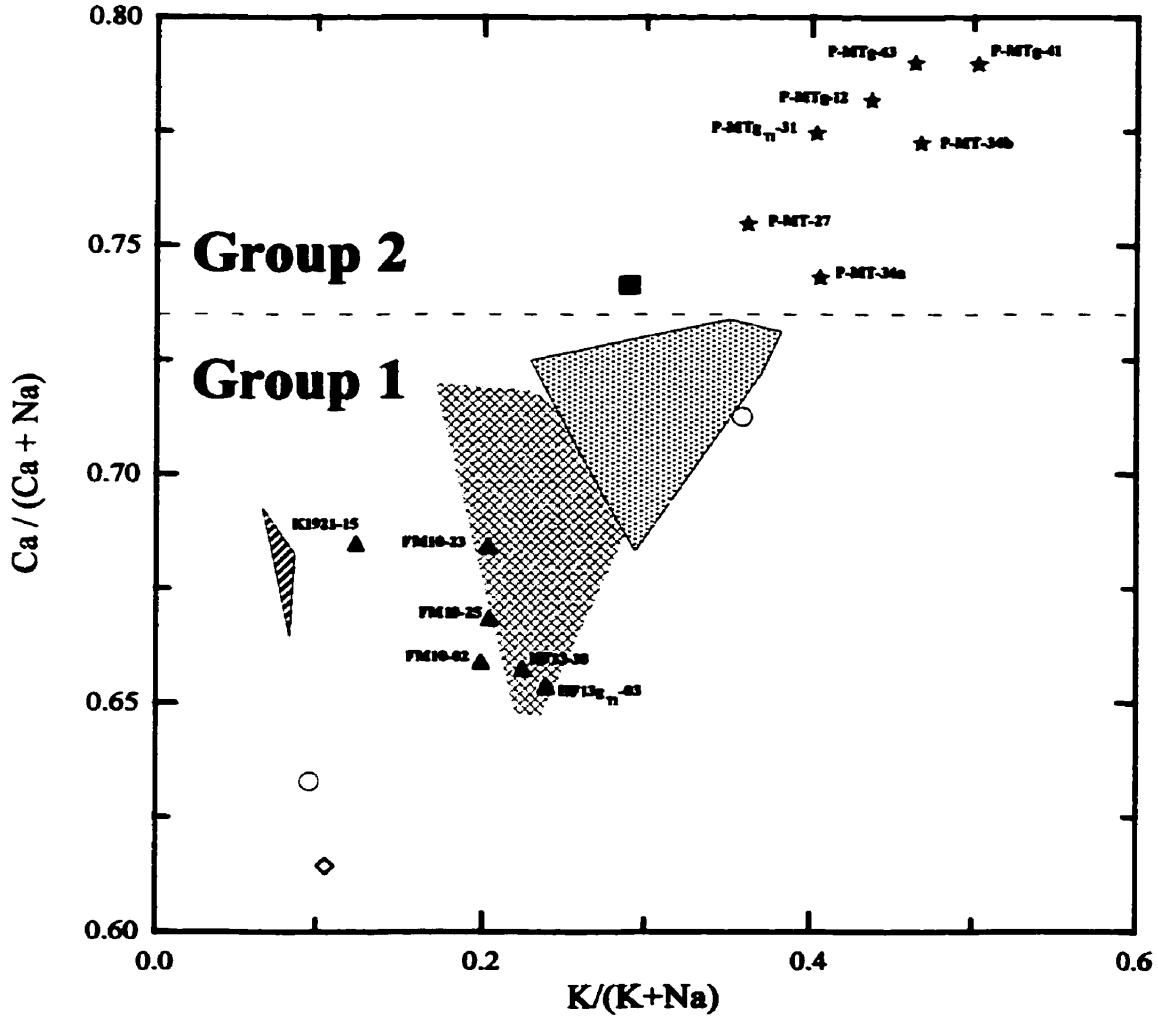
0.80
0.75
0.70
0.65
0.60
0.0
0.2
0.4
0.6
Ca / (Ca + Na)
K/(K+Na)
Group 2
Group 1
P-MTg-43
P-MTg-41
P-MTg-12
P-MT-34b
P-MT-27
P-MT-34a
K1921-15
FM10-23
FM10-25
FM10-02

their high Mg# (*i.e.*, 86, 93, and 93, respectively; Fig. 3.3 and Table 3.5). Furthermore, the zoned amphiboles that crystallized in P-MT-34 showed an ambivalent behaviour between both groups for their ^{IV}Si, ^{IV}Al contents in the *T*(1,2) sites and ^{VIII}Ca content in the *M*(4) sites (Table 3.5). Also noted was a distinct characteristic of high ^{VI}Al content, greater than 0.600 apfu, which was the maximum observed in amphiboles from both groups (Table 3.5).

The concentration levels of LILE, HFSE, and REE in both groups of calcic amphiboles lay within one standard deviation of each other (Table 3.4). However, a general trend observed in both groups was that the average concentrations of all these trace elements were higher for experimentally produced amphiboles using natural bulk rock materials. This tendency was due to the trace element contents of the different starting materials. Alkaline and nephelinitic basaltic rocks contained higher trace element contents than natural pargasite or kaersutite.

3.4.1.2. Mica

Relatively large euhedral (~175-800 μm along their longest axis) and homogeneous micas were crystallized in P-MT-27, P-MT-34, P-MTg-12, P-MTg-41, P-MTg-43, and FM10-02 runs at different pressures (1.5-2.5 GPa) and temperatures (1040-1100°C; Table 3.3). They were classified as phlogopite according to the Mg-Al-Fe_t diagram (Fe_t = total Fe; Mitchell 1995) using a structural formula based on 22 atoms of oxygen (Deer *et al.* 1992) (Table 3.8). Because the Fe^{3+}/Fe^{2+} ratio in micas is not well constrained I preferred to use the

Table 3.8. Phlogopite compositions in experiments and their formula unit

sm	P-MT		P-MT		P-MTg		P-MTg		P-MTg	
run#	27		34		12		41		43	
n	6		8		3		12		4	
(wt.%)										
SiO_2	37.32	(0.13)	37.70	(0.38)	37.21	(0.09)	37.81	(0.22)	37.36	(0.09)
TiO_2	3.68	(0.04)	2.13	(0.14)	4.61	(0.25)	1.42	(0.06)	2.60	(0.20)
Al_2O_3	18.14	(0.13)	17.10	(0.11)	19.09	(0.27)	17.41	(0.23)	17.54	(0.36)
FeO	4.43	(0.14)	4.00	(0.46)	5.56	(0.18)	4.59	(0.20)	5.20	(0.33)
MnO	blld		blld		blld		blld		0.03	(0.01)
MgO	21.20	(0.16)	22.41	(0.31)	20.78	(0.21)	22.67	(0.19)	21.90	(0.13)
CaO	0.16	(0.02)	0.08	(0.06)	0.13	(0.02)	0.09	(0.04)	0.11	(0.03)
Na_2O	0.84	(0.05)	0.47	(0.03)	0.43	(0.06)	0.63	(0.21)	0.60	(0.05)
K_2O	9.32	(0.06)	9.83	(0.22)	9.26	(0.17)	9.91	(0.16)	9.68	(0.11)
Total	95.09		93.72		97.07		94.53		95.02	
(apfu)										
Tetrahedral site (Z)										
Si	5.315		5.442		5.207		5.430		5.354	
Al	2.685		2.558		2.793		2.570		2.646	
$\sum$	8.000		8.000		8.000		8.000		8.000	
Octahedral site (Y)										
Al	0.360		0.352		0.356		0.376		0.317	
Ti	0.394		0.231		0.485		0.153		0.281	
Mn	blld		blld		blld		blld		0.004	
Fe^{2+}	0.528		0.483		0.651		0.551		0.623	
Mg	4.500		4.823		4.336		4.853		4.679	
$\sum$	5.782		5.888		5.828		5.934		5.899	
Interstitial site (X)										
Ca	0.024		0.012		0.020		0.014		0.017	
Na	0.231		0.132		0.117		0.175		0.166	
K	1.694		1.810		1.654		1.816		1.769	
$\sum$	1.949		1.954		1.790		2.005		1.953	
Total	15.731		15.842		15.618		15.939		15.852	

Table 3.8. (continued)

sm	FM10	
run#	02	
n	5	
(wt.%)		
SiO_2	37.93	(0.05)
TiO_2	2.90	(0.11)
Al_2O_3	16.03	(0.09)
FeO	8.49	(0.11)
MnO	0.05	(0.01)
MgO	20.20	(0.12)
CaO	0.11	(0.01)
Na_2O	1.27	(0.06)
K_2O	8.54	(0.13)
Total	95.52	
(apfu)		
Tetrahedral site (Z)		
Si	5.468	
Al	2.532	
$\sum$	8.000	
Octahedral site (Y)		
Al	0.191	
Ti	0.314	
Mn	0.006	
Fe^{2+}	1.024	
Mg	4.341	
$\sum$	5.876	
Interstitial site (X)		
Ca	0.017	
Na	0.355	
K	1.571	
$\sum$	1.942	
Total	15.818	

Abbreviations: sm-starting material (see Table 3.1), run#-run number (see Table 3.3), apfu-atoms per formula unit (based on 22 atoms of oxygen; Deer *et al.* 1992).

$\sum$Fe-Mg exchange coefficient (*i.e.*, $K_D^{\Sigma Fe/Mg}$) instead of the Fe^{2+}-Mg exchange coefficient to evaluate if equilibrium existed between mica and quenched melt during experiments. The calculated $\sum$Fe-Mg exchange coefficients (*i.e.*, $K_D^{\Sigma Fe/Mg}$) between micas and liquids were similar (*i.e.*, 0.19, 0.29, 0.40, 0.39, 0.29 for P-MT-27, P-MTg-12, P-MTg-41, P-MTg-43, and FM10-02, respectively) or higher (0.62 for P-MT-34) to the range reported or calculated from other experimentally produced micas (*i.e.*, ~0.24 to ~0.30: Jakobsson and Holloway 1986, Fig. 8; 0.03-0.25: Guo and Green 1990, runs#: 1076, 1163, 1165, 1234, 1235, 1244; 0.24: Adam *et al.* 1993, run#: 1394; 0.34: LaTourrette *et al.* 1995, run#: 3047T-1). However, the $K_D^{\Sigma Fe/Mg}$ for mica is not well calibrated, leaving a doubt, similar to the case for amphibole, as to the acceptable range of equilibrium values. I inferred that the relatively low and high $K_D^{\Sigma Fe/Mg}$ values observed for P-MT-27 and P-MT-34 experiments between phlogopite and quenched melt, respectively, could be explained by a dominant number of analyses performed in the glass close to the crystal rims (*e.g.*, P-MT-27) or by iron-loss from the charge to the container (*e.g.*, P-MT-34). However, no phlogopite zoning was observed in the P-MT-34 experiment unlike that observed in the coexisting amphibole suggesting that phlogopite completed the crystallization prior to iron-loss. This observation demonstrates that the iron-loss was a late process for P-MT-34 experiment.

The Al_{total} content in the tetrahedral and octahedral sites (*i.e.*, $^{IV}Al + {}^{VI}Al = 2.723$-$3.149$ apfu), Fe^{2+} in the octahedral site (*i.e.*, $^{VI}Fe^{2+} = 0.483$-1.024 apfu), and Mg content in the octahedral site (*i.e.*, $^{VI}Mg = 4.336$-4.853 apfu) were very similar to micas reported by

Adam *et al.* (1993; run#: 1394) and LaTourrette *et al.*'s (1995; run#: 3047T-1) experiments using basanitic materials. However phlogopites which crystallized from pargasitic materials (*i.e.*, P-MT-27, P-MT-34, P-MTg-12, P-MTg-41, P-MTg-43) had a higher Al_{total} and a lower Fe_{total} content than the phlogopite which crystallized from the alkali basalt material (*i.e.*, FM10-02; Table 3.8) and those from basanitic materials of Adam *et al.* (1993) and LaTourrette *et al.*'s (1995) experiments. No significant difference exists between the ^{VI}Mg content of our phlogopites (*i.e.*, pargasitic and alkali basalt materials) and the one reported by Adam *et al.* (1993) (*i.e.*, > 4.000 apfu) while I observed a lower ^{VI}Mg (*i.e.*, < 4.000 apfu) content compared to the one reported by LaTourrette *et al.*'s (1995).

Because crystal thickness is a major problem for LAM-ICP-MS analysis, no trace element analyses were done on these micas due to our inability to estimate their thicknesses. However, in a previous study on partitioning between phlogopite and nephelinitic-basanitic liquid Dalpé and Baker (1993) reported some partition coefficients values for Na (0.56 ±0.14), Ti (0.71 ±0.10), Ga (0.42 ±0.13), Rb (0.25 ±0.20), Sr (0.55 ±0.24), Y (0.49 ±0.20), Nb (0.44 ±0.16), and Zr (0.40 ±0.28) using the synchrotron X-ray-fluorescence microprobe (SXRFM) (see also Green 1994).

3.4.1.3. Pyroxene

Two distinct crystal shapes of pyroxenes, anhedral and euhedral, were found in the run products. Anhedral pyroxenes were relatively small crystals (~50-200 μm along their

longest axis) surrounded by amphibole and/or mica (Fig. 3.1b). I found anhedral pyroxenes in all run products from different pressures (1.5-2.5 GPa) and temperatures (1000-1100 °C) with the exception of the K-HD-08 run where pyroxenes were absent and K1921-15 run where only euhedral pyroxenes were present. Pyroxene composition varied from Ca-rich diopside ($Wo_{52}En_{41}Fs_7$) to augite ($Wo_{42}En_{46}Fs_{12}$) according to the classification of Morimoto (1989) on the basis of 6 atoms of oxygens per formula unit (Table 3.9). Euhedral crystals were relatively large (~300-350 μm along their longest axis) and were in contact with amphibole and/or mica and glass (Figs. 3.1c and 3.1d). Euhedral pyroxenes were produced in P-MTg_{Ti}-31, HF13-38, HF13g_{Ti}-03, K1921-15, and FM10-25 runs and were classified as augite ($Wo_{43}En_{45}Fs_{12}$ to $Wo_{41}En_{47}Fs_{12}$; Morimoto 1989). However in the K1921-15 run, an intergrown of pyroxenes was observed in which compositions were augite ($Wo_{41}En_{47}Fs_{12}$) and a Ca-poor pyroxene ($Wo_5En_{78}Fs_{17}$), corresponding to a pigeonitic composition.

Based upon suspicious Fe^{2+}-Mg exchange coefficients (*i.e.*, K_D) between anhedral pyroxenes and liquids (i.e., K_D values were higher or lower than previously reported values of 0.23 to 0.36; Dunn 1987, Sisson and Grove 1993), I believe that those anhedral pyroxenes represent a non-equilibrium state at the final run conditions. These anhedral pyroxenes may have formed during the cooling process when the temperature of the assembly decreased to the final run temperature. Similar anhedral pyroxenes surrounded by amphibole were observed in Brenan *et al.*'s (1995; see Fig. 2) experiments. Pyroxenes crystallized from P-MT and P-MTg materials had a higher wollastonite and a lower ferrosilite content (*i.e.*, Wo > 49 and Fs < 7 %, respectively) than anhedral pyroxenes crystallized from HF13, HF13g_{Ti}, and

Table 3.9. Pyroxene compositions in experiments and their formula unit

sm	P-MT		P-MT		P-MTg		P-MTg		P-MTg	
run#	27		34		12		41		43	
n	5		2		3		11		3	
cs	a		a		a		a		a	
(wt.%)										
SiO_2	45.60	(0.09)	48.99	(0.26)	44.34	(1.15)	48.40	(0.74)	47.27	(2.02)
TiO_2	2.80	(0.10)	1.67	(0.07)	3.32	(0.68)	1.43	(0.20)	1.98	(0.14)
Al_2O_3	11.00	(0.34)	8.10	(0.18)	12.96	(1.01)	8.23	(0.86)	6.76	(0.39)
FeO	3.14	(0.07)	2.54	(0.10)	3.83	(0.08)	3.47	(0.23)	3.86	(0.16)
MnO	0.05	(0.01)	0.06	(0.01)	0.06	(0.02)	0.03	(0.01)	0.05	(0.03)
MgO	13.37	(0.22)	15.41	(0.07)	12.74	(0.60)	14.50	(0.42)	14.73	(0.33)
CaO	22.37	(0.09)	22.09	(0.20)	22.16	(0.20)	23.27	(0.30)	23.79	(0.13)
Na_2O	0.52	(0.09)	0.70	(0.01)	0.53	(0.01)	0.62	(0.05)	0.37	(0.01)
K_2O	blld		blld		blld		blld		blld	
Total	98.85		99.56		99.94		99.95		98.81	
(apfu)										
Tetrahedral site										
Si	1.690		1.789		1.631		1.775		1.767	
Al	0.310		0.211		0.369		0.225		0.233	
$\sum$	2.000		2.000		2.000		2.000		2.000	
Octahedral sites M(1,2)										
Al	0.170		0.137		0.193		0.131		0.064	
Ti	0.078		0.046		0.092		0.039		0.056	
Fe^{2+}	0.097		0.077		0.118		0.106		0.121	
Mn	0.002		0.002		0.002		0.001		0.002	
Mg	0.739		0.839		0.699		0.793		0.821	
Ca	0.888		0.864		0.874		0.914		0.953	
Na	0.037		0.049		0.038		0.044		0.027	
K	blld		blld		blld		blld		blld	
$\sum$	2.011		2.015		2.015		2.030		2.042	
Total	4.011		4.015		4.015		4.030		4.042	

Table 3.9. (continued)

sm	P-MTg$_{Ti}$		HF13		HF13		HF13g$_{Ti}$	HF13g$_{Ti}$
run#	31		38		38		03	03
n	3		2		2		1	1
cs	a (+e)[a]		e		a		a	e
(wt.%)								
SiO_2	47.07	(1.44)	50.45	(1.04)	52.21	(0.11)	49.89	53.35
TiO_2	3.13	(0.63)	1.42	(0.25)	0.69	(.002)	2.66	0.79
Al_2O_3	8.91	(1.42)	5.10	(0.90)	3.11	(0.01)	6.44	2.46
FeO	1.65	(0.07)	6.61	(0.16)	6.36	(0.10)	5.74	5.00
MnO	0.08	(0.01)	0.15	(0.01)	0.19	(.001)	0.18	0.17
MgO	15.19	(0.55)	14.59	(0.04)	14.64	(0.04)	14.03	16.41
CaO	22.69	(0.19)	19.71	(1.22)	21.23	(0.07)	20.08	21.11
Na_2O	0.50	(0.04)	1.39	(0.29)	0.96	(0.01)	1.30	0.93
K_2O	bild		bild		bild		bild	bild
Total	99.22		99.42		99.41		100.38	100..25
(apfu)								
Tetrahedral site								
Si	1.727		1.869		1.934		1.828	1.946
Al	0.273		0.131		0.066		0.172	0.054
$\sum$	2.000		2.000		2.000		2.000	2.000
Octahedral sites M(1,2)								
Al	0.113		0.092		0.070		0.106	0.051
Ti	0.086		0.040		0.019		0.073	0.022
Fe^{2+}	0.051		0.205		0.197		0.176	0.152
Mn	0.002		0.005		0.006		0.006	0.005
Mg	0.831		0.806		0.809		0.766	0.892
Ca	0.892		0.782		0.843		0.788	0.825
Na	0.036		0.100		0.069		0.092	0.066
K	bild		bild		bild		bild	bild
$\sum$	2.011		2.030		2.013		2.006	2.013
Total	4.011		4.030		4.013		4.006	4.013

Table 3.9. (continued)

sm	K1921		K1921		FM10		FM10	
run#	15		15		23		25	
n	4		8		7		7	
cs	e[b]		e[b]		a		e	
(wt.%)								
SiO_2	50.67	(1.23)	54.27	(0.43)	50.49	(0.92)	49.60	(0.77)
TiO_2	1.16	(0.36)	0.37	(0.04)	0.88	(0.22)	0.71	(0.11)
Al_2O_3	4.97	(1.11)	2.94	(0.40)	5.27	(1.03)	6.09	(0.33)
FeO	7.31	(0.81)	11.55	(0.41)	7.14	(0.40)	9.29	(0.46)
MnO	0.16	(0.02)	0.21	(0.02)	0.19	(0.02)	0.22	(0.01)
MgO	15.79	(1.00)	28.67	(0.25)	15.32	(0.76)	12.95	(0.33)
CaO	19.07	(0.46)	2.35	(0.40)	19.78	(0.76)	19.33	(0.29)
Na_2O	0.52	(0.03)	0.07	(0.01)	0.65	(0.06)	1.03	(0.05)
K_2O	blld		blld		blld		blld	
Total	99.65		100.43		99.72		99.22	
(apfu)								
Tetrahedral site								
Si	1.870		1.922		1.865		1.860	
Al	0.130		0.078		0.135		0.140	
$\sum$	2.000		2.000		2.000		2.000	
Octahedral sites M(1,2)								
Al	0.086		0.044		0.095		0.129	
Ti	0.032		0.010		0.024		0.020	
Fe^{2+}	0.226		0.342		0.221		0.291	
Mn	0.005		0.006		0.006		0.007	
Mg	0.869		1.513		0.844		0.724	
Ca	0.754		0.089		0.783		0.777	
Na	0.037		0.005		0.047		0.075	
K	blld		blld		blld		blld	
$\sum$	2.009		2.010		2.019		2.023	
Total	4.009		4.010		4.019		4.023	

Abbreviations: sm-starting material, run#-run number, n-number of analyses, cs-crystal shape, a-anhedral, e-euhedral, apfu-atoms per formula unit (based on 6 atoms of oxygen; Deer *et al.* 1992), blld-concentration below the lower limit of detection.

[a] Run products contained both crystal shapes. [b] Intergrown crystals of Ca-rich and Ca-poor pyroxene (see text).

FM10 materials (*i.e.*, Wo < 45 and Fs > 8 %, respectively) at similar pressure and temperature conditions. Moreover, the P-MT and P-MTg anhedral pyroxenes had a composition similar to those reported by Chazot *et al.* (1996) sampled from natural spinel lherzolites and to experimentally produced pyroxenes from LaTourrette and Burnett (1992; runs#: D and H) using a modified alkali basalt. The anhedral pyroxenes found in alkaline materials (*i.e.*, HF13, $HF13g_{Ti}$ and FM10) had compositions similar to those found in other experimental studies using different basaltic compositions (Nicholls and Harris 1980, Adam and Green 1994, Skulski *et al.* 1994).

The K_D values of euhedral pyroxenes were within the range of 0.23 to 0.36. They were 0.27, 0.29, and 0.29 for P-MTg_{Ti}-31, HF13-38, and $HF13g_{Ti}$-03 runs, respectively. However, lower K_D values were observed for the imbricated pyroxenes found in the K1921-15 run (*i.e.*, 0.21 and 0.19) and a higher K_D value for pyroxenes found in the FM10-25 run (*i.e.*, 0.45). These euhedral pyroxenes were similar in composition to the pyroxenes found by Nicholls and Harris (1980), Adam and Green (1994), and Skulski *et al.* (1994).

We did not perform trace element analyses on the different pyroxenes (*i.e.*, anhedral and euhedral) due to the suspicious aspect of their equilibrium, zoning, crystal size (too small for the ablation grids used by the LAM-ICP-MS analyses), and finally the incapacity of each starting material to produce large and homogeneous euhedral pyroxenes for analysis and comparison between them.

3.4.1.4. Olivine

Small anhedral olivines (<100 μm along their longest axis) surrounded by pyroxene and/or amphibole and/or mica were found in runs using pargasitic materials (*i.e.*, P-MT-27, P-MTg-12, P-MTg-41, P-MTg-43, and P-MTg$_{Ti}$-31; Table 3.3), and were classified as Mg-rich olivine (Fo_{88-93}; Deer *et al.* 1992). The Fe^{2+}-Mg exchange coefficients calculated between the olivine and melt (*i.e.*, K_D) were all slightly offset (*i.e.*, 0.21 to 0.41) from the accepted value of 0.30 ± 0.03 from Roeder and Emslie (1970). In the experiments where the starting materials were similar (*i.e.*, P-MT, P-MTg, P-MTg$_{Ti}$; Table 3.1), lower K_D values were measured for olivines which crystallized from experiments at 1.5 GPa and at low oxygen fugacity (*i.e.*, P-MT-27 and P-MTg-12 runs with K_D = 0.22 and 0.21, respectively, both at NNO-2), higher K_D ratios were measured for experiments at 1.5-2.5 GPa and at high oxygen fugacity (*i.e.*, P-MTg-43 and P-MTg-41 runs with K_D = 0.41 and 0.44, respectively, both at NNO+1.7), whereas the K_D ratio measured in the P-MTg$_{Ti}$-31 run was relatively close to the accepted value (0.35). The K_D value between olivine and melt was demonstrated to be relatively insensitive to temperature and oxygen fugacity (Roeder and Emslie 1970) but increases with pressure (Ulmer 1989, Jones 1995), and decreases in Ti-rich basaltic magmas due to titanium complexation with ferrous iron in the liquid (*e.g.*, forming a $FeTi_2O_5$ species), leaving a fraction of the total FeO available for partitioning into olivine (Jones 1988).

For our anhedral olivines, the variation observed in the K_D values could be related to the effect of pressure and the bulk titanium content but it seems that the olivines underwent

similar crystallization problems as the anhedral pyroxenes. The olivines were probably in equilibrium with their host liquid when they crystallized from higher temperatures. During the cooling process to the run conditions, clinopyroxene, amphibole, or mica nucleated and grew around the olivines, making a barrier between olivine crystals and the evolved liquids. Due to the small crystals and non-equilibrium state at the run conditions, no trace element analyses were performed on olivines.

3.4.1.5. Glass

Major and trace element analyses of the different glass run products are listed in Table 3.6. In some experiments, the quenching process of the hydrous basaltic liquids results in micro-spinifex texture glass ($\leq$ 5 μm grain size). In such cases, multiple point analyses were necessary with the electron microprobe to obtain a representative liquid composition. However, some liquid compositions quenched as a homogeneous glass (Figs. 1a and 1b). The difference in homogeneity between both types of quenched glasses can be observed by comparison of the standard deviations attached to each major element in Table 3.6 (*e.g.*, P-MT-34 versus P-MTg_{Ti}-31). For the trace elements, because LAM-ICP-MS analyses used a larger volume of the sample compared to electron microprobe analyses, no significant differences were observed in the RSD values attached to the trace elements analyzed in the micro-spinifex glass versus those done in the homogeneous glass (both referred to as quenched glass). All measurements of major and trace elements in the quenched glass were

collected beyond the quench-modified glass zone with the exception of the P-MT-27 run as discussed previously. I checked the homogeneity of the synthesized glass in all experiments by performing line traverses across it and calculating the relative standard deviation from the multiple analyses. The average RSD's calculated from different analyses in glass run products gave: SiO_2 (3.75 %), TiO_2 (5.2 %), Al_2O_3 (5.5 %), FeO (6.9 %), MgO (13 %), CaO (8.3 %), Na_2O (20 %), and K_2O (20 %). The high RSD calculated for MgO, Na_2O, and K_2O in the glass (specially for Na_2O in FM10 experiments for which the RSD value is up to 44 %,Table 3.6) were attributed to quench crystal formation as mentioned above. The Na-loss during microprobe analyses in these hydrous glasses at relatively low concentrations is normally found to be less than the RSD value attached to FM10 experiments (*i.e.*, maximum calculated loss of ~ 20 % relative; Baker, pers. comm., 1998). The Fe_2O_3 and FeO proportion (*i.e.*, Fe^{3+}/Fe^{2+} ratio) was calculated using total iron from the electron microprobe at run conditions (*i.e.*, pressure, temperature), and the oxygen fugacity maintained during the experiment (*i.e.*, NNO-2 and NNO+1.7; Kress and Carmichael 1991).

The compositions of the different quenched glasses showed a relatively wide range of composition based on their major elements (Table 3.6). The quenched glass compositions of P-MT-27, P-MT-34, P-MTg-12, P-MTg-41, P-MTg-43, P-MTg_{Ti}-31, K-HD-08, HF13-38, HF13g_{Ti}-03, and FM10-02 experiments were all classified as alkaline basaltic compositions based on their Na_2O, K_2O, and SiO_2 contents according to Miyashiro (1978) and Cox *et al.* (1979) nomenclatures (not normalized to 100 %). The weight percent of normative nepheline

associated with these glasses varied from 0-5 wt.% (P-MT-34, P-MTg$_{Ti}$-31, K-HD-08), 5-15 wt.% (P-MT-27, P-MTg-12, P-MTg-41, P-MTg-43), and >15 wt.% (HF13-38, HF13g$_{Ti}$-03, FM10-02). These alkaline basaltic quenched glasses were similar in major element concentrations to those produced by Adam *et al.* (1993), Adam and Green (1994), and LaTourrette *et al.* (1995). However, the quenched glass compositions of K1921-15, FM10-23, and FM10-25 experiments were classified as sub-alkaline basalt to basaltic andesite compositions (Miyashiro 1978, Cox *et al.* 1979). For these three quenched glasses, the weight percents of the normative hypersthene were all > 21 wt.% and they were different in composition from all previous experimental studies. The alkali index (Middlemost 1975) of K1921-15, FM10-23, and FM10-25 quenched glasses were 2.65, 6.57, and 3.06, respectively (using values in Table 3.6 without normalisation to 100). The high alkali indices observed for the FM10-23 glass composition suggests a high-alumina basaltic affinity (or calc-alkaline basaltic affinity based on Middlemost's 1975 classification). However, the alkali index of the K1921-15 and FM10-25 quenched glasses were similar to those observed by Green and Pearson's [1985a; runs#: 998 and 955 (HM)], and by Nicholls and Harris (1980; runs#: 4749, 4754, 4755, and 4756) experiments, but had a lower Al_2O_3 content (< 16.5 wt.%; Table 3.6).

Experiments performed with the pargasitic materials (P-MT and P-MTg) showed a reduction in SiO_2 content of the quenched glass as pressure increased from 1.5 to 2.5 GPa (*i.e.*, P-MT-27 and P-MT-34, P-MTg-43 and P-MTg-41, respectively), independent of oxygen fugacities while this trend was reversed (*i.e.*, SiO_2 content increased) for the alkalic

basalt material (FM10-23 and FM10-25) at the high oxygen fugacity condition (Table 3.6). These trends reflect the modal proportions of amphibole and clinopyroxene observed in the experiments where amphibole decreased and clinopyroxene increased as pressure increased for P-MT compositions (*e.g.*, P-MT-27, P-MT-34, P-MTg-43, and P-MTg-41), whereas modal proportions of amphibole increased and clinopyroxene decreased as pressure increased for FM10 bulk composition (*e.g.*, FM10-23 and FM10-25; Table 3.3).

The range of calculated $Mg\#_t$ of the different quenched glasses varied from 62 to 86 (*e.g.*, P-MT-27, P-MT-34, P-MTg-12, P-MTg-41, P-MTg43, P-MTg_{Ti}-31, K-HD-08), 53 to 63 (*e.g.*, HF13-38, HF13g_{Ti}-03), 45 (*e.g.*, K1921-15), 41 to 55 (*e.g.*, FM10-02, FM10-23, FM10-25) as a function of pressure, oxygen fugacity, temperature, and starting material composition (Table 3.6).

In summary it appears that the different quenched glasses (referred hereafter as melt) and the amphibole run products were homogeneous in major, minor, and trace elements. Furthermore due to the long run durations used in this study (*i.e.*, ≥ 24 h), partitioning of major, minor, and trace elements between amphibole and melt demonstrate equilibrium behaviour at run conditions.

3.5 Results and comparison with previous studies

Partition coefficients were calculated using multiple spot or grid analyses performed

by electron microprobe and LAM-ICP-MS (Table 3.10). The concentrations of trace elements (*i.e.*, Nb, Th, U, Tm, and Lu) in the amphibole for some experiments were below the lower limit of detection of the LAM-ICP-MS (Table 3.4). In such cases, the derived partition coefficient (on a qualitative basis) was calculated using the lower limit of detection of the element (*i*) attached to the LAM-ICP-MS divided by the concentration of each respective element (*i*) in the quenched glass (*i.e.*, D_i = lld_i / concentration of the $element_i$ in the quenched glass; Tables 3.2 and 3.6). These partition coefficients were assumed to be maximum values (*i.e.*, D_{max}). In one experiment, the uranium concentration in the quenched glass was below the lower limit of detection (P-MTg_{Ti}-31; Table 3.6). In this case the maximum partition coefficient could not be estimated. As mentioned above for the P-MT-34 experiment, the concentrations of Eu, Gd, Tb, Dy, Ho, and Er were similar based on two standard deviations between both zones of the amphibole run products [*i.e.*, Fe-rich (core) and Fe-poor (rim); Table 3.4] In this case, I used the calculated partition coefficients between the Fe-rich zone and melt.

3.5.1. Effects of melt compositions on partitioning

Because different bulk starting materials were used in this study at different pressures, temperatures, and oxygen fugacities, the variation in partitioning due to the effects of bulk starting material can be a complex parameter to isolate from the physical conditions (*e.g.*, P, T, fO_2). I observed that differing oxygen fugacities can significantly affect the melt

Table 3.10. Measured partition coefficients

sm	P-MT		P-MT[a]		P-MTg		P-MTg		P-MTg	
run#	27		34		12		41		43	
T	1100		1050		1100		1075		1050	
P	1.5		2.5		1.5		2.5		1.5	
fO_2	low		low		low		high		high	
Ti	0.87	(0.05)	0.51	(0.06)	0.98	(0.07)	0.40	(0.05)	0.68	(0.08)
Al	1.08	(0.06)	1.14	(0.12)	0.97	(0.14)	1.08	(0.09)	1.01	(0.06)
Ca	0.92	(0.05)	1.12	(0.25)	0.97	(0.11)	1.08	(0.12)	0.99	(0.05)
Na	1.38	(0.28)	1.75	(0.57)	1.15	(0.19)	1.16	(0.12)	1.27	(0.20)
K	1.52	(0.36)	1.81	(0.68)	1.59	(0.51)	2.20	(0.47)	1.72	(0.26)
Rb	0.32	(0.08)	0.63	(0.08)	0.33	(0.10)	1.04	(0.18)	0.54	(0.13)
Sr	0.45	(0.02)	0.44	(0.05)	0.52	(0.03)	0.50	(0.02)	0.58	(0.04)
Y	0.41	(0.03)	0.44	(0.02)	0.46	(0.04)	0.38	(0.01)	0.40	(0.03)
Zr	0.16	(0.02)	0.09	(0.01)	0.19	(0.02)	0.08	(0.01)	0.21	(0.01)
Nb	0.08	(0.01)	0.04[c]		0.10	(0.02)	0.03[c]		0.08	(0.03)
Ba	0.42	(0.06)	0.42	(0.03)	0.47	(0.08)	0.72	(0.04)	0.72	(0.08)
Hf	0.32	(0.06)	0.18	(0.02)	0.35	(0.06)	0.12	(0.06)	0.35	(0.02)
Ta	0.08	(0.03)	0.05	(0.01)	0.15	(0.02)	0.03[c]		0.11	(0.03)
Th[c]	0.16		0.50		0.22		0.31		0.19	
U[c]	0.27		0.44		0.36		0.57		0.36	
La	0.06	(0.01)	0.03	(.002)	0.08	(0.01)	0.08	(0.01)	0.11	(0.03)
Ce	0.10	(0.02)	0.08	(0.01)	0.12	(0.02)	0.12	(.004)	0.17	(0.03)
Pr	0.15	(0.02)	0.13	(0.01)	0.18	(0.02)	0.17	(0.01)	0.23	(0.03)
Nd	0.21	(0.02)	0.18	(0.02)	0.24	(0.01)	0.23	(0.01)	0.29	(0.03)
Sm	0.34	(0.04)	0.30	(0.04)	0.31	(0.05)	0.31	(0.02)	0.42	(0.03)
Eu	0.43	(0.12)	0.28	(0.05)	0.44	(0.04)	0.34	(0.06)	0.46	(0.03)
Gd	0.46	(0.15)	0.43	(0.08)	0.48	(0.04)	0.39	(0.02)	0.45	(0.01)
Tb	0.49	(0.16)	0.48	(0.03)	0.45	(0.06)	0.42	(0.04)	0.44	(0.03)
Dy	0.50	(0.17)	0.45	(0.04)	0.49	(0.04)	0.38	(0.02)	0.42	(0.02)
Ho	0.45	(0.16)	0.53	(0.02)	0.47	(0.06)	0.35	(0.03)	0.42	(0.02)
Er	0.42	(0.15)	0.45	(0.07)	0.49	(0.06)	0.34	(0.04)	0.40	(0.05)
Tm	0.30[c]		0.43[c]		0.51	(0.06)	0.33[c]		0.35	(0.03)
Yb	0.32	(0.10)	0.40	(0.12)	0.43	(0.04)	0.23	(0.06)	0.34	(0.01)
Lu	0.27[c]		0.40[c]		0.51	(0.07)	0.41	(0.11)	0.36	(0.07)

Table 3.10. (continued)

sm	P-MTg$_{Ti}$		K-HD[b]		HF13		HF13g$_{Ti}$		K1921	
run#	31		08		38		03		15	
T	1130		1100		1020		1040		1020	
P	1.5		1.5		1.5		1.5		1.5	
fO_2	low		low		low		low		low	
Ti	0.72	(0.03)	0.76[b]	(0.05)	1.20	(0.06)	1.17	(0.10)	1.46	(0.10)
Al	0.99	(0.02)	1.01	(0.07)	1.01	(0.04)	0.96	(0.04)	0.90	(0.01)
Ca	1.00	(0.01)	1.01	(0.08)	1.00	(0.05)	1.11	(0.07)	1.31	(0.03)
Na	0.97	(0.07)	1.29	(0.23)	0.77	(0.10)	0.49	(0.05)	1.43	(0.06)
K	1.46	(0.07)	1.27[b]	(0.63)	1.05	(0.25)	0.67	(0.08)	0.73	(0.06)
Rb	0.45	(0.03)	0.22[b]	(0.04)	0.16	(0.01)	0.14	(.004)	0.21	(0.03)
Sr	0.57	(0.02)	0.37	(0.01)	0.16	(.004)	0.20	(.004)	0.41	(0.04)
Y	0.48	(0.03)	0.33[b]	(0.03)	0.25	(0.01)	0.33	(0.01)	0.79	(0.09)
Zr	0.24	(0.04)	0.12[b]	(0.01)	0.19	(.001)	0.24	(0.01)	0.21	(0.02)
Nb	0.20	(0.02)	0.05[b]	(0.01)	0.13	(.003)	0.12	(0.01)	0.18	(0.03)
Ba	0.59	(0.03)	0.27	(0.01)	0.11	(.005)	0.18	(0.01)	0.28	(0.03)
Hf	0.35	(0.13)	0.32	(0.05)	0.41	(0.02)	0.46	(0.05)	0.31	(0.06)
Ta	0.27	(0.06)	0.07[b]	(0.02)	0.16	(0.01)	0.18	(0.01)	0.16	(0.03)
Th[c]	0.24		0.38		0.01		0.01		0.04	
U[c]	blld		0.08		0.01		0.01		0.05	
La	0.21	(0.03)	0.04[b]	(0.01)	0.04	(.001)	0.07	(.002)	0.11	(0.02)
Ce	0.23	(0.03)	0.07[b]	(.002)	0.08	(.003)	0.11	(.002)	0.19	(0.02)
Pr	0.27	(0.03)	0.10	(0.01)	0.11	(.002)	0.15	(.002)	0.27	(0.03)
Nd	0.32	(0.02)	0.14[b]	(0.01)	0.16	(0.01)	0.21	(.003)	0.36	(0.05)
Sm	0.36	(0.09)	0.18	(0.07)	0.25	(0.01)	0.24	(0.01)	0.64	(0.17)
Eu	0.45	(0.06)	0.33	(0.02)	0.26	(0.01)	0.29	(0.02)	0.53	(0.13)
Gd	0.42	(0.05)	0.36	(0.02)	0.29	(0.01)	0.33	(0.02)	0.60	(0.05)
Tb	0.37	(0.06)	0.38	(0.02)	0.31	(0.02)	0.33	(0.02)	nd	
Dy	0.38	(0.05)	0.40	(0.01)	0.31	(0.01)	0.35	(0.01)	0.66	(0.19)
Ho	0.39	(0.05)	0.34	(0.04)	0.30	(0.02)	0.33	(0.03)	0.64	(0.14)
Er	0.41	(0.04)	0.35	(0.01)	0.28	(0.02)	0.30	(0.03)	0.87	(0.12)
Tm	0.53	(0.08)	0.28	(0.03)	0.30	(0.04)	0.21	(0.03)	0.79	(0.15)
Yb	0.53	(0.03)	0.34	(0.04)	0.24	(0.01)	0.21	(0.02)	0.65	(0.11)
Lu	0.40[c]		0.24	(0.03)	0.25	(0.08)	0.23	(0.06)	0.56	(0.21)

Table 3.10. (continued)

sm	FM10		FM10		FM10	
run#	02		23		25	
T	1040		1000		1000	
P	1.5		1.5		2.2	
fO_2	low		high		high	
Ti	1.20	(0.12)	0.96	(0.07)	1.01	(0.08)
Al	1.02	(0.09)	0.83	(0.06)	0.89	(0.06)
Ca	0.96	(0.11)	1.43	(0.16)	1.40	(0.19)
Na	0.85	(0.19)	1.61	(0.41)	2.05	(0.90)
K	0.71	(0.11)	1.21	(0.38)	1.40	(0.46)
Rb	0.23	(0.05)	0.23	(0.03)	0.27	(0.03)
Sr	0.23	(0.02)	0.44	(0.03)	0.30	(0.02)
Y	0.36	(0.06)	0.63	(0.03)	0.61	(0.03)
Zr	0.25	(0.04)	0.16	(0.02)	0.09	(0.01)
Nb	0.14	(0.02)	0.10	(0.01)	0.07	(0.02)
Ba	0.16	(0.02)	0.34	(0.04)	0.24	(0.02)
Hf	0.44	(0.09)	0.26	(0.05)	0.15	(0.02)
Ta	0.18	(0.02)	0.12	(0.02)	0.07	(0.02)
Th[c]	0.01		0.04		0.03	
U[c]	0.01		0.06		0.04	
La	0.07	(0.02)	0.10	(0.02)	0.06	(0.01)
Ce	0.12	(0.02)	0.16	(0.02)	0.12	(0.01)
Pr	0.17	(0.02)	0.25	(0.02)	0.19	(0.02)
Nd	0.23	(0.03)	0.36	(0.04)	0.25	(0.02)
Sm	0.33	(0.06)	0.51	(0.10)	0.42	(0.04)
Eu	0.33	(0.05)	0.59	(0.07)	0.46	(0.08)
Gd	0.33	(0.03)	0.60	(0.06)	0.61	(0.06)
Tb	0.33	(0.03)	0.66	(0.06)	0.59	(0.03)
Dy	0.33	(0.02)	0.68	(0.04)	0.65	(0.09)
Ho	0.32	(0.03)	0.67	(0.04)	0.65	(0.04)
Er	0.34	(0.10)	0.60	(0.07)	0.64	(0.08)
Tm	0.39	(0.08)	0.50	(0.06)	0.58	(0.07)
Yb	0.35	(0.14)	0.45	(0.02)	0.56	(0.08)
Lu	0.35	(0.09)	0.44	(0.06)	0.55	(0.04)

Abbreviations: sm-starting material (Table 3.1), run#-run number (see Table 3.3), T-run temperature in °C, P-run pressure in GPa, fO_2-oxygen fugacity maintained during experiment (see section 3.2.2.2.), blld-concentration below the lower limit of detection in both phases (*i.e.*, amphibole and melt), nd-not determined. [a] Partition coefficients were calculated using the Fe-rich zone only (i.e., P-MT-34a; see Table 3.4). [b] Reported values taken from Dalpé *et al.* (1995) and performed by LAM-ICP-MS [partition coefficients different than Dalpé and

Table 3.10. (continued)

Baker (1994) and Dalpé *et al.* (1995) resulted from reanalyzed amphibole and melt].

[c] Maximum partition coefficients were obtained from the relationship: lower limit of detection of LAM-ICP-MS (Table 3.2) divided by the concentration of the element in the respective melt from run products (see Table 3.6). Values in parentheses are based on one standard deviation from the relationship: $\sigma_D = [(c_{am}^2 \times \sigma_{melt}^2 / c_{melt}^4) + (\sigma_{am}^2 / c_{melt}^2)]^{0.5}$ where: σ-standard deviation, *D*-partition coefficient, c-concentration, am-amphibole, melt-melt in equilibrium with amphibole (Watson and Ryerson 1986). Note that D_{Ti}, D_{Ab}, D_{Ca}, D_{Na}, and D_K seem to be in the Henry's law region as discussed in text.

compositions for some experiments performed at the same temperature and pressure, FM10-02 *vs.* FM10-23 experiments. For these two experiments large variations in partition coefficients were observed between amphibole and melt (*e.g.*, D_{Sr} = 0.23 and 0.44, respectively) while others were similar (*e.g.*, D_{Rb} = 0.23). In other experiments, different bulk starting materials produced similar melt compositions but distinct amphibole compositions at different run conditions. An example of this are K1921-15 and FM10-25 experiments where similar partition coefficients for some elements were observed between amphibole and melt (*e.g.*, D_{Dy} = 0.66 and 0.65, D_{Ho} = 0.64 and 0.65, respectively) whereas others were different (*e.g.*, D_{Zr} = 0.21 and 0.09, D_{Ta} = 0.16 and 0.07, respectively). Furthermore, because these experiments do not correspond to the same starting materials or run conditions (*i.e.*, P, T, fO_2) as previous experimental studies I will first evaluate the variation in partition coefficients based on melt compositions, whose importance has been demonstrated in some previous studies (Watson 1977, Green and Pearson 1985b, Adam *et al.* 1993, Kohn and Schofield 1994, Klein *et al.* 1997). Then to complete the comparison of partitioning between amphibole and melt, I will discuss trends between partitioning and the amphibole crystal chemistry. Crystal chemistry seems to play a major role for partitioning in this study and was demonstrated to be important in other mineral / liquid partitioning studies (Drake and Weill 1975, Philpotts 1978, Colson *et al.* 1988, McKay 1989, Blundy and Wood 1991a, -b, Wood and Blundy 1997). Furthermore, the effects of pressure, oxygen fugacity, and titanium content will be discussed separately in Chapters 4 and 5 to better distinguish their effects on

partitioning.

The different bulk starting materials were subdivided by their "chemical affinity" into four different groups (*i.e.*, see "ca" in Table 3.11). These are:

Chemical affinity

- the amphibole group (referred to as "amph."; where P-MT, P-MTg, P-MTg_{Ti}, K-HD were used as starting materials),
- the olivine-normative nephelinite group or HF (referred to as "ol-norm. neph."; where HF13, HF13g_{Ti} were used as starting materials),
- the tholeiite group or K1921 (referred to as "thol."; where K1921 was used as starting material), and finally
- the alkaline basalt group or FM10 (referred to as "alk.-bas."; where FM10 was used as starting material) (Table 3.11).

Furthermore, to compare our results with previous experimental studies, I subdivided these "chemical affinity" into different subgroups based on their melt composition using Miyashiro (1978), Cox *et al.* (1979), and Middlemost's (1975) classifications. This was necessary due to the large variation in melt compositions obtained from FM10 experiments. In such cases, the melt compositions obtained from experiments using the different group compositions defined above were classified as:

Melt composition

1- basanitic to nephelinitic melt compositions when I used the "amph." group as

Table 3.11. Average of partition coefficients between calcic amphibole and quenched basaltic melt compositions from experiments

	This study				
ca	"amph."	"ol-norm. neph."	"thol."	"alk.-bas."	
mc	basan. to neph.	neph.	thol.	neph.	subalk.-bas. to thol.
Ti	0.70 (0.08)	1.19 (0.10)	1.46 (0.10)	1.20 (0.12)	0.99 (0.08)
K	1.65 (0.68)	0.86 (0.24)	0.73 (0.06)	0.71 (0.11)	1.31 (0.46)
Rb	0.50 (0.17)	0.15 (0.01)	0.21 (0.03)	0.23 (0.05)	0.25 (0.03)
Sr	0.49 (0.05)	0.18 (0.004)	0.41 (0.04)	0.23 (0.02)	0.37 (0.03)
Y	0.41 (0.04)	0.29 (0.01)	0.79 (0.08)	0.36 (0.06)	0.62 (0.03)
Zr	0.16 (0.04)	0.22 (0.01)	0.21 (0.02)	0.25 (0.04)	0.13 (0.02)
Nb	0.08 (0.03)	0.12 (0.01)	0.18 (0.03)	0.14 (0.02)	0.09 (0.02)
Ba	0.52 (0.08)	0.15 (0.01)	0.28 (0.03)	0.16 (0.01)	0.29 (0.03)
Hf	0.28 (0.13)	0.43 (0.05)	0.31 (0.06)	0.44 (0.08)	0.21 (0.05)
Ta	0.11 (0.06)	0.17 (0.01)	0.16 (0.03)	0.18 (0.02)	0.10 (0.02)
Th	0.29[s]	0.01[s]	0.04[s]	0.01[s]	0.04[s]
U	0.30[s]	0.01[s]	0.05[s]	0.01[s]	0.05[s]
(*REE*)					
La	0.09 (0.03)	0.05 (0.002)	0.11 (0.02)	0.07 (0.02)	0.08 (0.02)
Ce	0.13 (0.03)	0.09 (0.003)	0.19 (0.02)	0.12 (0.02)	0.14 (0.02)
Pr	0.17 (0.03)	0.13 (0.002)	0.27 (0.03)	0.17 (0.03)	0.22 (0.02)
Nd	0.23 (0.03)	0.18 (0.01)	0.36 (0.05)	0.23 (0.03)	0.31 (0.04)
Sm	0.32 (0.09)	0.24 (0.01)	0.64 (0.17)	0.33 (0.06)	0.47 (0.10)
Eu	0.39 (0.12)	0.27 (0.02)	0.53 (0.13)	0.33 (0.05)	0.53 (0.08)
Gd	0.43 (0.14)	0.31 (0.02)	0.60 (0.05)	0.33 (0.02)	0.61 (0.06)
Tb	0.43 (0.16)	0.32 (0.02)	nd	0.33 (0.03)	0.63 (0.06)
Dy	0.43 (0.17)	0.33 (0.01)	0.66 (0.19)	0.33 (0.02)	0.67 (0.09)
Ho	0.42 (0.16)	0.31 (0.03)	0.64 (0.14)	0.32 (0.03)	0.66 (0.04)
Er	0.41 (0.15)	0.29 (0.03)	0.87 (0.12)	0.34 (0.09)	0.62 (0.08)
Tm	0.39 (0.08)	0.25 (0.04)	0.79 (0.15)	0.39 (0.08)	0.54 (0.07)
Yb	0.37 (0.13)	0.22 (0.03)	0.65 (0.11)	0.35 (0.14)	0.51 (0.08)
Lu	0.37 (0.11)	0.24 (0.08)	0.56 (0.21)	0.35 (0.09)	0.50 (0.06)

Table 3.11. (continued)

Other experimental studies

ca	alk.-bas.[a]		tholeiite[b] neph."		basanite[c]		basanite[d]		basanite[e]		basanite[f]	
mc	subalk.-basalt		alk.- to subalk.-bas.		alk.-bas. to basan.		neph.		basan.		alk.-bas.	
Ti	1.75	(0.07)	2.33	(0.20)	1.26	(0.11)	0.92	(0.14)	1.29	(0.03)	1.09	(0.40)
K	0.79	(0.11)	0.54	(0.04)	0.80	(0.25)	0.85	(0.17)	0.58	(0.03)		
Rb					0.20	(0.02)	0.37	(0.08)	0.20	(0.012)		
Sr			0.41	(0.10)	0.31	(0.07)	0.26	(0.02)	0.30	(0.006)		
Y					0.55	(0.10)	0.63	(0.30)	0.52	(0.04)		
Zr					0.33	(0.07)	0.24	(0.05)	0.13	(0.009)	0.21	(0.11)
Nb					0.09	(0.01)	0.08	(0.01)	0.16	(0.005)		
Ba					0.65	(0.21)	0.41	(0.12)	0.16	(0.012)		
Hf									0.33	(0.18)	0.27	(0.19)
Ta					0.14	(0.02)	0.08	(0.01)				
Th									0.004	(0.001)		
U									0.004	(0.001)		
(*REE*)												
La	0.2	(0.1)			0.12	(0.05)	0.09	(0.07)	0.06	(0.006)		
Ce									0.10	(0.014)		
Pr									0.17	(0.013)		
Nd									0.25	(0.03)		
Sm	0.8	(0.1)	0.53	(0.07)	0.54	(0.14)	0.37	(0.02)				
Eu												
Gd									0.32	(0.03)		
Tb												
Dy												
Ho	1.1	(0.1)	0.95	(0.14)	0.58	(0.12)	0.44	(0.06)	0.62	(0.06)		
Er									0.57	(0.07)		
Tm									0.51	(0.05)		
Yb	0.8	(0.1)										
Lu			0.76	(0.11)	0.41	(0.07)	0.34	(0.06)	0.43	(0.10)		

Abbreviations: ca-chemical affinity (see text), mc-melt composition from run products based on the classification of Cox *et al.* (1979) and Miyashiro (1978) (not normalized to 100 %), basan.-basanitic, neph.-nephelinitic, thol.-tholeiitic, subalk.-bas.-subalkaline-basaltic, alk.-bas.-alkaline-basaltic, nd-not determined. [a] Nicholls and Harris (1980; runs#: 4749, 4754, 4755, 4756). [b] Green and Pearson [1985a; runs#: 998, 955(HM)]. [c] Adam *et al.* (1993; run#: 1409) and Adam and Green (1994; runs#: 1446, 1447, 1452, 1518, 1549). [d] Adam *et al.* (1993; runs#: 1388, 1389, 1393, 1395) and Adam and Green (1994; run#: 1442).. [e] LaTourrette *et al.* (1995; run#: 3048T-1). [f] Fujinawa and Green (1997; runs#: 1702, 1680, 1661, 1642, 1705, 1666, 1686, 1632b, 1632a, 1664, 1633, 1707, 1659). [g] Maximum calculated partition coefficients (see Table 3.10). Value in parentheses are based on the maximum standard deviation calculated within each melt composition (mc).

starting material,

2- nephelinitic melt composition when I used the "ol-norm. neph." group as starting material,

3- tholeiitic melt composition when I used the "thol." group as starting material, and finally as

4- nephelinitic (for: FM10-02; 1.5 GPa, low fO_2), and subalkaline-basaltic to tholeiitic (for: FM10-23 and FM10-25; 1.5-2.5 GPa, respectively, both at high fO_2) melt compositions when I used the "alk.-bas." as starting material (Table 3.11).

Melt compositions from previous experimental studies were classified using the same classifications as mentioned above. Melts were classified as subalkaline-basaltic for Nicholls and Harris experiments (1980; runs#: 4749, 4754, 4755, and 4756), alkaline- to subalkaline-basaltic compositions for Green and Pearson's experiments (1985a; runs#: 998 and 955(HM)], alkaline-basaltic to basanitic for Adam *et al.*'s (1993; run#: 1409) and Adam and Green's (1994; runs#: 1446, 1447, 1452, 1518, 1549) experiments, as nephelinitic for Adam *et al.*'s (1993; runs#: 1388, 1389, 1393, 1395) and Adam and Green's (1994; run#: 1442) experiments, as basanitic for LaTourrette *et al.*'s experiment (1995; run#: 3048T-1), and finally as alkaline-basaltic for Fujinawa and Green's experiments (1997; runs#: 1702, 1680, 1661, 1642, 1705, 1666, 1686, 1632b, 1632a, 1664, 1633, 1707, 1659) (Table 3.11). All these previous experiments represent different pressures, temperatures, and oxygen fugacities conditions.

Chapter 3

The calculated average partition coefficients (*i.e.*, D_i^{avg}) from different melt compositions are shown in Table 3.11. These D_i^{avg} were calculated independently of the pressure, temperature, and oxygen fugacity effects. Figure 3.5 shows the variation in partition coefficients calculated between amphibole and the different melt compositions from this study and those from previous experimental studies. Elements are listed in the standard order from more incompatible on the left to less incompatible on the right. The different fields (Figs. 3.5a, -b, -c, -d, -e; results from this study) or symbol ranges (Fig. 3.5f; results from previous experimental studies) plotted on Figure 3.5 were constructed by using the minimum and maximum values of one relative standard deviation (1σ) attached to each partition coefficient within each quenched glass composition defined in Table 3.11 and as mentioned above (*i.e.*, $D_i^{min} = D_i^{avg} - 1\sigma_i^{avg}$ and $D_i^{max} = D_i^{avg} + 1\sigma_i^{avg}$). So in other words, the variations plotted on these diagrams include ±1 standard deviation from multiple analyses.

The general trends observed in partition coefficients (Figs. 3.5a, -b, -c, -d, -e) are similar based on their shape. This might suggest, as proposed by some criteria of Watson's (1985) study, that partition coefficients show an adherence to Henry's law at concentration levels ranging from sub-ppm to ppm (*e.g.*, LILE, HFSE, REE) to as high as wt.% (*e.g.*, K, Ti). Some peaks along the profile (*i.e.*, D_K^{avg}, D_{Sr}^{avg}, and D_{Ti}^{avg}) disturb the general trend and suggest that the order of incompatibility generally used for petrologic and experimental studies might not be the best order for amphibole partitioning. However, I keep this order to simplify the comparison of partition coefficients with other studies (*e.g.*, Green 1994).

Figure 3.5. Average partition coefficients between calcic amphibole and basaltic melt from this and previous studies. Variation in partition coefficients measured in this study within each melt composition based on one relative standard deviation from multiple analyses (see text). The area bounded by the dashed line (empty area) represents the minimum and maximum partition coefficients from this study (including one relative standard deviation). (a) Basanitic to nephelineitic melt (P-MT-27, P-MT-34a, P-MTg-12, P-MTg-43, P-MTg-41, P-MTg_{Ti}-31, and K-HD-08 experiments). (b) Nephelinitic melt (HF13-38 and HF13g_{Ti}-03 experiments). (c) Tholeiitic melt (K1921-15 experiment). (d) Nephelinitic melt (FM10-02 experiment). (e) Subalk.-bas. to tholeiitic melt (FM10-23 and FM10-25 experiments). Elements followed by an asterisk indicate that for some experiments the calculated partition coefficient corresponds to a maximum value based on the LLD of LAM-ICP-MS (see text and Table 3.10). (f) Comparison of partition coefficients from this study (area bounded by the dashed line) with other experimental determinations of partition coefficients between amphibole and basaltic melts (including one relative standard deviation; see Table 3.11). Abbreviations denote: 4749, 4754, 4755, and 4756 experiments from Nicholls and Harris (1980) [subalk.-basaltic melt (NH 80)]; 998 and 955(HM) experiments from Green and Pearson (1985a) [alk.- to subalk.-basaltic melt (GP 85a)]; 1409, 1446, 1447, 1452, 1518, and 1549 experiments from Adam *et al.* (1993) and Adam and Green (1994) [alk.-bas. to basanitic melt (AGS 93 & AG 94)]; 1388, 1389, 1393, 1395, and 1442 experiments from Adam *et al.* (1993) and Adam and Green (1994) [nephelinitic melt (AGS 93 & AG 94)]; 3048T-1 experiment from LaTourrette *et al.* (1995) [basanitic melt (LNH 95)]; 1702, 1680, 1661, 1642, 1705, 1666, 1686, 1632b, 1632a, 1664, 1633, 1707, and 1659 experiments from Fujinawa and Green (1997) [alk.-basaltic melt (FG 97)]. As mentioned in the text, variations in partition coefficients include one relative standard deviation for each melt composition (see Table 3.11). It should be emphasized that a lot of experiments at different P, T, and fO_2 conditions have been averaged so that at least some of the difference (and variation) reflects these different conditions.

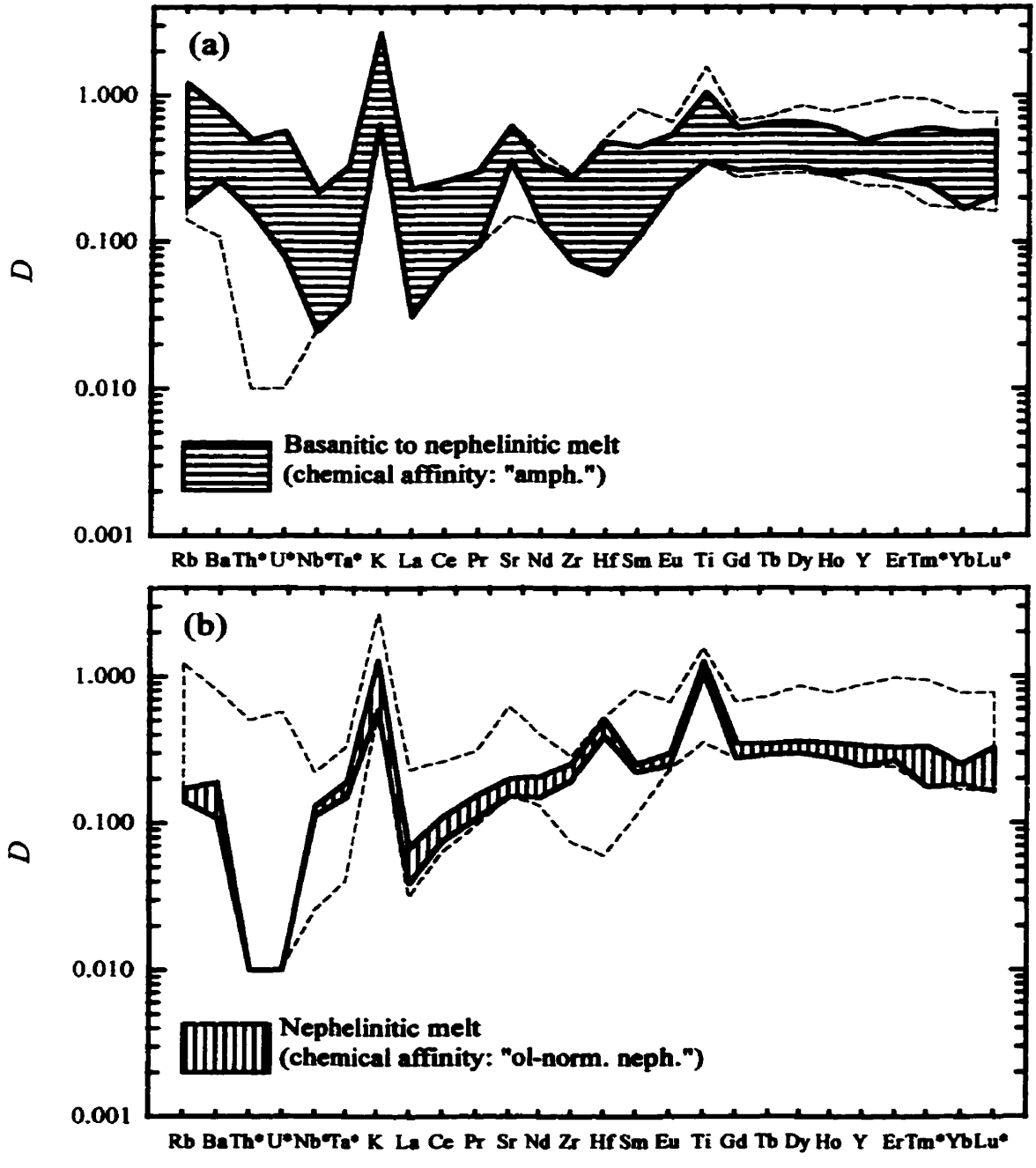
(a)
1.000
0.100
0.010
0.001
D
Basanitic to nephelinitic melt
(chemical affinity: "amph.")
Rb BaTh* U* Nb* Ta* K La Ce Pr Sr Nd Zr Hf Sm Eu Ti Gd Tb Dy Ho Y ErTm* Yb Lu*
(b)
1.000
0.100
0.010
0.001
D
Nephelinitic melt
(chemical affinity: "ol-norm. neph.")
Rb BaTh* U* Nb* Ta* K La Ce Pr Sr Nd Zr Hf Sm Eu Ti Gd Tb Dy Ho Y ErTm* Yb Lu*

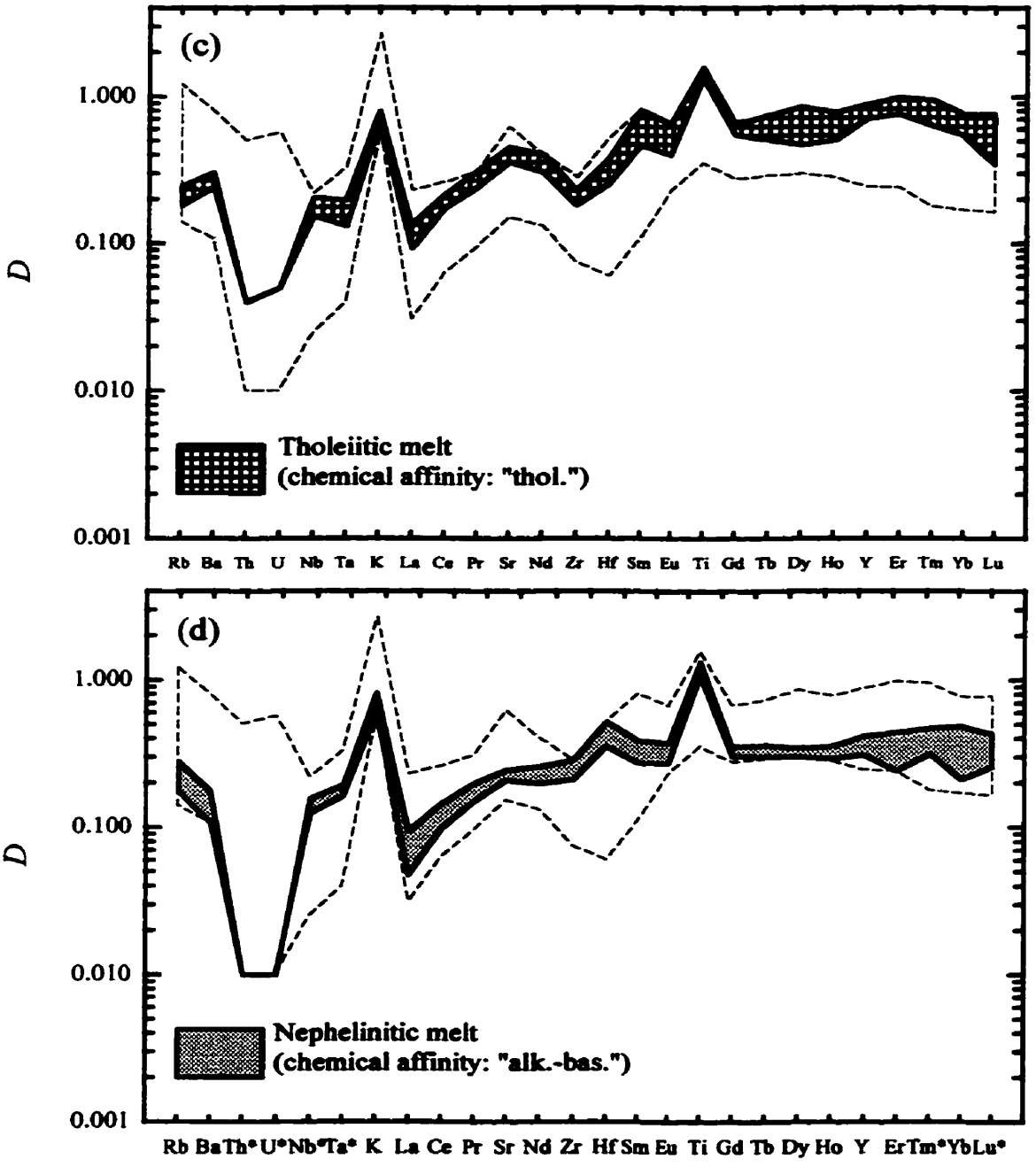
(c)
1.000
0.100
0.010
0.001
D
Tholeiitic melt
(chemical affinity: "thol.")
Rb Ba Th U Nb Ta K La Ce Pr Sr Nd Zr Hf Sm Eu Ti Gd Tb Dy Ho Y Er Tm Yb Lu
(d)
1.000
0.100
0.010
0.001
D
Nephelinitic melt
(chemical affinity: "alk.-bas.")
Rb BaTh* U*Nb*Ta* K La Ce Pr Sr Nd Zr Hf Sm Eu Ti Gd Tb Dy Ho Y ErTm*YbLu*

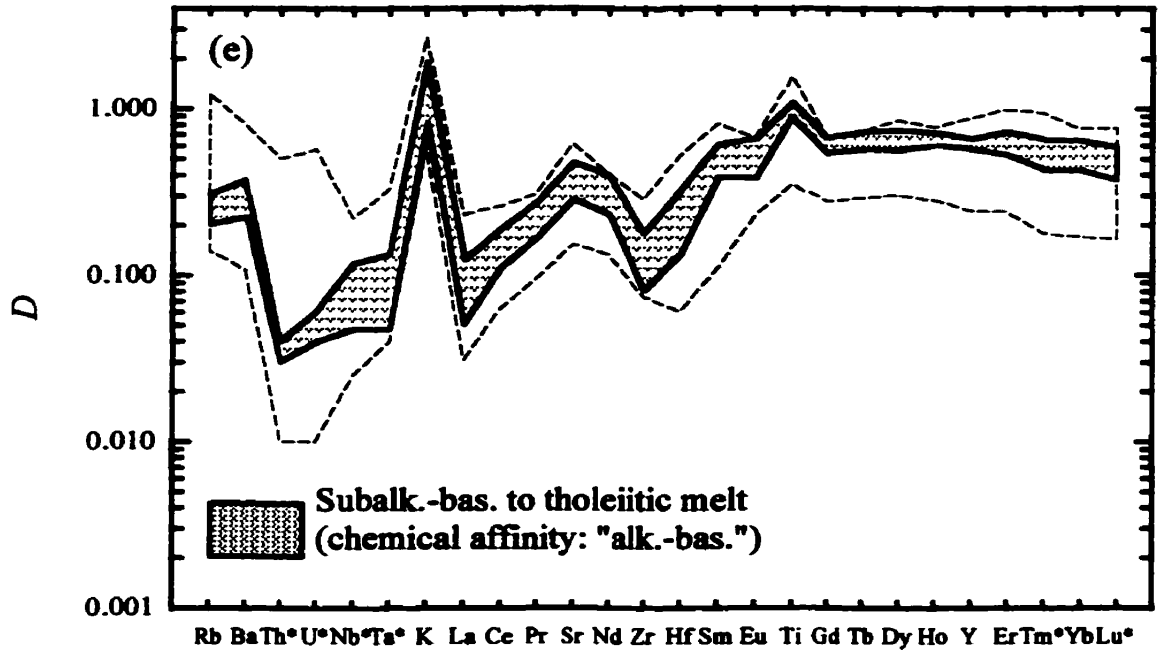
(e)
1.000
0.100
0.010
0.001
D
Subalk.-bas. to tholeiitic melt
(chemical affinity: "alk.-bas.")
Rb Ba Th* U* Nb* Ta* K La Ce Pr Sr Nd Zr Hf Sm Eu Ti Gd Tb Dy Ho Y Er Tm* Yb Lu*

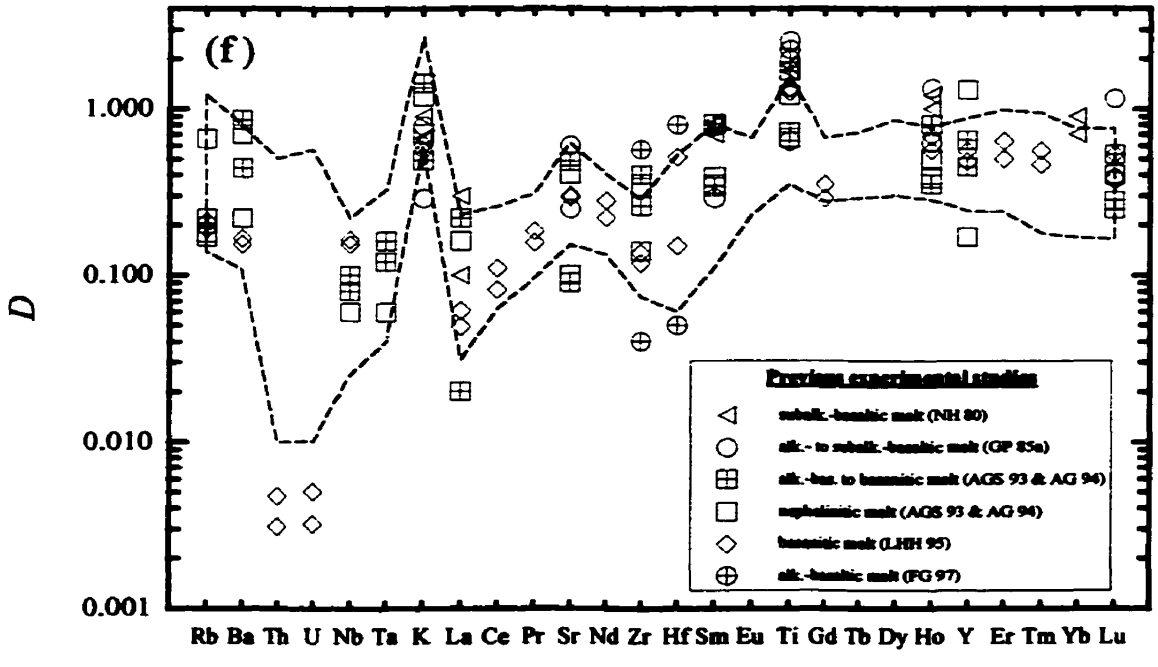
(f)
1.000
0.100
0.010
0.001
D
Previous experimental studies
subalk.-basaltic melt (NH 80)
alk.- to subalk.-basaltic melt (GP 85a)
alk.-bas. to basanitic melt (AGS 93 & AG 94)
nephelinitic melt (AGS 93 & AG 94)
basanitic melt (LHH 95)
alk.-basaltic melt (FG 97)
Rb Ba Th U Nb Ta K La Ce Pr Sr Nd Zr Hf Sm Eu Ti Gd Tb Dy Ho Y Er Tm Yb Lu

3.5.2. Partition coefficients of LILE (Rb, Ba, K, Sr)

Within the four "chemical affinities" described in Table 3.11 (*i.e.*, "amph.", "ol-norm. neph.", "thol.", "alk.-bas."), I observed in Figure 3.5a that using the "amph." as starting material D_K^{avg}, D_{Rb}^{avg}, D_{Sr}^{avg}, and D_{Ba}^{avg} were in general higher by a factor of 1.3 to 2.3 for K (D_K^{avg} = 1.65), 2.0 to 3.3 for Rb (D_{Rb}^{avg} = 0.50), 1.2 to 2.8 for Sr (D_{Sr}^{avg} = 0.49), and 1.8 to 3.5 for Ba (D_{Ba}^{avg} = 0.52) relative to the "ol-norm. neph." (D^{avg}s = 0.86, 0.15, 0.18, and 0.15, respectively), "thol." (D^{avg}s = 0.73, 0.21, 0.41, and 0.28, respectively), and "alk.-bas." (D^{avg}s = 1.31, 0.25, 0.37, 0.29, respectively, for the subalkaline-basaltic to tholeiitic melt composition) based on average partition coefficient values (Table 3.11). The lowest D_{Rb}^{avg}, D_{Sr}^{avg}, and D_{Ba}^{avg} were measured in the "ol-norm. neph." materials (avgs. Ds = 0.15, 0.18, and 0.15, respectively) and the lowest D_K^{avg} was measured in the "alk.-bas." material (D_K^{avg} = 0.71, FM10-02 experiment), similar to the low D_K^{avg} of the "thol." material (Table 3.11). An important transition was observed in D_K and D_{Rb} which changed from incompatible element behaviour (*i.e.*, $D < 1$) to a compatible element behaviour (*i.e.*, $D > 1$). An increase in oxygen fugacity from NNO-2 to NNO+1.7 changed D_K from incompatible to compatible at the same pressure (*i.e.*, D_K = 0.71 and 1.21 for FM10-02 and FM10-23, respectively; see Table 3.10) while this transition seems to occur for D_{Rb} when I increased pressure from 1.5 to 2.5 GPa at a fixed oxygen fugacity buffer (*i.e.*, D_{Rb} = 0.54 to 1.04 for P-MTg-43 and P-MTg-41, respectively; Table 3.10). Transition from incompatible to compatible behaviour for D_K and D_{Rb} as a function of pressure and oxygen fugacity will be discussed in Chapter 4.

Philpotts and Schnetzler (1970) obtained partition coefficients for Rb, Ba, K, and Sr between a natural pargasite and its matrix from a Monteregian lamprophyre dike (*i.e.*, D_{Rb}, D_{Ba}, D_K, D_{Sr} = 0.427, 0.417, 1.40, and 0.548, respectively; sample GSFC 29) comparable to those experimentally obtained using the "amph." materials (Tables 3.10 and 3.11). In another study on the same unit, Gunn (1972) also obtained comparable partition coefficients for Rb, Ba, and Sr (*i.e.*, 0.3, 0.6, 0.5, respectively) but lower values for K (*i.e.*, 1.0). However, as mentioned previously, Gunn's (1972) samples were not 100 % pure phases which might explain some discrepancies with our *D*'s (Gunn 1972). Furthermore the amphibole compositions of Philpotts and Schnetzler (1970) and Gunn (1972) are not identical, only similar (Fig. 3.3).

Comparison of D_{LILE}^{ave} with previous experimental studies demonstrates a convincing similarity for all LILE, but the average values of D_K^{ave}, D_{Rb}^{ave}, and D_{Sr}^{ave} using the "amph." starting materials are higher by at least 1.9, 1.4, 1.2, respectively (Fig. 3.5b, Table 3.11). In simple systems, Watson (1977) and Kohn and Schofield (1994) demonstrated that the degree of melt polymerization was very important in controlling partition coefficients between olivine and silicate melts when SiO_2^{melt} is above ~ 60 wt.%. In contrast, Blundy and Wood (1991a, -b) suggested, based on the hydrothermal experiments of Lagache and Dujon (1987) and from a large data set of experimental and natural volcanic partition coefficients between plagioclase and silicate melt, that crystal chemistry exerts a powerful influence on trace element partitioning, larger than the effects of temperature, pressure, and fluid or melt composition.

However, this idea does not coincide with those of other studies which invoke the importance of liquid composition in plagioclase partitioning for natural systems (Morse 1982, 1991).

The observed high average in D_K, D_{Rb}, and D_{Sr} were all measured in group 2 amphiboles (Table 3.7) when using the "amph." as the starting material whereas the melt compositions are comparable to those obtained by Adam *et al.* (1993), Adam and Green (1994), and LaTourrette *et al.*'s (1995) experiments (*i.e.*, $SiO_2 < 47$ wt.% in the melt). This suggests at some point that crystal-chemistry may control partitioning instead of melt compositions. Mysen (1988) discussed the effect of water which acts as a depolymerizing agent in general on melt structure. In such a case, the effect of melt polymerization on partitioning as demonstrated by Watson (1977), Kohn and Schofield (1994), and Klein *et al.* (1997) for silica-rich liquids should not be significant for these experiments using silica-poor melts with a relatively high amount of dissolved water [*e.g.*, ~ 10 wt.%, Table 3.6; mainly as molecular water (H_2O) according to Jakobsson and Holloway (1986)]. This might suggest that the control of melt composition on partition coefficients between amphibole and basaltic melt (which are depolymerized) is practically insignificant in this study and in previous ones.

Adam and Green (1994) have shown that D_{Sr} decreased as the pressure increased using a basanitic starting material. In this study the same relationship between D_{Sr} and pressure was observed for some run conditions (*i.e.*, using the "amph." material: P-MTg-43 and P-MTg-41, and using the "alk.-bas." material: FM10-23 and FM10-25; Table 3.10). However in three experiments using the "amph." materials (*i.e.*, P-MTg-12, P-MT-27, and

K-HD-08), D_{Sr} decreased at fixed run conditions (*i.e.*, pressure, temperature, and fO_2; Table 3.10). This behaviour of D_{Sr} suggests instead crystal-chemical controls by the amphibole. In these experiments, a decrease in D_{Sr} corresponds to a decrease in the Ca/(Ca+Na) ratio of the amphibole [*i.e.*, D_{Sr} = 0.52, 0.45, 0.44, 0.37 and Ca/(Ca+Na) = 0.782, 0.755, 0.741, for P-MTg-12, P-MT-27, and K-HD-08, respectively; see Tables 3.5 and 3.10]. The same behaviour was observed between D_{Sr} and the Ca/(Ca+Na) ratio for the FM10-23 and FM10-25 pair (*i.e.*, D_{Sr} = 0.44, 0.30 and Ca/(Ca+Na) = 0.684, 0.668, for FM10-23 and FM10-25, respectively, Tables 3.5 and 3.10) and in some runs from Adam and Green's (1994; runs#: 1452, 1447, 1446) experiments, for which D_{Sr} also decreases with increasing pressure. However, the variation of D_{Sr} as a function of Ca/(Ca+Na) ratio is not a straightforward relationship because it can not explain the entire range of variation observed in Adam and Green's (1994; run#: 1452, 1447, 1446, 1442) experiments and requires pressure effects. In these cases, it seems difficult to isolate the effects of pressure and crystal-chemistry on the variations observed in D_{Sr}. Furthermore oxygen fugacity may influence D_{Sr} at a fixed pressure which will be discussed in Chapter 4.

For Ba, high partition coefficients were measured in group 2 amphiboles (*i.e.*, using "amph." materials; D_{Ba}^{avg} = 0.52) and in group 1 amphiboles from the alkaline basaltic to basanitic melt composition of Adam *et al.*'s (1993; run#: 1409) experiment (*i.e.*, D_{Ba} = 0.65; Tables 3.7 and 3.11). However, the crystal-chemistry of the amphibole run products from Adam *et al.* (1993; runs#: 1388, 1389, 1393, 1395) and Adam and Green (1994; run#: 1442)

respect, in general, all the criteria of group 1 amphiboles described in Table 3.7 with the exception of their high K/(K+Na) ratios which were all above 0.290, similar to group 2 amphiboles. Figure 3.6 shows the variation of D_{Ba} as a function of the K/(K+Na) ratio observed for the different amphibole run products. The vertical line shows the empirical limit of K/(K+Na) ratio (0.290) separating group 1 from group 2 amphiboles (Table 3.7).

Considering both groups of amphibole run products, a general increase in D_{Ba} as the K/(K+Na) ratio increases can be observed, suggesting a possible crystal-chemical control of amphibole on D_{Ba} for similar basaltic melt compositions. Furthermore, the observed positive linear relationship between D_{Sr} and D_{Ba} in our experiments and the one reported by LaTourrette *et al.* (1995) supports this interpretation. As discussed below, Sr should partition into the *M*(4) site whereas some ambivalency seems to exist for Ba between the *M*(4) and the *A* sites (Brenan *et al.* 1995). Because D_{Ba} displays a good correlation with the K/(K+Na) ratio of the amphiboles, whereas D_{Sr} correlates better with the Ca/(Ca+Na) ratio of the amphiboles, this suggests that a complex coupled substitution may exist between Ca, Na, K, Ba, and Sr into the *M*(4) and *A* sites for these calcic amphiboles; or may even involve other major elements from coupled substitutions on other sites as discussed below.

3.5.3. Partition coefficients of HFSE (Nb, Ta, Zr, Hf, Ti, Y, Th, U)

No systematic variations seem to occur within one particular chemical affinity for D^{ave}_{HFSE} (*i.e.*, "amph.", "ol-norm. neph.", "thol.", "alk.-bas."; see Table 3.11). However the

Figure 3.6. Variation of D_{Ba} as function of the K/(K+Na) ratio in amphibole. Symbols: same as in Figs. 3.5 and 3.3. The dashed line represents the limit between the two amphibole groups (see Table 3.7).

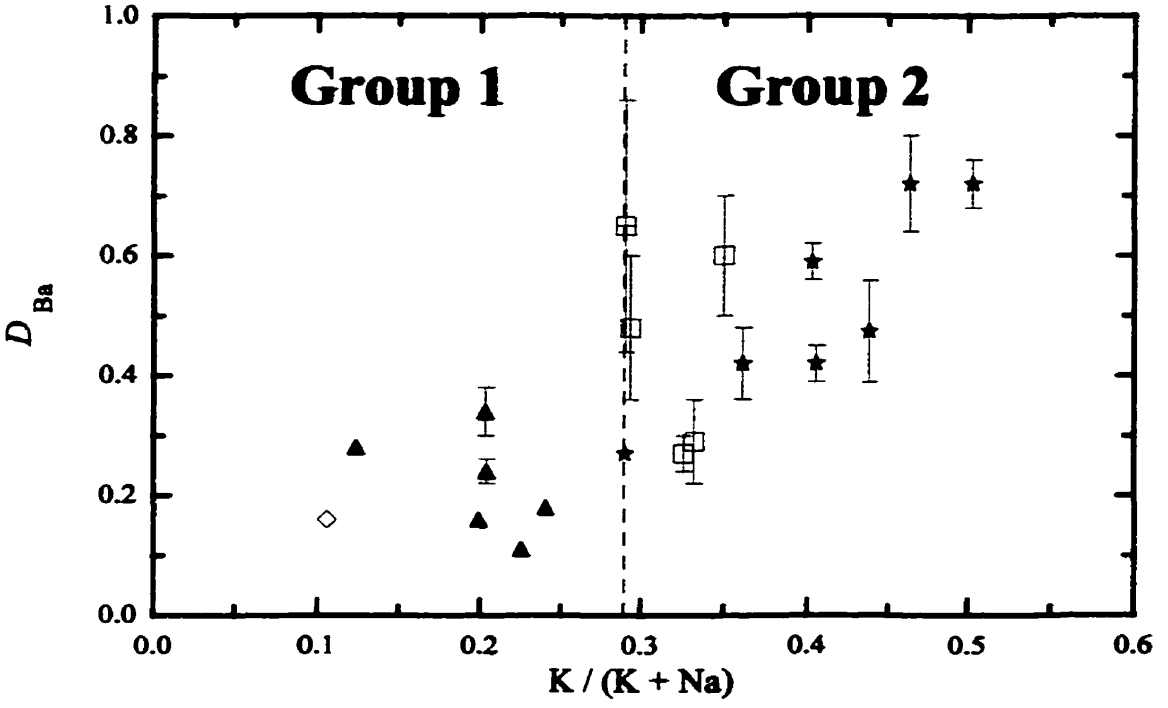
Group 1
Group 2
1.0
0.8
0.6
0.4
0.2
0.0
D_{Ba}
0.0
0.1
0.2
0.3
0.4
0.5
0.6
K / (K + Na)

average values of D_{Nb}, D_{Ti}, and D_Y for the "thol." were all higher (D^{avg}s = 0.18, 1.46, and 0.79, respectively) than using other starting materials (Table 3.11). D_{Ti} behaved as an incompatible element when using the "amph." materials ($D_{Ti}^{avg} = 0.70$), as a neutral element when using the "alk.-bas." at high oxygen fugacity (D_{Ti}^{avg} ~1 for FM10-23, -25 experiments), or as a compatible element when using the "ol-norm. neph.", the "thol.", and the "alk.-bas." materials ($D_{Ti}^{avg} = 1.19$, 1.46, 1.20, respectively). The lowest D_{Nb}^{avg}, D_{Ta}^{avg}, D_{Zr}^{avg}, D_{Hf}^{avg}, and D_{Ti}^{avg} were observed in the "amph." (D^{avg}s = 0.08, 0.11, 0.16, 0.28, and 0.70, respectively) and in the "alk.-bas." materials (FM10-23, -25 experiments, D^{avg}s = 0.09, 0.10, 0.13, 0.21, and 0.99, respectively). However, the highest D_{Hf} was measured in nephelinitic quenched melts using different starting materials (*i.e.*, D_{Hf}^{avg}s = 0.43 and 0.44 for "ol-norm. neph." and "alk.-bas." materials, respectively; Table 3.11). For the "amph." materials, there is a reverse relationship between D_{LILE} (highest average values) with respect to D_{HFSE} (lowest average values) when compared with other chemical affinities from this study (*i.e.*, "ol-norm. neph.", "thol.", "alk.-bas.").

Comparison of experimentally determined partitioning with natural amphibole/matrix pairs demonstrates some similarities. Gunn (1972) obtained comparable values for D_{Ti} and D_Y of 0.95 and 0.43, respectively, between pargasite and matrix from a Monteregian lamprophyre dike. Comparison with other experimental studies demonstrates that partition coefficients of Nb, Ta, Zr, Hf, and Ti all agree based on the calculated average values (Fig. 3.5b). However, some variations seem to be important. The highest partition coefficient for

Zr was observed in the alkaline basaltic melt of Fujinawa and Green's (1997; run#: 1702) experiment ($D_{Zr} = 0.46$). A high D_{Zr} was also observed in the alkaline basaltic to basanitic melt of Adam *et al.*'s (1993; run#: 1409) experiment ($D_{Zr} = 0.33$), and in a nephelinitic melt of Adam and Green's (1994; run#: 1393) experiment ($D_{Zr} = 0.33$). In the present study, I observed the highest D_{Zr} in the nephelinitic melt using the "alk.-bas." material (*i.e.*, FM10-02 experiment; see Table 3.10). D_{Ta} measured by Adam *et al.* (1993; runs#: 1393, 1389, 1393, 1395) and Adam and Green (1994; run#: 1442) between amphibole and a nephelinitic melt composition ($D_{Ta}^{Avg} = 0.08$) was very low compared to the high D_{Ta}^{Avg} (0.17 and 0.18) measured for two nephelinitic melt compositions in this study (*i.e.*, using the "ol-norm. neph." and the "alk.-bas." materials, respectively), suggesting that bulk starting material may affect partitioning (Table 3.11). Regarding D_{Ti}, Green and Pearson (1985a) measured a high D_{Ti} using a tholeiitic starting material (*i.e.*, $D_{Ti} = 2.33$ between amphibole and alk.- to subalk.-basaltic glasses), different than D_{Ti} measured in the "thol." material (*i.e.*, $D_{Ti} = 1.46$; Table 3.11). Adam *et al.* (1993; runs#: 1388, 1389, 1393, 1395) and Adam and Green's (1994; runs#: 1442) experiments have measured a $D_{Ti} < 1$ between amphibole and nephelinitic melt, similar to our low D_{Ti} observed in the "amph." material (*i.e.*, between amphibole and basanitic to nephelinitic melts; Table 3.11). However, the low D_{Ti} (0.78) observed by Adam and Green (1994; run#: 1549) between amphibole and basanitic melt was performed at a higher oxygen fugacity (hematite-magnetite buffer) than in this study. All these discrepancies between partition coefficients measured in previous studies and this study suggest that melt

composition, in the broadly basaltic range, has little effect on partitioning.

In an opposing view, Adam *et al.* (1993) suggested that low partition coefficients between their amphibole and melt for Ti, Zr, Nb, and Ta compared to natural pairs were related to differences in SiO_2 content of the melt or glass. Regarding this idea of Adam *et al.* (1993), when looking at the relationship between D_{Ti}, D_{Zr}, D_{Ta} and SiO_2^{melt} of Green and Pearson (1985a), Adam *et al.* (1993), Adam and Green (1994), LaTourrette *et al.* (1995), Fujinawa and Green (1997), and experiments of this study, a weak increase in D_{Ti} was observed as the melt composition changed from ~ 34 to ~ 53 wt.% SiO_2 (not normalized to 100 %) and no correlation was observed between D_{Zr} or D_{Ta} with the SiO_2 content of the melt. Furthermore, a negative relationship (*i.e.*, D_{Ti} decreases as SiO_2^{melt} increases) was observed by Green and Pearson [1985a; runs#: 998 and 955(HM)], Adam and Green's (1994; runs#:1452 and 1447) and also in the "amph." materials (*i.e.*, P-MTg-12, P-MT-27, and K-HD-08; Tables 3.6 and 3.10), where these latter experiments were performed at similar run conditions (*i.e.*, P, T, and fO_2). Adam and Green (1994) showed that the partition coefficient for Ti decreased with pressure similar to the effects of pressure on D_{Sr} mentioned above. Based on the same study, a transition from compatible (*i.e.*, $D > 1$) to incompatible (*i.e.*, $D < 1$) behaviour for Ti occurred when pressure increased from 1.5 to 2.0 GPa using a basanitic starting material at an oxygen fugacity buffered between NNO and magnetite-wüstite (Adam and Green 1994). In the present study, the same relation between Ti and pressure was not observed at either oxygen fugacity studied (*i.e.*, NNO-2 and NNO+1.7), but it appears that

D_{Ti} may be affected by pressure and bulk composition as well as the oxygen fugacity (see Chapter 4). In such cases, it is difficult to isolate the effects of melt composition from other physical conditions (*i.e.*, P, T, fO_2) or even the crystal-chemical controls of amphibole on partitioning as mentioned previously for D_{LILE}.

Because element concentrations of Th and U were below the lower limit of detection of the LAM-ICP-MS in the different amphibole run products, the calculated D_{max} reported in Table 3.10 and shown in Figure 3.5 suggests that D_{Th}^{ave} and D_{U}^{ave} calculated from the "ol-norm. neph.", "thol.", and "alk.-bas." starting materials are 1 order of magnitude lower than when using the "amph." starting material (*i.e.*, D_{max} = LLD of Th or LLD of U / concentration of Th or U in the quenched melt). Although this tendency can not be confirmed without further experiments, it seems to be supported by LaTourrette *et al.*'s (1995) experiments on D_{Th} and D_{U} using basanitic material (Fig. 3.5b).

3.5.4. Partition coefficients of REE (La, Ce, Pr, Nd, Sm Eu, Gd, Tb, Dy, Ho, Er, Tm, Yb, Lu)

The partition coefficients for La, Ce, Pr, Nd, Sm, Er, Tm, Yb, and Lu between amphibole and tholeiitic melt (*i.e.*, K1921-15 experiment) were observed to be higher by a factor of 1.3 to 2.1 for La (D_{La} = 0.11), 1.4 to 2.1 for Ce (D_{Ce} = 0.19), 1.2 to 2.1 for Pr (D_{Pr} = 0.27), 1.2 to 2.0 for Nd (D_{Nd} = 0.36), 1.4 to 2.7 for Sm (D_{Sm} = 0.64), 1.4 to 3.0 for Er (D_{Er} = 0.87), 1.5 to 3.1 for Tm (D_{Tm} = 0.79), 1.3 to 2.9 for Yb (D_{Yb} = 0.65), and by a factor of 1.1

to 2.4 for Lu (D_{Lu} = 0.56) relative to the "amph." , the "ol-norm. neph.", and the "alk.-bas." chemical affinities (Table 3.11). Figure 3.5c shows clearly the high partition coefficients (*i.e.*, D_{LREE} and D_{HREE}) generally obtained for the K1921 experiment compared to other melt compositions. However, similar partition coefficients were obtained for Eu, Gd, Dy, and Ho between the tholeiitic melt (*i.e.*, K1921-15 experiment) and the subalkaline-basaltic to tholeiitic melt compositions of FM10-23 and FM10-25 experiments (Table 3.11). The lowest partition coefficients for La, Ce, Pr, Nd, Sm, Eu, Er, Tm, Yb, and Lu were observed in the nephelinitic melt composition using the "ol-norm. neph." materials (D^{avg}s = 0.05, 0.09, 0.13, 0.18, 0.24, 0.27, 0.29, 0.25, 0.22, and 0.24, respectively) whereas their D_{Gd}, D_{Tb}, D_{Dy}, and D_{Ho} were similar to the nephelinitic melt using the "alk.-bas." material (FM10-02 experiment; Table 3.11).

When comparing partition coefficients of the rare-earth elements to previous experimental studies, it is observed that D_{La}^{avg}, D_{Ce}^{avg}, D_{Pr}^{avg}, D_{Nd}^{avg}, and D_{Gd}^{avg} for the nephelinitic quenched glass composition using the "alk.-bas." material are identical, or similar, to those measured by LaTourrette *et al.* (1995) for basanitic melt but different for D_{Ho}, D_{Er}, D_{Tm}, D_{Lu} (*i.e.*, D_{HREE}; Table 3.11). Nicholls and Harris (1980) measured partition coefficients between amphibole and subalkaline-basaltic melt for La, Sm, Ho, and Yb (0.20, 0.80, 1.10, and 0.8, respectively) which are higher by a factor of 1.6 to 2.5 than our average partition coefficients measured in similar compositions (*i.e.*, subalkaline basaltic to tholeiitic melts from FM10-23 and FM10-25 experiments; Table 3.11). In such cases, the discrepancies observed between

our D_{HREE} values and those measured by LaTourrette *et al.* (1995) for basanitic melt compositions and also the large variation observed between our D_{REE}'s and those measured by Nicholls and Harris (1980) for similar melt compositions suggest that melt composition does not play a major role during partitioning. Furthermore, regarding D_{Ho} and D_{Lu}, Adam and Green (1994) showed a linear relationship between partition coefficient and pressure based on different experiments performed at similar temperatures and oxygen fugacities. They showed that D_{Sm}, D_{Ho} and D_{Lu} decreased as pressure increased from 0.5 to 2.0 GPa and followed two different slopes where the variation of D_{Sm} and D_{Ho} were more pronounced than D_{Lu} (see Adam and Green 1994; Fig. 1). In this study three experiments using the "amph." materials (*i.e.*, P-MTg-12, P-MT-27, and K-HD-08) showed a similar range of variation in D_{Ho} and D_{Lu} at fixed conditions (*i.e.*, pressure, temperature, and fO_2). Furthermore, in these three experiments a decrease in D_{Ho} and D_{Lu} was accompanied by a decrease of the Ca/(Ca+Na) ratio in the amphibole [*i.e.*, $D_{Ho} = 0.47, 0.45, 0.34$, $D_{Lu} = 0.51, 0.27, 0.24$, and Ca/(Ca+Na) = 0.782, 0.755, 0.741, for P-MTg-12, P-MT-27, and K-HD-08, respectively; see Tables 3.5 and 3.10]. However, the behaviour of D_{Ho} and D_{Lu} cannot be correlated with the Ca/(Ca+Na) ratio obtained in Adam and Green's (1994) experiments and in other experimental studies. A similar problem was mentioned earlier between the D_{Sr} of this study with those observed by Adam and Green (1994) when compared against the Ca/(Ca+Na) ratio of the amphibole composition. However, an alternative explanation for variations between the D_{REE} of this study and those measured previously is the possibility of more complex inter-

element, coupled-substitution involving cations in different crystallographic sites. Dalpé *et al.* (1995) inferred that slight differences in amphibole composition (*e.g.*, $^{VI}Ti_{M(1,2,3)}$) could have a significant effect on the partition coefficients of REE based upon their relatively low D_{REE} values compared to previous experimental studies. To better understand the behaviour between D_{REE} and possible crystal-chemistry effects by the amphibole, a series of diagrams where D_{REE} were plotted against ratios involving host cations in different crystallographic sites [*i.e.*, in *M*(1,2,3), *M*(4), and *A* sites] were constructed. Figure 3.7 shows one of the best results obtained. Partition coefficients of La, Sm, Ho, and Lu were plotted against $\{[Ca/(Ca+Na)]_{M(4)} / [(Mg+Ti) / (Al+Fe_{total})]_{M(1,2,3)}\}$ ratio (abbreviated as CN/MTAF hereafter) measured in different amphibole run products.

Even though a general increase in D_{REE} as the CN/MTAF ratio of the amphibole increases is observed, the entire variation observed in partition coefficients for Sm, Ho, and Lu in Adam and Green's (1994) experiments cannot be explained without inferring a pressure effect on partitioning. As an example, two experiments of Adam and Green (1994) with similar CN/MTAF ratios, but performed at 1.0 and 2.0 GPa show different D_{Sm} and D_{Ho} (*i.e.*, CN/MTAF = 0.332 for runs# 1447 and 1442 where D_{Sm} = 0.64 ±0.14 and 0.37 ±0.02, and D_{Ho} = 0.63 ±0.05 and 0.44 ±0.06, respectively; see Adam and Green 1994; Table 4). Similar trends were observed for D_{Ce}, D_{Pr}, D_{Nd}, D_{Eu}, D_{Gd}, D_{Tb}, D_{Dy}, D_{Er}, D_{Tm}, D_{Yb} *vs.* CN/MTAF (not shown). However, even if poor correlation coefficients (r^2) were calculated for these relationships (Fig. 3.7), this subtle increase in D_{REE} with increasing CN/MTAF ratio of the

Figure 3.7. Variation of partition coefficients for La, Sm, Ho, Lu against the $[Ca/(Ca+Na)]_{M(4)} / [(Mg+Ti) / (Al+Fe_{total})]_{M(1,2,3)}$ ratio of the different amphibole run products. Abbreviations denote: P-MT-27, P-MT-34a, P-MTg-12, P-MTg-43, P-MTg-41, P-MTg$_{Ti}$-31, and K-HD-08 experiments (This study: P-MT, P-MTg, P-MTg$_{Ti}$, K-HD); HF13-38, HF13g$_{Ti}$-03, K1921-15, FM10-02, FM10-23, and FM10-25 experiments (This study: HF13, HF13g$_{Ti}$, K1921, FM10); 4749, 4754, 4755, and 4756 experiments of Nicholls and Harris (1980) [NH (80)]; 998 and 955(HM) experiments of Green and Pearson (1985a) [GP (85a)]; 1442, 1446, 1447, 1452, 1518, and 1549 experiments of Adam and Green (1994) [AG (94)]; 3048T-1 experiment of LaTourrette *et al.* (1995) [LHH (95)]. Note that each equation represents the best linear fit using this study's and previous experimental partition coefficients.

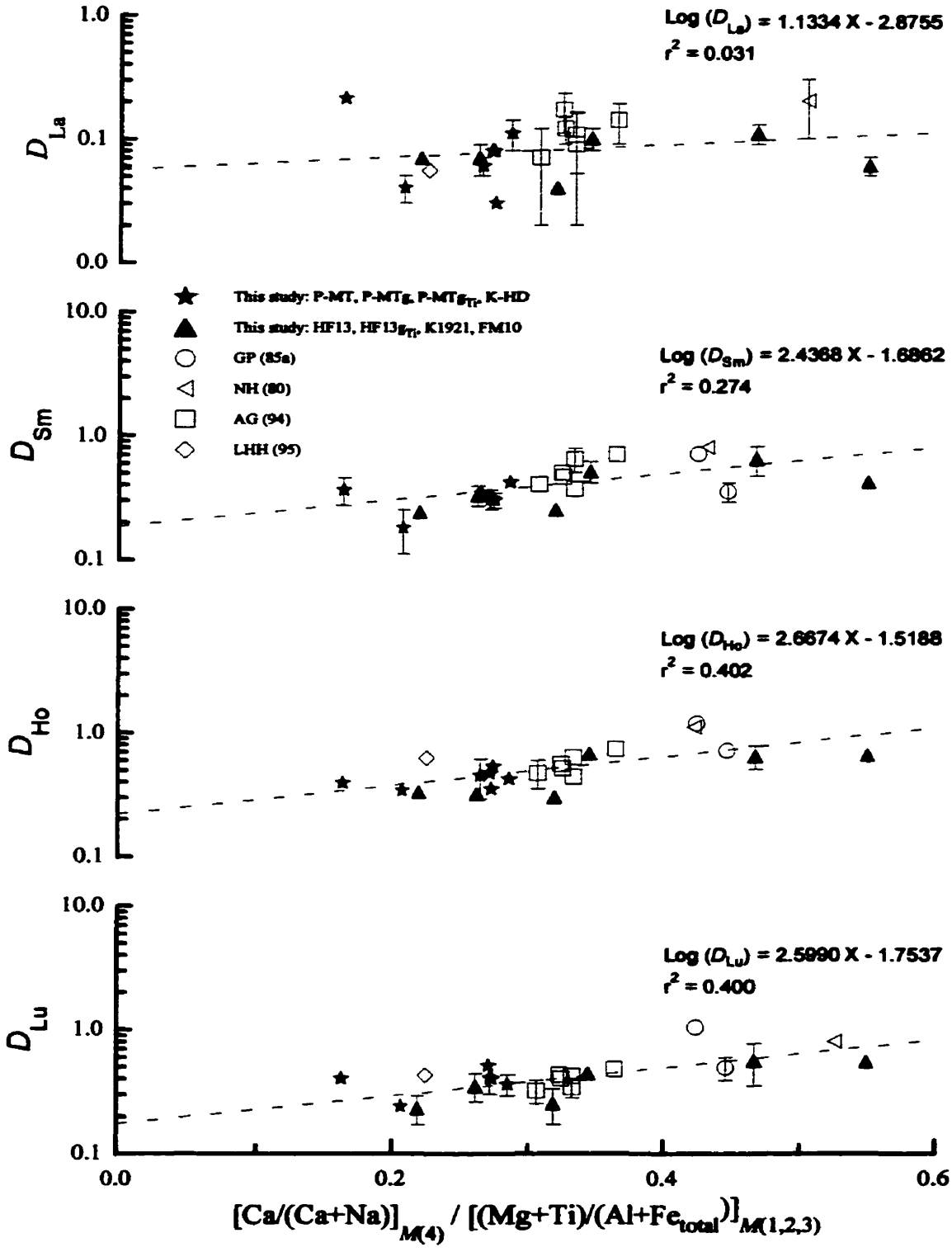
Log (D_{La}) = 1.1334 X - 2.8755
r^2 = 0.031
Log (D_{Sm}) = 2.4368 X - 1.6862
r^2 = 0.274
Log (D_{Ho}) = 2.6674 X - 1.5188
r^2 = 0.402
Log (D_{Lu}) = 2.5990 X - 1.7537
r^2 = 0.400
This study: P-MT, P-MTg, P-MTg_{Ti}, K-HD
This study: HF13, HF13g_{Ti}, K1921, FM10
GP (85a)
NH (80)
AG (94)
LHH (95)
D_{La}
D_{Sm}
D_{Ho}
D_{Lu}
1.0
0.1
0.0
10.0
1.0
0.1
10.0
1.0
0.1
10.0
1.0
0.1
0.0
0.2
0.4
0.6
[Ca/(Ca+Na)]$_{M(4)}$ / [(Mg+Ti)/(Al+Fe$_{total}$)]$_{M(1,2,3)}$

amphibole can be viewed as a complex inter-element coupled substitution where pressure, temperature, starting composition, and oxygen fugacity (*e.g.*, Fe^{3+}/Fe^{2+} ratio) of the experiment may play an important role on the crystal-chemistry of amphibole which governs partitioning.

3.5.5. Summary

Our experimental results on partitioning can be summarized as follows:

3.5.5.1. The effect of bulk compositions

General observations can be extracted from this study even if the comparison of bulk chemistry of the equilibrium melt is a difficult parameter to isolate for experiments performed at different run conditions.

3.5.5.2. LILE

The highest D_{Rb}, D_{Ba}, D_K, and D_{Sr} between pargasite and basaltic melt were measured in the experiments using the natural amphibole and pargasitic glass compositions (*i.e.*, P-MT, P-MTg, P-MTg_{Ti} and K-HD) whereas the lowest D_{Rb}, D_{Sr}, and D_{Ba} were measured in the ol-normative nephelinite bulk rock and the lowest D_K was obtained in experiments performed with the alkaline basalt bulk rock.

3.5.5.3. HFSE

The highest D_{Nb}, D_{Ti}, and D_{Y} were measured in experiments using the tholeiite bulk composition whereas the highest D_{Hf} was observed in the ol-normative nephelinite and in the alkaline-basalt (FM10-02 experiment). In contrast, the lowest D_{Nb}, D_{Ta}, D_{Zr}, D_{Hf}, and D_{Ti} were measured in experiments using the natural amphibole and pargasitic glass compositions as well as in the alkaline-basalt (FM10-23 and FM10-25 experiments). In our experiments, U and Th concentrations in the amphibole run products were both below the LLD of the LAM-ICP-MS; thus it was impossible to determine *D*'s quantitatively.

3.5.5.4. REE

The highest D_{La}, D_{Ce}, D_{Pr}, D_{Nd}, D_{Sm}, D_{Er}, D_{Tm}, D_{Yb}, and D_{Lu} were measured in the tholeiitic bulk composition whereas the lowest partition coefficients of these elements and D_{Eu} were measured in the ol-normative nephelinite bulk compositions.

3.5.5.5. The effect of crystal chemistry

It was shown that the variation in partition coefficients between amphibole and basaltic melt could be controlled by some ratios of major elements substituting into a specific site (or sites) of the amphibole. One example of such chemical control, demonstrated in previous pages, was the variation in D_{Ba} which is a function of the relative variation of K and Na concentrations in the amphibole run products. It was also noted that a more complex

coupled substitution might be involved when a REE substitutes in the crystal structure of the amphibole. However, these chemical parameters seem to be complexly related to run conditions (*i.e.*, pressures, temperatures, and oxygen fugacities). The effect of pressure and oxygen fugacity will be discussed in detail below (Chapter 4).

3.6 The association between major, minor, and trace elements in calcic amphibole

The crystal structure of amphibole is one of great compliance; the wide variations in chemistry may accommodate cations of different charges (*i.e.*, +1 to +5), ionic radii (*i.e.*, 0.026 to 0.161 nm), and in various coordinations (*i.e.*, four-, six-, eight- and twelve-fold coordinations). Cation site occupancies of major and minor elements in pargasite and kaersutite (*e.g.*, Si, Ti, Al, Cr, Fe^{2+}, Fe^{3+}, Mn, Mg, Ca, Na, K) are well established using different analytical techniques such as X-ray diffraction Rietveld structure refinement (XRD), Fourier-transform infrared (FTIR) spectroscopy, magic-angle-spinning nuclear magnetic resonance (MAS NMR), synchrotron-radiation X-ray absorption (XAS) spectroscopy, and Raman spectroscopy (Hawthorne 1983, Della Ventura *et al.* 1991, Paris *et al.* 1993, Hawthorne *et al.* 1995, Hawthorne *et al.* 1996b, Jenkins *et al.* 1997, Leake *et al.* 1997). However, site occupancies of LILE, HFSE, and REE are not well established and few studies have reported direct observations. Della Ventura and Robert (1990) and Robert *et al.* (1993)

proposed that Sr substitutes into the *M*(4) site in richterite (a sodic-calcic amphibole). Some studies assumed that the trace elements occupy only regular crystallographic sites, thus excluding interstitial and defect sites (Onuma *et al.* 1968, Philpotts 1978, Watson 1985, Beattie 1994, Blundy and Wood 1994, Wood and Blundy 1997). Other experimental studies at very low concentrations of trace element incorporation into crystals invoked substitutions into defect sites, although at higher concentrations the defect sites become saturated and the trace elements enter normal crystallographic sites (Navrotsky 1978, Harrison and Wood 1980). However, trace element site occupancies for amphibole (and other silicate minerals) are largely structurally controlled by relationships between partition coefficients and ionic radii, ionic volumes, and ionic charges which indicate that trace elements partition into regular crystallographic sites (Jensen 1973, Möller 1988, Liu *et al.* 1992, Robert *et al.* 1993, Brenan *et al.* 1995, LaTourrette *et al.* 1995, Klein *et al.* 1997).

For the LILE there is a consensus that Rb should substitute into the *A* site, while Ba and Sr may substitute into either the *A* site, as proposed by Jensen (1973; for Ba), Brenan *et al.* (1995; for Ba), and LaTourrette *et al.* (1995; for Ba and Sr), or the *M*(4) site, as proposed by Jensen (1973; for Sr), Möller (1988), and Brenan *et al.* (1995; for Sr). LaTourrette *et al.* (1995; Fig. 7b) assumed that both Ba and Sr occupy the *A* site but under two different coordinations (*i.e.*, a twelve and ten-fold coordination, respectively). If Ba and Sr occupy the same site, both should be in the same coordination (*i.e.*, twelve-fold coordination with an ionic radius for ^{XII}Sr and ^{XII}Ba of 0.131 and 0.161 nm, respectively; Shannon 1976).

However, in this study Sr is presumed to occupy the *M*(4) site in eight-fold coordination while Ba occupies the *A* site in twelve-fold coordination based on the partitioning results shown below using Onuma's diagram. For the REE (*i.e.*, La to Lu) and the HFSE (Nb, Ta, Zr, Hf, Ti) there is a consensus that they substitute into the *M*(4) and *M*(2) sites, respectively (Jensen 1973, Liu *et al.* 1992, Brenan *et al.* 1995, LaTourrette *et al.* 1995, Leake *et al.* 1997). However based on the charge and ionic radius of Y^{3+} (HFSE), it is assumed that it substitutes into the *M*(4) site. In summary, the cation site-assignments in calcic amphibole (pargasite and kaersutite) are:

		Major and minor elements	Trace elements
^{XII}A	:	K^{+}, Na^{+}	Rb^{+}, Ba^{2+}
$^{VIII}M(4)$	:	Na^{+}, Ca^{2+}, Mn^{2+}, Fe^{2+}, Mg^{2+}	REE^{3+} (*i.e.*, La^{3+} to Lu^{3+}), Y^{3+}, Sr^{2+}
$^{VI}M(1)$	:	Mn^{2+}, Fe^{2+}, Mg^{2+}	
$^{VI}M(2)$	:	Ti^{4+}, Al^{3+}, Fe^{3+}, Cr^{3+}	Zr^{4+}, Hf^{4+}, Nb^{5+}, Ta^{5+}
^{IV}T	:	Si^{4+}, Al^{3+}	

Note that no distinction is made in this study between the different cavities in the *A* site [*i.e.*, *A*(2), *A*(m), *A*(2/m)], between the *M*(1) and *M*(3) sites, and between the *T*(1) and *T*(2) sites [referred here and thereafter as *A*, *M*(1), and *T* sites, respectively]. Furthermore for pargasite and kaersutite compositions, the *A* site is always partially filled (or totally in some cases) by Na and/or K.

3.6.1. Thermodynamic model

Different thermodynamic and empirical models have been developed to explain or to predict partition coefficient behaviour between structurally simple mineral phases (*e.g.*, sodium nitrate, sylvite, olivine, plagioclase, clinopyroxene, orthopyroxene) and melt (Nagasawa 1966, Onuma *et al.* 1968, Philpotts 1978, Colson *et al.* 1988, Möller 1988, Beattie *et al.* 1991, Beattie 1994, Blundy and Wood 1991a, -b, Blundy and Wood 1994, Blundy *et al.* 1996, Purton *et al.* 1996, Purton *et al.* 1997, Wood and Blundy 1997). The partition coefficients can elucidate some physical and structural characteristics of the mineral (*e.g.*, the site in a mineral which a given element is occupying, the lattice site Young's modulus, the optimum ionic radius of a given lattice site) without other detailed analytical techniques. However, if a trace element substitutes into two different crystal lattice sites, as suggested by Brenan *et al.* (1995) for Ba, this would complicate the above trace element site occupancy assignments. Multiple lattice site occupancies of trace elements can only be resolved by detailed analytical studies. In this section, it is assumed that trace elements partition into a single crystal lattice site as suggested for Sr by Della Ventura and Robert (1990).

Onuma *et al.* (1968) showed that partition coefficients between pyroxene and melt of a series of isovalent elements (*e.g.*, REE^{3+}) follow an inverse parabola when plotted against their ionic radius. Furthermore, they were able to establish the major, minor, and trace element's lattice site occupancy based on the relative positions of the different parabolae

(Onuma *et al.* 1968). Blundy and Wood (1994) developed a quantitative model based on thermodynamic principles and the relationship described by Onuma *et al.* (1968) and applied it to different silicate minerals. The general idea behind the thermodynamic model of Blundy and Wood (1994) is based on the substitution behaviour of major, minor, and trace elements (cations) into lattice sites of a silicate mineral. It can be used to extract important physical properties of the mineral at different pressures, temperatures, and compositions (Brenan *et al.* 1995, LaTourrette *et al.* 1995, Schmidt *et al.* 1996, Wood and Blundy 1997). Furthermore, knowing certain physical properties of the mineral, Blundy and Wood's (1994) model can be used to predict partition coefficients (Blundy and Wood 1994, Brenan *et al.* 1995, Wood and Blundy 1997). Due to its simplicity and its success in previous studies, this model will be used to better understand the behaviour of partition coefficients between amphibole and basaltic melt and to explain, if possible, the relationship between the results of our experiments and those of previous studies.

Blundy and Wood's (1994) model is based upon an approximation which relates the partition coefficient with the Gibbs free energies of fusion and of elemental exchange between the crystal and the melt:

$$D_i = exp\left(\frac{\Delta G^{y}_{fusion}}{RT}\right) \times exp\left(\frac{\Delta G^{y-i}_{exchange}}{RT}\right) \quad (1)$$

where D_i is the partition coefficient of a cation (i) between mineral and melt, ΔG^{y}_{fusion} is the standard-state free energy of fusion of the host mineral (in Joule·mol^{-1}). It governs the partitioning between the mineral and melt of the host cation (y) into the crystal lattice-site of interest as a function of pressure and temperature, R is the gas constant (in Joule·K^{-1}·mol^{-1}), and T is the temperature (in degrees K), $\Delta G^{y-i}_{exchange}$ is the free energy required to remove a host cation (y) from the crystal and insert into the same lattice-site a cation (i), differing in size and/or charge from (y) (in Joule·mol^{-1}). The exchange free energy term for two cations [*i.e.*, second parameter in eqn. (1)] can be approximated using Brice's (1975) equation relating the difference in the lattice strain free energy (ΔG_{strain}) as a function of the Young's modulus for the lattice site and the size of the mismatch between two cations, one from the host crystal lattice site (y) and one from the liquid phase (i):

$$\Delta G^{y-i}_{exchange} \approx \Delta G_{strain} = 4\pi \bar{E} N_A \left[\frac{r_o}{2}\left(r_i - r_o\right)^2 + \frac{1}{3}\left(r_i - r_o\right)^3 \right] \qquad (2)$$

where ΔG_{strain} stands for the mechanical strain free energy around an isovalent cation which does not fit into the lattice-site (in bar·nm^3·mol^{-1}), $\bar{E}$ is the Young's modulus of the lattice site (in bar) which varies in an approximately linear function with the cation charge, N_A is Avogadro's number (in mol^{-1}), r_o is the optimum ionic radius of the lattice-site (in nm), and r_i is the ionic radius of the exchanged cation from the melt (in nm). The mechanical strain free energy of substitution may be controlled by the relative elasticity of the host lattice-site

instead of the ability of the host mineral to control the local charge balance [*e.g.*, $^{VIII}La^{3+}$ substitutes into the *M*(4) site where $^{VIII}Ca^{2+}$ resided which results in the need for charge balance; Blundy and Wood 1991a]. However, the overall neutrality of the structural unit must be maintained without exception. The first parameter in equation (1) can be described as the "strain-compensated partition coefficient" [*i.e.*, $D_o = \exp(\Delta G^{\gamma}_{fusion} / RT)$ or RT ln $D_o = \Delta G^{\gamma}_{fusion}$] of a cation (or element) into the crystal lattice site where the ideal cation has an ionic radius identical to r_o (*i.e.*, $r_i = r_o$). However, in most minerals D_o does not correspond to the partition coefficient of a major element in the lattice-site as shown below for amphibole.

Then, following Blundy and Wood (1994) the general equation can be rewritten as:

$$D_i(P,T,X) = D_O(P,T,X) \times exp\left[\frac{-4\pi \bar{E} N_A\left[\frac{r_o}{2}\left(r_i - r_o\right)^2 + \frac{1}{3}\left(r_i - r_o\right)^3\right]}{RT}\right] \qquad (3)$$

where $D_i(P,T,X)$ is the measured partition coefficient of a cation at the pressure, temperature, and composition of interest, $D_o(P,T,X)$ represents the maximum partition coefficient of the lattice-site for a series of isovalent cations at the same pressure, temperature, and composition as D_i. For such behaviour the bulk crystal is assumed to behave as a perfect elastic material and the substitution of a cation into a lattice-site is reversible from liquid to crystal and does not create permanent deformation (*i.e.*, the individual Young's modulus of the crystal lattice

site remains constant and is in the *elastic domain*). Comodi *et al.* (1991) observed an almost constant variation in cell volume as pressure increased from 0.0001 to 3.7 GPa at room temperature for tremolite and glaucophane (*i.e.*, a calcic and sodic amphiboles, respectively) which suggests constant bulk moduli (K) in the range of pressure studied. However, Comodi *et al.* (1991) observed a weak change in K for tremolite at around 2.0 GPa. The variation observed for tremolite was interpreted either as a progressive variation of K from 0.0001 to 4.1 GPa or as an abrupt change occurring near 2.0 GPa where K changed from 72.0 to 99.0 GPa (Comodi *et al.* 1991). The Young's modulus of the lattice site ($\bar{E}$) is very sensitive to the compositional variations of each lattice site in a crystal whereas the bulk modulus (K) remains practically identical (same order of magnitude) within each mineral group (*i.e.*, amphibole, pyroxene, epidote: Comodi *et al.* 1991, Comodi *et al.* 1995, Comodi and Zanazzi 1997, Zhang *et al.* 1997).

Equation (3) can be used to fit the partition coefficients of an isovalent series of cations which occupy the same lattice site [*e.g.*, $REE^{3+} + Y^{3+}$ into the $M(4)$ site]. Figure 3.8 shows a typical diagram where partition coefficients are plotted against the ionic radius for the P-MT-27 experiment. This fitting procedure yields apparent values for r_o, $\bar{E}$, and D_o. These parabolae describe the capacity of a lattice site to accommodate cations of different ionic radius and/or charges.

The narrower the parabola, the higher the rigidity of the site and the more difficult it is to accommodate cations of different ionic radius than the ideal ionic radius of the lattice site

Figure 3.8. Calculated least-squares regression lines obtained for the different partition coefficient groups of cations against the ionic radius for P-MT-27 experiment. Letters denote: tetrahedral sites $^{IV}[T(1)$ and $T(2)]$; octahedral sites $^{VI}[M(1)$ and $M(2)]$; distorted cubic site $^{VIII}[M(4)]$; distorted cuboctahedron site $^{XII}(A)$. Lines denote: unconstrained non-linear least-squares regressions (filled and large dashed, see Table 3.12); constrained non-linear least-squares regressions (small dashed).

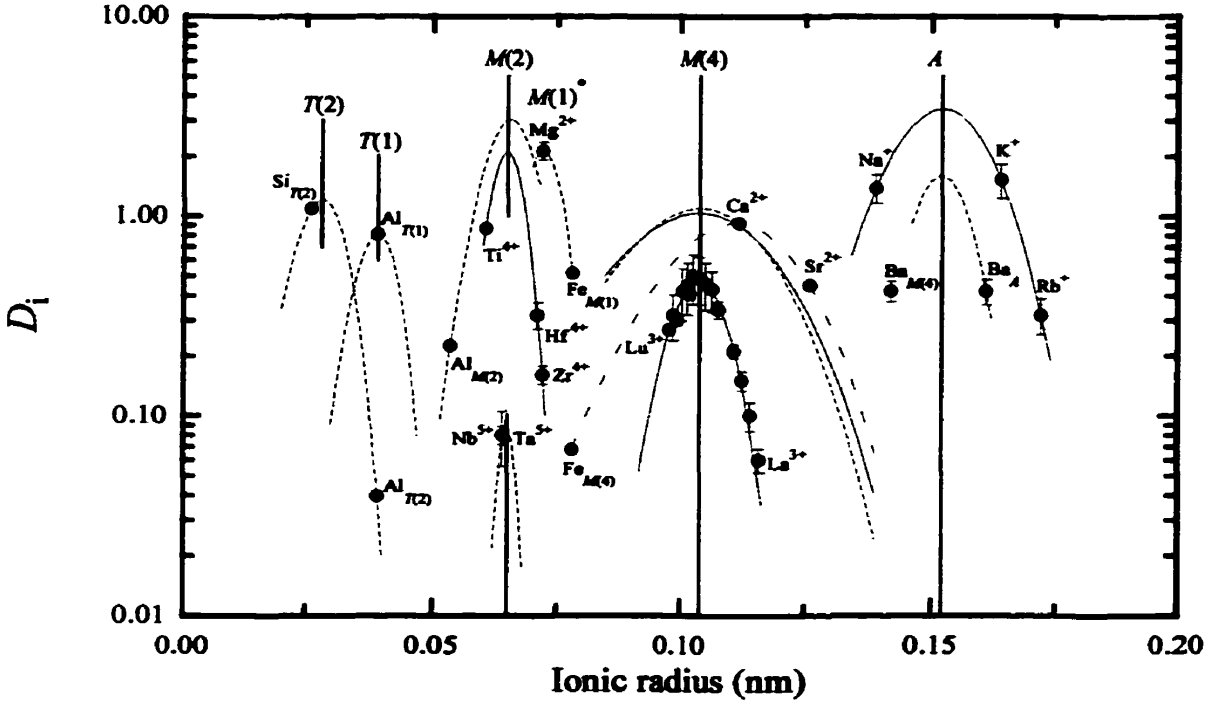
10.00
1.00
0.10
0.01
D_i
0.00
0.05
0.10
0.15
0.20
Ionic radius (nm)
T(2)
T(1)
M(2)
M(1)
M(4)
A
Si T(2)
Al T(1)
Al T(2)
Mg2+
Ti4+
Fe M(1)
Hf4+
Zr4+
Al M(2)
Nb5+
Ta5+
Fe M(4)
Ca2+
Lu3+
La3+
Sr2+
Na+
K+
Ba M(4)
Ba A
Rb+

(*i.e.*, r_o). For calcic amphiboles (*i.e.*, tremolite and pargasite), the measured Young's modulus of the different lattice-sites are in general $\bar{E}_{M(3)} > \bar{E}_{M(1)} > \bar{E}_{M(4)} > \bar{E}_{M(2)} > \bar{E}_A$ (Comodi *et al.* 1991), whereas the calculated Young's modulus from partition coefficient values of the different lattice-sites are in general $\bar{E}_{M(1,3)} > \bar{E}_{M(2)} > \bar{E}_{M(4)} > \bar{E}_A$ (for pargasite: Brenan *et al.* 1995, LaTourrette *et al.* 1995). Furthermore as mentioned above, the Young's modulus of a specific lattice-site (*i.e.*, rigidity) increases as the valency of the cation series increases as shown in Figure 3.8 by the opening of the different parabolae between the $(Fe, Ca, Sr, Ba)^{2+}_{M(4)}$ and $(REE, Y)^{3+}_{M(4)}$ series (*i.e.*, the calculated Young's modulus $\bar{E}_{M(4)}$ increases from 74.9 to 445.4 GPa for the divalent and trivalent cation series, respectively; Table 3.12) (Blundy and Wood 1994). By fitting a non-linear least-squares regression to each isovalent cation series, r_o, $\bar{E}$, and D_o values can be extracted for each lattice site at the temperature, pressure, and composition of the experiment. However, the non-linear least-squares regression can not be used directly when an isovalent series has less than three D_i values [*e.g.*, $^{VI}(Mg, Fe)_{M(1)}$ and $^{VI}(Nb, Ta)_{M(2)}$]. In such cases, it was necessary to constrain a value (*e.g.*, r_o) in equation (3) due to the occurrence of a non-converging solution (*i.e.*, three equations with two unknowns; Fig. 3.8). As shown in Figure 3.8, it was possible to calculate D_o, $\bar{E}$, and r_o values for $(Ti, Hf, Zr)_{M(2)}$, $(Fe, Ca, Sr)_{M(4)}$, $(REE, Y)_{M(4)}$, and $(Na, K, Rb)_A$ without constrained values. These results are listed in Table 3.12. For the P-MT-27 experiment, the calculated and estimated Young's moduli are $\bar{E}_{T(1,2)} > \bar{E}_{M(2)} > \bar{E}_{M(1,3)} > \bar{E}_{M(4)} > \bar{E}_A$ for similar ionic charges [*i.e.*, 4+ in the *T vs. M*(2) sites, 3+ in the *M*(2) *vs. M*(4)], which are closely related to the range of values

Table 3.12. Calculated and estimated lattice-site parameters for P-MT-27 experiment.

Lattice-site	Charge	Coord.	Cation	D_o	$\bar{E}$ (GPa)	r_o (nm)
A	1+	12	Na, K, Rb	3.44	110.425	0.152
	2+	12	Ba	[1.60[a]]	[315.552[b]]	[0.152[c]]
M(4)	2+	8	Fe[d], Ca, Sr	1.096	74.964	0.104[e]
				[0.922[f]]	[80.699[f]]	[0.111[f]]
	3+	8	REE, Y	0.476	445.436	0.104
M(1)[g]	2+	6	Mg, Fe[h]	2.12[i]	1645.362	0.072[j]
M(2)	3+	6	Al[k]	[3.03[a]]	[937.844[b]]	[0.065[l]]
	4+	6	Ti, Hf, Zr	2.097	2213.58	0.065
	5+	6	Nb, Ta	[0.09[a]]	[7887.84[b]]	[0.065[l]]
T(1)	3+	4	Al[m]	[0.814[n]]	[2484.26[b]]	[0.039[o]]
T(2)	4+, 3+	4	Si, Al[p]	1.21	2484.26	0.028

Abbreviation: Coord.-coordination. Values in brackets represent qualitative results.

[a] Estimated value. [b] Calculated using estimated D_o and assuming r_o constant for a given site. [c] r_o was regressed from the 1+ cations of the *A* site. [d] D_{Fe} was calculated allowing 11.6 % of the total ferrous-iron allocated to the *M*(4) site (see Tables 3.4 and 3.5). [e] r_o was regressed from the 3+ cations of the *M*(4) site. [f] Values obtained without constrained values. [g] *M*(1) denotes the *M*(1) and *M*(3) sites combined. [h] D_{Fe} was calculated allowing 88.6 % of the total ferrous-iron allocated to the *M*(1) site (Tables 3.4 and 3.5). [i] D_o was assumed to be D_{Mg}. [j] r_o was assumed to be the ionic radius of ^{VI}Mg. [k] D_{Al} was calculated allowing 20.8 % of the total aluminium allocated to the *M*(2) site (see Tables 3.4 and 3.5). [l] r_o was regressed from the 4+ cations of the *M*(2) site. [m] D_{Al} was calculated allowing 95.4 % of the total tetrahedral aluminium (100-20.8$_{Al\ in\ M(2)}$ = 79.2 %) allocated to the *T*(1) site (see Tables 3.4 and 3.5). [n] D_o was assumed to be D_{Al} calculated for the *T*(1) site. [o] r_o was assumed to be the ionic radius of ^{IV}Al. [p] D_{Al} was calculated allowing 4.6 % of the total tetrahedral aluminium (100-20.8$_{Al\ in\ M(2)}$ = 79.2 %) allocated to the *T*(2) site (see Tables 3.4 and 3.5).

reported by Brenan *et al.* (1995) and LaTourrette *et al.* (1995). The calculated optimum ionic radius of the *M*(4) site corresponds to the ionic radius of Tb (*i.e.*, ionic radius of ^{VIII}Tb $= r_o = 0.104$ nm; Figure 3.8). However, this optimum ionic radius does not correspond to the ionic radius of a major divalent element such as Ca which occupies the same lattice site (ionic radius of ^{VIII}Ca = 0.112 nm). Similar observations were reported by Brenan *et al.* (1995) and LaTourrette *et al.* (1995) for pargasites of similar compositions. For Ba, two different ionic radii corresponding to the two different coordinations (*i.e.*, the eight- and twelve-fold coordinations) are shown. When Ba^{2+} was assumed to occupy the same lattice site as Fe^{2+}, Ca^{2+}, and Sr^{2+} [*i.e.*, *M*(4)], a poor fit was obtained due to similar partition coefficients between Ba and Sr but relatively large differences in their ionic radii (*i.e.*, ionic radii = 0.142 and 0.131 nm for ^{VIII}Ba and ^{VIII}Sr, respectively, Shannon 1976). In such a case where the regression line does not show a good fit, it seems reasonable to assume that Ba may substitute into the large *A* site as shown in Figure 3.8 for the twelve-fold coordination. The possibility of Ba occupying the large *A* site has never been reported before due to the lack of natural or synthetic Ba-rich calcic amphibole, rendering it impossible for structural refinement. Oberti *et al.* (1995), Hawthorne *et al.* (1996a), and Oberti *et al.* (1997) reported significant amounts of Ca^{2+} in the *A* site for synthetic fluor-pargasite and natural fluor-cannilloite, respectively (both are calcic amphiboles). Such a divalent cation in the *A* site might suggest that the substitution of Ba into the *A* site is reasonable to assume based on its partition coefficient, ionic radius, and ionic charge. Similar observations for Ba in the twelve-fold coordinated site

were proposed for biotite and phlogopite (Guo and Green 1990, Edgar 1992, LaTourrette *et al.* 1995, Henderson and Foland 1996, Shaw and Penczak 1996). However due to the limited site occupancies of Ba in clinopyroxene, it was reported to occupy the eight-fold coordinated site similar to Ca (*i.e.*, in the *M*(2) site; Papike 1987, Blundy and Wood 1994, Fig. 1). Therefore the D_{Ba} between clinopyroxene and basaltic melt is at least two orders of magnitude lower than D_{Sr} (Hart and Dunn 1993, Green 1994), which is not the case for amphibole and biotite (*i.e.*, D_{Ba} and D_{Sr} are in the same order of magnitude).

Before comparing the different elastic properties determined in this study with previous ones it is important to distinguish if a 15 relative % variation (a typical relative standard deviation observed from partitioning) applied to the unconstrained D_o and $\bar{E}$ values calculated previously significantly affects the unconstrained least-squares regression line observed relating partitioning and ionic radius of the trivalent cations in the *M*(4) site using equation (3) (P-MT-27 experiment; Table 3.12). Furthermore, a variation of ±50 °C was applied on the run temperature (T) to investigate any significant modifications which would also disturb the original unconstrained regression line and to investigate the effect of temperature on the model (corresponding in this case to ~ 5 relative % variation of the measured temperature). Figure 3.9 shows the modified regression lines obtained from equation (3) for the P-MT-27 experiment when D_o and $\bar{E}$ were used as fixed values from which I applied a variation of 15 relative % to their initial unconstrained values and also by modifying the run temperature by ±50 °C (*e.g.*, Fig. 3.9a, $D_o + 0.15D_o$ and $D_o - 0.15D_o$ where

Figure 3.9. Variations in the calculated models for P-MT-27 experiment using the 4+ cations of the $M(4)$ site. (a) Constrained model using a fixed D_o by applying a variation of 15 relative % to the original value (Table 3.12; $\bar{E}$ and r_o were unconstrained). (b) Constrained model using a fixed $\bar{E}$ by applying a variation of 15 relative % to the original $\bar{E}$ value (Table 3.12; D_o and r_o were unconstrained). (c) Unconstrained model using a variation of ±50 °C to the run temperature (D_o, $\bar{E}$, and r_o were unconstrained). Lines denote: non-linear least-squares regression using unconstrained parameters (bold, see Table 3.12); non-linear least-squares regression using different variations (small dashed).

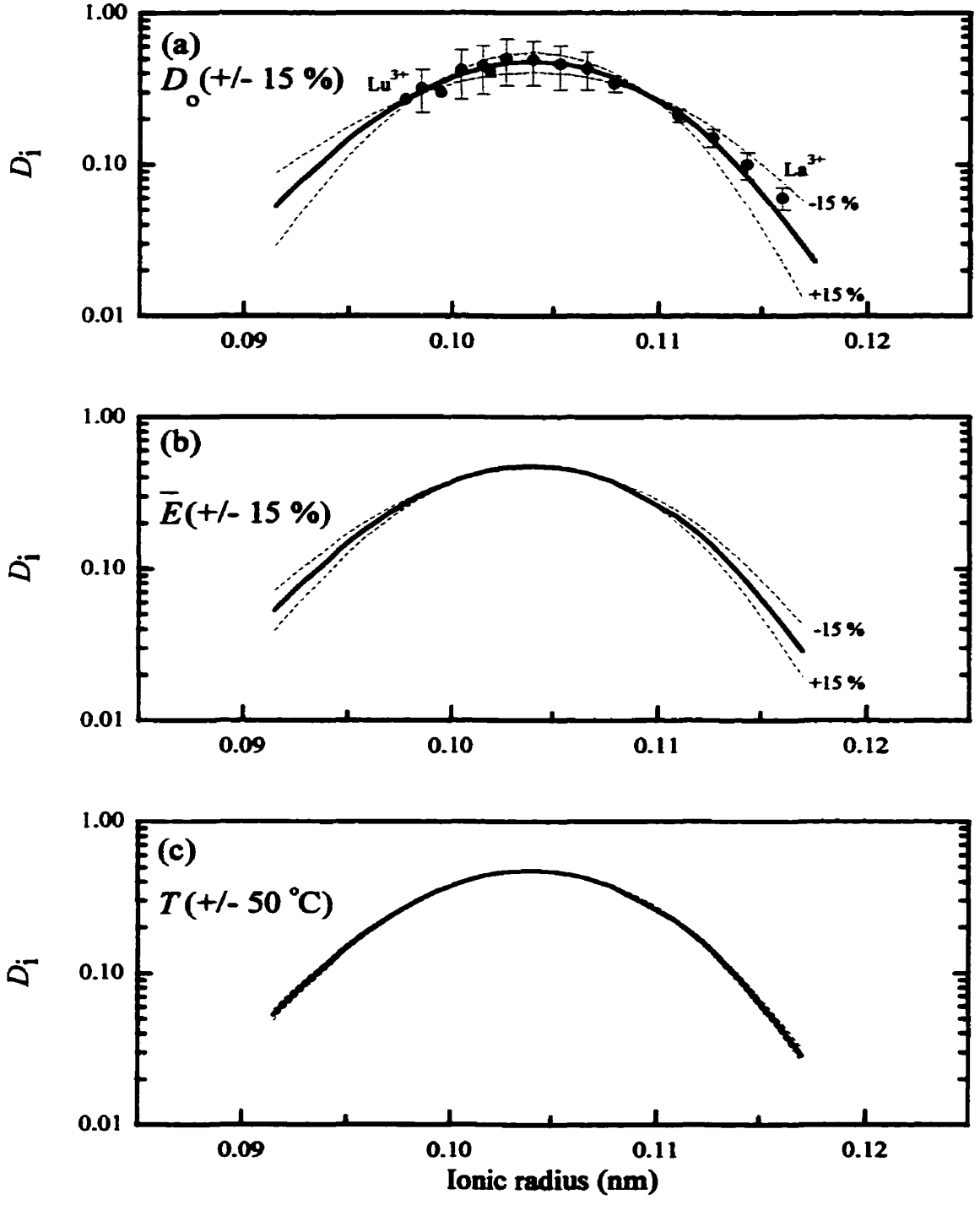
(a)
D_o(+/- 15 %)
Lu3+
La3+
-15 %
+15 %
(b)
$\bar{E}$(+/- 15 %)
-15 %
+15 %
(c)
T(+/- 50 °C)
D_i
1.00
0.10
0.01
0.09
0.10
0.11
0.12
Ionic radius (nm)

$\bar{E}$ and T were fixed). Based on the different regression lines obtained when I applied the different errors on each individual parameter, the pre-exponential variable in equation (3) (*i.e.*, D_o) seemed to be the most sensitive while the temperature had little effect on the final calculated model. However, the variations observed when modifying D_o were close to (LREE) or within (MREE + HREE + Y) one standard deviation of the partition coefficient values (Fig. 3.9a). For all the different possibilities of D_o, $\bar{E}$, or T investigated, the calculated optimum ionic radius (*i.e.*, $r_o = 0.104$ nm) of the lattice site when using equation (3) remained constant, suggesting that r_o is insensitive to the model used when plotting D *vs.* ionic radius and is intrinsic to the dataset.

Because partition coefficients of the REE have been investigated in the majority of previous experimental studies (Table 3.11), these trivalent cations will be focussed upon to determine if there is a relationship between the elastic properties of the amphibole run products and their chemistry using equation (3). Previously, it was shown that D_{REE} could be governed by the chemistry of the amphibole (Fig. 3.7). By fitting a least-squares regression line for D_{REE} obtained from these experiments and those from previous experimental studies (Nicholls and Harris 1980, Green and Pearson 1985a, Adam and Green 1994, LaTourrette *et al.* 1995), D_o, $\bar{E}$, and r_o for each dataset were independently calculated. Figure 3.10 shows a positive linear relationship between D_{La}, D_{Sm}, D_{Ho}, and D_{Lu} and the calculated maximum partition coefficient (D_o) based on one standard deviation attached to each partition coefficient for La, Sm, Ho, and Lu. A remarkable relationship between D_{REE} and D_o indicates

Figure 3.10. Variations of partition coefficient for La, Sm, Ho, Lu against the calculated maximum partition coefficient (D_o) for the trivalent cations in the $M(4)$ site. Symbols: same as in Fig. 3.7.

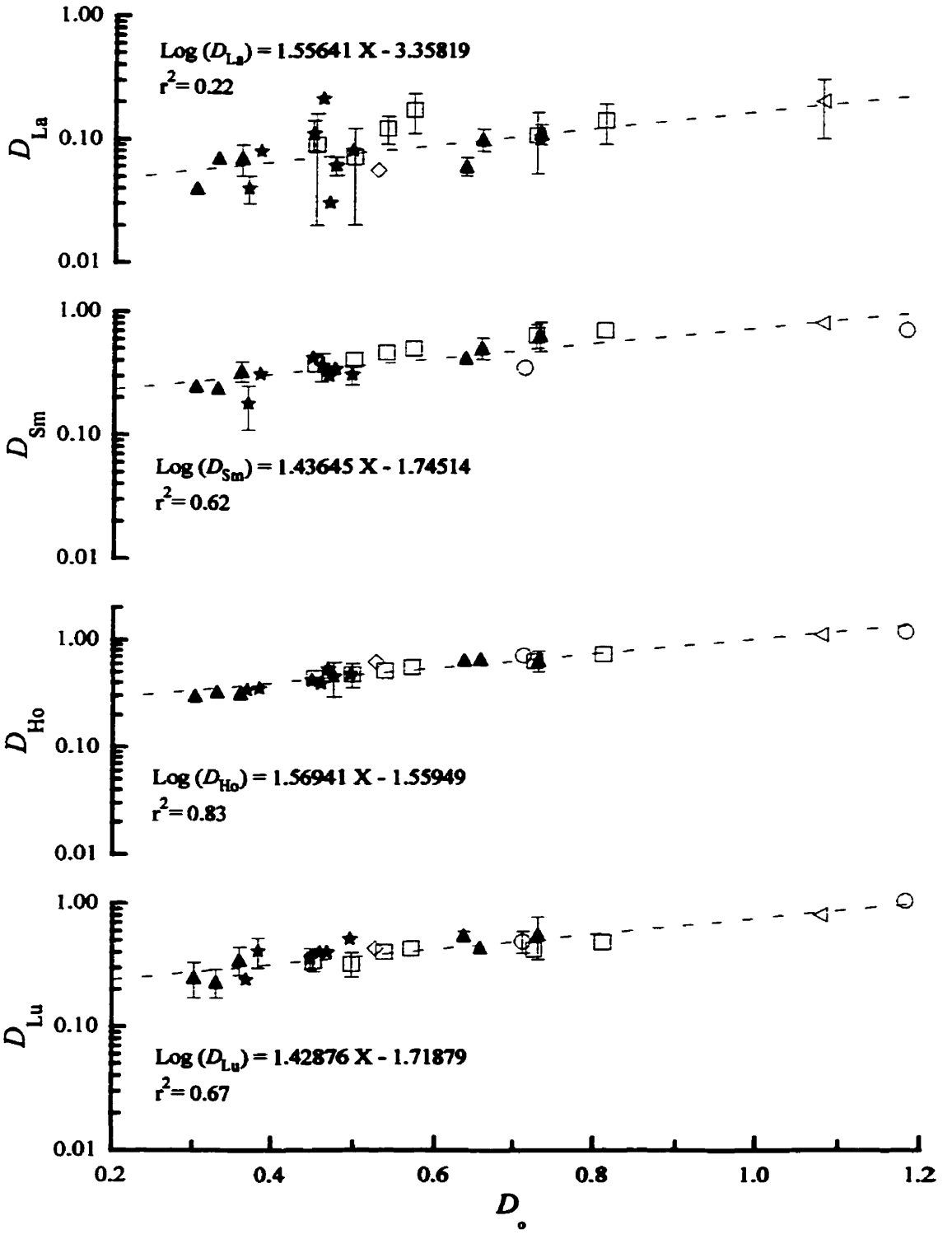
1.00
0.10
0.01
D_{La}
Log (D_{La}) = 1.55641 X - 3.35819
r^2= 0.22
D_{Sm}
Log (D_{Sm}) = 1.43645 X - 1.74514
r^2= 0.62
D_{Ho}
Log (D_{Ho}) = 1.56941 X - 1.55949
r^2= 0.83
D_{Lu}
Log (D_{Lu}) = 1.42876 X - 1.71879
r^2= 0.67
0.2
0.4
0.6
0.8
1.0
1.2
D_o

that as the overall partition coefficients for an isovalent group of cations increases the calculated maximum partition coefficient of the lattice site also increases.

Figure 3.11 shows the variations of the calculated maximum partition coefficient (D_o) as a function of the amphibole chemistry. The maximum variation observed in D_o corresponds to ~ 291 relative % [*i.e.*, 0.302 to 1.18 for HF13-38 and Nicholls and Harris (1980) experiments, respectively]. However, even if there is only a weak correlation coefficient between D_o and the CN/MTAF ratio (0.59), it seems to suggest that a complex process of cation exchange occurs in the amphibole structure to charge balance the trivalent cations as their partitioning into amphibole increases.

The relatively large variation of $\bar{E}$ (*i.e.*, 61.5 to 579.4 GPa) which corresponds to ~ 850 relative % shows a similar correlation with the major element composition of the amphibole run products. However, the relatively small variation of r_o (*i.e.*, 0.097 to 0.105 nm) which corresponds to ~ 8 relative % is less obviously correlated with mineral composition (Fig. 3.12). In fact, minimum values of $\bar{E}$ and r_o were calculated for the P-MTg$_{Ti}$-31 experiment (Fig. 3.12). This particular experiment has kaersutite in the run products and shows the minimum CN/MTAF ratio of 0.163 (Fig. 3.11). However, the maximum values of $\bar{E}$ and r_o calculated for the trivalent cations in the M(4) site does not correspond to the maximum CN/MTAF ratio. For these parameters (*i.e.*, $\bar{E}$ and r_o), the maximum value calculated for the Young's modulus corresponds to run #955(HM) of Green and Pearson (1985a; $\bar{E}$ = 579.4 GPa) which has a CN/MTAF ratio of 0.446 (Figs. 3.11 and

Figure 3.11. Variation of the maximum partition coefficient (D_o) calculated for the trivalent cations in the $M(4)$ site against the major element ratio of the amphibole run products. Symbols: same as in Fig. 3.7. Run numbers are identified for experiments which showed minimum and maximum $\bar{E}$ and/or r_o values calculated from the least-squares regression (see text).

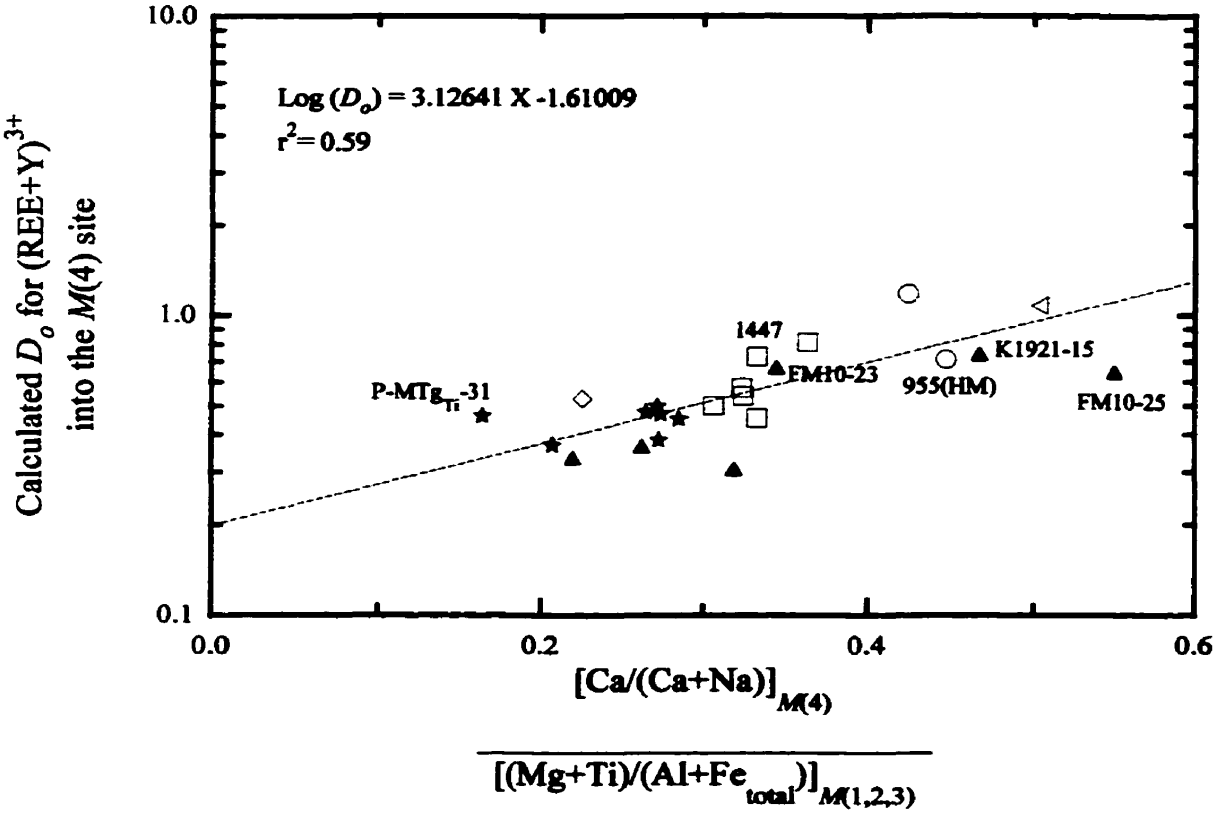
Log (D_o) = 3.12641 X -1.61009
r^2= 0.59
Calculated D_o for $(REE+Y)^{3+}$ into the $M(4)$ site
10.0
1.0
0.1
0.0
0.2
0.4
0.6
1447
FM10-23
K1921-15
955(HM)
FM10-25
P-MTg$_{Ti}$-31
$[Ca/(Ca+Na)]_{M(4)}$
$[(Mg+Ti)/(Al+Fe_{total})]_{M(1,2,3)}$

Figure 3.12. Maximum and minimum values of the calculated Young's modulus $\bar{E}$ and optimum ionic radius r_o for trivalent cations in different amphibole run products. (a) $\bar{E}$. (b) r_o. Lines denote: P-MTg$_{Ti}$-31 experiment (dashed); 955(HM) experiment from Green and Pearson (1985a) (filled). (b) r_o. Lines denote: P-MTg$_{Ti}$-31 experiment (dashed); 1447 experiment from Adam and Green (1994) (filled).

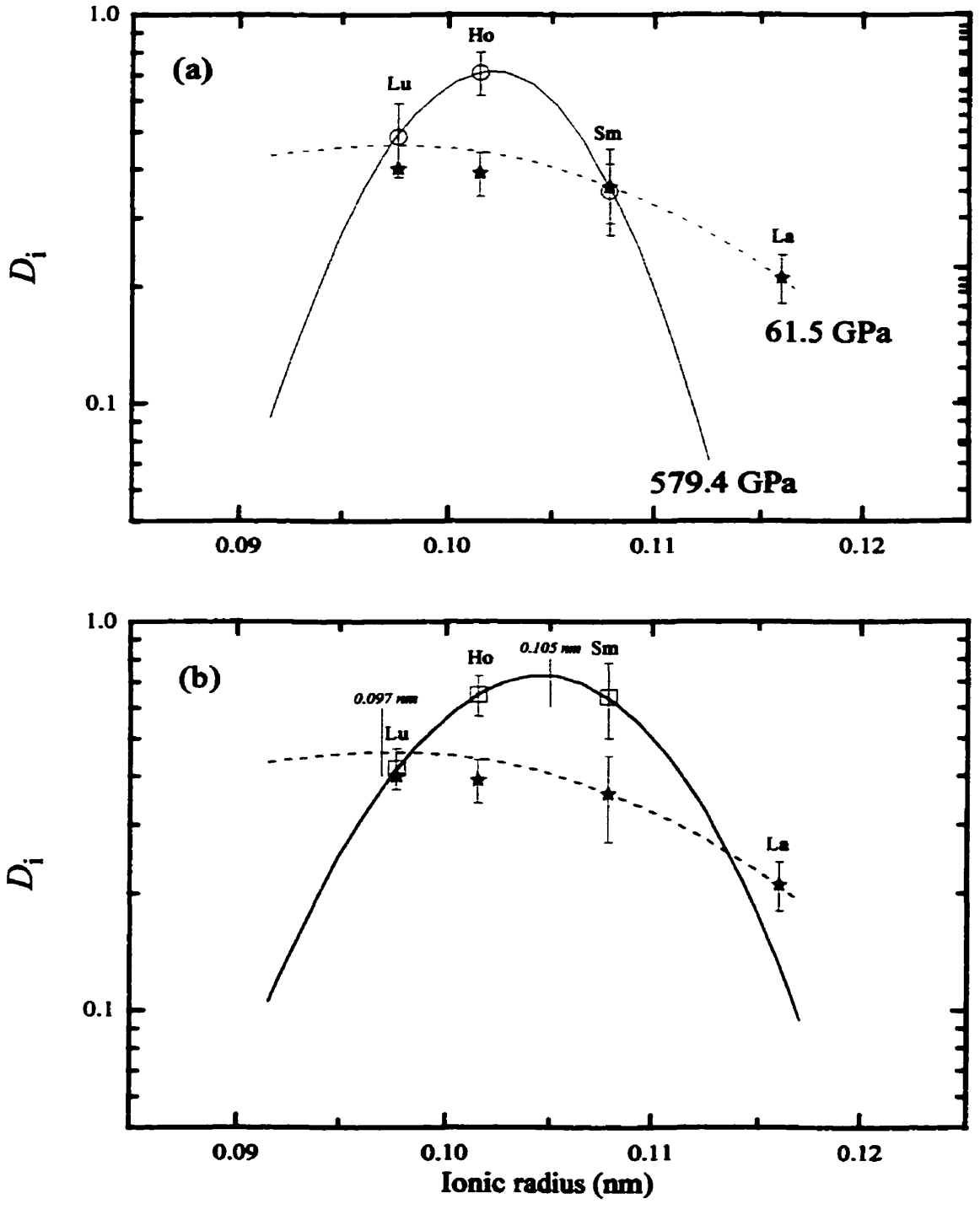
(a)
Ho
Lu
Sm
La
61.5 GPa
579.4 GPa
1.0
0.1
D_i
0.09
0.10
0.11
0.12
(b)
0.097 nm
0.105 nm
Ho
Lu
Sm
La
1.0
0.1
D_i
0.09
0.10
0.11
0.12
Ionic radius (nm)

3.12a). As mentioned previously, a modification in the amphibole composition can increase the Young's modulus of a lattice site [*e.g.* the $\bar{E}_{M(4)}$ site] and will therefore result in a narrower parabola (Fig. 3.12a). For the optimum ionic radius, the maximum value obtained is for run #1447 of Adam and Green (1994; r_o = 0.105 nm) which has a CN/MTAF ratio of 0.332 (Figs. 3.11 and 3.12b).

An increase in the optimum ionic radius of a specific lattice site in the amphibole structure can be due to a modification of the relative proportion of the different cations occupying the lattice site which can influence the whole structure of the amphibole. As an example, Comodi *et al.* (1991) calculated the bulk modulus of the *M*(4) polyhedra for divalent cations (referred here as the Young's modulus of the lattice site) based on compressibility measurements for tremolite and pargasite equal to 74.0 and 53.0 GPa , respectively. For these amphiboles, the cation site populations for the *M*(4) site were very close to each other [*i.e.*, 100 % Ca and 99 % Ca - 1 % Fe in the *M*(4) site for tremolite and pargasite, respectively]. Furthermore, the calculated mean bond-length distance (*i.e.*, <*M*(4)-O>) was higher in tremolite than in pargasite (*e.g.*, 0.2506 and 0.2492 nm for tremolite and pargasite, respectively, at 0.0001 GPa experiments; Comodi *et al.* 1991). At these conditions, substituting a smaller cation into the *M*(4) lattice site (*i.e.*, ionic radius of $^{VI}Fe_{M(4)}$ = 0.078 nm for $^{VIII}Ca_{M(4)}$ = 0.112 nm) will decrease its Young's modulus and also the mean bond-length distance. Evidently decreasing the mean bond-length distance of a lattice site will directly decrease the optimum ionic radius (r_o) of the lattice site. In summary, the variations observed

for the calculated D_o, $\bar{E}$, and r_o from partitioning data correspond in general to the effect of the amphibole composition. However different processes can also influence these parameters such as pressure and oxygen fugacity (Chapter 4), and the bulk titanium (Chapter 5) content of the amphibole.

Chapter 4

Experimental investigation on partitioning of LILE, HFSE, and REE between calcic amphibole and basaltic melt:

II- The effects of pressure and oxygen fugacity on partitioning

4.1 Introduction

The effects of pressure and oxygen fugacity on partition coefficients between silicate minerals and melts may be important because many studies reported that the generation of basaltic melts in the upper mantle could encompass a range of pressure greater than 1.0 GPa and a range in oxygen fugacity greater than ± 2 log units away from the FMQ buffer (Haggerty and Tompkins 1983, Christie *et al.* 1986, Wood and Virgo 1989). However, results of previous experimental studies have not lead to a general consensus concerning the effect of pressure on partitioning between various silicate minerals and melts. Mysen (1976; for olivine), Green and Pearson (1985a; for amphibole), Guo and Green (1990; for phlogopite), Sweeney *et al.* (1992; for amphibole), Adam and Green (1994; for amphibole), and Fujinawa and Green (1997; for amphibole) observed a decrease in D with increasing pressure whereas Drake and Holloway (1977; for amphibole), Green and Pearson (1983; for sphene and clinopyroxene), and Green and Pearson (1985b; for clinopyroxene) observed the opposite relationship. As for amphibole / melt partitioning there is a general consensus that D decreases with increasing pressure (Green and Pearson 1985a, Sweeney *et al.* 1992, Adam and Green 1994, Fujinawa and Green 1997). However, Dalpé and Baker (1997) observed an ambivalent behaviour of D_{Rb} and D_{HFSE} with increasing pressure between amphibole and

basaltic melt.

The effect of oxygen fugacity on partition coefficients is more subtle. Green and Pearson (1985a, -b) found that partitioning between clinopyroxene and melt ($D^{cpx/melt}$) and partitioning between amphibole and melt ($D^{amph/melt}$) increases with increasing oxygen fugacity; LaTourrette and Burnett (1992) found that $D_U^{cpx/melt}$ decreases while $D_{Th}^{cpx/melt}$ increases with increasing oxygen fugacity whereas Adam and Green (1994) did not find any significant effects for $D^{amph/melt}$ but observed an increase in $D_{Ti}^{cpx/melt}$ and $D_{REE}^{cpx/melt}$ with increasing oxygen fugacity.

4.1.1. Procedure used to investigate the effects of pressure and oxygen fugacity

Three starting materials were used to evaluate if pressure and oxygen fugacity significantly affect partition coefficients. These materials were grouped into two bulk compositions: pargasitic and alkaline basaltic materials with different major, minor, and trace elements. The first group included a pargasite crystal and a pargasitic glass (*i.e.*, P-MT and P-MTg, respectively; Table 3.1). The second group consisted of an alkaline basalt (*i.e.*, FM10; Table 3.1). Temperatures of experiments at the low and high pressures were similar, 1100 and 1050 °C for P-MT and P-MTg materials performed at the low oxygen fugacity (~NNO-2), 1050 and 1075 °C for P-MTg material performed at the high oxygen fugacity (~NNO+1.7), or an identical temperature (*i.e.*, 1000 °C) for the FM10 material performed at the high oxygen fugacity (~NNO+1.7). For experiments used to evaluate the effect of oxygen fugacity on partitioning at a constant run pressure, the temperatures of the P-MT and

FM10 experiments were similar (*i.e.*, within 25 to 50 °C). Experimental conditions and run products are listed in Table 3.3 (P-MT-27, P-MT-34, P-MTg-12, P-MTg-43, P-MTg-41, FM10-02, FM10-23, and FM10-25). As it can be seen in Table 3.3, run products were identical (P-MTg-43 *vs.* P-MTg-41) or very similar (P-MT-27 *vs.* P-MT-34, P-MTg-12 *vs.* P-MT-34, and FM10-23 *vs.* FM10-25) for pairs of experiments performed at the low and high pressures using a fixed oxygen fugacity. However, for pairs of experiments performed at a fixed run pressure but at different oxygen fugacities, run products were either similar (P-MT-27 *vs.* P-MTg-43 and P-MTg-12 *vs.* P-MTg-43) or different (P-MT-34 *vs.* P-MTg-41, and FM10-02 *vs.* FM10-23). As mentioned previously the compositions of these phases are not identical, only similar. No garnet was observed in any high pressure experiment (*i.e.*, 2.2 and 2.5 GPa). In the FM10-25 experiment, ilmenite was observed in the run products. With the alkaline basalt starting composition (*i.e.*, FM10), the maximum pressure stability field of amphibole was located between 2.2 and 2.5 GPa for the high oxygen fugacity buffer (*i.e.*, ~NNO+1.7). For this starting material, the highest run pressure used was 2.2 GPa instead of 2.5 GPa for P-MT materials.

4.1.2. The variations in amphibole compositions with increasing pressure at a fixed oxygen fugacity

For the major element concentrations in the amphibole run products, an increase in $Al_{M(1,2,3)}$, K_A, and a decrease in $Ti_{M(1,2,3)}$, $Ca_{M(4)}$ was observed as pressure increased (Table 3.5). Similar variations were observed by Adam and Green (1994) and Fujinawa and Green (1997).

The Fe_{total} in the *M*(1,2,3) sites decreased for the amphiboles which crystallized from the P-MT and P-MTg experiments while it increased in the amphiboles which crystallized from the FM10 experiments as pressure increased. The $Mg_{M(1,2,3)}$ behaved inversely to Fe_{total} in the amphiboles. Figure 3.3 shows variations in Ti, Fe^{2+}, and Mg in the different amphibole run products as pressure increased using different starting materials (P-MT-27 *vs.* P-MT-34a, P-MTg-12 *vs.* P-MT-34a, P-MTg-43 *vs.* P-MTg-41, and FM10-23 *vs.* FM10-25).

For experiments performed at the low oxygen fugacity (*i.e.*, P-MT-27 *vs.* P-MT-34a and P-MTg-12 *vs.* P-MT-34a), the concentrations in LILE (Sr), HFSE (Nb, Ta, Zr, Hf, Y), and REE (La, Ce, Pr, Nd, Sm, Dy) decrease in the amphibole with increasing pressure based on two standard deviations (Table 3.4). For experiments performed at a higher oxygen fugacity using the same material (*i.e.*, P-MTg-43 *vs.* P-MTg-41), the concentrations in LILE (Ba, Sr), HFSE (Nb, Ta, Zr, Hf, Y), and REE (La, Ce, Pr, Nd, Sm, Eu, Gd, Tb, Dy, Ho, Er, Yb) also decrease in the amphibole with increasing pressure. There is little variation in trace element concentrations for the amphiboles formed in alkaline basalt experiments performed at the high oxygen fugacity (*i.e.*, FM10-23 *vs.* FM10-25). In these experiments, La decreases while Y, Tm, and Yb increase in the amphibole with increasing pressure. Adam and Green (1994) and Fujinawa and Green (1997) observed similar trends for trace element concentrations of their amphibole run products.

4.1.3. The variation in amphibole compositions with increasing oxygen fugacity at a fixed pressure

The variation in major element concentrations in the amphibole run products from the four pairs of experiments (*i.e.*, P-MT-27 *vs.* P-MTg-43, P-MTg-12 *vs.* P-MTg-43, P-MT-34a *vs.* P-MTg-41, and FM10-02 *vs.* FM10-23) shows an increase in $Al_{T(1,2)}$ and $Ca_{M(4)}$ while $Ti_{M(1,2,3)}$ decreases with increasing oxygen fugacity (Table 5). Moreover, but not surprisingly, the estimated proportions of the Fe^{3+}/Fe^{2+} ratio in the amphibole produced from the pargasite material increase as the oxygen fugacity increases. Adam and Green (1994) observed the same trend for the $Ti_{M(1,2,3)}$ and Fe^{3+}/Fe^{2+} ratio in amphibole run products with increasing oxygen fugacity. However, the Fe^{3+}/Fe^{2+} ratio trend was not observed in the amphiboles crystallized from the alkaline basalt material due to the absence of any estimated Fe^{3+} (see section 3.4.1.1. Amphibole). Other variations observed for the pargasite materials obtained at both pressures (*i.e.*, P-MT-27 *vs.* P-MTg-43 and P-MTg-34a *vs.* P-MTg-41, respectively) were an increase in K_A and a decrease in $Al_{M(1,2,3)}$, $Fe^{2+}_{M(4)}$ with increasing oxygen fugacity. In the amphiboles which crystallized from the alkaline basalt (*i.e.*, FM10-02 *vs.* FM10-23 experiments), $Al_{M(1,2,3)}$ and $Fe^{2+}_{M(4)}$ increased while K_A decreased with increasing oxygen fugacity. An opposite behaviour for the Mg# in the amphiboles was observed using the pargasite materials (*i.e.*, Mg# shows an increase for P-MT-27 *vs.* P-MTg-43, P-MTg-12 *vs.* P-MTg43, P-MT-34a *vs.* P-MTg-41 pairs) and the alkaline basalt material (*i.e.*, Mg# shows a decrease for FM10-02 *vs.* FM10-23 pair) as the oxygen fugacity increased (Fig. 3.3).

No systematic variation in trace element concentrations within two standard deviations

of the analytical uncertainties was observed between the four different pairs of experiments (Table 3.4). However for the P-MT-34a *vs.* P-MTg-41 experiments performed at 2.5 GPa the concentrations of LILE (Rb, Ba, Sr) and REE (Ce) increase while Ta and Ho decrease with increasing oxygen fugacity. Similarities were observed between these latter experiments and the FM10-02 *vs.* FM10-23 pair of experiments for Ba and Ta as the oxygen fugacity increased (Table 3.4). Furthermore, the LILE (Sr), HFSE (Nb, Zr, Hf), and REE (La, Ce, Pr, Nd, Sm, Eu, Gd, Tb) concentrations decreased for this FM10 pair.

4.1.4. The effect of pressure on partition coefficients at a fixed oxygen fugacity

Figure 4.1 shows the effect of pressure on partition coefficients for the four pairs of experiments (*i.e.*, P-MT-27 *vs.* P-MT-34a, P-MTg-12 *vs.* P-MT-34a, P-MTg-43 *vs.* P-MTg-41, and FM10-23 *vs.* FM10-25). Based on one standard deviation D_{LILE} (D_{Rb}) increases while D_{HFSE} (D_{Nb}, D_{Zr}, D_{Hf}, D_{Ti}) and D_{REE} (D_{La}) decrease with increasing pressure for the experiments maintained at the low oxygen fugacity (*i.e.*, P-MT-27 *vs.* P-MT-34a and P-MTg12 *vs.* P-MT-34a; Figs. 4.1a, -b and Table 3.10). For experiments at a higher oxygen fugacity (*i.e.*, P-MTg-43 *vs.* P-MTg-41 and FM10-23 *vs.* FM10-25; Figs. 4.1c, -d), D_{LILE} (D_{Sr}), D_{HFSE} (D_{Ta}, D_{Zr}, D_{Hf}), and D_{REE} (D_{Ce}, D_{Pr}, D_{Nd}) decrease with increasing pressure. Comparison of the high oxygen fugacity experiments, FM10-23 *vs.* FM10-25, demonstrates that D_{REE} (D_{Yb}, D_{Lu}) increases and D_{LILE} (D_{Ba}) and D_{REE} (D_{La}) decrease with increasing pressure (Fig. 4.1d). As mentioned before, the range of pressures between both P-MTg experiments and both FM10 experiments at the high oxygen fugacity buffer were not identical

Figure 4.1. The effect of pressure on partition coefficients for different oxygen fugacities. (a) and (b) Low oxygen fugacity experiments. (c) and (d) High oxygen fugacity experiments. Variations include one standard deviation from multiple analyses (Table 3.10). Elements followed by an asterisk indicate that the calculated partition coefficient corresponds to a maximum value for a single or both experiments (*i.e.*, the trace element concentration in the amphibole was below the LLD; see Tables 3.4 and 3.8).

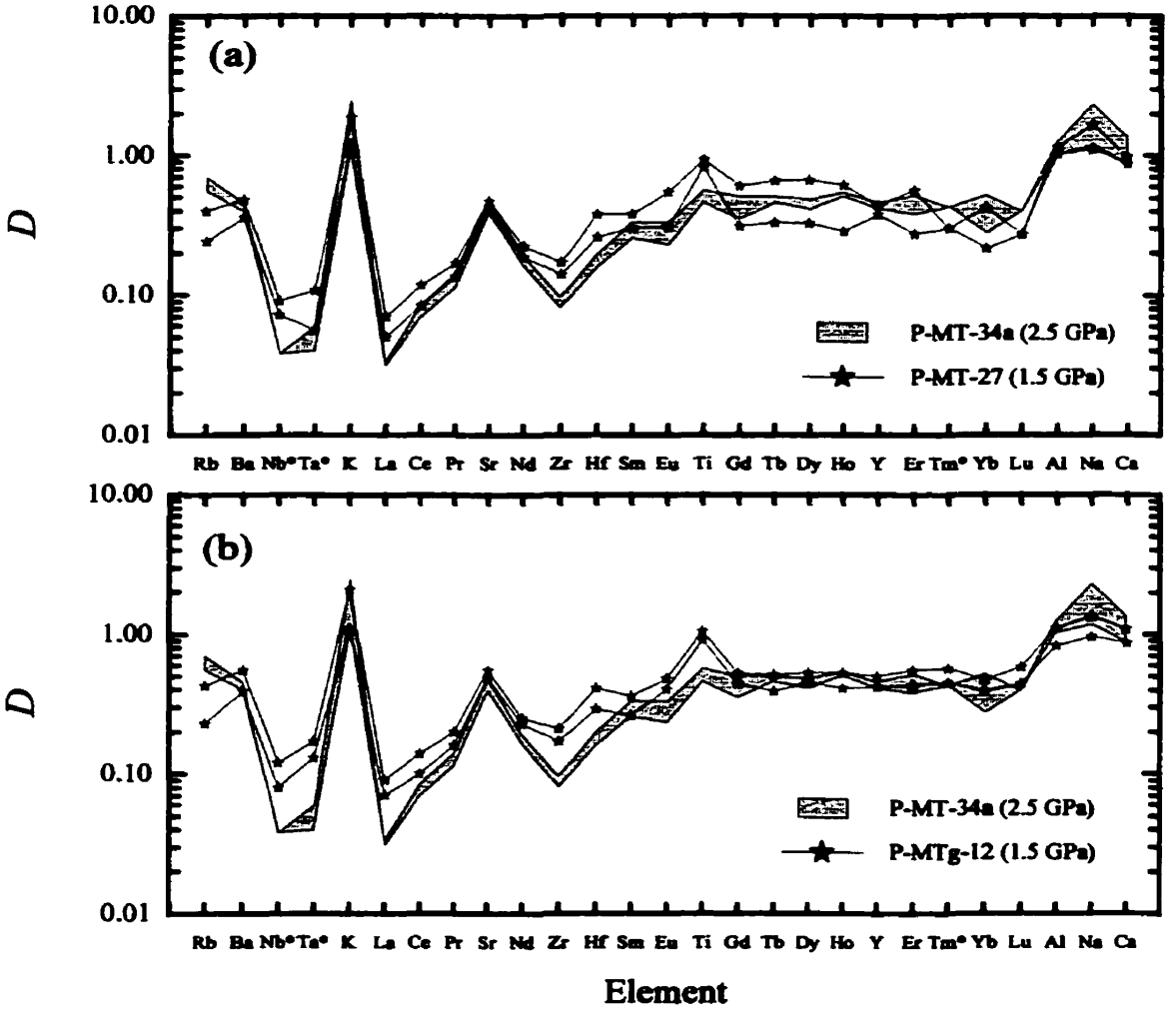
(a)
10.00
1.00
0.10
0.01
D
P-MT-34a (2.5 GPa)
P-MT-27 (1.5 GPa)
Rb Ba Nb* Ta* K La Ce Pr Sr Nd Zr Hf Sm Eu Ti Gd Tb Dy Ho Y Er Tm* Yb Lu Al Na Ca
(b)
10.00
1.00
0.10
0.01
D
P-MT-34a (2.5 GPa)
P-MTg-12 (1.5 GPa)
Rb Ba Nb* Ta* K La Ce Pr Sr Nd Zr Hf Sm Eu Ti Gd Tb Dy Ho Y Er Tm* Yb Lu Al Na Ca
Element

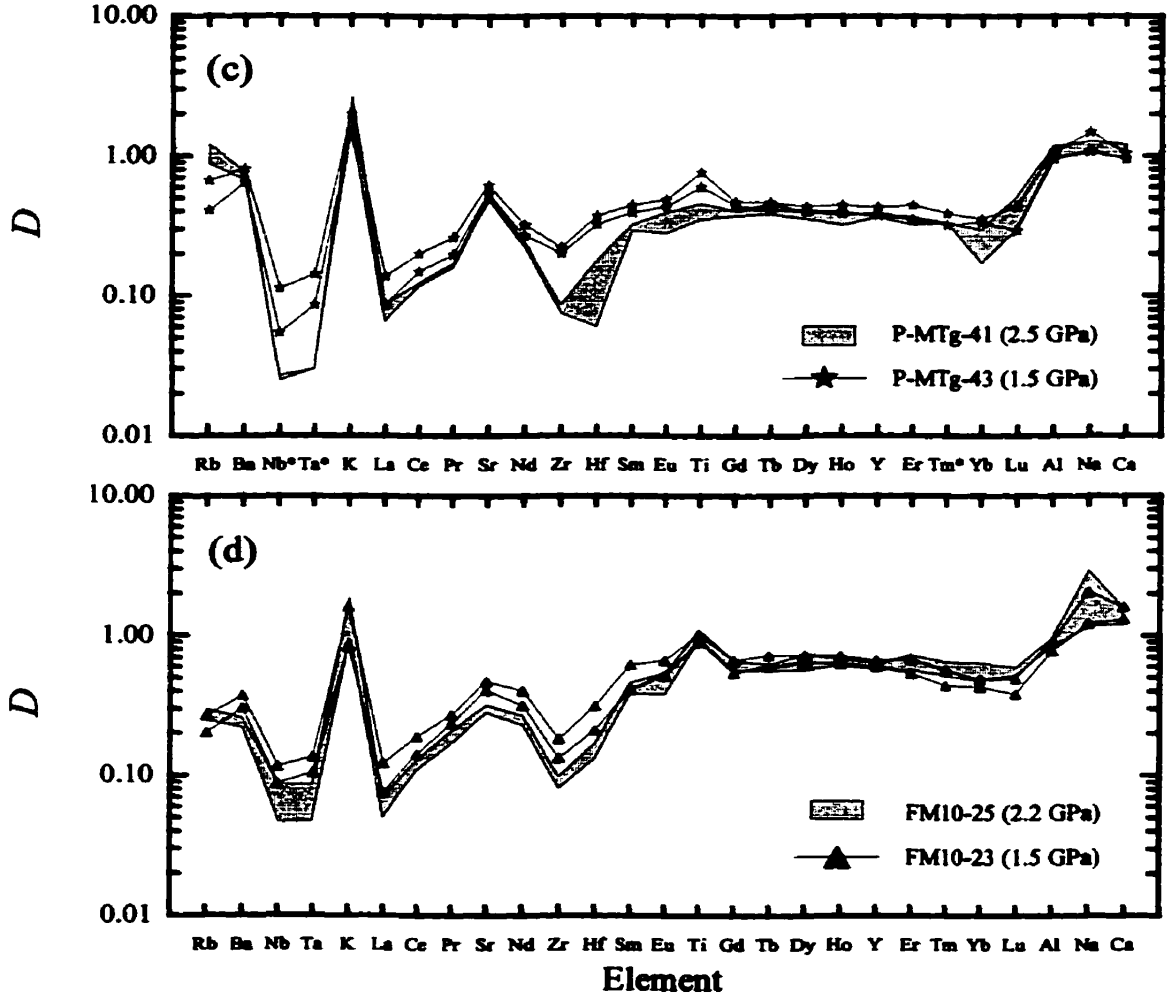
(c)
10.00
1.00
0.10
0.01
D
P-MTg-41 (2.5 GPa)
P-MTg-43 (1.5 GPa)
Rb Ba Nb* Ta* K La Ce Pr Sr Nd Zr Hf Sm Eu Ti Gd Tb Dy Ho Y Er Tm* Yb Lu Al Na Ca
(d)
10.00
1.00
0.10
0.01
D
FM10-25 (2.2 GPa)
FM10-23 (1.5 GPa)
Rb Ba Nb Ta K La Ce Pr Sr Nd Zr Hf Sm Eu Ti Gd Tb Dy Ho Y Er Tm Yb Lu Al Na Ca
Element

(*i.e.*, a range of 1.0 and 0.7 GPa, respectively; Table 3.3).

The negative relationships observed between D_{Sr}, D_{HFSE} (D_{Zr}, D_{Hf}, D_{Ti}), and D_{REE} (D_{Ho}) and pressure are similar to previous results of Adam and Green (1994) for D_{Sr}, D_{Ti}, D_{Ho} and of Fujinawa and Green (1997) for D_{Zr} and D_{Hf}. However, D_{Rb} shows an inverse relationship (*i.e.*, D_{Rb} increases with pressure, Figs. 4.1a, -b, -c) as opposed to other trace elements with increasing pressure for the P-MT and P-MTg experiments performed at both oxygen fugacitites. Adam *et al.* (1993) mentioned a similar behaviour of increasing D_{Rb} (~ 2-fold) with increasing pressure (*i.e.*, 1.0 to 2.0 GPa) for experiments performed at similar temperatures using an F-doped basanitic material (runs#: 1409 and 1388). The increase in D_{Rb} can also be observed when using the alkaline basalt material, but remains within one standard deviation (Fig. 4.1d). This could be the result of the smaller range of pressures used for the FM10 experiments (0.7 GPa) compared to the P-MT and P-MTg experiments (1.0 GPa).

A variation in the partition coefficient with increasing pressure can result from a change in the stability field of different phases (*e.g.*, olivine in the P-MT-27 and P-MTg-12 runs and ilmenite in the FM10-25 run; Table 3.3). Adam and Green (1994) mentioned that the continuing growth of REE-rich minerals (*e.g.*, garnet, apatite, allanite) after amphibole ceases to crystallize would impoverish the liquid in its REE content, thus producing apparently higher partition coefficients between amphibole and melt. They mentioned that such differences between their results and those from Green and Pearson (1985b) might be due to continuous growth of REE-bearing minerals in Green and Pearson's (1985b)

experiments at a lower pressure, producing a positive relationship between the *D*'s and pressure. For the experiments of this study the appearance of olivine in the P-MT-27 experiment can not account for a significant effect on amphibole-melt partitioning due to its small modal proportion (trace amount; Table 3.3) and to the low partition coefficients observed for many different trace elements (D_{LILE}, D_{HFSE}, $D_{REE} < \sim 10^{-2}$; Green 1994). For the FM10-25 experiments, amphibole and clinopyroxene finished crystallizing after ilmenite based on back-scattered electron images (all oxides are surrounded by a silicate mineral). However in an extreme case, it can be assumed that some ilmenite crystals may have completed their growth after amphibole ceased to crystallize, in which case, it could affect the Nb and Ta in the melt because D_{Nb} and D_{Ta} are close to 1 for the ilmenite-basalt pair whereas D_{Zr} and D_{Hf} are similar to those obtained between the amphibole and basaltic melt pair (Green 1994). By simple mass balance calculations using the mineral and melt modes of the FM10-25 experiment in Table 3.3 and assuming a $D_{Nb}^{ilmenite/basalt}$ of ~ 0.8 (McCallum and Charette 1978) and a $D_{Nb}^{clinopyroxene/basalt}$ of 0.01 (Adam *et al.* 1993; run#: 1389), a 1 modal % of late growth of ilmenite (extreme value in this case) in the FM10-25 experiment will represent ~ 1.9 % of the total Nb of the starting material which is relatively insignificant compared to ~ 90 and ~ 8 % of the total Nb stored in the melt and amphibole, respectively. Therefore the pressure effect appears to be the major factor modifying the partitioning between the amphibole and basaltic melt.

The variation in partition coefficients could be controlled by complex coupled substitution into specific sites, such as the CN/MTAF ratio (see Fig. 3.7). Variations of the

CN/MTAF ratio for amphibole in the P-MT experiments (*i.e.*, P-MT-27 *vs.* P-MT-34a, P-MTg-12 *vs.* P-MT-34a, and P-MTg-43 *vs.* P-MTg-41) and those for Adam and Green (1994; runs#: 1452, 1447, 1446, 1442) and Adam and Green (1993; runs#: 1395 and 1409) are small (Fig. 4.2) as opposed to the relatively large variation observed for amphibole in the FM10 experiments (*i.e.*, 0.344 to 0.550 for FM10-23 *vs.* FM10-25, respectively). Such a difference in the CN/MTAF ratio between the P-MT, P-MTg, and FM10 experiments seems to result in part from the proportion of the Fe_{total} and Mg cations in the *M*(1,2,3) sites as discussed above. The CN/MTAF ratio in amphibole for the FM10 experiments indicates a positive relationship with pressure while remaining practically constant for our P-MT and P-MTg experimental amphiboles and for those from Adam and Green (1994) and Adam *et al.*'s (1993) experiments. Furthermore, the CN/MTAF ratio seems to be unaffected by the oxygen fugacity of the experiment (compare P-MT and P-MTg experiments at the low and high fO_2).

Figure 4.3 shows a clear relationship between the partition coefficient of Zr as a function of the Ti/Al ratio observed in different amphibole run products with increasing pressure. Increasing pressure directly affects amphibole composition, modifying its partition coefficient. However, based on the relationship between D_{Zr} and the Ti/Al ratio obtained in these experiments, oxygen fugacity may possibly influence partitioning (compared to the P-MT and P-MTg experiments at the low fO_2 *vs.* the P-MTg experiments at the high fO_2), but the variations are within one standard deviation.

Figure 4.2. Variation of the CN/MTAF ratio of the amphibole run products as a function of the run pressure. Legend: P-MT-27, P-MTg-12, and P-MT-34a experiments (P-MT + P-MTg experiments at low fO_2); P-MTg-43 and P-MTg-41 experiments (P-MTg experiments at high fO_2); FM10-23 and FM10-25 experiments (FM10 experiments at high fO_2); runs# 1442, 1446, 1447, and 1452 from Adam and Green (1994) [AG (94)]; runs# 1395 and 1409 from Adam *et al.* (1993) [AGS (93)].

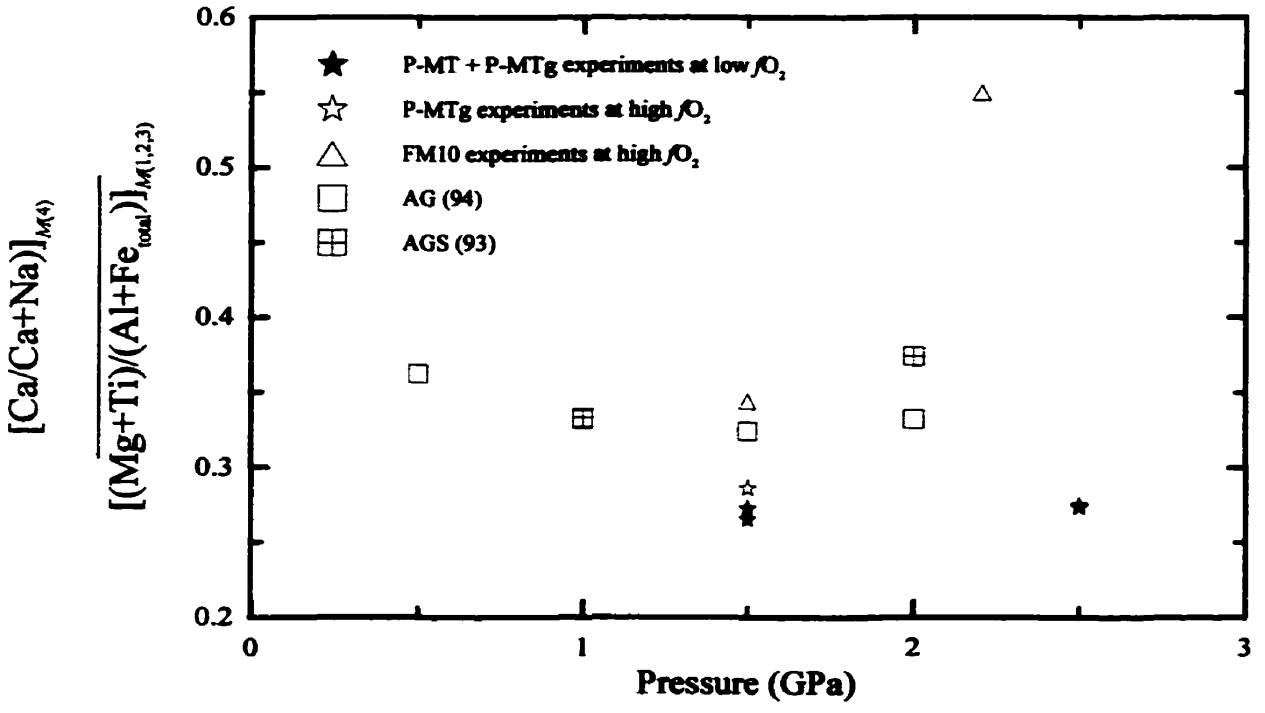
0.6
0.5
0.4
0.3
0.2
0
1
2
3
Pressure (GPa)
P-MT + P-MTg experiments at low fO_2
P-MTg experiments at high fO_2
FM10 experiments at high fO_2
AG (94)
AGS (93)
$[Ca/Ca+Na)]_{M(4)}$
$\overline{[(Mg+Ti)/(Al+Fe_{(total)})]}_{M(1,2,3)}$

Figure 4.3. Variation of D_{Zr} with the Ti/Al ratio in $M(1,2,3)$ octahedral sites of amphibole run products as a function of pressure. Legend: P-MT-27, P-MTg-12, and P-MT-34a experiments at low oxygen fugacity [P-MT, P-MTg (low fO_2)]; P-MTg-43 and P-MTg-41 experiments at high oxygen fugacity [P-MTg (high fO_2)]; FM10-23 and FM10-25 experiments at high oxygen fugacity [FM10 (high fO_2)]; runs# 1395 and 1409 from Adam *et al.* (1993) [AGS (93)]; runs# 1702, 1705, 1666, 1664, and 1707 from Fujinawa and Green (1997) [FG (97)]. Numbers denote: run pressure in GPa (*italic numbers* referred to other experimental studies). Field denotes: experiments from this study at 1.5 and 2.2-2.5 GPa.

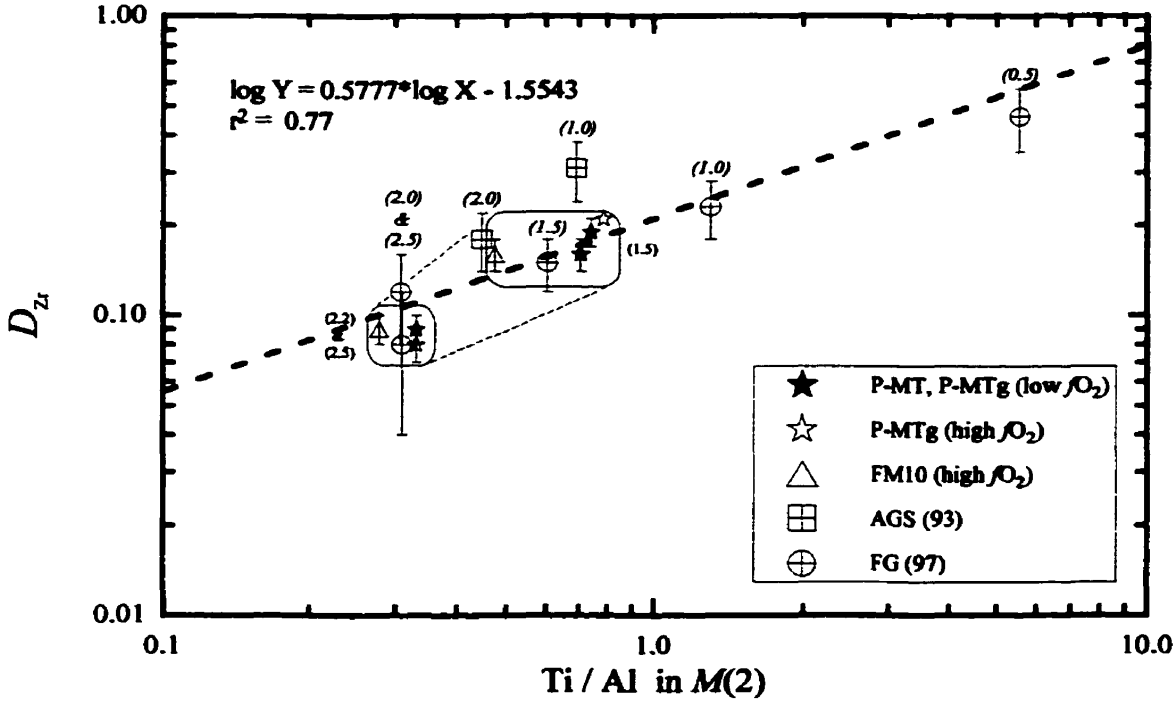
log Y = 0.5777*log X - 1.5543
r² = 0.77
1.00
0.10
0.01
0.1
1.0
10.0
D_Zr
Ti / Al in M(2)
(0.5)
(1.0)
(1.0)
(2.0)
(2.0)
(2.5)
(1.5)
(1.5)
(2.2)
(2.5)
P-MT, P-MTg (low fO2)
P-MTg (high fO2)
FM10 (high fO2)
AGS (93)
FG (97)

4.1.5. The effect of oxygen fugacity on partition coefficients at a fixed pressure

Figure 4.4 shows the effect of oxygen fugacity on partition coefficients for four different pairs of experiments (*i.e.*, P-MT-27 *vs.* P-MTg-43, P-MTg-12 *vs.* P-MTg-43, P-MT-34a *vs.* P-MTg-41, and FM10-02 *vs.* FM10-23). For experiments performed at lower pressures using the pargasite materials (*i.e.*, P-MT-27 *vs.* P-MTg-43 and P-MTg-12 *vs.* P-MTg-43), D_{LILE} (D_{Ba}) and D_{REE} (D_{Ce}, D_{Nd}, D_{Sm}) increase while D_{Ti} decreases with increasing oxygen fugacity (Figs. 4.4a, -b and Table 3.10). Also, increases in D_{LILE} (D_{Rb}, D_{Sr}), D_{HFSE} (D_{Zr}), and D_{REE} (D_{La}, D_{Pr}, D_{Tm}, D_{Lu}) for the P-MT-27 *vs.* P-MTg-43 experiments were observed as oxygen fugacity increased (Fig. 4.4a). Similar variations were observed for experiments performed at 1.5 GPa using the alkaline basalt material (*i.e.*, FM10-02 *vs.* FM10-23; Fig. 4.4c) where D_{LILE} (D_{Ba}, D_{Sr}), D_{Y}, and D_{REE} (D_{Pr}, D_{Sm}, D_{Eu}, D_{Gd}, D_{Tb}, D_{Dy}, D_{Ho}, D_{Er}) increase whereas D_{HFSE} (D_{Nb}, D_{Ta}, D_{Zr}, D_{Hf}, D_{Ti}) decreases with increasing oxygen fugacity.

For experiments performed at a higher pressure (*i.e.*, P-MT-34a *vs.* P-MTg-41), D_{LILE} (D_{Rb}, D_{Ba}) and D_{REE} (D_{La}, D_{Ce}, D_{Pr}, D_{Nd}) increase while D_{HFSE} (D_{Ta}, D_{Ti}, D_{Y}) and D_{REE} (D_{Tb}, D_{Dy}, D_{Ho}, D_{Er}) decrease with increasing oxygen fugacity. For the different pargasite experiments performed at both low and high pressures (Figs. 4.4a, -b, -c), identical behaviours were observed with increasing oxygen fugacity whereas D_{Rb}, D_{Ba}, and D_{LREE} (D_{Ce}, D_{Nd}) increase while D_{Ti} decreases. For experiments using the alkaline basalt (*i.e.*, FM10-02 *vs.* FM10-23), D_{LILE} (D_{Ba}, D_{Sr}), D_{Y}, D_{REE} (D_{Pr}, D_{Nd}, D_{Sm}, D_{Eu}, D_{Gd}, D_{Tb}, D_{Dy}, D_{Ho}, D_{Er}), and D_{K}, D_{Na}, D_{Ca} increase with increasing oxygen fugacity while D_{HFSE} (D_{Nb}, D_{Ta}, D_{Zr}, D_{Hf}, D_{Ti}) and D_{Al} decreases (Fig. 4.4c).

Figure 4.4. The effect of oxygen fugacity on partition coefficients at different run pressures. (a), (b), and (c) 1.5 GPa. (d) 2.5 GPa. Same legend as in Figure 4.1.

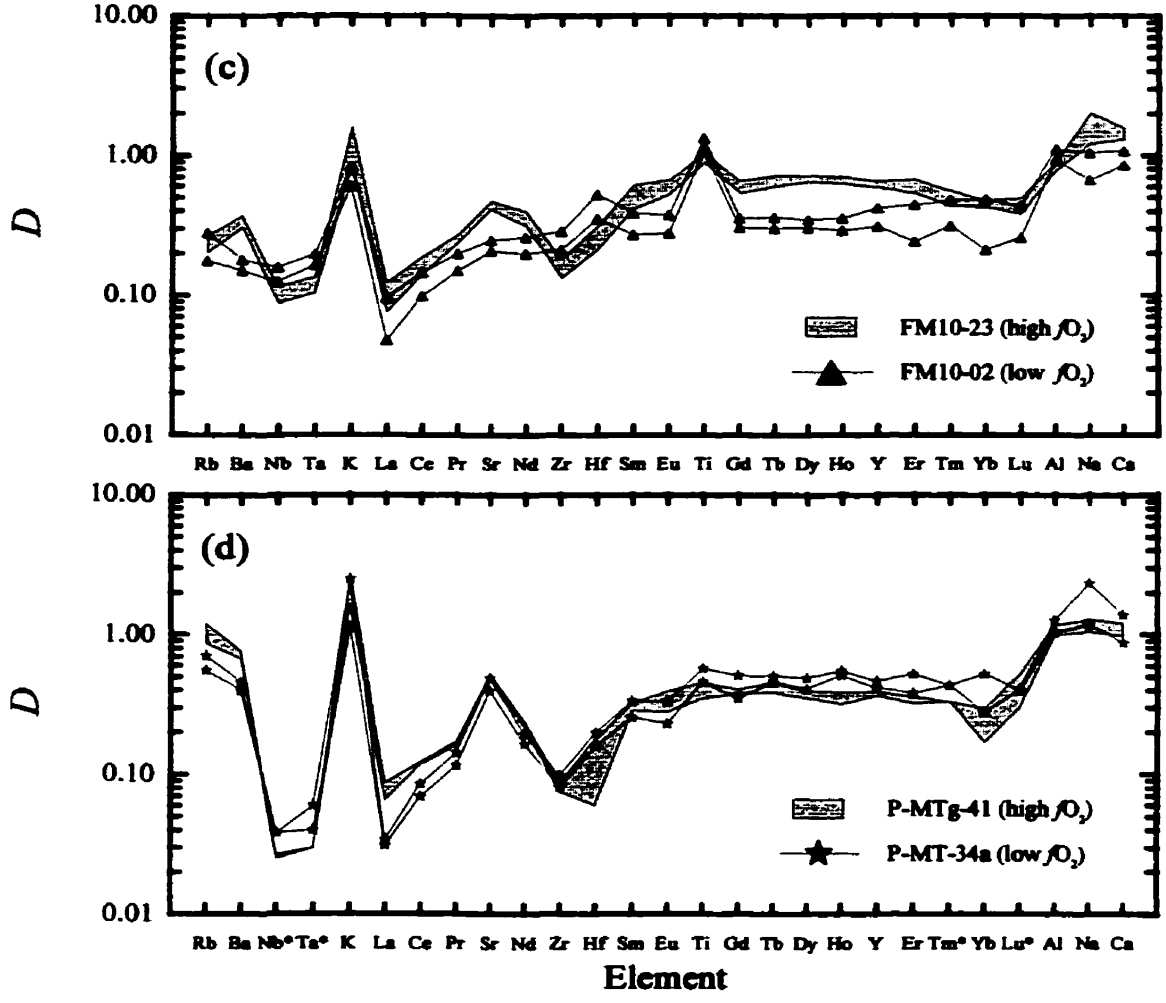
(c)
10.00
1.00
0.10
0.01
D
FM10-23 (high fO_2)
FM10-02 (low fO_2)
Rb Ba Nb Ta K La Ce Pr Sr Nd Zr Hf Sm Eu Ti Gd Tb Dy Ho Y Er Tm Yb Lu Al Na Ca
(d)
10.00
1.00
0.10
0.01
D
P-MTg-41 (high fO_2)
P-MT-34a (low fO_2)
Rb Ba Nb* Ta* K La Ce Pr Sr Nd Zr Hf Sm Eu Ti Gd Tb Dy Ho Y Er Tm* Yb Lu* Al Na Ca
Element

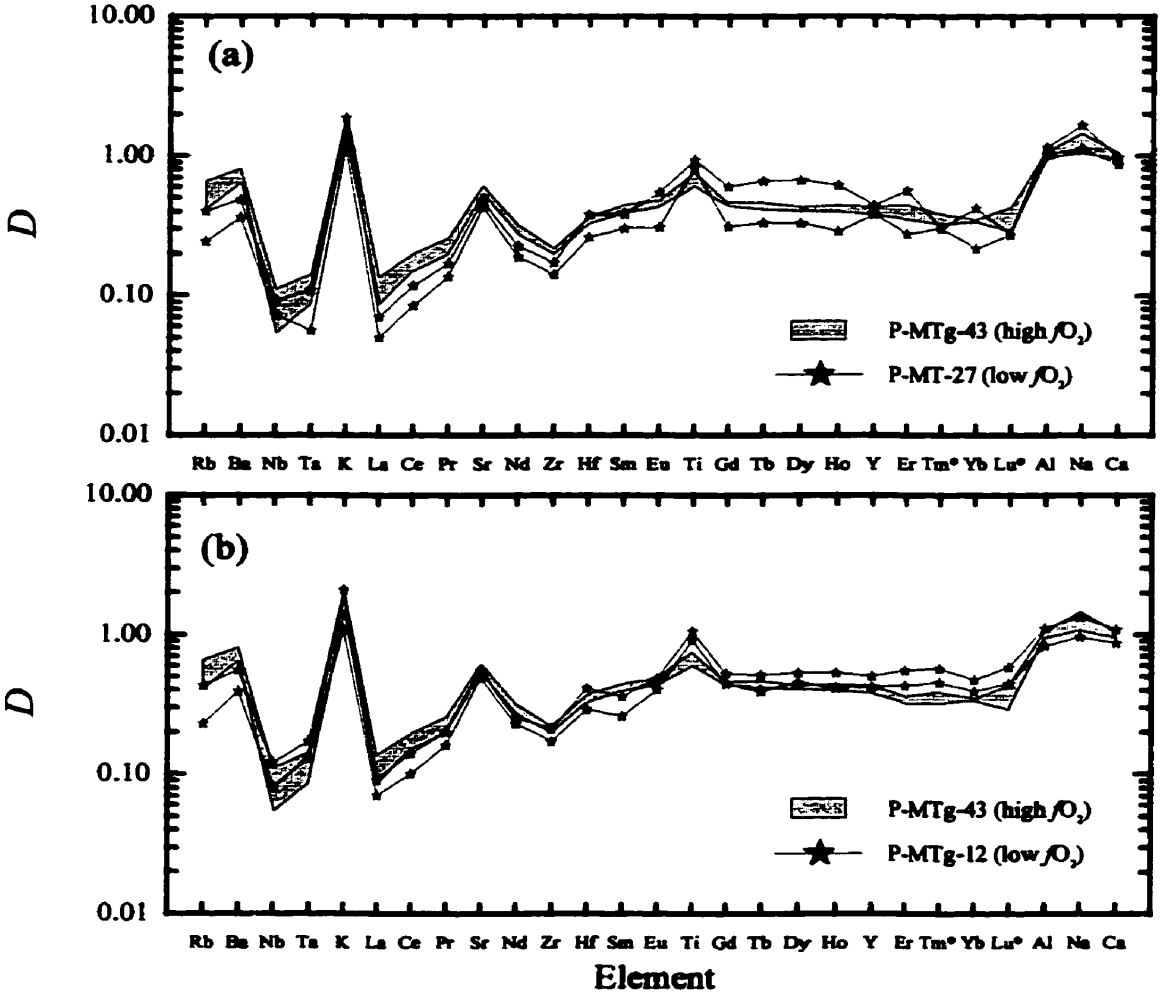
10.00
1.00
0.10
0.01
D
(a)
P-MTg-43 (high fO_2)
P-MT-27 (low fO_2)
Rb Ba Nb Ta K La Ce Pr Sr Nd Zr Hf Sm Eu Ti Gd Tb Dy Ho Y Er Tm* Yb Lu* Al Na Ca
10.00
1.00
0.10
0.01
D
(b)
P-MTg-43 (high fO_2)
P-MTg-12 (low fO_2)
Rb Ba Nb Ta K La Ce Pr Sr Nd Zr Hf Sm Eu Ti Gd Tb Dy Ho Y Er Tm* Yb Lu* Al Na Ca
Element

Comparing the four different pairs of experiments demonstrates identical behaviours for D_{Ba} and D_{Nd} which both increase whereas D_{Ti} decreases with increasing oxygen fugacity. Such observations were not noted in previous experimental studies on partitioning between amphibole and silicate melt. Green and Pearson (1985a) observed a decrease in D_{REE} between amphibole and andesitic melt as the oxygen fugacity increased from the magnetite-wüstite to the hematite-magnetite buffers for experiments performed at 0.75 GPa. However, these variations were within one standard deviation of the partition coefficients.

Figure 4.5 shows variations in partition coefficients for some LILE (Rb, Ba), HFSE (Ti, Zr, Hf), and REE (La, Nd) observed in our experiments as a function of oxygen fugacity at constant pressure. The increase in D_{Rb} for the P-MT and P-MTg experiments as a function of oxygen fugacity is similar at both low and high pressures (*i.e.*, 0.32 to 0.54 and 0.63 to 1.04 for P-MT-27 *vs.* P-MTg-43 and P-MT-34a *vs.* P-MTg-41, respectively; Fig. 4.4a and Table 3.10). However, it appears that a 1.0 GPa pressure increase has a greater positive effect on D_{Rb} (~ 97 %) than an ~ 3 log unit increase in oxygen fugacity (~ 65 to 69 % increase) for the P-MT and P-MTg experiments (Table 3.10). Furthermore, at 2.5 GPa, Rb changes from an incompatible element at low fO_2 (D_{Rb} <1) to a compatible element (D_{Rb} >1) at high fO_2. Variations in D_{Rb} were within one standard deviation as pressure or oxygen fugacity was increased for the FM10 experiments (Fig. 4.5a). Pressure does not have a significant effect on the partition coefficient of Ba in either starting composition. The observed variations are within one standard deviation for the P-MT and P-MTg experiments at different pressures while D_{Ba} changes considerably between the NNO-2 to the NNO+1.7

Figure 4.5. Variations of partition coefficients plotted against oxygen fugacity for the P-MT, P-MTg, and FM10 experiments performed at the low (1.5 GPa) and high (2.2 and 2.5 GPa) pressures. (a) Rb. (b) Ba. (c) Ti. (d) Hf. (e) Zr. (f) La. (g) Nd.

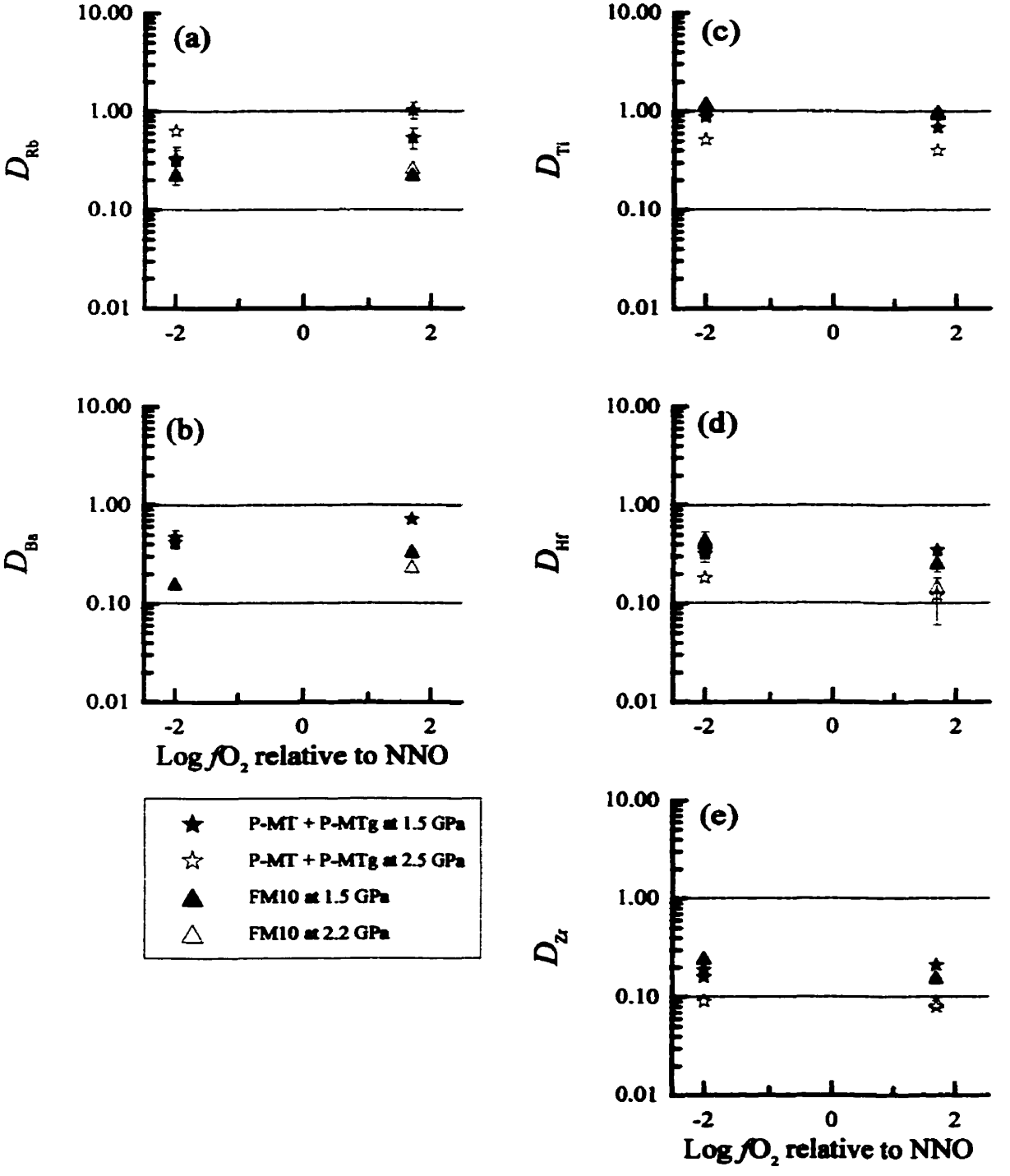
(a)
(b)
(c)
(d)
(e)
D_{Rb}
D_{Ba}
D_{Ti}
D_{Hf}
D_{Zr}
10.00
1.00
0.10
0.01
-2
0
2
Log fO_2 relative to NNO
P-MT + P-MTg at 1.5 GPa
P-MT + P-MTg at 2.5 GPa
FM10 at 1.5 GPa
FM10 at 2.2 GPa

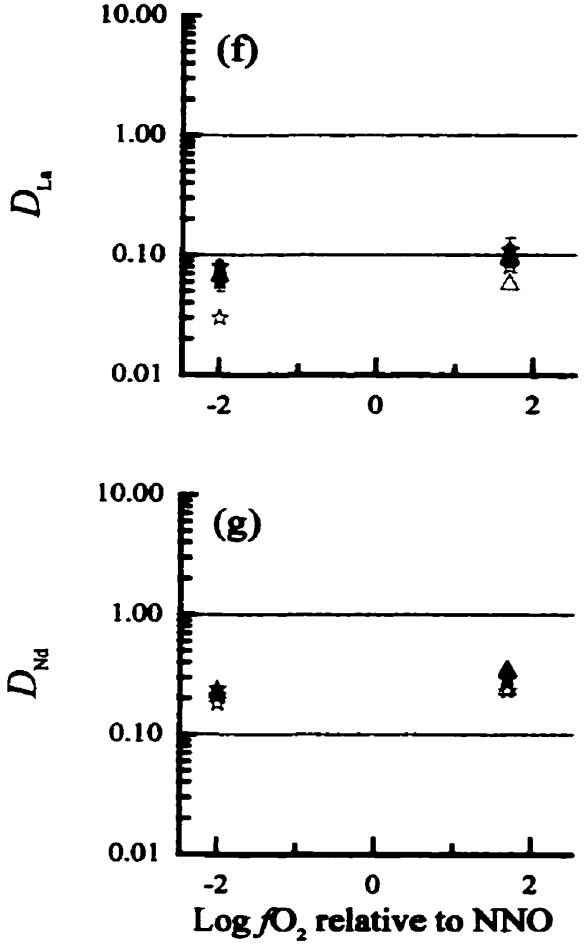
10.00
(f)
1.00
D_{La}
0.10
0.01
-2
0
2
10.00
(g)
1.00
D_{Nd}
0.10
0.01
-2
0
2
Log fO_2 relative to NNO

buffers (*i.e.*, 0.42 to 0.72 and 0.16 to 0.34 for P-MT-27 *vs.* P-MTg-43 and FM10-02 *vs.* FM10-23, respectively; Fig. 4.5b and Table 3.10).

A positive relationship between some D_{LILE}'s and oxygen fugacity (Figs. 4.5a, -b) seems to be opposite to the relationship for some D_{HFSE}'s (Figs. 4.5c, -d, -e) but similar to that for some D_{REE}'s (Figs. 4.5f, -g). A decrease in D_{Ti} was observed as oxygen fugacity and pressure increased for P-MT and P-MTg experiments (Fig. 4.5c). However, increasing pressure has a greater negative effect on D_{Ti} (~ 41 %) than increasing oxygen fugacity (~ 22 %) for the P-MT and P-MTg experiments (Table 3.10). For the FM10 experiments the oxygen fugacity modifies D_{Ti} whereas pressure has no observable effect (*i.e.*, variation is within the standard deviations). Furthermore, the partition coefficient of Ti shows a transition from compatible to incompatible behaviour at 1.5 GPa as oxygen fugacity increases from NNO-2 to NNO+1.7 (Fig. 4.5c).

The observed effect of pressure on D_{Hf} is greater (~ 44 to 66 % of decrease) than that of the increase in oxygen fugacity (the variation is within the standard deviations) for P-MT and P-MTg experiments while pressure and oxygen fugacity have similar negative effects (~ 41 %) for D_{Hf} using the FM10 material (Fig. 4.5d and Table 3.10). Similar variations were observed for D_{Zr} (Fig. 4.5e). For D_{La} measured between amphibole and basaltic melt in P-MT and P-MTg experiments, I observed a greater relative variation for the increase in the oxygen fugacity (~ 83 to 166 % increase) compared to the increase in pressure (~ 27 to 50 % decrease) (Fig. 4.5f and Table 3.10). However, similar variations were observed for D_{La} in FM10 experiments when pressure increased (~ 40 % decrease in D_{La}) as when oxygen

fugacity increased (~ 43 % increase in D_{La}). Finally, D_{Nd} shows a similar but inverse behaviour as pressure and oxygen fugacity increase. The increasing of the oxygen fugacity has a relatively greater effect (~ 28 to 38 % increase in D_{Nd}) than the pressure effect (~ 14 to 21 % decrease in D_{Nd}) using the P-MT and P-MTg materials (Fig. 4.5g). The variation of D_{Nd} for the FM10 experiments show a similar behaviour as oxygen fugacity (~ 56 % increase) or pressure (~ 31 % decrease) increase.

In summary, increasing pressure may affect positively the partition coefficient of a monovalent cation such as Rb (LILE) or negatively a divalent cation such as Ba (LILE) and other trace elements such as Ti^{4+}, Hf^{4+}, and Zr^{4+} (HFSE) and La^{3+} and Nd^{3+} (REE). For the fO_2, increasing the oxygen fugacity from NNO-2 to NNO+1.7 positively affects the partition coefficient of Rb and Ba (LILE), La and Nd (REE) while it affects negatively Ti, Hf, and Zr (HFSE). However, all of these effects are small for the amphiboles and melts produced in this study.

4.2 Variations of the amphibole lattice-site parameters as a function of the pressure and oxygen fugacity

In order to investigate further the role of pressure and oxygen fugacity on amphibole partitioning, D_o, $\bar{E}$, and r_o were calculated for three lattice-sites [A, $M(4)$, $M(2)$] using partition coefficients measured in experiments performed at a fixed oxygen fugacity and at a fixed pressure, respectively.

4.2.1. Role of pressure

Figure 4.6 shows the variations in partition coefficients as a function of pressure for which a non-linear least-squares regression fit was obtained for each experiment using Eq. (3). Table 4.1 shows the results calculated for the different lattice-sites.

An increase in pressure affects at least three lattice-sites of the amphibole structure as can be seen by the different unconstrained regressions (Fig. 4.6 and Table 4.1). The relatively large variations observed in D_o and $\bar{E}$ can not result from run temperature variations as shown previously (see Fig. 3.9c) but result from pressure variations. In general, the calculated Young's modulus decreases for the three lattice-sites with increasing pressure from 1.5 to 2.2 or 2.5 GPa (Fig. 4.6 and Table 4.1). However, those $\bar{E}$ values are within variations calculated from standard deviation attached to partitioning (Table 4.1). This behaviour indicates that the mechanical strain energy around a substitute, homovalent cation in the amphibole decreases as pressure increases [see Eq. (2)], which might suggest that partitioning becomes more favourable. In this case, the parabolae become wider (*e.g.*, the *A* site; Figs. 4.6a, -c). However, this is not true for all the lattice-sites mentioned where the maximum partition coefficient (*i.e.*, D_o) also plays a major role in the determination of partitioning behaviour. The D_o is directly related to the overall behaviour of an isovalent cation group which substitutes into a given lattice-site [*e.g.*, a decrease in D_{REE} and D_Y will automatically decrease D_o^{3+} of the *M*(4) site]. Furthermore, as can be seen in Table 4.1, D_o also decreases as pressure increases (with the exception of the *A* site for FM10 experiments). This implies that partitioning decreases unlike what is predicted by the behaviour of $\bar{E}$. The

Figure 4.6. Variations of partition coefficients as a function of ionic radius at different pressures. (a) and (b) Low oxygen fugacity experiments using P-MT and P-MTg materials (~NNO-2). (c) and (d) High oxygen fugacity experiments using P-MTg and FM10 materials (~NNO+1.7). Symbols denote regression based on partition coefficients obtained for the low pressure experiments (filled line); regression based on partition coefficients obtained for the high pressure experiments (small dashed line); r_o's regressed from P-MT-27 experiment (vertical thick dashed line; see Table 3.10).

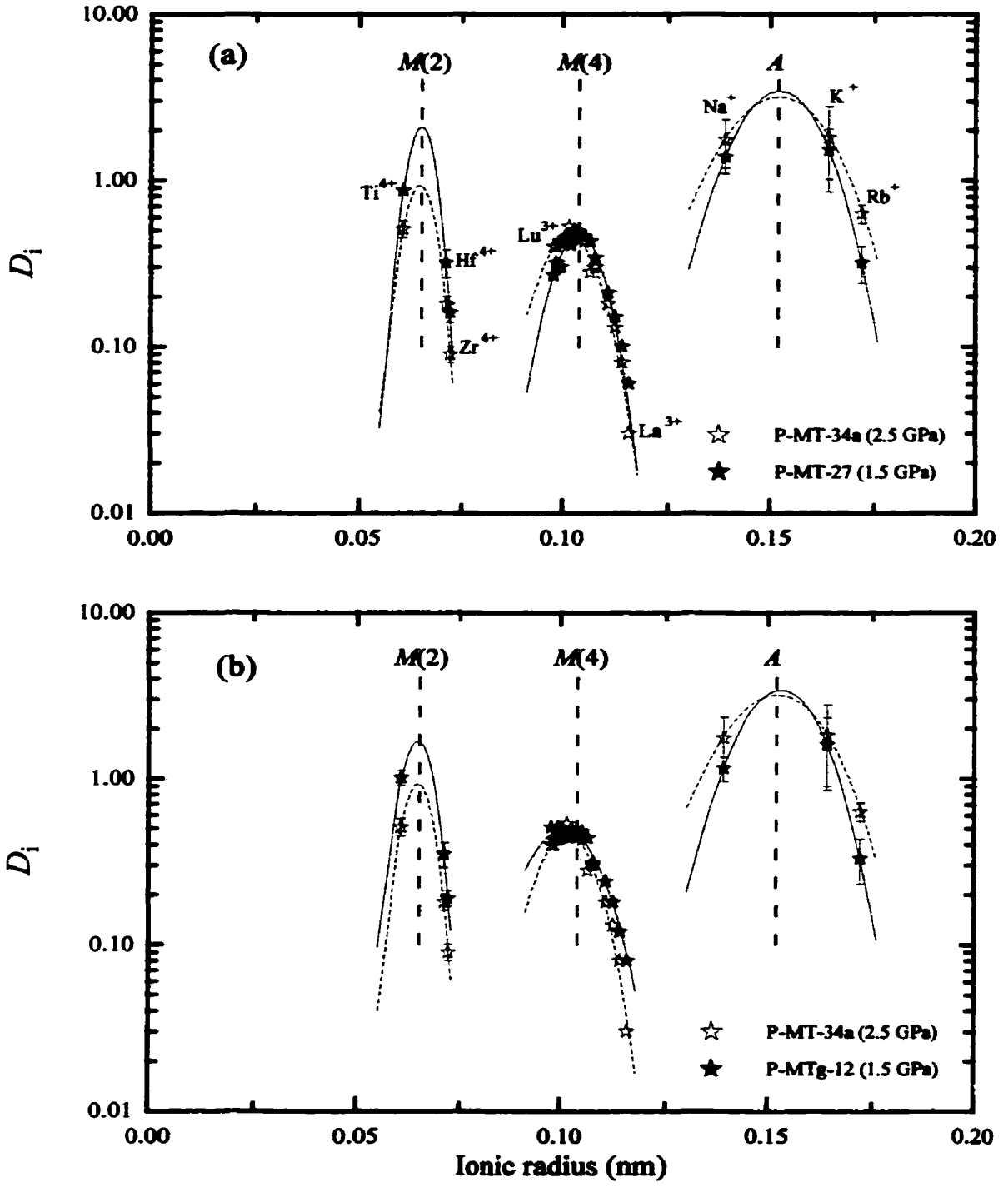
(a)
M(2)
M(4)
A
Ti4+
Hf4+
Zr4+
Lu3+
La3+
Na+
K+
Rb+
P-MT-34a (2.5 GPa)
P-MT-27 (1.5 GPa)
(b)
P-MT-34a (2.5 GPa)
P-MTg-12 (1.5 GPa)
Di
Ionic radius (nm)
10.00
1.00
0.10
0.01
0.00
0.05
0.10
0.15
0.20

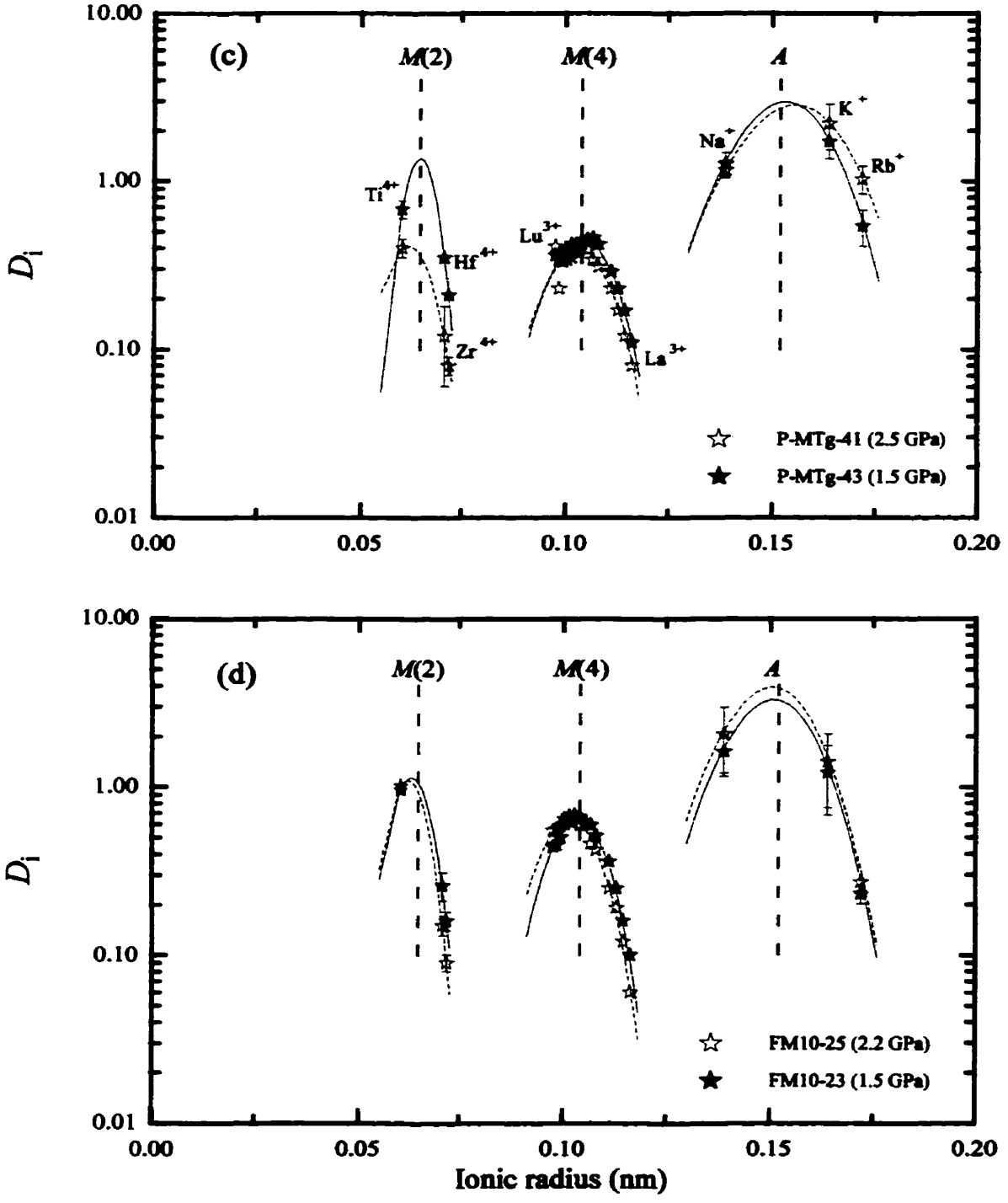
(c)
M(2)
M(4)
A
Ti4+
Hf4+
Zr4+
Lu3+
La3+
Na+
K+
Rb+
P-MTg-41 (2.5 GPa)
P-MTg-43 (1.5 GPa)
(d)
FM10-25 (2.2 GPa)
FM10-23 (1.5 GPa)
Di
Ionic radius (nm)
10.00
1.00
0.10
0.01
0.00
0.05
0.10
0.15
0.20

Table 4.1. Calculated lattice-site parameters (unconstrained) for experiments performed at different pressures and oxygen fugacities

run #	P (GPa)	fO_2 buffer	Site[a]	D_o	$\bar{E}$ (GPa)	r_o (nm)
			At a fixed oxygen fugacity			
P-MT-27	1.5	low	*A*	3.44 (0.78)	110.43 (0.73)	0.152[a]
			M(4)	0.48 (0.14)	445.44 (134.1)	0.104
			M(2)	2.10 (0.97)	2213.58 (562.4)	0.065
vs.						
P-MT-34$_a$	2.5	low	*A*	3.18 (1.64)	71.32 (22.4)	0.152 (0.001)
			M(4)	0.47 (0.05)	325.15 (16.2)	0.102
			M(2)	0.93 (0.41)	1711.53 (406.5)	0.065
P-MTg-12	1.5	low	*A*	3.40 (1.06)	117.01 (10.6)	0.153 (0.001)
			M(4)	0.50 (0.06)	207.56 (9.44)	0.101
			M(2)	1.68 (1.11)	1649.20 (684.8)	0.065 (0.001)
vs.						
P-MT-34$_a$	2.5	low	*A*	3.18 (1.64)	71.32 (22.4)	0.152 (0.001)
			M(4)	0.47 (0.05)	325.15 (16.2)	0.102
			M(2)	0.93 (0.41)	1711.53 (406.5)	0.065
P-MTg-43	1.5	high	*A*	2.96 (0.34)	84.60 (9.3)	0.153
			M(4)	0.45 (0.02)	252.71 (53.07)	0.104
			M(2)	1.37 (0.20)	1601.47 (78.57)	0.065
vs.						
P-MTg-41	2.5	high	*A*	2.84 (0.79)	66.47 (12.77)	0.156 (0.001)
			M(4)	0.38 (0.03)	243.09 (49.43)	0.103 (0.001)
			M(2)	0.49 (0.41)	1027.06 (805.37)	0.063 (0.002)
FM10-23	1.5	high	*A*	3.28 (1.26)	100.23 (15.20)	0.151 (0.001)
			M(4)	0.66 (0.06)	322.83 (13.47)	0.104
			M(2)	1.13 (0.26)	1012.56 (204.54)	0.063 (0.001)
vs.						
FM10-25	2.2	high	*A*	3.90 (0.99)	97.11 (15.31)	0.150 (0.001)
			M(4)	0.64 (0.07)	284.2 (9.40)	0.102
			M(2)	1.10 (0.17)	1092.09 (144.21)	0.062 (0.001)

Table 4.1. (continued)

run #	P (GPa)	fO_2 buffer	Site[a]	D_o	$\bar{E}$ (GPa)	r_o (nm)
			At a fixed pressure			
P-MT-27	1.5	low	*A*	3.44 (0.78)	110.43 (0.73)	0.152
			M(4)	0.48 (0.14)	445.44 (134.1)	0.104
			M(2)	2.10 (0.97)	2213.58 (562.4)	0.065
vs.						
P-MTg-43	1.5	high	*A*	2.96 (0.34)	84.60 (9.3)	0.153
			M(4)	0.45 (0.02)	252.71 (53.07)	0.104
			M(2)	1.37 (0.20)	1601.47 (78.57)	0.065
P-MTg-12	1.5	low	*A*	3.40 (1.06)	117.01 (10.6)	0.153 (0.001)
			M(4)	0.50 (0.06)	207.56 (9.44)	0.101
			M(2)	1.68 (1.11)	1649.20 (684.8)	0.065 (0.001)
vs.						
P-MTg-43	1.5	high	*A*	2.96 (0.34)	84.60 (9.3)	0.153
			M(4)	0.45 (0.02)	252.71 (53.07)	0.104
			M(2)	1.37 (0.20)	1601.47 (78.57)	0.065
FM10-02	1.5	low	*A*	1.39 (0.21)	70.51 (8.59)	0.151 (0.001)
			M(4)	0.36 (0.08)	155.53 (91.47)	0.101 (0.003)
			M(2)	2.20 (0.53)	1658.64 (218.74)	0.065 (0.001)
vs.						
FM10-23	1.5	high	*A*	3.28 (1.26)	100.23 (15.20)	0.151 (0.001)
			M(4)	0.66 (0.06)	322.83 (13.47)	0.104
			M(2)	1.13 (0.26)	1012.56 (204.54)	0.063 (0.001)
P-MT-34$_g$	2.5	low	*A*	3.18 (1.64)	71.32 (22.4)	0.152 (0.001)
			M(4)	0.47 (0.05)	325.15 (16.2)	0.102
			M(2)	0.93 (0.41)	1711.53 (406.5)	0.065
vs.						
P-MTg-41	2.5	high	*A*	2.84 (0.79)	66.47 (12.77)	0.156 (0.001)
			M(4)	0.38 (0.03)	243.09 (49.43)	0.103 (0.001)
			M(2)	0.49 (0.41)	1027.06 (805.37)	0.063 (0.002)

Abbreviations: D_o-maximum partition coefficient, $\bar{E}$-Young's modulus, r_o-optimum ionic radius. [a] Calculated lattice-site parameters using D_{Na}, D_K, and D_{Rb} for the *A* site, D_{REE} (D_{La} up to D_{Lu}) and D_Y for the *M*(4) site, and D_{Ti}, D_{Hf}, and D_{Zr} for the *M*(2) site. The parameters were calculated using Eq. (3) (see text). Values in parentheses represent the maximum variation calculated for each unconstrained lattice-site parameters using one standard deviation (*i.e.*, $D + 1\sigma$ and $D - 1\sigma$) attached to each partition coefficient in Table 3.10. [a] Optimum ionic radius which does not have parentheses imply the absence of significant calculated variations.

decrease of $\bar{E}$ for the majority of the different lattice sites with increasing pressure also suggests that cations with radii far from r_o of a specific isovalent parabola are relatively more affected by pressure than those closer to the optimum ionic radii. This relationship was found to be more complicated than that regarding the relative variations in D's and more experiments, which encompass a larger pressure range, are needed to prove this hypothesis. However D_{Rb}, which has ionic radius far from the r_o value for the A site, increases more rapidly than D_{Na} and D_K with increasing pressure, thus producing a lower calculated Young's modulus (parabola becomes wider) with increasing pressure (Fig. 4.6). This observation of the behaviour of D_{Rb} is particularly interesting since it has never been reported that increasing pressure increases partitioning of one set of elements which substitute into the large cavity of the A site (*e.g.*, D_{Na}, D_K, and D_{Rb}) whereas for other lattice-sites partitioning decreases [*e.g.*, D_{LREE} in the $M(4)$ and D_{HFSE} in the $M(2)$ lattice-sites] with increasing pressure for the same amphibole / basaltic melt pair.

Based on compressibility experiments of a natural pargasite crystal, Comodi *et al.* (1991) observed a weak decrease in the different mean bond-lengths (*e.g.*, $\langle A\text{-O}\rangle$, $\langle M(4)\text{-O}\rangle$, and $\langle M(2)\text{-O}\rangle$), which are indirectly related to the optimum ionic radius, with increasing pressure (0.0001 to 3.5 GPa). In these experiments it is difficult to generalize the effect of pressure on the size of the sites. However the r_o of the A and $M(2)$ lattice-sites are, in general, higher in amphiboles produced from P-MT and P-MTg compared to amphiboles synthesized from FM10, whereas the r_o of the $M(4)$ site is practically identical in both sets of amphiboles. These relative differences can be observed by the location of the fixed optimum

ionic radii used from the P-MT-27 experiment (compare Figs. 4.6a, -b, -c, -d). Such relative displacements of the optimum ionic radii in the FM10 experiments were caused by the relatively higher D_{Na} (smaller cation) compared to D_K and D_{Rb} (larger cations) in the A site and a higher D_{Ti} (smaller cation) compared to D_{Hf} and D_{Zr} (larger cations) in the $M(2)$ site as opposed to the P-MT and P-MTg experiments. The relationship between the optimum ionic radius and the mean bond-length suggests that amphiboles which crystallized from the FM10 material have lower $\langle A\text{-O}\rangle$ and $\langle M(2)\text{-O}\rangle$ mean bond-lengths than those crystallized from P-MTg material at an identical pressure (1.5 GPa) at high fO_2 (Figs. 4.6c, -d). This is consistent with the higher proportion of large cations observed in the $M(2)$ and A sites, $Ti_{M(1,2,3)}$ and K_A, for amphiboles crystallized in P-MTg-43 and P-MTg-41 compared to those crystallized in FM10-23 and FM10-25 experiments performed at identical or similar run conditions (Table 5). However those variations in r_o are within errors calculated from partitioning and, in such a case, only detailed compressibility measurements may answer these trends.

4.2.2. Role of oxygen fugacity

Figure 4.7 shows the variations in partition coefficients as a function of the oxygen fugacity and Table 4.1 shows the results calculated for the different lattice sites at a fixed pressure. A change in oxygen fugacity affects at least three lattice-sites in the amphibole structure, similar to the pressure effects. Again, the relatively large variations observed in partitioning at a fixed run pressure can not be due to the variations in the run temperature but are mainly affected by the oxygen fugacity in the experiment. Increasing the oxygen fugacity

Figure 4.7. Variations of partition coefficients as a function of ionic radius at different oxygen fugacities. (a), (b) and (c) Low pressure experiments (1.5 GPa). (d) High pressure experiments (2.5 GPa). Symbols denote regression based on partition coefficients obtained for the low oxygen fugacity experiments (filled line); regression based on partition coefficients obtained for the high oxygen fugacity experiments (small dashed line); r_o (see Fig. 4.6).

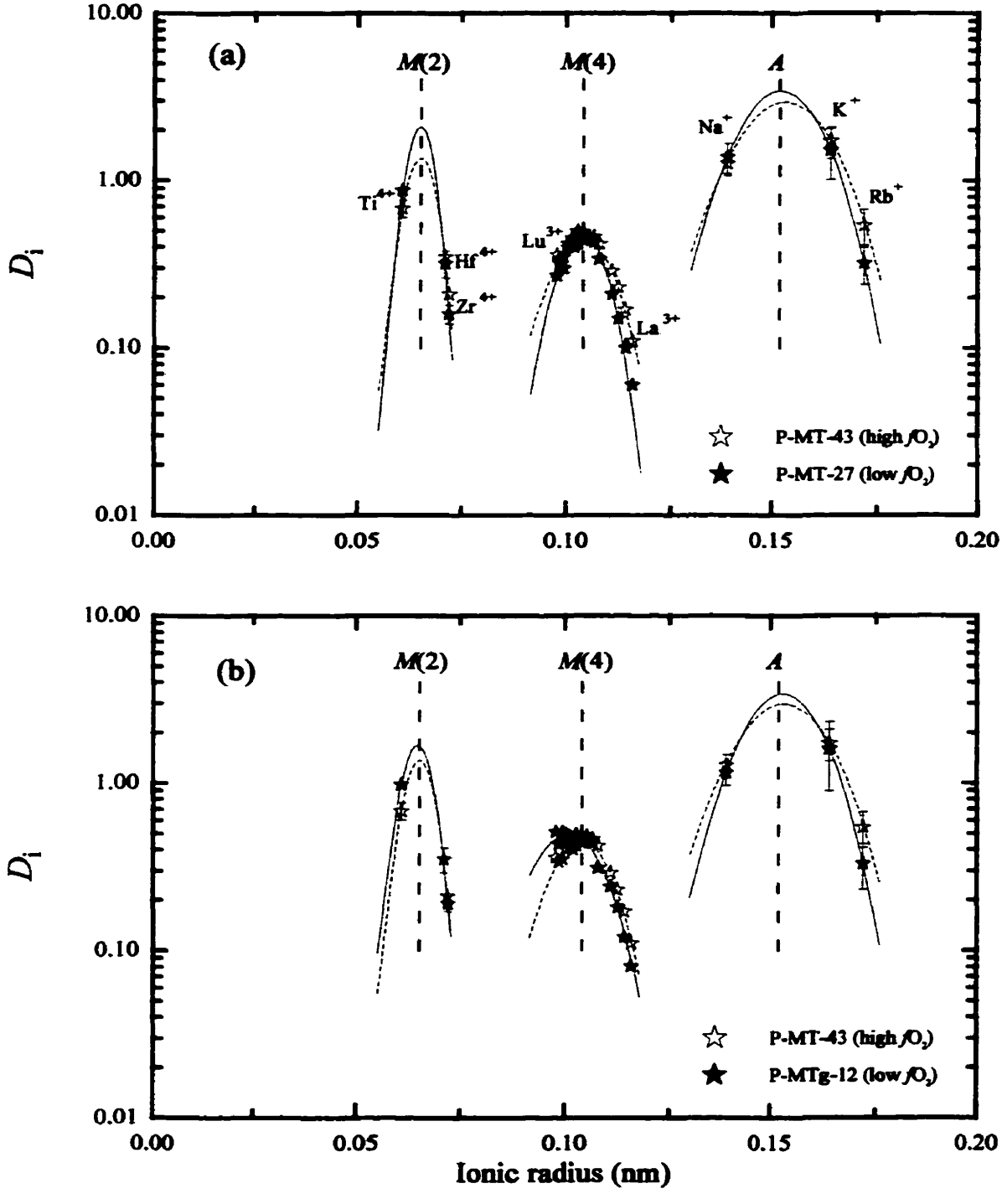
(a)
M(2)
M(4)
A
Ti4+
Hf4+
Zr4+
Lu3+
La3+
Na+
K+
Rb+
P-MT-43 (high fO2)
P-MT-27 (low fO2)
(b)
P-MT-43 (high fO2)
P-MTg-12 (low fO2)
Di
Ionic radius (nm)
10.00
1.00
0.10
0.01
0.00
0.05
0.10
0.15
0.20

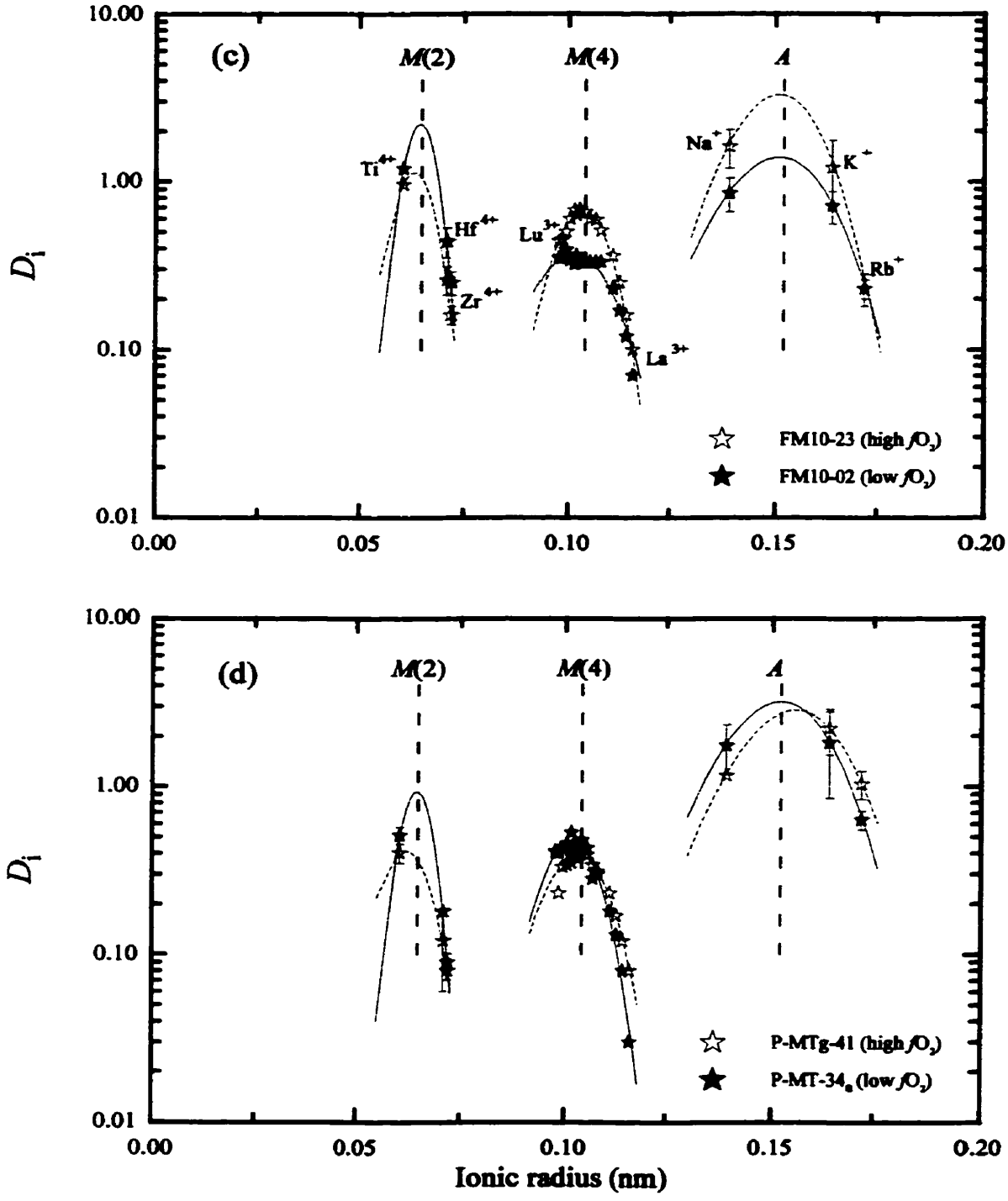
(c)
M(2)
M(4)
A
Ti4+
Hf4+
Zr4+
Lu3+
La3+
Na+
K+
Rb+
FM10-23 (high fO2)
FM10-02 (low fO2)
(d)
P-MTg-41 (high fO2)
P-MT-34a (low fO2)
Di
Ionic radius (nm)
10.00
1.00
0.10
0.01
0.00
0.05
0.10
0.15
0.20

has a similar effect on the lattice site parameters of the amphibole structure as increasing pressure which both decrease D_o, $\bar{E}$, and r_o (Table 4.1). The cause for the decrease in the calculated Young's modulus ($\bar{E}$) for the *A* site with increasing fO_2 can be explained by a greater relative change in D_K and D_{Rb} as opposed to D_{Na} for P-MT and P-MTg experiments, similar to the pressure effect variations. Such partitioning behaviour also affects the optimum ionic radius of the *A* site where in general it increases. Relative shifts in r_o can be observed in the different P-MT and P-MTg experiments, especially for the P-MTg-34 *vs.* P-MTg-41 pair of experiments performed at high pressures (Fig. 4.7d). The variation in D_o as fO_2 increases is greater for the *M*(2) site in general (~ 18 to 56 % decrease) where variations in partition coefficients are more important than the two other lattice-sites [*i.e.*, ~ 11 to 14 % and ~ 6 to 19 % decrease for *A* and *M*(4) sites, respectively; Fig. 4.7]. For the P-MT and P-MTg experiments, increasing the oxygen fugacity preferentially increases some D_{LREE}'s (*e.g.*, D_{La}, D_{Ce}, D_{Pr}, D_{Nd}) to the detriment of some D_{HREE}'s (*e.g.*, D_{Tm}, D_{Yb}, D_{Lu}) which remain within one standard deviation. Such behaviour has the effect of decreasing the trivalent cation Young's modulus in the *M*(4) site (*i.e.*, $\bar{E}$ decreases; Figs. 4.7a, -b, -d). For the FM10 experiments, I observed a peculiar behaviour for the trivalent cations in the *M*(4) site. Some D_{LREE}'s (*i.e.*, D_{La}, D_{Ce}) and D_{HREE}'s (*i.e.*, D_{Tm}, D_{Yb}, D_{Lu}) remained within one standard deviation while the other trivalent cations reached a maximum increase by a factor of ~ 2 as the oxygen fugacity increased (Fig. 4.7c and Table 3.10). In such a case, the Young's modulus shows an increase with increasing fO_2. Similar variations also affect the monovalent cations in the *A* site where D_{Na} and D_K increase more rapidly from NNO-2 to NNO+1.7 as opposed to D_{Rb},

producing a higher $\bar{E}_A$ with increasing fO_2 (Fig. 4.7c).

Increasing the oxygen fugacity in the charge should directly affect the Fe^{3+}/Fe^{2+} ratio in the different run products. However, as mentioned above, the empirical model used to estimate the proportion of Fe^{3+} in one of our FM10 experiments (*i.e.*, FM10-23) can not confirm such a process because the proportion of Fe^{3+} in amphiboles produced at the high oxygen fugacity was found to be zero (Table 3.5). If the different cation proportions in the amphibole formulae remain identical as the oxygen fugacity increases, the oxidation process of iron will result in a reduction of the mean bond-length (*e.g.*, $\langle M(1,2,3)\text{-O}\rangle$) where the relatively large Fe^{2+} (ionic radius = 0.078 nm) is oxidized to give a smaller cation (*i.e.*, Fe^{3+}; ionic radius = 0.0645 nm). However, as mentioned in the previous sections, I observed a complex substitution in our amphibole run products where variations of the CN/MTAF ratio affected different lattice sites.

Although fO_2 and P affect partition coefficients, the effects can be explained by changes in major element chemistry [*e.g.*, $Al_{T(1)}$, $(Ti, Al)_{M(1,2,3)}$, $(Ca, Fe^{2+})_{M(4)}$, K_A] of the amphibole. I noted a general trend for partitioning between amphibole and basaltic melt as pressure increases where $D_{A\text{-site}}$ of monovalent cation increases whereas $D_{M(4)\text{-site}}$ of trivalent cation and $D_{M(2)\text{-site}}$ of quadrivalent cation decreases. Increasing the oxygen fugacity affects partitioning similarly to pressure where $D_{A\text{-site}}$ of monovalent and divalent cations and $D_{M(4)\text{-site}}$ of trivalent cations increase whereas $D_{M(2)\text{-site}}$ of quadrivalent cations decrease.

Chapter 5

Experimental investigation on partitioning of LILE, HFSE, and REE between calcic amphibole and basaltic melt: III- The effect of titanium

5.1 Introduction

The effect of titanium on partitioning between calcic amphibole and basaltic melt must be understood because many studies reported the association of a Ti-rich calcic amphibole (*i.e.*, Ti-rich pargasite or kaersutite) together with a Ti-poor calcic amphibole (*i.e.*, pargasite) in amphibole peridotite xenoliths (Wilshire *et al.* 1971, Francis 1976b, Bergman 1981, Wilkinson and LeMaître 1987, Zanetti *et al.* 1994). Furthermore, these calcic amphiboles observed in xenoliths are chemically distinct in their major element (*e.g.*, TiO_2, Cr_2O_3) and trace element compositions (*e.g.*, MREE; Ionov and Hofmann 1995). Therefore, our goal was to investigate the effects of Ti on the bulk chemistry of the amphibole and on amphibole / melt partition coefficients.

5.1.1. Procedure used to investigate the titanium effects

Five starting materials were used to evaluate if titanium significantly affects partition coefficients. These materials were grouped into compositions of pargasitic and of olivine nephelinitic materials with different major and trace element concentrations. The first group included a pargasite crystal, a pargasitic glass, and a Ti-doped pargasitic glass (*i.e.*, P-MT, P-MTg, and P-MTg_{Ti}, respectively, Table 3.1). The second group included an olivine

nephelinite bulk rock, and a Ti-doped olivine nephelinitic glass (*i.e.*, HF13, and HF13g_{Ti}, respectively, Table 3.1). To focus on the effect of only Ti, experiments were performed at an identical pressure (*i.e.*, 1.5 GPa) and oxygen fugacity (*i.e.*, low oxygen fugacity ~NNO-2 using the graphite inner capsule) as well as similar temperatures and volatile concentrations. Temperatures of experiments on Ti-doped and undoped starting materials were similar, 1130 and 1100 °C for P-MT materials and 1040 and 1020 °C for HF13 materials, respectively. Experimental conditions and run products are listed in Table 3.3 (P-MT-27, P-MTg-12, P-MTg_{Ti}-31, HF13-38, and HF13g_{Ti}-03). It is important to note that the different phases (*i.e.*, minerals and glass) obtained from doped and undoped materials in the run products are identical for the HF13 experiments and similar for the P-MT experiments. However, as mentioned previously, the chemistry of these phases are not identical, only similar. In the P-MTg_{Ti}-31 experiment, olivine crystallized at the expense of phlogopite. No Ti-oxide was observed in the five run products demonstrating that titanium solubility is high in these hydrous basaltic liquids at such a low oxygen fugacity. However, it was not my intention to saturate the basaltic melts in titanium but to increase the bulk amount of titanium in the amphibole structure. The Ti-doped run products crystallized Ti-rich pargasitic amphibole (Table 3.5), and in one run product (*i.e.*, P-MTg_{Ti}-31), kaersutite (Fig. 3.3). As the bulk titanium content increased for each group of compositions, the amphibole stability field increased to higher temperatures by 20 to 30 °C at the same pressure, water content, and oxygen fugacity. This characteristic has been observed previously in other experimental studies (Merrill and Wyllie 1975, Wallace and Green 1991) and also in natural calcic

amphiboles that have been processed in upper mantle and upper crustal environments (Hammarstrom and Zen 1986, Zanetti *et al.* 1994).

5.1.2. The oxidation state of Ti at low oxygen fugacity (NNO-2)

One critical parameter to investigate at this low oxygen fugacity is the valence state of titanium. If Ti^{3+} is present, it may partition in a different site than Ti^{4+} due to their differences in ionic size and charge (*i.e.*, ^{VI}0.067 and ^{VI}0.0605 nm, respectively; Shannon 1976), thus possibly affecting Ti partitioning between amphibole and melt. At high pressures where the graphite buffer is located above the iron-wüstite buffer, the valence state of titanium is expected to be 4+. However, to qualitatively distinguish if any Ti^{3+} is present at these conditions, an experiment using albitic glass + 5 wt.% TiO_2 (anatase form) with 5 wt.% deionized water in the double capsule assembly was performed at 1.5 GPa, 1200°C for 15 h. When trace amounts of Ti^{3+} are present in albitic glass (*e.g.*, > 1000 ppm), it should acquire a violet tint due to the absorption of Ti^{3+} at the visible wavelength of 550 nm (Schreiber *et al.* 1982). The experiment produced a clear glass without any visible violet tint, confirming that titanium was dominantly-to-completely in the 4+ valence state at the experimental conditions of this study. In the run products, the chemistry of amphibole showed that as titanium content in the crystal structure increased (*i.e.*, $^{VI}Ti_{M(1,2,3)}$, Table 3.5), the Mg number increased also [*i.e.*, Mg# = 100Mg/(Mg+Fe^{2+})] (Fig. 3.3). This increase in Mg number must have been at least partially responsible for the increase in amphibole stability to higher temperatures.

5.1.3. Variations in element concentrations between the undoped and Ti-doped experiments

For these experiments, it is important to determine how both amphibole and melt compositions have been modified bu the addition of titanium. If titanium merely acts as a diluent, its effect on partition coefficients will be inconsequential. From both P-MT and HF13 data sets, I observed in general that the addition of titanium shifts the Mg number of the amphibole to higher values and increases the LREE's (*i.e.*, La, Ce, Pr, and Nd), and in some cases the HFSE's (*i.e.*, Nb, Ta, Zr, and Y), and the LILE's (Ba and Sr) concentrations in the amphibole run products. These increases can be explained by small variations in amphibole composition (*e.g.*, bulk titanium content and Mg#; Fig. 3.3). On the basis of major element concentrations, TiO_2 in the P-MT melts showed an increase of ~74 relative % with respect to the undoped melts (*i.e.*, P-MT-27 and P-MTg-12) while FeO showed a decrease by ~60 relative % which increased the $Mg\#_t$ to higher values as titanium increased (*i.e.*, from 61.6 and 66.1 to 81.5 for P-MT-27, P-MTg-12, and P-MTg_{Ti}-31, respectively; Table 3.6). This is not surprising because no Ti-oxide (or phlogopite which is another moderately Ti-rich phase) was stable at the conditions studied for the P-MTg_{Ti}-31 experiment. The decrease in FeO is due to a modification in the different phases present and their proportions as titanium increases, not due to iron-loss to the container. For major elements in HF13 melts, TiO_2, Al_2O_3, and Na_2O increased whereas FeO decreased (Table 3.6). Again, the $Mg\#_t$ increased as titanium content increased (*i.e.*, from 53.4 to 63.0 for HF13-38 and HF$13g_{Ti}$-03, respectively; Table 3.6), and FeO is affected by the same processes as in the P-MT runs.

Table 5.1 shows the variations observed in different trace elements between the

Table 5.1. Relative variations observed in trace element concentrations between undoped and Ti-doped run products

phase	amphibole (doped *vs.* undoped)			glass (doped *vs.* undoped)		
sm	P-MT		HF13	P-MT		HF13
run#	31 *vs.* 27	31 *vs.* 12	03 *vs.* 38	31 *vs.* 27	31 *vs.* 12	03 *vs.* 38
Rb	≡	≡	≡	↓(22)	≡	≡
Ba	≡	≡	↑(67)	↓(23)	↓(11)	↑(4)
Nb	↑(112)	↑(92)	↓(13)	↓(13)	≡	↓(7)
Ta	↑(194)	≡	≡	≡	≡	↓(15)
La	↑(217)	↑(445)	↑(57)	≡	↑(108)	↓(89)
Ce	↑(137)	↑(275)	↑(29)	≡	↑(98)	↓(7)
Pr	≡	↑(122)	↑(32)	↓(11)	↑(45)	↓(5)
Sr	≡	≡	↑(23)	↓(14)	≡	↓(2)
Nd	↑(42)	↑(72)	↑(26)	↓(9)	↑(29)	↓(4)
Zr	≡	≡	↑(27)	≡	≡	≡
Hf	≡	≡	≡	≡	≡	≡
Sm	≡	≡	≡	≡	≡	↓(6)
Eu	≡	≡	≡	≡	≡	≡
Gd	≡	≡	≡	≡	≡	≡
Tb	≡	≡	↑(8)	≡	≡	≡
Dy	≡	≡	↑(10)	≡	≡	≡
Ho	≡	≡	≡	≡	≡	≡
Y	≡	≡	↑(24)	↓(9)	≡	↓(7)
Er	≡	≡	≡	≡	≡	≡
Tm	≡	≡	≡	≡	≡	≡
Yb	↑(103)	↑(72)	≡	≡	↑(39)	≡
Lu	≡	≡	≡	≡	↓(44)	≡
avg	(134)	(180)	(29)	(14)	(54)	(15)

Abbreviations and symbols denote: sm-starting material (P-MT included: P-MT, P-MTg, and P-MTg_{Ti}; HF13 included: HF13 and HF12g_{Ti}), run#-run number, 31 *vs.* 27-P-MTg_{Ti}-31 *vs.* P-MT-27, 31 *vs.* 12-P-MTg_{Ti}-31 *vs.* P-MTg-12, 03 *vs.* 38-HF13g_{Ti}-03 *vs.* HF13-38, ≡-variations in concentration are within 2σ, ↑-concentration increases, ↓-concentration decreases, avg-average of the different variations observed for this pair of run products. Values in parentheses represent the relative variation calculated from the element concentrations of Tables 3.4 and 3.6 (in %; *e.g.*, for P-MTg_{Ti}-31 *vs.* P-MT-27 the Nb concentration in amphibole has increased by 112 %).

undoped and Ti-doped experimental pairs for the different amphiboles and their respective melts. All these changes observed in Table 5.1 are greater than two standard deviations away from the analytical uncertainty of the element concentrations. The trace element concentrations of the kaersutite in P- MTg_{Ti}-31 relative to Ti-rich pargasite in P-MT-27 run products showed an increase in Nb, Ta, La, Ce, Nd, and Yb (Table 5.1). The same trends were also observed between the kaersutite in P-MTg_{Ti}-31 relative to Ti-rich pargasite in P-MTg-12 run products in which Nb, La, Ce, Pr, Nd, and Yb increased (Table 5.1). The relative variations observed in trace element concentrations for P-MTg_{Ti}-31 amphibole were between 42 to 445 % with an average of 134 and 180 % compared to their respective undoped P-MT-27 and P-MTg-12 amphiboles, respectively. The melt compositions in P-MT experiments displayed much lower variations in their trace element concentrations. Between P-MTg_{Ti}-31 and P-MT-27 melts, I observed decreases in Rb, Ba, Nb, Pr, Sr, Nd, and Y between 9 to 23 relative % with an average of 14 relative % as titanium increased (Table 5.1). Comparing P-MTg_{Ti}-31 and P-MTg-12 experiments, the P-MTg_{Ti}-31 melt showed a decrease in Ba and Lu but an increase in La, Ce, Pr, Nd, and Yb between 11 to 108 relative % with an average of 54 relative %. However, the variation in concentrations for Nb, Ta, La, Ce, Pr, Nd, and Yb in the P-MT melts was smaller than those observed for the amphiboles as titanium increased (Table 5.1). However, the different behaviours observed for P-MT materials reflect different degrees of crystallization as shown in Table 3.3. The trace element concentrations for the pargasite and the Ti-rich pargasite from $HF13g_{Ti}$-03 and HF13-38 run products showed an increase in Ba, La, Ce, Pr, Sr, Nd, Zr, Tb, Dy, Y and a decrease in Nb (Table 5.1).

The increase observed in trace element concentrations for HF13g_{Ti}-03 relative to the undoped amphibole, HF13-38, were between 8 to 67 % with an average of 29 %. Again, the melt compositions of HF13 experiments demonstrated lower variations in their trace element concentrations. Comparing HF13-g_{Ti}-03 and HF13-38 melts, I observed a decrease in Nb, Ta, La, Ce, Pr, Sr, Nd, Sm, Y and an increase in Ba between 2 to 89 relative % with an average of 15 relative percent (Table 5.1). In summary, the variation in concentrations for Ba, Nb, Ce, Pr, Sr, Nd, Zr, and Y in the different melt compositions were relatively smaller than those observed for the amphiboles. Lanthanum, however, showed a larger relative variation in the melt than in the amphibole run products (Table 5.1). Based upon these observations I can anticipate that the effect of titanium on partition coefficients will be directly related to the behaviour of titanium in our calcic amphibole.

5.1.4. The mechanism of Ti substitution into the amphibole structure

The goal of these experiments is to understand the mechanism of $^{VI}Ti^{4+}$ substitution in calcic amphibole and its behaviour with respect to major elements (Al, Mg, Fe^{2+}, Mn) occupying the same octahedral sites, as well as its interaction with other HFSE (^{VI}[Nb, Ta, Zr, Y, Hf]$_{M(1,2,3)}$). It is also important to understand its possible effect on trace elements occupying different crystallographic sites in calcic amphibole (*e.g.*, ^{VIII}[LILE and REE]$_{M(4)}$). Adam and Green (1994) noted a positive relationship between Ti and REE concentrations in one of their zoned pargasite run products. Furthermore, Dalpé *et al.* (1995) suggested that their lower D_{REE} measured between a Ti-rich pargasite and quenched basanitic melt compared

to other experimental studies (*e.g.*, Nicholls and Harris 1980, Green and Pearson 1985a, Adam *et al.* 1993, Adam and Green 1994) could be due to slight differences in the ^{VI}Ti content.

The incorporation of Ti into amphibole can occur by different substitutions of Ti for other major elements (Della Ventura *et al.* 1991). The Tschermak substitution was proposed by Helz (1973) for silica-poor calcic amphibole:

$$[^{VI}Al + {}^{IV}Si]_{-1} \rightleftharpoons [^{VI}Ti + {}^{IV}Al].$$

The deprotonation substitution was suggested by Oba *et al.* (1982) for oxy-kaersutite:

$$[^{VI}Al + {}^{O(3)}OH^{-1}]_{-1} \rightleftharpoons [^{VI}Ti^{4+} + {}^{O(3)}O^{2-}].$$

The octahedral vacancy substitution was proposed by Forbes and Flower (1974) for Ti-rich phlogopite which seems theoretically possible for amphiboles:

$$[2\,{}^{VI}Mg]_{-1} \rightleftharpoons [^{VI}Ti + {}^{VI}\square].$$

The tetrahedral isovalent substitution was suggested by Wagner and Velde (1986) for Ti-rich richterite in lamproites:

$$[^{IV}Si]_{-1} \rightleftharpoons [^{IV}Ti],$$

and the kaersutite substitution proposed by Oberti *et al.* (1992) for richterite in lamproites:

$$[^{VI}(Mg,Fe)^{2+} + 2(OH,F)^{-}]_{-1} \rightleftharpoons [^{VI}Ti^{4+} + 2O^{2-}].$$

Another mechanism of substitution in kaersutite was suggested by Popp and Bryndzia (1992) combining a ferric oxy-amphibole and titanium substitutions where charge is not balanced:

$$Ti^{4+}_{apfu} = 0.23\ (\pm 0.09)_{apfu} + 0.47\ Fe^{3+}\ (\pm 0.11)_{apfu}.$$

However, none of these substitutions can be directly applied to our calcic amphibole because

the titanium and magnesium increase while ferrous iron and aluminium decrease in the octahedral sites [*i.e.*, *M*(1,2,3); Table 3.5]. Figure 5.1 shows the relationship between $^{VI}Fe^{2+}$, ^{VI}Al, ^{VI}Ti, and ^{VI}Mg observed in the octahedral sites for the undoped and Ti-doped experiments. I observed that $^{VI}Fe^{2+}$ and ^{VI}Al have the same behaviour while the ^{VI}Ti and ^{VI}Mg, which form another pair in the octahedral sites, behave in the opposite manner to $^{VI}Fe^{2+}$ and ^{VI}Al. Furthermore in our amphibole run products, the tetrahedral sites were completely filled by ^{IV}Si and ^{IV}Al leaving an extra aluminium which partitioned into the octahedral *M*(1,2,3) sites (*i.e.*, $^{VI}Al^{3+}$; see Table 3.5), eliminating any possible titanium substitution in the tetrahedral sites. Another point to mention is that the ferric-iron (*i.e.*, Fe^{3+}) did not seem to be stable in amphibole at the oxygen fugacities of the experiments (see above).

We plotted the amphibole run products on the diagram $^{VI}[Ti^{4+} + Mg^{2+}]$ against $^{VI}[Fe^{2+} + Al^{3+}]$ (Fig. 5.2a). The undoped and doped experiments followed a trend involving a mechanism of coupled substitution between ferropargasite $[NaCa_2(Fe^{2+}_4Al^{3+})Si_6Al_2O_{22}(OH)_2]$ and kaersutite $[NaCa_2(Mg^{2+}_4Ti^{4+})Si_6Al_2O_{23}(OH)]$ end-members (Leake *et al.* 1997). For such a substitution, I need to incorporate the participation of the *O*(3) site for charge balancing which gives a completed coupled substitution such as:

$$[(Fe^{2+}_4 + Al^{3+})_{M(1,2,3)} + (OH^-)_{O(3)}]_{-1} \rightleftharpoons [(Mg^{2+}_4 + Ti^{4+})_{M(1,2,3)} + (O^{2-})_{O(3)}].$$

This coupled substitution occurs in the octahedral sites similar to the one proposed by Oba *et al.* (1982) as mentioned previously for oxy-kaersutite. However, this is a tentative coupled substitution which can only be verified by analysing the water content in the different amphiboles. Additionally, it does not include minor [*i.e.*, $(Mn, Cr)_{M(1,2,3)}$] or trace elements (*i.e.*, $HFSE_{M(1,2,3)}$) which occupy the same octahedral sites as Fe^{2+}, Al, Ti, and Mg.

Figure 5.1. Variations of some major element concentrations observed in the octahedral *M*(1,2,3) sites between undoped and Ti-doped experiments. (a) Fe^{2+} against Al. (b) Ti against Mg (see Table 5). Symbols denote P-MT-27 and P-MTg-12 experiments (Undoped P-MT and P-MTg); P-MTg_{Ti}-31 experiment (Ti-doped P-MTg); HF13-38 experiment (Undoped HF13); HF$13g_{Ti}$-03 experiment (Ti-doped HF13g).

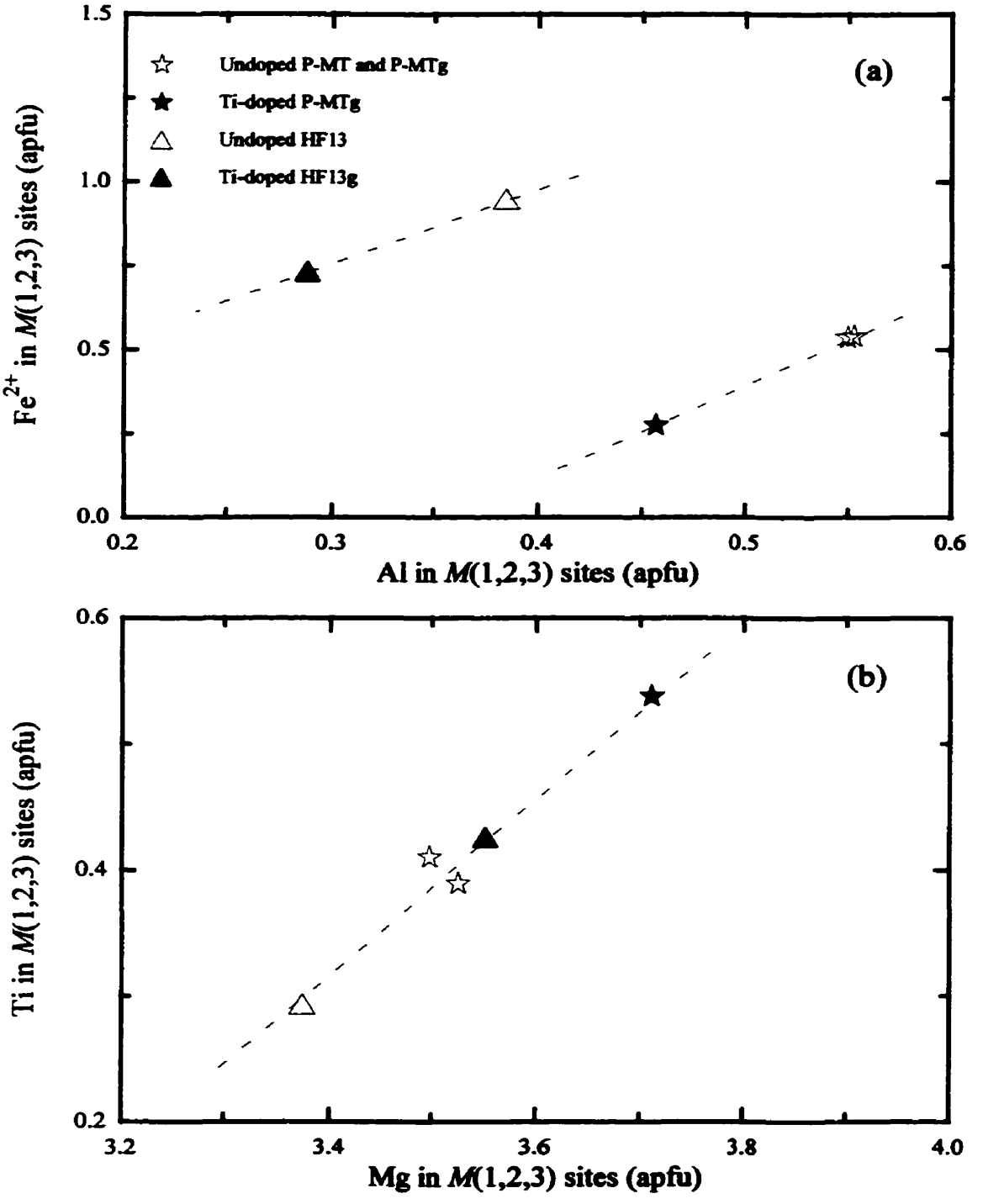
(a)
Undoped P-MT and P-MTg
Ti-doped P-MTg
Undoped HF13
Ti-doped HF13g
Fe^{2+} in M(1,2,3) sites (apfu)
Al in M(1,2,3) sites (apfu)
1.5
1.0
0.5
0.0
0.2
0.3
0.4
0.5
0.6
(b)
Ti in M(1,2,3) sites (apfu)
Mg in M(1,2,3) sites (apfu)
0.6
0.4
0.2
3.2
3.4
3.6
3.8
4.0

Figure 5.2. Variation of composition in the $M(1,2,3)$ octahedral sites of calcic amphiboles. (a) $(Mg + Ti^{4+})_{M(1,2,3)}$ *vs.* $(Fe^{2+} + Al)_{M(1,2,3)}$ between undoped and Ti-doped experiments from this study. Symbols same as in Fig. 5.1. The solid line represents the coupled substitution between two end-members, kaersutite and ferropargasite (see text). $(Mg + Ti^{4+})_{M(1,2,3)}$ *vs.* $(Fe_{total} + Al)_{M(1,2,3)}$ for calcic amphiboles from: (b) This study using P-MT, P-MTg, and K-HD as starting materials (P-MT-34a, P-MTg-41, P-MTg-43, K-HD-08), and K1921 and FM10 as starting materials (K1921-15, FM10-02, FM10-23, and FM10-25); (c) Other experimental studies (sources: Mysen and Boettcher 1975, Nicholls and Harris 1980, Green and Pearson 1985a, Adam *et al.* 1993, Adam and Green 1994, Brenan *et al.* 1995, LaTourrette *et al.* 1995, and Fujinawa and Green 1997); (d) Natural samples (sources: Campbell and Schenk 1950, Dickey 1968, Best 1970, Philpotts and Schnetzler 1970, Varne 1970, Wilshire *et al.* 1971, Wilshire and Trask 1971, Gunn 1972, Kesson and Price 1972, White *et al.* 1972, Best 1974, Ellis 1976, Embey-Isztin 1976, Francis 1976a, Francis 1976b, Boettcher and O'Neil 1980, Bergman *et al.* 1981, Bonatti *et al.* 1981, Dawson and Smith 1982, Liotard *et al.* 1983, Wilkinson and LeMaître 1987, Neal 1988, O'Reilly *et al.* 1991, Dyar *et al.* 1992, Dyar *et al.* 1993, Richter and Carmichael 1993, Ionov and Hofmann 1995, Oberti *et al.* 1995, and Chazot *et al.* 1996). The solid line in (b), (c), and (d) represents the coupled substitution between the kaersutite and ferropargasite-hastingsite end-members. The insert diagram in (d) shows $(Mg + Ti^{4+})$ *vs.* $(Fe_{total} + Al + Cr)$ for natural amphiboles.

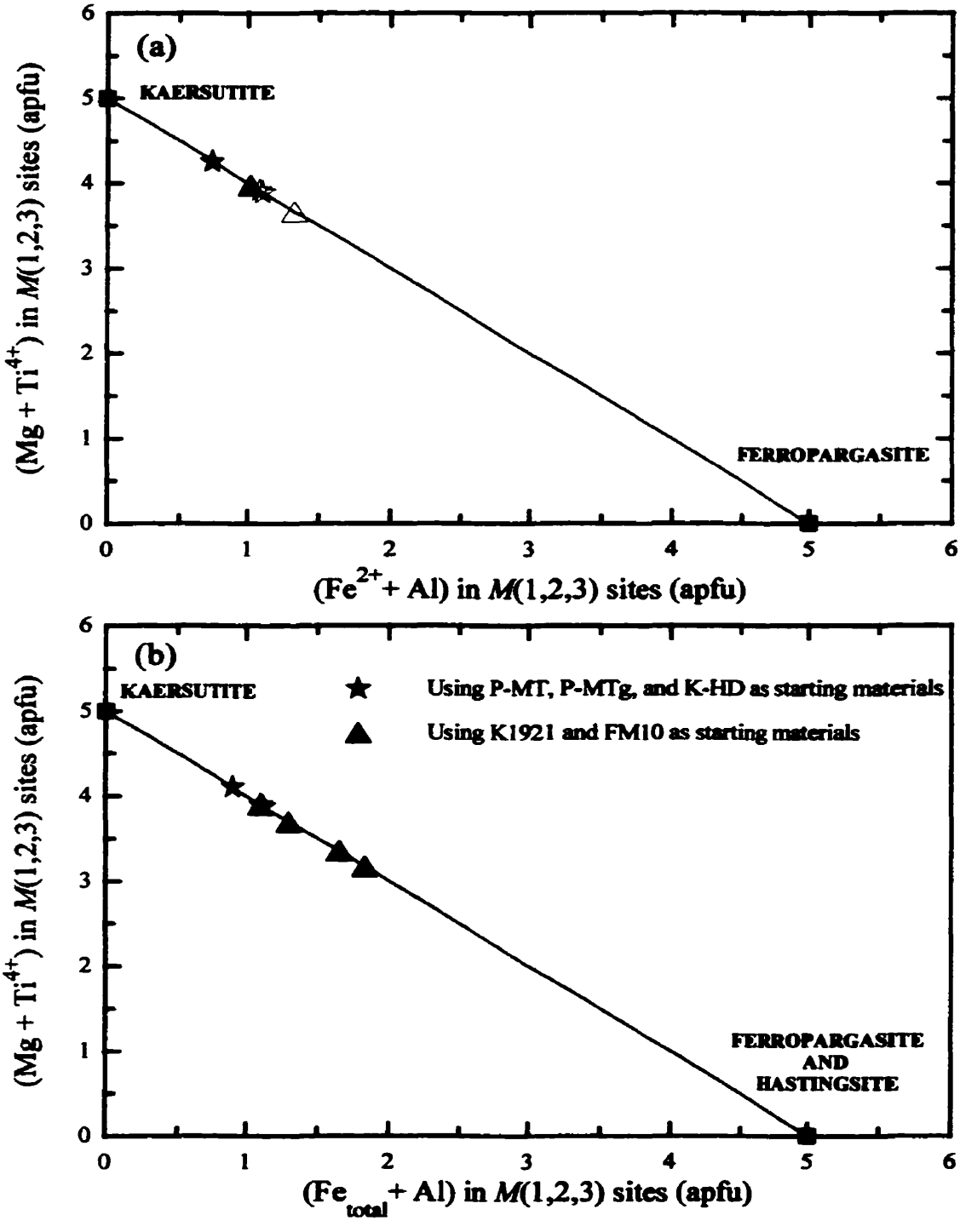
(a)
KAERSUTITE
FERROPARGASITE
(Mg + Ti4+) in M(1,2,3) sites (apfu)
(Fe2+ + Al) in M(1,2,3) sites (apfu)
(b)
KAERSUTITE
Using P-MT, P-MTg, and K-HD as starting materials
Using K1921 and FM10 as starting materials
FERROPARGASITE AND HASTINGSITE
(Mg + Ti4+) in M(1,2,3) sites (apfu)
(Fetotal + Al) in M(1,2,3) sites (apfu)

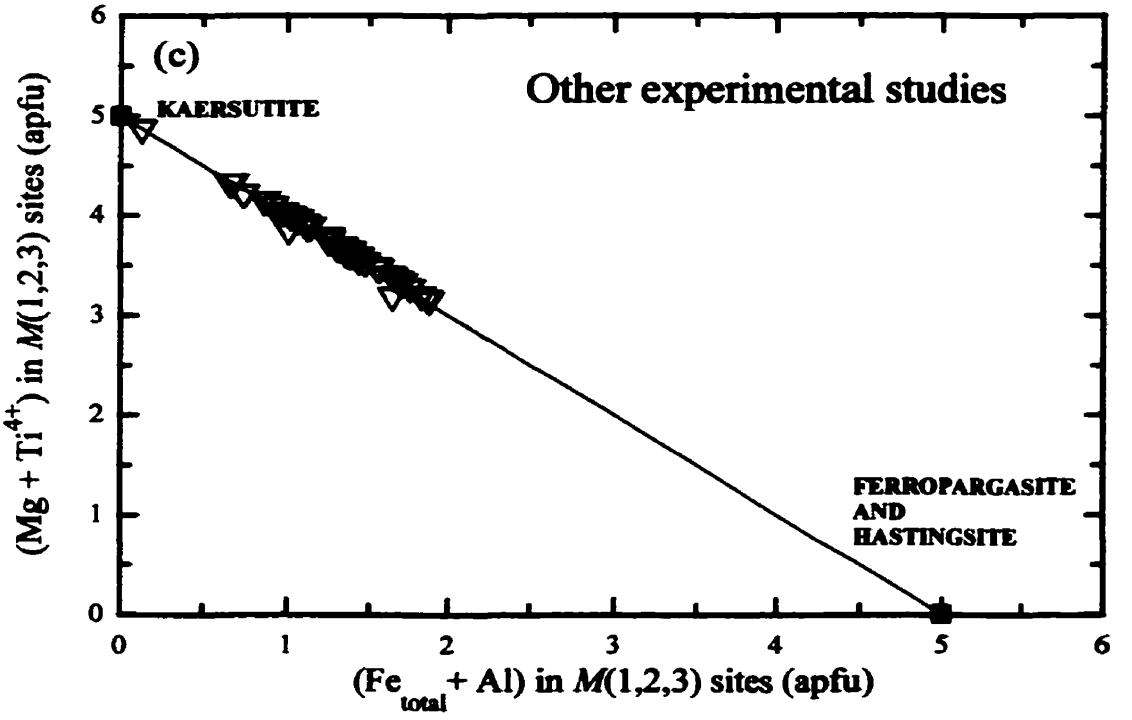
(c)
Other experimental studies
KAERSUTITE
FERROPARGASITE AND HASTINGSITE
(Mg + Ti4+) in M(1,2,3) sites (apfu)
(Fetotal + Al) in M(1,2,3) sites (apfu)
0
1
2
3
4
5
6

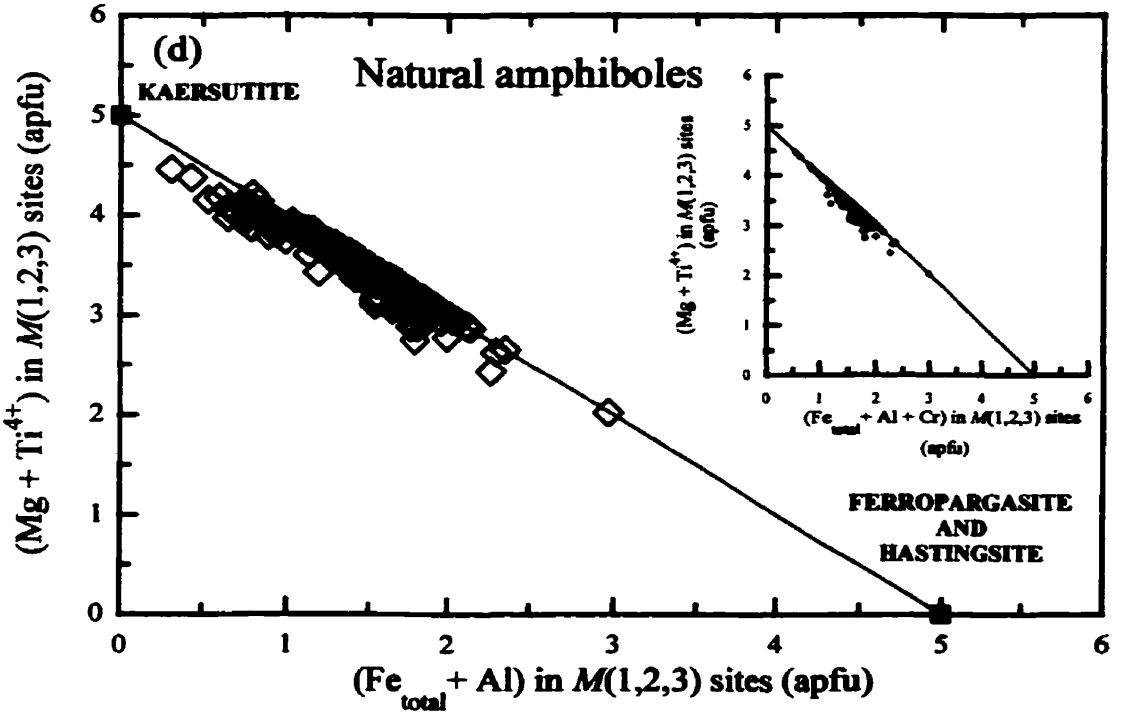
(d)
Natural amphiboles
KAERSUTITE
FERROPARGASITE AND HASTINGSITE
(Mg + Ti4+) in M(1,2,3) sites (apfu)
(Fetotal + Al) in M(1,2,3) sites (apfu)
(Mg + Ti4+) in M(1,2,3) sites (apfu)
(Fetotal + Al + Cr) in M(1,2,3) sites (apfu)
0
1
2
3
4
5
6

For some natural and synthetic amphibole compositions the ferric-iron (Fe^{3+}) content was indirectly estimated or even measured suggesting that the above coupled substitution could not be directly applied for these amphiboles. To compensate for the rigidity of the above substitution I included ferric-iron (Fe^{3+}) of the left-hand side. In such a case, another possible coupled substitution can be written as:

$$[\{Fe^{2+}_4 + (Al^{3+}, Fe^{3+})\}_{M(1,2,3)} + (OH)_{O(3)}]_{-1} \rightleftharpoons [(Mg^{2+}_4 + Ti^{4+})_{M(1,2,3)} + (O^{2-})_{O(3)}].$$

Figures 5.2b, -c, and -d show the variation in compositions of the natural and other experimentally produced calcic amphiboles into which I included both ferrous- and ferric-iron from the estimated or measured concentrations. In this case, the Mg-Ti end-member was occupied by kaersutite [*i.e.*, $NaCa_2(Mg^{2+}_4Ti^{4+})Si_6Al_2O_{23}(OH)$] while the Fe^{2+}-Fe^{3+}-Al "end-member" was occupied by ferropargasite / hastingsite amphiboles [*i.e.*, $NaCa_2(Fe^{2+}_4Al^{3+})Si_6Al_2O_{22}(OH)_2$, $NaCa_2(Fe^{2+}_4Fe^{3+})Si_6Al_2O_{22}(OH)_2$, respectively; Leake *et al.* 1997]. I observed for the experimentally produced amphiboles a very close relationship between the kaersutite - ferropargasite/hastingsite tie-line while some scatter can be seen for natural compositions of which the majority plot below the line (Figs. 5.2b, -c, -d). However I observed for the natural calcic amphiboles an inverse relationship between Ti and Cr concentrations in the octahedral sites (*i.e.*, when $Ti_{M(1,2,3)}$ increases, $Cr_{M(1,2,3)}$ decreases). For the experimentally produced calcic amphibole this behaviour between Ti and Cr is not obvious due to the scarcity of Cr analyses (Adam *et al.* 1993, Adam and Green 1994). When I included Cr^{3+} in the modified coupled substitution shown above the majority of natural amphibole compositions plot closer to the line (insert of Fig. 5.2d). By a modification of the previous coupled substitution applied to calcic amphiboles formed at high pressure and high

temperature, we obtain:

$$[\{Fe_4^{2+} + (Al^{3+}, Fe^{3+}, Cr^{3+})\}_{M(1,2,3)} + (OH^-)_{O(3)}]_{-1} \rightleftharpoons [(Mg_4^{2+} + Ti^{4+})_{M(1,2,3)} + (O^{2-})_{O(3)}].$$

However, again I observed that some natural amphiboles plot under the tie-line. The plotted position of some amphiboles can be explained by the high ferric-iron content in their chemistry, where some have 100 % iron as Fe^{3+}. The oxidation of an amphibole on this diagram will shift its composition along the tie-line to the left with a gentle decrease in the $(Mg + Ti)_{M(1,2,3)}$ content. For oxidized amphiboles [*i.e.*, $(Fe^{3+}/Fe^{2+})_{M(1,2,3)} > 0.250$], the

$$[\{Fe_4^{2+} + (Al^{3+}, Fe^{3+}, Cr^{3+})\}_{M(1,2,3)} + (OH^-)_{O(3)}]_{-1} \rightleftharpoons [(Mg_4^{2+} + Ti^{4+})_{M(1,2,3)} + (O^{2-})_{O(3)}]$$

coupled substitution could not be applied, due to their high proportion of Fe^{3+}, without affecting the charge balance of the coupled substitution.

5.1.5. Variations of partitioning with titanium

The observed variations in partition coefficients due to the effect of titanium are shown in Figure 5.3 for both P-MT and HF13 runs. The plotted range of partition coefficients includes one standard deviation based upon multiple analyses. In Figure 5.3a, the undoped experiments (*i.e.*, P-MT-27 and P-MTg-12) were averaged together for better clarity. For these experiments (*i.e.*, P-MT-27 and P-MTg-12), the variations observed for undoped experiments represent the minimum and the maximum values of -1 standard deviation and +1 standard deviation attached to each element, respectively (see Table 3.10).

If I select elements which have similar behaviours within the two groups of compositions, this study shows that as the $^{VI}Ti^{4+}$ content in calcic amphibole increases, the partition coefficients of D_{Ba}, D_{Ta}, D_{La}, D_{Ce}, D_{Pr}, D_{Sr}, D_{Nd}, and D_{Zr} increase (*i.e.*, become more

Figure 5.3. Effect of titanium on partition coefficients between amphibole and melt. (a) P-MT materials. Symbol and field denote: P-MTg-12 and P-MT-27 experiments (Undoped P-MT and P-MTg); P-MTg$_{Ti}$-31 experiment (Ti-doped P-MTg). (b) HF13 materials. Symbol and field denote: HF13-38 experiment (Undoped HF13); HF13g$_{Ti}$-03 experiment (Ti-doped HF13g). The minimum and maximum partition coefficients within each undoped and Ti-doped groups included ±1 standard deviation attached to each element (see Table 3.8).

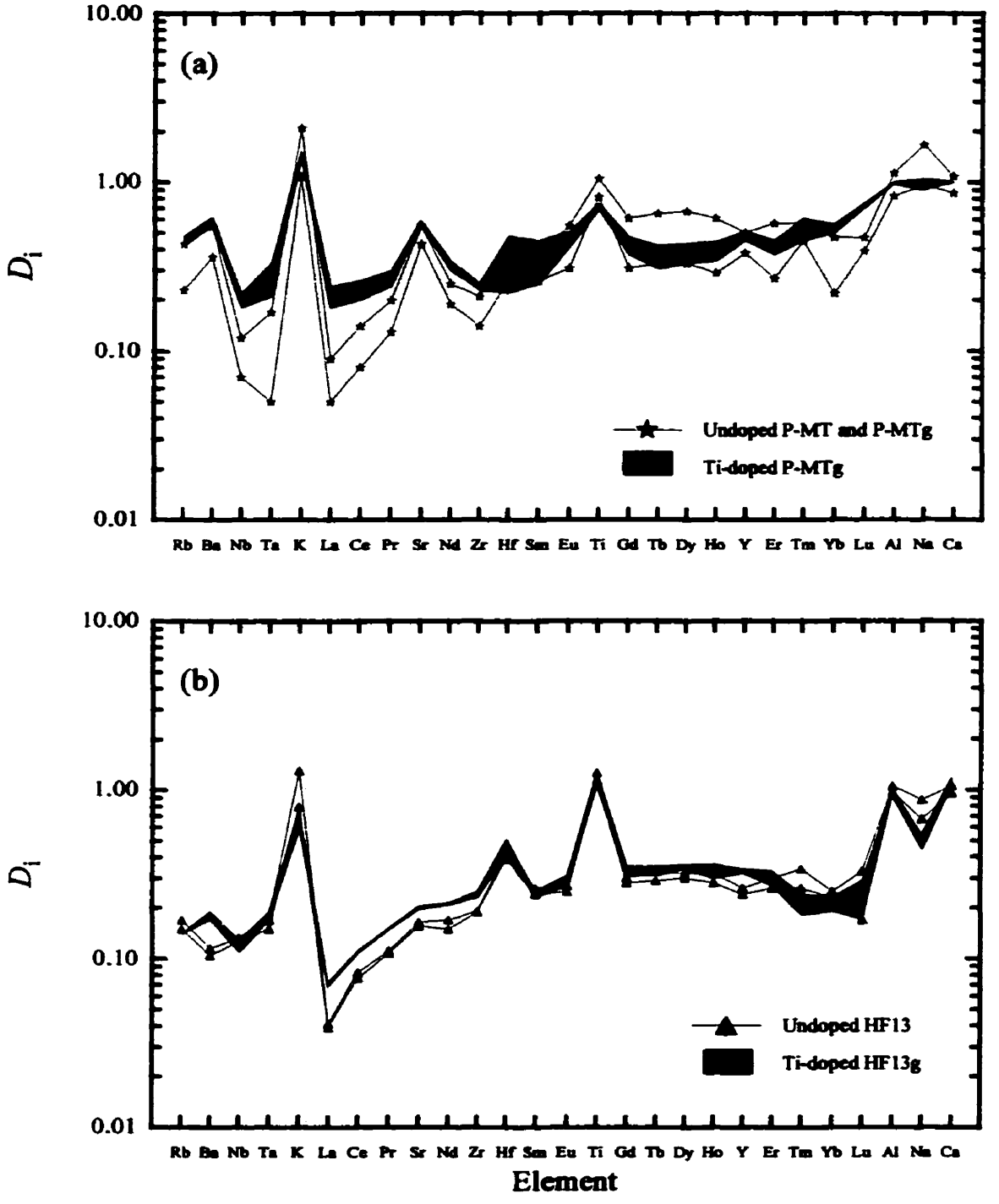
(a)
10.00
1.00
0.10
0.01
D_i
Undoped P-MT and P-MTg
Ti-doped P-MTg
Rb Ba Nb Ta K La Ce Pr Sr Nd Zr Hf Sm Eu Ti Gd Tb Dy Ho Y Er Tm Yb Lu Al Na Ca
(b)
10.00
1.00
0.10
0.01
D_i
Undoped HF13
Ti-doped HF13g
Rb Ba Nb Ta K La Ce Pr Sr Nd Zr Hf Sm Eu Ti Gd Tb Dy Ho Y Er Tm Yb Lu Al Na Ca
Element

compatible) at the same pressure, water content, oxygen fugacity, similar temperatures, and similar melt compositions. Only D_{Ti} decreases in P-MT runs whereas D_{Rb}, D_K, D_{Tm}, and D_{Na} decrease in HF13 runs as the bulk titanium increases (Figs. 5.3a, -b). Furthermore, there are no real significant differences between undoped and Ti-doped experiments for D_{Hf}, D_{Sm}, D_{Gd}, D_{Tb}, D_{Ho}, D_{Er}, D_{Al}, and D_{Ca} whereas as mentioned previously in Chapter 3 these partition coefficients are in general lower for the HF13 materials than those measured in the P-MT materials due to the bulk composition differences. The relative variation of D_{Ba}, D_{Sr}, and D_{Ta} with increasing titanium may also be influenced by the bulk composition differences (compared Figs. 5.3a *vs.* 5.3b). Figure 5.4 shows the variations in partition coefficients against the trace element ionic radius. As mentioned previously, the HFSE (*e.g.*, Ta^{5+}, Zr^{4+}) will partition in the octahedral *M*(1,2,3) sites but along two hyperbolic curves due to their difference in charge (see Fig. 3.8). The REE (*e.g.*, La, Ce, Pr, Nd) and LILE (*e.g.*, Sr) will partition in the *M*(4) site (into VIII-fold coordination), again along two different hyperbolic curves due to difference in their charge (*i.e.*, 3+ and 2+, respectively). Ba (LILE), should partition into the *A* site as based on the ionic radius and partition coefficient arguments discussed previously.

Based upon site occupancies, Figure 5.4 shows that the addition of titanium to the *M*(2) site affects partition coefficients in at least two other crystallographic sites, *M*(4) and *A*. I observed from the undoped P-MT experiments that D_{LILE} (Sr and Ba) and D_{LREE} (La, Ca, Pr, Nd) were higher by a factor of ~3.5 and ~1.5, respectively, than the undoped HF13 experiments as previously discussed. These observations were similar between both Ti-doped P-MTg_{Ti}-31 and HF13g_{Ti}-03 experiments where D_{LILE} and D_{LREE} were higher by a factor of

Figure 5.4. Variation in partition coefficient observed for different crystal lattice-sites of amphibole run products due to the effect of titanium. (a) P-MT materials. Symbols denote: P-MT-27 and P-MTg-12 experiments (Undoped P-MT and P-MTg); P-MTg_{Ti}-31 experiment (Ti-doped P-MTg). (b) HF13 materials. Symbols denote: HF13-38 experiment (Undoped HF13); HF13g_{Ti}-03 experiment (Ti-doped HF13g).

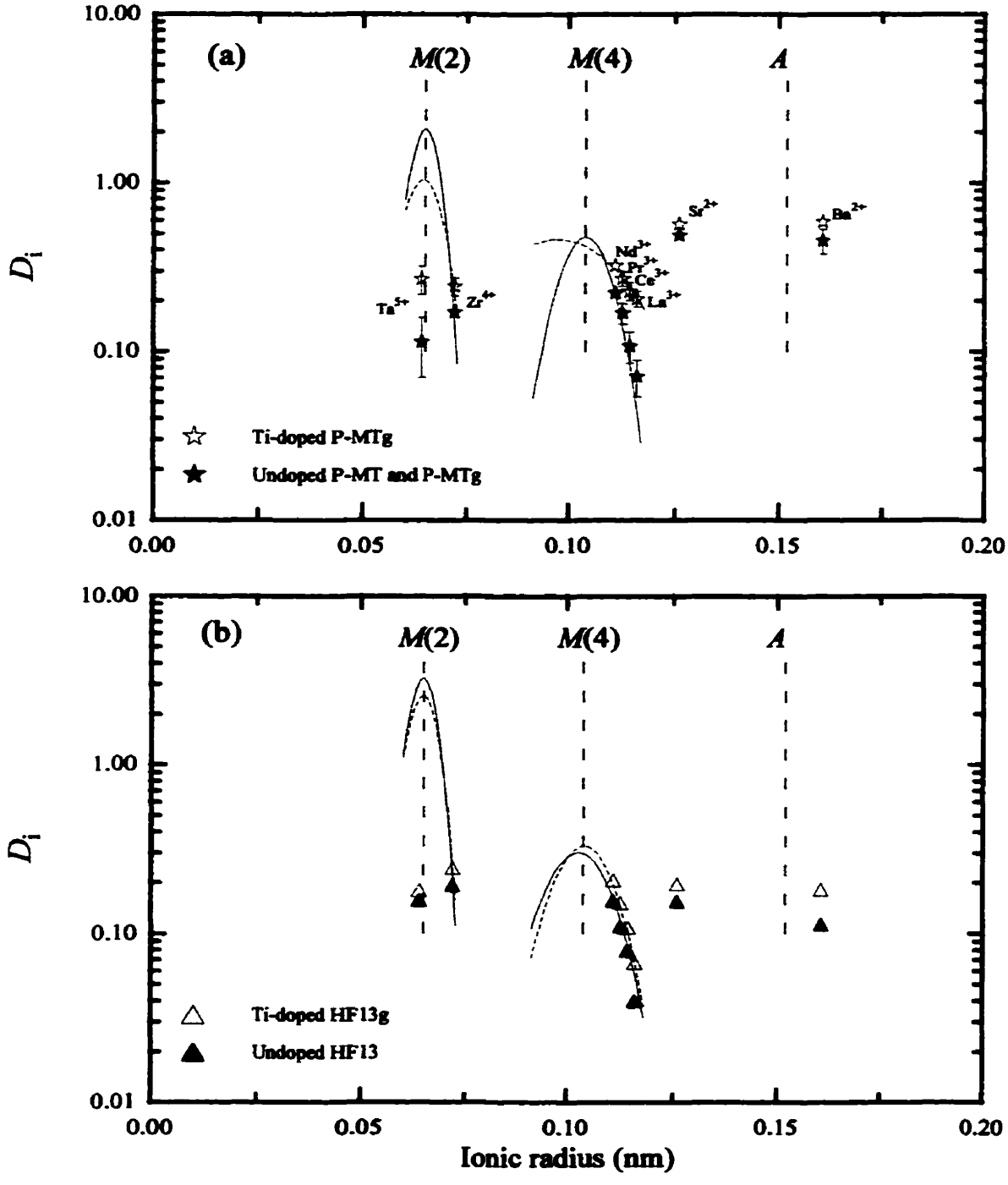
(a)
M(2)
M(4)
A
10.00
1.00
0.10
0.01
D_i
Ta^{5+}
Zr^{4+}
Nd^{3+}
Pr^{3+}
Ce^{3+}
La^{3+}
Sr^{2+}
Ba^{2+}
Ti-doped P-MTg
Undoped P-MT and P-MTg
0.00
0.05
0.10
0.15
0.20
(b)
M(2)
M(4)
A
10.00
1.00
0.10
0.01
D_i
Ti-doped HF13g
Undoped HF13
0.00
0.05
0.10
0.15
0.20
Ionic radius (nm)

~3.0 and ~1.4, respectively. Based on these experiments it is difficult to determine if titanium ($^{VI}Ti_{M(2)}$) will affect partitioning in other sites such as $T(1)$, and $T(2)$ sites.

The different lattice-site parameters for the $M(4)$ and $M(2)$ were calculated for each undoped and Ti-doped experiments using Eq.(3) based on partition coefficients (Table 5.2). In general, the D_o and $\bar{E}$ decrease as the $Ti^{4+}_{M(2)}$ increases for the $M(4)$ and $M(2)$ sites. Such a decrease in the Young's modulus (*i.e.*, $\bar{E}$) indicates that the mechanical strain energy [see Eq. (2)] around a substitute, homovalent cation in the amphibole decreases as $Ti^{4+}_{M(2)}$ increases, which implies that partitioning becomes more favourable. Those variations, however, are within error from partitioning. I observe also that r_o of the $M(2)$ site remains constant while some variations occur for the $M(4)$ site as the $Ti^{4+}_{M(2)}$ increases (Table 5.2). This suggests that any increases in the mean bond-length of the $\langle M(2)\text{-O}\rangle$ during the substitution of a larger cation (*e.g.*, Ti *vs.* Al) into the $M(2)$ site might not be observable based upon partition coefficient data.

An opposite behaviour was observed for D_o and $\bar{E}$ calculated for the $M(4)$ site of the HF13 experiments when the $Ti^{4+}_{M(2)}$ increases (Table 5.2). In such a case, D_o and $\bar{E}$ increased while r_o decreased for similar run conditions as mentioned above. A difference in the bulk composition of the amphibole run product might explain the different behaviours of the Ti-doped P-MT and HF13 experiments (*i.e.*, kaersutite *vs.* Ti-rich pargasite; see Fig. 3.3). However, the Ti-rich pargasite which crystallized from the $HF13g_{Ti}$-03 experiment has similar $\bar{E}$ and r_o values to those of the undoped P-MT-27 and P-MTg-12 experiments (Table 5.2) and all amphiboles in these experiments have similar compositions for some major elements (see Fig. 3.3 and Table 3.5).

Table 5.2. Calculated lattice-site parameters (unconstrained) for undoped and Ti-doped experiments

run #	site[a]	D_o	$\bar{E}$ (GPa)	r_o (nm)
P-MT-27	*M*(4)	0.48 (0.14)	445.44 (134.1)	0.104[a]
P-MTg-12		0.50 (0.06)	207.56 (9.44)	0.101
P-MTg_{Ti}-31		0.46 (0.05)	61.49 (33.30)	0.097 (0.013)
P-MT-27	*M*(2)	2.10 (0.97)	2213.58 (562.4)	0.065
P-MTg-12		1.68 (1.11)	1649.20 (684.8)	0.065 (0.001)
P-MTg_{Ti}-31		1.05 (0.79)	1161.83 (786.65)	0.065 (0.006)
HF13-38	*M*(4)	0.30 (0.02)	259.97 (53.31)	0.103 (0.001)
HF13g_{Ti}-03		0.33 (0.02)	302.44 (28.90)	0.104 (0.001)
HF13-38	*M*(2)	3.27 (0.48)	2329.75 (154.75)	0.065
HF13g_{Ti}-03		2.69 (0.70)	1991.22 (269.72)	0.065

Abbreviations: D_o-maximum partition coefficient, $\bar{E}$-Young's modulus, r_o-optimum ionic radius. [a] Calculated lattice-site parameters using D_{REE} (D_{La} up to D_{Lu}) and D_Y for the *M*(4) site and D_{Ti}, D_{Hf}, and D_{Zr} for the *M*(2) site. The parameters were calculated using Eq. (3) (see text). [a] Optimum ionic radius which does not have parentheses imply the absence of significant variations obtained from calculations.

The trace elements mentioned above do not partition into the same crystallographic sites (*e.g.*, LREE's and Sr in *M*(4) site, HFSE's in the *M*(1,2,3) sites, Rb and Ba in the *A* site). Increasing trace element concentrations, which partition at different sites other than *M*(1,2,3), in calcic amphiboles could be possible if modifications occur in the crystal unit-cell dimensions (*i.e.*, **a**, **b**, **c**, and **β**). Della Ventura and Robert (1990) inferred that the increases in **a**, **b**, and **β** cell parameters of Sr-bearing richterite are due to the substitution of ^{VIII}Sr (ionic radius = 0.126 nm) for ^{VIII}Ca (ionic radius = 0.112 nm) in the *M*(4) site while **c** remains practically the same. In another study, Della Ventura *et al.* (1993) showed that the cell volume increases regularly in response to increasing the size of cations partitioning into the *M*(1,2,3) sites for synthetic nickel-magnesium-cobalt-potassium richterite. They showed that as nickel (ionic radius = 0.069 nm), magnesium (ionic radius = 0.072 nm), and cobalt (ionic radius = 0.0745 nm) substitute and fill the *M*(1,2,3) sites of their potassium richterites, the cell parameters **a** and **b** increases, while **c** remains stable and **β** decreases. In this regard, isovalent substitution of a host cation for a larger or smaller cation in a given site will tend to modify the cell parameters of the mineral. In our mechanism of substitution, I confidently believe that the cell parameters of calcic amphibole undergo modifications to accommodate a higher proportion of trace elements in the crystal structure due to: (1) the mechanism of coupled substitution occurring between cations of a different ionic radii where ^{VI}(Mg^{2+}, Ti^{4+}) have ionic radii of 0.072 and 0.0605 nm, respectively, and ^{VI}(Fe^{2+}, Al^{3+}) have an ionic radii of 0.078 and 0.0535 nm, respectively; (2) this heterovalent coupled substitution will force modifications of other cations in other sites (*e.g.*, $[OH^{-}_{O(3)}]_{-1} \rightleftharpoons [O_{O(3)}]$) to ensure overall electrical neutrality of the

unit cell (*i.e.*, charge balance between cations and anions). However, I can not explain why $^{VI}Mg^{2+}$ and $^{VI}Ti^{4+}$ concentrations increase in the crystal structure of amphibole and why the larger cations such as the ^{VIII}LREE, ^{VI}HFSE, and ^{XII}LILE concentrations increase simultaneously. Hawthorne (1983; Fig. 55) showed that as the mean bond-length of the octahedral sites (*i.e.*, $\langle M(1,2,3)\text{-O}\rangle$) increases in different amphibole groups (*e.g.*, alkali, sodic-calcic, and calcic amphibole), the mean bond-length between the $M(4)$ cation and its neighbouring oxygen anions increases too (*i.e.*, $\langle M(4)\text{-O}\rangle$ increases). Furthermore, this effect of octahedral cation sizes on the mean bond-length $\langle M(4)\text{-O}\rangle$ seems to be more dominant than the size of the $M(2)$ cation (Hawthorne 1983). This study shows that by keeping the same pressure and practically the same temperatures (*i.e.*, within 20 to 30 °C) between the undoped and Ti-doped experiments, the variations in LREE and other trace elements in amphibole run products are the result of the bulk Ti content (*i.e.*, $^{VI}Ti_{M(1,2,3)}$). Following this relationship between the ionic radius of the cation in $M(2)$ site with respect to the $\langle M(4)\text{-O}\rangle$, a tentative explanation for our experiments is that as the coupled substitution mentioned above occurred (*i.e.*, $[\{Fe_4^{2+} + (Al^{3+}, Fe^{3+}, Cr^{3+})\}_{M(1,2,3)} + (OH^-)_{O(3)}]_{-1} \rightleftharpoons [(Mg_4^{2+} + Ti^{4+})_{M(1,2,3)} + (O^{2-})_{O(3)}]$), the larger cation ^{VI}Ti (0.0605 nm) replaced the smaller cation ^{VI}Al (0.0535 nm) into the $M(2)$ site (*i.e.*, both cations should partition into the $M(2)$ site; Oberti *et al.* 1995), thus increasing the $\langle M(1,2,3)\text{-O}\rangle$ and the $\langle M(4)\text{-O}\rangle$ mean bond-lengths to accommodate larger cations (*e.g.*, $^{VIII}[Sr, LREE]_{M(4)}$ and $^{VI}[Ta, Zr]_{M(1,2,3)}$).

5.1.6. Comments on the behaviour of D_{Ti}

The titanium in P-MT experiments becomes more incompatible as the bulk titanium concentration increases (*i.e.*, 0.98 to 0.72 for P-MTg-12 and P-MTg_{Ti}-31, respectively; Table 8). In these experiments, the addition of titanium eliminated phlogopite from the stable phase assemblage and olivine + clinopyroxene (where some were equilibrium phases as discussed before) crystallized prior or together with amphibole instead of phlogopite due to the increase in the $Mg\#_t$ of the liquid, while liquid SiO_2 contents remained virtually invariable (*i.e.*, 37 and 38 wt.% SiO_2 for P-MTg-12 and P-MTg_{Ti}-31, respectively). For the HF13 runs, the D_{Ti} and SiO_2 content of the liquids were constant (*i.e.*, D_{Ti}~1.2 and $SiO_2^{liquids}$~36 wt.%) while the $Mg\#_t$ increased (Tables 3.6 and 3.10). The positive relationship observed by Adam *et al.* (1993) between D_{Ti} and SiO_2 content of the liquid or matrix phase is not supported by the P-MT and HF13 experiments. The variation observed for D_{Ti} ranges from slightly incompatible (*i.e.*, 0.72 ; for P-MTg_{Ti}-31) to compatible (*i.e.*, 1.20; for HF13-38). Such variation in D_{Ti} should correspond to at least a 5 wt.% SiO_2 variation in the liquid using Adam *et al.*'s (1993; see Fig. 1) diagram which is not what I observed (*i.e.*, 38 to 37 wt.% SiO_2 for P-MTg_{Ti}-31 and HF13-38, respectively; Table 3.6). However, the absence of ferric-iron in these low oxygen fugacity experiments make comparison with other experimental work performed at higher fO_2's (*e.g.*, Nicholls and Harris 1980, Green and Pearson 1985a, Adam *et al.* 1993, Adam and Green 1994) difficult because different mechanisms of substitution could occur between titanium and Fe^{3+} at higher fO_2's (Dyar *et al.* 1993, Popp and Bryndzia 1992, Popp *et al.* 1995).

5.1.7. The general trends observed by modifying the bulk titanium

In general, the effect of increasing the bulk titanium concentrations in these experiments can be summarized in the following manner. At a given temperature increasing TiO_2 increases the Mg# of calcic amphibole and its respective equilibrium liquid. Addition of titanium decreases the stability field of phlogopite and increases olivine's due to the increase in the $Mg\#_t$ of the liquid. The incorporation of Ti into the amphibole structure involves a coupled substitution between $[Fe^{2+}, Al^{3+}]_{M(1,2,3)}$ and $[Ti^{4+}, Mg^{2+}]_{M(1,2,3)}$ which occurs at the octahedral sites. Addition of Ti to amphibole results in Ba, Ta, La, Ce, Pr, Sr, Nd, and Zr becoming more compatible (*i.e.*, partitioning increases).

Chapter 6

Petrogenetic implications: The role of pressure and oxygen fugacity at upper mantle conditions

In this study, I have shown that partition coefficients between amphibole and basaltic melt were modified by increasing pressure (1.5 to 2.5 GPa) and/or by increasing oxygen fugacity (log fO_2 between NNO-2 to NNO+1.7). One important conclusion from these effects is the opposite variation in D_{HFSE} (*e.g.*, Nb, Zr) *vs.* D_{LILE} (*e.g.*, Rb) between amphibole and basaltic melt with respect to pressure and fO_2 whereas D_{MREE} and D_{HREE} varied by less than approximately one standard deviation. The observed variations in partition coefficients between amphibole and basaltic melt can be used to discriminate and evaluate the role of amphibole in the petrogenetic evolution of an alkaline magmatic basaltic rock series formed at different pressures and fO_2's.

Figure 6.1 shows the variation of HFSE/Rb ratios *vs.* HFSE (*i.e.*, Nb and Zr) for some basaltic lava flows of the Northern Canadian Cordillera. The most enriched rocks in incompatible elements (*i.e.*, ol-nephelinite and basanite referred as Ol-NEPH and BASAN, respectively) demonstrate a larger scatter in their Nb/Rb ratio (*i.e.*, 1.6 to 8 and 2.1 to 4.5 for Ol-NEPH and BASAN, respectively) and in their Zr/Rb ratio (*i.e.*, 6.1 to 33 and 8 to 19 for Ol-NEPH and BASAN, respectively) compared to those rocks with less incompatible elements (*i.e.*, alkaline olivine basalts referred as AOB) where Nb/Rb and Zr/Rb ratios range between 1.3 to 1.9 and 7 to 9, respectively.

Francis and Ludden (1995) suggested that nephelinite lava flows from the Northern Canadian Cordillera could result directly from the melting of amphibole in peridotite

Figure 6.1. Variation in incompatible elements within three alkaline lava suites located in the Northern Canadian Cordillera. (a) Nb/Rb ratio against Nb. (b) Zr/Rb against Zr. Symbols denote: olivine nephelinites (Ol-NEPH); basanites (BASAN); alkaline olivine basalts (AOB). Data sources: Eiché *et al.* (1987), Francis and Ludden (1990), Francis and Ludden (1995), and Francis D. (pers. comm., 1997).

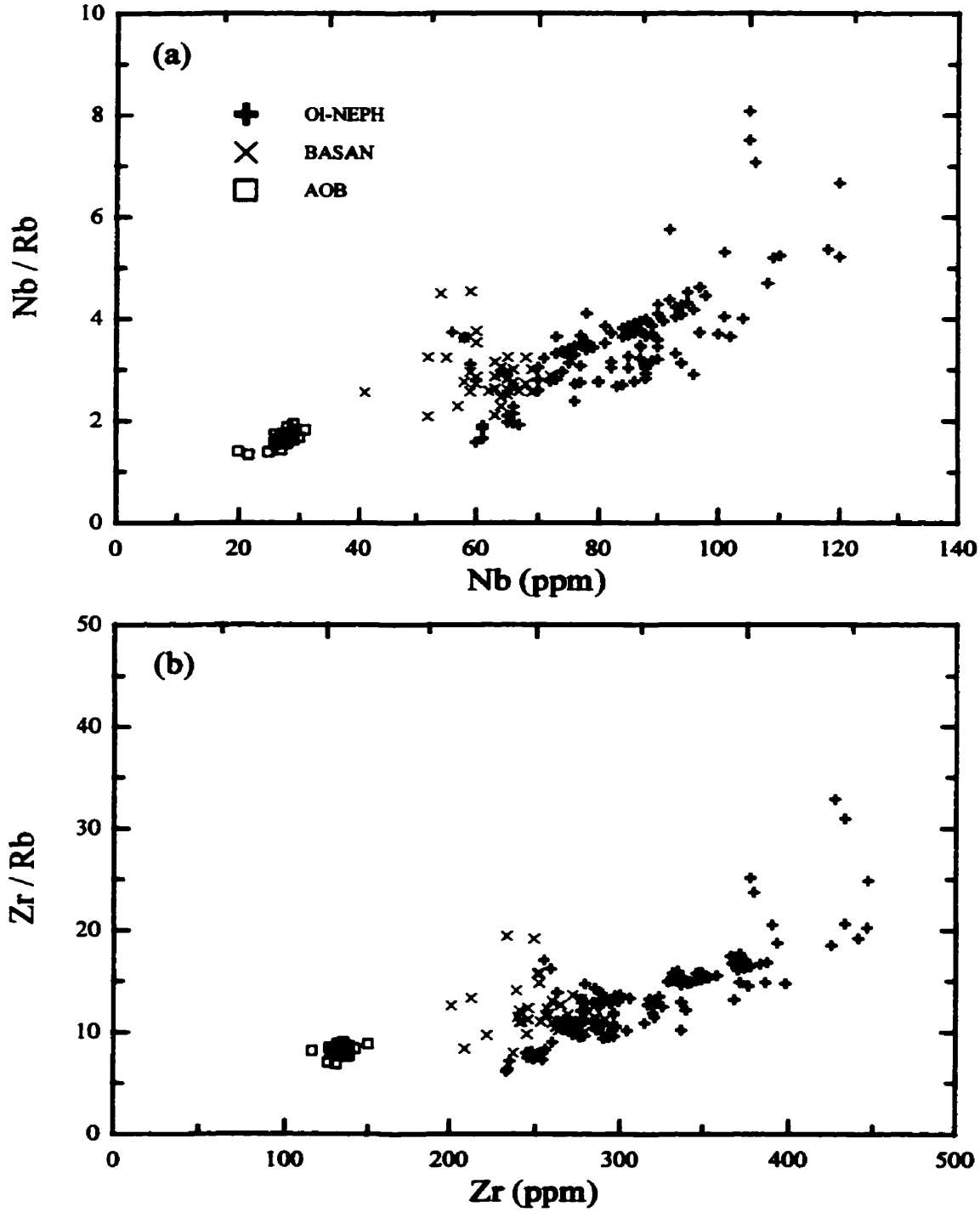
(a)
Ol-NEPH
BASAN
AOB
Nb / Rb
Nb (ppm)
0
2
4
6
8
10
0
20
40
60
80
100
120
140
(b)
Zr / Rb
Zr (ppm)
0
10
20
30
40
50
0
100
200
300
400
500

(*i.e.*, amphibole-bearing lherzolite source). Furthermore, they proposed that the amphibole in the source remains as a residual phase during the production of ol-nephelinites and basanites up to 6 wt.% of melting, at which point amphibole disappeared from the source (amph-out), and continuous melting of the residue involved anhydrous peridotitic minerals (*i.e.*, clinopyroxene, orthopyroxene, olivine, garnet; Francis and Ludden 1995). Based on our experiments performed with P-MT and P-MTg materials (*i.e.*, P-MT-27, P-MT-34, P-MTg-43, and P-MTg-41), I will demonstrate that the relatively large scatter observed in the Nb/Rb and Zr/Rb ratios for the ol-nephelinites and basanites can possibly be explained by partial melting of similar-composition amphibole-bearing lherzolite sources at different mantle pressures and oxygen fugacities.

In our model, I used mineral proportions identical to Francis and Ludden's (1995) model with the exception of the amphibole (*i.e.*, 14 % instead of 10 % in modal proportion) and garnet (*i.e.*, 1 % instead of 5 % in modal proportion). These modifications were necessary because I chose a bulk peridotite composition different than the Francis and Ludden (1995) source since Rb, Nb, and Zr concentrations were not considered in their modelled source. The initial amphibole-bearing lherzolite used in modelling was a natural sample taken from O'Reilly and Griffin (1988; sample: WGBM 16) for Rb (1.07 ppm), Nb (2 ppm), Zr (12 ppm), and Ce (3.5 ppm). This composition was chosen because no amphibole-bearing lherzolites have yet been found in the Canadian Cordillera (Francis and Ludden 1990, Francis and Ludden 1995, Lang *et al.* 1997). This amphibole-bearing lherzolite composition was normalized to obtain 6 ppm of Ce which was the value used by Francis and Ludden (1995)

for their modelled source. Such a normalisation process is necessary to reproduce the most evolved rocks such as the basanites (BASAN) and the alkaline olivine basalts (AOB) using our bulk starting composition. The normalization does not affect the conclusions of the modelling. Table 6.1 shows the parameters used for the modelling of the non-modal melting of an amphibole-bearing lherzolite by continuing and collecting melt [*i.e.*, separating melts aggregate together in a well-mixed reservoir, see Shaw 1970; Eq. (14)]. The modelled melting of the amphibole-bearing lherzolite occurred by two main processes as proposed by Francis and Ludden (1995). As mentioned above, the first melting process involves the melting of amphibole to form clinopyroxene, garnet, and melt:

1.0 amph → 0.1 cpx + 0.3 gt + 0.6 melt (in wt.%; Francis and Ludden 1995)

After all the amphibole is consumed, which corresponds to ~6 % of the total melting (*i.e.*, f = 0.06), the second melting process involves the reaction where clinopyroxene, orthopyroxene, and garnet melt to form olivine and melt:

0.5 cpx + 0.5 gt + 0.3 opx → 0.3 ol + 1.0 melt (in wt.%; Francis and Ludden 1995)

During the different melting processes, I fixed the *D*'s for clinopyroxene, orthopyroxene, olivine, and garnet while the *D*'s for amphibole (*i.e.*, D_{Rb}, D_{Nb}, and D_{Zr}) were modified according to the different pressure and fO_2 conditions (Table 6.1). Even if pressure and oxygen fugacity have an effect on partition coefficients between clinopyroxene, orthopyroxene, olivine, garnet and basaltic melt, they are insignificant during the first melting process. They could however be important during the second melting process. In any case, there are no experimental studies showing the effect of pressure and oxygen fugacity on D_{Rb},

Table 6.1. Parameters used for the non-modal melting of an amphibole-bearing lherzolite.

			amphibole/melt partition coefficient			
Element	amph-lh.[1] (ppm)	amph-lh[2] (ppm)	P-MT-27 (1.5, low)[3]	P-MT-34a (2.5, low)	P-MTg-43 (1.5, high)	P-MTg-41 (2.5, high)
Ce	3.5	6.0				
Rb	1.07	1.83	0.32	0.63	0.54	1.04
Nb	2	3.43	0.08	0.04	0.08	0.03
Zr	12	20.6	0.16	0.09	0.21	0.08

	mineral/melt partition coefficient			
	cpx[4]	opx[5]	ol[6]	gt[7]
Rb	0.02	0.0002	0.0002	0.007
Nb	0.01	0.0014	5.0E-5	0.004
Zr	0.22	0.0033	6.8E-4	0.5

Bulk partition coefficient (first process[8])

	P-MT-27	P-MT-34a	P-MTg-43	P-MTg-41
Rb	0.047	0.090	0.078	0.148
Nb	0.013	0.007	0.013	0.005
Zr	0.050	0.041	0.057	0.039

Bulk partition coefficient (second process[9])

Rb	0.003
Nb	0.002
Zr	0.057

[1] Amphibole-bearing lherzolite from O'Reilly and Griffin (1988; sample: WGBM 16) where the modal proportion of hydrous phase is <1 % (amphibole and mica). [2] Normalized to 6 ppm of Ce (see text). [3] Number indicates run pressure (in GPa) and fO_2 (low ~NNO-2 and high ~NNO+1.7). [4] Values from Adam *et al.* (1993; run: 1389). [5] Values from Kennedy *et al.* (1993; run: RPII 45) with the exception of D_{Rb} (best estimated value); [6] Values from Kennedy *et al.* (1993; run: PO 49) with the exception of D_{Rb} (best estimated value). [7] Values from Adam *et al.* (unpubl.) [see Green (1995) and pers. comm.]. [8] Where amphibole, clinopyroxene, orthopyroxene, olivine, and garnet are involved. [9] Where clinopyroxene, orthopyroxene, olivine, and garnet are involved (amph-out). Note that garnet would be a metastable phase during the melting process at 1.5 GPa.

D_{Nb}, and D_{Zr} for clinopyroxene, orthopyroxene, olivine, and garnet so such possible effects had to be ignored.

The different models reproduce the scatter observed in the Nb/Rb and Zr/Rb ratios of the nephelinites and basanites from the Northern Canadian Cordillera (Fig. 6.2). As can be observed, both Nb/Rb and Zr/Rb ratios become horizontal or have a negative slope, respectively, when amphibole has been totally melted (*i.e.*, f = 0.06). This behaviour results in a change of the bulk partition coefficient (*i.e.*, $\bar{D}$) due to the loss of amphibole in the peridotite (see Table 6.1). A positive slope for the Nb/Rb and Zr/Rb ratios results in a higher $\bar{D}_{Rb}$ compared to $\bar{D}_{Nb}$ and $\bar{D}_{Zr}$ due to the presence of amphibole (*i.e.*, first process; Table 6.1). This relationship between Rb, Nb, and Zr is reversed when the amphibole in the source disappears and where clinopyroxene, orthopyroxene, olivine, and garnet are involved in the melting (*i.e.*, second process; Table 6.1). Such a reverse relationship is further emphasized for the Zr/Rb ratio where $\bar{D}_{Zr}$ is a factor of 19 larger than $\bar{D}_{Rb}$; which produces the negative slope.

The proposed models suggest that the scatter of some HFSE/Rb ratios observed in the most undersaturated alkaline basaltic lava flows of the Northern Canadian Cordillera may be due to the melting of hydrous amphibole-bearing lherzolite at different pressures and oxygen fugacities. This scenario can be envisaged if the upper mantle was zoned with respect to oxygen fugacity during or before the formation of Late-Tertiary-to-Recent olivine nephelinite magmas beneath the Northern Canadian Cordillera by metasomatic fluids (*e.g.*, Mattioli *et al.* 1989). Based on coexisting ilmenite-spinel pairs from kimberlitic xenoliths,

Figure 6.2. Non-modal melting of an amphibole-bearing lherzolite for different pressures and oxygen fugacities. (a) Nb/Rb ratio against Nb. (b) Zr/Rb ratio against Zr. Abbreviations denote: model using P-MT-27 experiment (1.5 GPa, low fO_2); model using P-MT-34a experiment (2.5 Gpa, low fO_2); model using P-MTg-43 experiment (1.5 Gpa, high fO_2); model using P-MTg-41 experiment (2.5 Gpa, high fO_2); pargasite compositions (Table 3.4) from P-MT-27, P-MT-34a, P-MTg-43, P-MTg-41 experiments (pargasite). Note that the amphibole-out limit corresponds to approximately 6 wt.% of melting (*i.e.*, f = 0.06, see text). Numbers indicate total fraction of melting (wt.%). Symbols same as in Fig. 6.1.

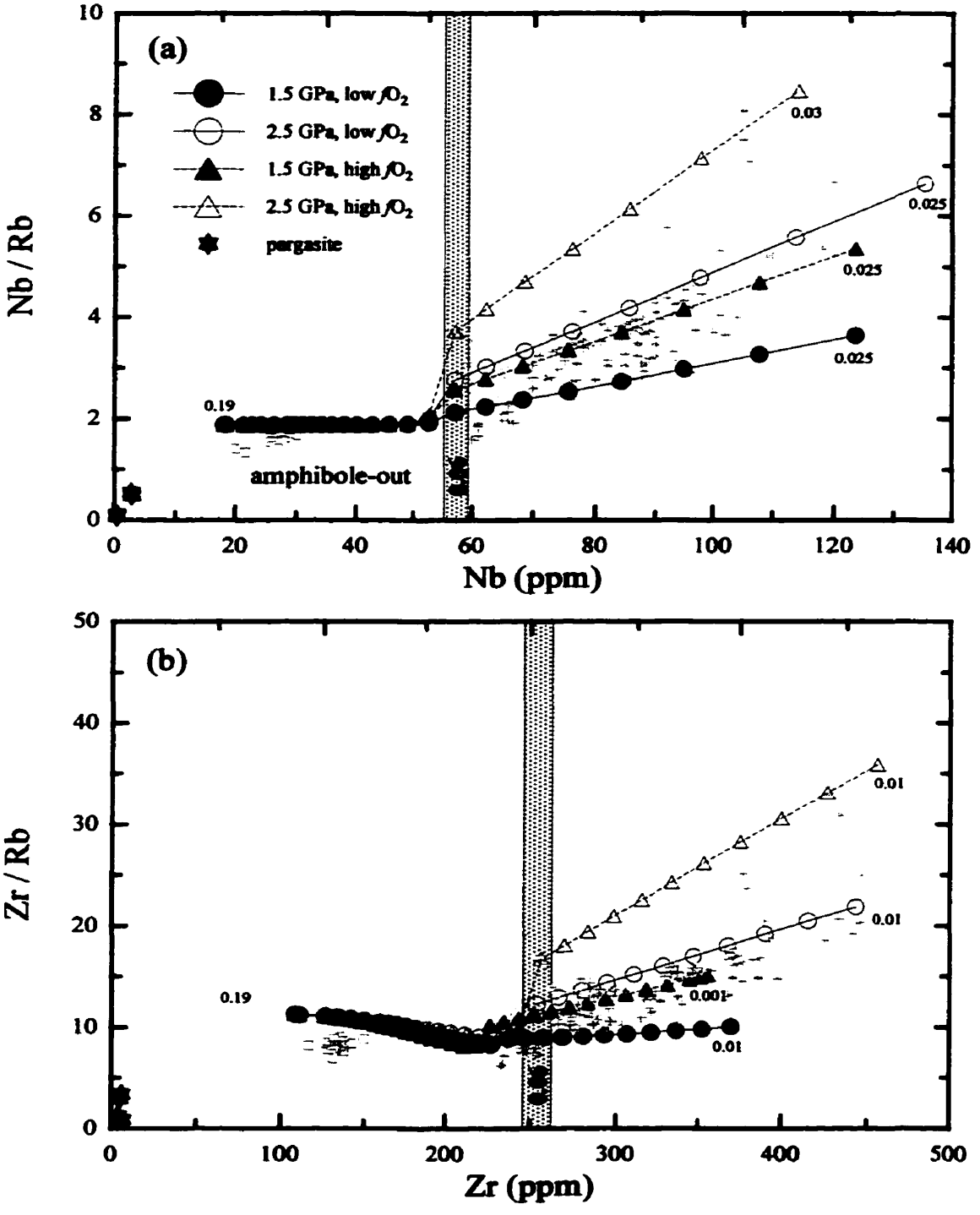
(a)
1.5 GPa, low fO_2
2.5 GPa, low fO_2
1.5 GPa, high fO_2
2.5 GPa, high fO_2
pargasite
0.03
0.025
0.025
0.025
0.19
amphibole-out
Nb / Rb
Nb (ppm)
0
2
4
6
8
10
0
20
40
60
80
100
120
140
(b)
0.01
0.01
0.001
0.19
0.01
Zr / Rb
Zr (ppm)
0
10
20
30
40
50
0
100
200
300
400
500

Haggerty and Tompkins (1983) have estimated different redox states of the lithosphere and asthenosphere depending upon the tectonic setting. They proposed that a fertile asthenosphere is relatively oxidized whereas depleted lithosphere is relatively reduced which can encompass a range of oxygen fugacities between the Iron-Wüstite (IW) to the QFM buffers, respectively (Haggerty and Tompkins 1983). Shi *et al.* (in press) suggest that their bimodal xenolith suite (lherzolite and harzburgite) sampled from different localities along the Northern Canadian Cordillera represents lithospheric mantle that may have been influenced by an underlying hot asthenospheric mantle transporting volatiles. Such a process could, according to the estimation of Haggerty and Tompkins (1983), influence the regional redox state of the lithosphere beneath the Northern Canadian Cordillera. Thus, when melted at differing fO_2 conditions and pressures the amphibole-bearing lherzolite could produce melts of significantly different trace element concentrations.

Studies of xenoliths support the presence of a range of redox conditions in the upper mantle below the Canadian Cordillera. Mattioli *et al.* (1989) estimated the redox state of various spinel-bearing lherzolite and harzburgite xenoliths sampled from various localities in the Northern Canadian Cordillera between ~0.5 log unit below QFM to ~2.0 log unit above the QFM for conditions between 900 to 1100 °C, 1.5 GPa. However, due to the absence of amphibole in xenoliths brought to the surface in the Northern Canadian Cordillera (Francis and Ludden 1990, Francis and Ludden 1995, Shi *et al.* in press) and the absence of quenched alkali-rich melts, it is difficult to prove this hypothesis. However, our model does not conflict with the proposed model of Francis and Ludden (1995) regarding the presence or absence of

amphibole in a metasomatized peridotite source, but it brings a new critical look at some of the scatter observed in the most undersaturated bulk rock analyses.

Chapter 7

Conclusion

A large suite of major, minor, and trace element (LILE, HFSE, REE) partition coefficients between calcic amphibole and basaltic melt were reported over a pressure range of 1.5 to 2.5 GPa, an oxygen fugacity range of NNO-2 to NNO+1.7, and a temperature range of 1000 to 1130 °C using natural basaltic compositions including a pargasite, kaersutite, ol-normative nephelinite, tholeiite, alkali basalt, and two Ti-doped basaltic materials. Two microbeam instruments (SXRFM and LAM-ICP-MS) were used to determine the equilibrium partition coefficient of the trace elements between experimentally produced calcic amphibole and basaltic melt. Similar to identical *D's* were obtained by SXRFM compared to those measured by LAM-ICP-MS on the same run products of a single experiment. However, the LAM-ICP-MS has a better overall lower limit of detection (LLD) (1.3 ppm or less), better precision (±10 to 15 %), and can analyze a larger suite of trace elements.

Amphiboles which crystallized from bulk amphibole materials (*i.e.*, pargasite and kaersutite) were distinct in their high Ca/(Ca+Na) and K/(K+Na) contents compared to those crystallized from the bulk rock materials (*i.e.*, ol-normative nephelinite, tholeiite, alkali basalt). Such differences affect partitioning where the D_{LILE} measured between amphibole and basaltic melt using the bulk amphibole materials was found in general to be higher by a factor of 1.2 to 3.5 relative to those measured in experiments using the ol-normative nephelinite, tholeiite, and the alkaline basalt compositions. A positive relationship was observed between the K/(K+Na) ratio of the crystallized amphibole and D_{Ba} and between the Ca/(Ca+Na) and D_{Sr}, suggesting a crystal chemical control on partitioning. Regarding other trace element

partitioning, I showed that D_{REE} between amphibole and basaltic melt could be controlled by a complex coupled substitution involving Ca, Na, Mg, Ti, Al, and Fe_{total} in the $M(4)$ and $M(1,2,3)$ sites of the amphibole. Increasing pressure showed an ambivalent behaviour on partitioning for D_{LILE}, D_{HFSE}, and D_{REE}. D_{Rb} increases whereas D_{Zr}, D_{Hf}, D_{Ti}, and D_{La} decrease when pressure increases by 0.7 or 1.0 GPa depending upon the bulk composition. The decrease of D_{Zr} with increasing pressure can be explained by a gradual decrease of the Ti/Al ratio in the $M(2)$ site of the amphibole. Increasing the oxygen fugacity at 1.5 GPa or 2.5 GPa by approximately 3 orders of magnitude (NNO-2 to NNO+1.7) increases D_{Rb}, D_{Ba}, D_{La}, and D_{Nd}, whereas D_{Ti}, D_{Hf}, and D_{Zr} decrease. Experiments investigating the role of titanium on partitioning demonstrate that the incorporation of $^{VI}Ti^{4+}$ into the amphibole structure involves a coupled substitution between $(Fe^{2+}, Al^{3+})_{M(1,2,3)}$ and $(Ti^{4+}, Mg^{2+})_{M(1,2,3)}$ which occurs at the octahedral sites and results in Ba, Sr, Ta, Zr, La, Ce, Pr, and Nd becoming more compatible, thus increasing partitioning. Based on these variations in partition coefficients, I calculated significant differences in the Rb/HFSE ratios formed during partial melting of an amphibole-bearing lherzolite occurring at different pressures and oxygen fugacities. Such P and fO_2 effects can help to explain some scatter observed in the most undersaturated rocks of an alkaline basaltic suite.

References

Adam J, Green TH, Sie SH (1993) Proton microprobe determined partitioning of Rb, Sr, Ba, Y, Zr, Nb and Ta between experimentally produced amphiboles and silicate melts with variable F content. Chem Geol 109 : 29-49

Adam J, Green TH, Sie SH (unpublished) An experimental study of trace element partitioning between peridotite minerals and melts of carbonatite and basanite composition.

Adam J, Green TH (1994) The effects of pressure and temperature on the partitioning of Ti, Sr and REE between amphibole, clinopyroxene and basanitic melts. Chem Geol 117 : 219-233

Allègre CJ, Minster JF (1978) Quantitative models of trace element behavior in magmatic processes. Earth Planet Sci Lett 38 : 1-25

Allègre CJ, Treuil M, Minster J-F, Minster B, Albarède F (1977) Systematic use of trace element in igneous process. I. Fractional crystallization processes in volcanic suites. Contrib Mineral Petrol 60 : 57-75

Bajt S, Rivers M, Sutton S (1992) X-ray fluorescence microprobe. In: Workshop on applications of synchrotron radiation to Earth materials. National Synchrotron Light Source, Brookhaven National Laboratory, Upton, N.Y.

Baker DR (1993) Measurement of diffusion at high temperatures and pressures in silicate systems. In: Short course handbook on experiments at high pressure and applications to the Earth's mantle (Luth RW ed). Mineral Assoc Can (Nepean), 21 : 305-355

Basu AR, Murthy VR (1977) Kaersutites, suboceanic low-velocity zone, and the origin of mid-oceanic ridge basalts. Geology 5 : 365-368

Beattie P (1994) Systematics and energetics of trace-element partitioning between olivine and silicate melts: implication for the nature of mineral/melt partitioning. Chem Geol 117 : 57-71

Beattie P, Ford C, Russell D (1991) Partition coefficients for olivine-melt and orthopyroxene-melt systems. Contrib Mineral Petrol 109 : 212-224

Bergman SC, Foland KA, Spera FJ (1981) On the origin of an amphibole-rich vein in a peridotite inclusion from the Lunar crater volcanic field, Nevada, U.S.A. Earth Planet Sci Lett 56 : 343-361

Best MG (1974) Mantle-derived amphibole within inclusions in alkalic-basaltic lavas. J Geophys Res 79 : 2107-2113

Best MG (1970) Kaersutite-peridotite inclusions and kindred megacrysts in basanitic lavas, Grand Canyon, Arizona. Contrib Mineral Petrol 27 : 25-44

Blundy J, Wood B (1991a) Crystal-chemical controls on the partitioning of Sr and Ba between plagioclase feldspar, silicate melts, and hydrothermal solutions. Geochim Cosmochem Acta 55 : 193-209

Blundy J, Wood B (1991b) Partitioning of strontium between plagioclase and melt: Reply to the comment by S.A. Morse. Geochim Cosmochem Acta 55 : 1739-1741

Blundy J, Wood B (1994) Prediction of crystal-melt partition coefficients from elastic moduli. Nature 372 : 452-454

Blundy J, Wood B, Davies A (1996) Thermodynamics of rare earth element partitioning between clinopyroxene and melt in the system CaO-MgO-Al_2O_3-SiO_2. Geochim Cosmochim Acta 60 : 359-364

Boettcher AL, O'Neil JR (1980) Stable isotope, chemical, and petrographic studies of high-pressure amphiboles and micas: Evidence for metasomatism in the mantle source regions of alkali basalts and kimberlites. Am J Sci 280-A : 594-621

Bonatti E, Hamlyn P, Ottonello G (1981) Upper mantle beneath a young oceanic rift: peridotites from the island of Zabargad (Red Sea). Geology 9 : 474-479

Bohlen (1984) Equilibria for precise pressure calibration and a frictionless furnace assembly for the piston-cylinder apparatus. Neues Jahrbuch für Mineralogie Monatshefte 9 : 404-412

Bos AJJ, Vis RD, Verheul H, Prins M, Davies ST, Bowen DK, Makjanič J, Valkovič V (1984) Experimental comparison of synchrotron radiation with other modes of excitation of X rays for trace element analysis. Nucl Instrum Methods Phys Res B3 : 232-240

Bottinga Y, Weill D, Richet P (1982) Density calculations for silicate liquids. I. Revised method for aluminosilicate compositions. Geochim Cosmochem Acta 46 : 909-919

Boyd FR, England JL (1960) Apparatus for phase-equilibrium measurements at pressures up to 50 kilobars and temperatures up to 1750 °C. J Geophys Res 65 : 741-748

Boyd FR, Finger LW (1975) Homogeneity of minerals in mantle rocks from Lesotho. Carnegie Inst Wash Yearbook 74 : 519-525

Brenan JM, Shaw HF, Ryerson FJ, Phinney DL (1995) Experimental determination of trace element partitioning between pargasitic amphibole and a synthetic hydrous andesitic melt. Earth Planet Sci Lett 135 : 1-11

Brice JC (1975) Some thermodynamic aspects of the growth of strained crystals. J Crystal Growth 28 : 249-253

Campbell I, Schenk ET (1950) Camptonite dikes near Boulder Dam, Arizona. Am Mineral 35 : 671-692

Charles RW (1980) Amphibole on the joint pargasite-ferropargasite. Am Mineral 65 : 996-1001

Chazot G, Menzies MA, Harte B (1996) Determination of partition coefficients between apatite, clinopyroxene, amphibole, and melt in natural spinel lherzolites from Yemen: implications of wet melting of the lithospheric mantle. Geochim Cosmochim Acta 60 : 423-437

Cheatham MM, Sangrey WF, White WM (1993) Sources of error in external calibration ICP-MS analysis of geological samples and an improved non-linear drift correction procedure. Spectrochim Acta 48B : E487-E506

Christie DM, Carmichael ISE, Langmuir CH (1986) Oxidation states of mid-ocean ridge basalt glasses. Earth Planet Sci Lett 79 : 397-411

Colson RO, McKay GA, Taylor LA (1988) Temperature and composition dependencies of trace element partitioning: Olivine/melt and low-Ca pyroxene/melt. Geochim Cosmochim Acta 52 : 539-553

Comodi P, Zanazzi PF (1997) The pressure behavior of clinozoisite and zoisite: An X-ray diffraction study. Am Mineral 82 : 61-68

Comodi P, Mellini M, Ungaretti L, Zanazzi PF (1991) Compressibility and high pressure structure refinement of tremolite, pargasite and glaucophane. Eur J Mineral 3 : 485-499

Comodi P, Princivalle F, Tirone M, Zanazzi PF (1995) Comparative compressibility of clinopyroxenes from mantle nodules. Eur J Mineral 7 : 141-149

Cox KG, Bell JD, Pankhurst RJ (1979) The interpretation of igneous rocks. London, George Allen G and Unwin Ltd, 450p

Currie LA (1968) Limits for qualitative detection and quantitative determination. Anal Chem 40 : 586-593

Dalpé C, Baker DR (1993) The importance of amphibole and mica in the generation of alkali basaltic suites. Geol Assoc Can - Mineral Assoc Can 18 : A-22 (abstr)

Dalpé C, Baker DR (1994a) Partition coefficients for rare-earth elements between calcic amphibole and Ti-rich basanitic glass at 1.5 GPa, 1100°C. In: VM Goldschmidt Conference, Mineral Mag 58A : 207-208

Dalpé C, Baker DR (1994b) Pargasite - basanitic melt partition coefficients determined by laser-ablation ICP-MS. EOS (Trans Am Geophys Union) 75 : 372 (abstr)

Dalpé C, Baker DR (1997) Evidence of pressure effects on LILE, HFSE and REE partitioning between calcic amphibole and basaltic liquid. In: Geol Assoc Can - Mineral Assoc Can 22 : A-34 (abstr)

Dalpé C, Baker DR, Sutton SR (1992) Partition coefficient of Ti, Cr, Ga, Rb, Sr, Y, Nb, and Zr between pargasite and nephelinic melt at 1.5 GPa. Eos (Trans Am Geophys Union) 73 : 372 (abstr)

Dalpé C, Baker DR, Sutton SR (1995) Synchrotron x-ray-fluorescence and laser-ablation ICP-MS microprobes: useful instruments for analysis of experimental run-products. Can Mineral 33 : 481-498

Damon PE, Laughlin AW, Percious JK (1967) Problem of excess argon-40 in volcanic rocks. In: Radioactive dating and methods of low-level counting, IAEA - ICSU symposium, Monaco, Proceeding : 463-481

Dawson JB, Smith JV (1982) Upper-mantle amphiboles: a review. Mineral Mag 45 : 35-46

De Bièvre P, Barnes IL (1985) Table of the isotopic composition of the elements as determined by mass spectrometry. Int J Mass Spectrom Ion Proc 65 : 211-230

Deer WA, Howie RA, Zussman J (1992) An introduction to the rock-forming minerals. Longman, Edinburgh Gate, Union Kingdom

Della Ventura G, Robert J-L (1990) Synthesis, XRD and FTIR studies of strontium richterites. Eur J Mineral 2 : 171-175

Della Ventura G, Robert J-L, Bény J-M (1991) Tetrahedrally coordinated Ti^{4+} in synthetic Ti-rich potassic richterite: evidence from XRD, FITR, and Raman studies. Am Mineral 76 : 1134-1140

Della Ventura G, Robert J-L, Raudsepp M, Hawthorne FC (1993) Site occupancies in monoclinic amphiboles: Rietveld structure refinement of synthetic nickel magnesium cobalt potassium richterite. Am Mineral 78 : 633-640

Dickey JS Jr (1968) Eclogite and other inclusions in the mineral breccia member of the Deborah Volcanic Formation at Kakanui, New Zealand. Am Mineral 53 :1304-1319

Drake MJ, Weill DF (1975) The partition of Sr, Ba, Ca, Y, Eu^{2+}, Eu^{3+}, and other REE between plagioclase feldspar and magmatic liquid: an experimental study. Geochim Cosmochim Acta 39 : 689-712

Drake MJ, Holloway JR (1977) Partitioning of Sm between plagioclase, clinopyroxene, amphibole, and hydrous silicate liquid at high pressures. In: Papers presented to the international conference on experimental trace element geochemistry, 21-23 (abstr)

Dunn T (1987) Partitioning of Hf, Lu, Ti, and Mn between olivine, clinopyroxene and basaltic liquid. Contrib Mineral Petrol 96 : 476-484

Dunn T (1993) The piston-cylinder apparatus. In: Short course handbook on experiments at high pressure and applications to the Earth's mantle (Luth RW ed). Mineral Assoc Can (Nepean), 21 : 39-94

Dyar MD, McGuire AV, Mackwell SJ (1992) Fe^{3+}/H^{+} and D/H in kaersutites - misleading indicators of mantle source fugacities. Geology 20 : 565-568

Dyar MD, Mackwell SJ, McGuire AV, Cross LR, Robertson JD (1993) Crystal chemistry of Fe^{3+} and H^{+} in mantle kaersutite: implications for mantle metasomatism. Am Mineral 78 : 969-979

Edgar AD (1992) Barium-rich phlogopite and biotite from some Quaternary alkali mafic lavas, West Eifel, Germany. Eur J Mineral 4 : 321-330

Eiché G, Francis D, Ludden J (1987) Primary alkaline magmas associated with Quaternary Alligator Lake volcanic complex, Yukon Territory, Canada. Contrib Mineral Petrol 95 : 191-201

Ellis DJ (1976) High pressure cognate inclusions in the Newer Volcanics of Victoria. Contrib Mineral Petrol 58 : 149-180

Embey-Isztin A (1976) Amphibolite/lherzolite composite xenolith from Szigliget, north of the lake Balaton, Hungary. Earth Planet Sci Lett 31 : 297-304

Federowich JS, Richards JP, Jain JC, Kerrich R, Fan J (1993) A rapid method for REE and trace-element analysis using laser sampling ICP-MS on direct fusion whole-rock glasses. Chem Geol 106 : 229-249

Feng R (1994) In situ trace element determination of carbonates by laserprobe inductively coupled plasma mass spectrometry using nonmatrix matched standardization. Geochim Cosmochim Acta 58 : 1615-1623

Feng R, Machado N, Ludden J (1993) Lead geochronology of zircon by laserprobe - inductively coupled plasma mass spectrometry (LP-ICPMS). Geochim Cosmochim Acta 57 : 3479-3486

Forbes WC, Flower MFJ (1974) Phase relations of titan-phlogopite, $K_2Mg_4TiAl_2Si_6O_{20}(OH)_4$, a refractory phase in the upper mantle? Earth Planet Sci Lett 22 : 60-66

Francis DM (1976a) The origin of amphibole in lherzolite xenoliths from Nunivak Island, Alaska. J Petrol 17 : 357-378

Francis DM (1976b) Amphibole pyroxenite xenoliths: cumulate or replacement phenomena from the upper mantle, Nunivak Island, Alaska. Contrib Mineral Petrol 58 : 51-61

Francis D, Ludden J (1990) The mantle source for olivine nephelinite, basanite, and alkaline olivine basalt at Fort Selkirk, Yukon, Canada. J Petrol. 31 : 371-400

Francis D, Ludden J (1995) The signature of amphibole in mafic alkaline lavas, a study in the Northern Canadian Cordillera. J Petrol 36 : 1171-1191

Fujinawa A, Green TH (1997) Partitioning behaviour of Hf and Zr between amphibole, clinopyroxene, garnet and silicate melts at high pressure. Eur J Mineral 9: 379-391

Gilbert MC (1966) Synthesis and stability relations of the hornblende ferropargasite. Am J Sci 264 : 698-742

Gordon BM (1982) Sensitivity calculations for multi-elemental trace analysis by synchrotron radiation induced X-ray fluorescence. Nucl Instrum Methods Phys Res 204 : 223-229

Govindaraju K (1989) Compilation of working values and sample description for 272 geostandards. Geostand Newslett 13 : 1-113

Green TH (1994) Experimental studies of trace-element partitioning applicable to igneous petrogenesis - Sedona 16 years later. Chem Geol 117 : 1-36

Green TH (1995) Significance of Nb/Ta as an indicator of geochemical processes in the crust-mantle system. Chem Geol 120 : 347-359

Green TH, Pearson NJ (1983) Effect of pressure on rare earth element partition coefficients in common magmas. Nature 305 : 414-416

Green TH, Pearson NJ (1985a) Experimental determination of REE partition coefficients between amphibole and basaltic to andesitic liquids at high pressure. Geochim Cosmochim Acta 49 : 1465-1468

Green TH, Pearson NJ (1985b) Rare earth element partitioning between clinopyroxene and silicate liquid at moderate to high pressure. Contrib. Mineral. Petrol. 91 : 24-36

Griffin WL, Murthy VR (1969) Distribution of K, Rb, Sr and Ba in some minerals relevant to basalt genesis. Geochim Cosmochim Acta 33 : 1389-1414

Guo J, Green TH (1990) Experimental study of barium partitioning between phlogopite and silicate liquid at upper-mantle pressure and temperature. Lithos 24 : 83-95

Gunn BM (1972) The fractionation effect of kaersutite in basaltic magmas. Can Mineral 11 : 840-850

Haggerty SF, Tompkins LA (1983) Redox state of Earth's upper mantle from kimberlitic ilmenites. Nature 303 : 295-300

Hammarstrom JM, Zen E-A (1986) Aluminum in hornblende: an empirical igneous geobarometer. Am Mineral 71 : 1297-1313

Hart SR, Dunn T (1993) Experimental cpx/melt partitioning of 24 trace elements. Contrib Mineral Petrol 113 : 1-8

Harrison WJ, Wood BJ (1980) An experimental investigation of the partitioning of REE between garnet and liquid with reference to the role of defect equilibria. Contrib Mineral Petrol 72 : 145-155

Hawthorne FC (1983) The crystal chemistry of amphiboles. Can Mineral 21 : 173-480

Hawthorne FC (1993) Minerals, mineralogy and mineralogists: past, present and future. Can Mineral 31 : 253-296

Hawthorne FC, Grundy HD (1973) The crystal chemistry of the amphiboles. II. Refinement of the crystal structure of oxy-kaersutite. Mineral mag 39 : 390-400

Hawthorne FC, Ungaretti L, Oberti R (1995) Site populations in minerals: Terminology and representation of results of crystal-structure refinement. Can Mineral 33 : 907-911

Hawthorne FC, Ventura GD, Robert J-L (1996b) Short-range order of (Na, K) and Al in tremolite: An infrared study. Am Mineral 81 : 782-784

Hawthorne FC, Oberti R, Ungaretti L, Grice JD (1996a) A new hyper-calcic amphibole with Ca at the A site: Fluor-cannilloite from Pargas, Finland. Am Mineral 81 : 995-1002

Helz RT (1973) Phase relations of basalts in their melting range at $PH_2O = 5$ kb as a function of oxygen fugacity. Part I. Mafic phases. J Petrol 14 : 249-302

Henderson CMB, Foland KA (1996) Ba- and Ti-rich primary biotite from the Brome alkaline igneous complex, Monteregian Hills, Quebec: mechanisms of substitution. Can Mineral 34 : 1241-1252

Hickson CJ, Juras SJ (1986) Sample contamination by grinding. Can Mineral 24 : 585-589

Higuchi H, Nagasawa H (1969) Partition of trace elements between rock-forming minerals and the host volcanic rocks. Earth Planet Sci Lett 7 : 281-287

Hofmann AW (1986) Nb in Hawaiian magmas: constraints on source composition and evolution. Chem Geol 57 : 17-30

Hudon P, Baker DR, Toft PB (1994) A high-temperature assembly for 1.91-cm (3/4-in.) piston-cylinder apparatus. Am Mineral 79 : 145-147

Ionov DA, Hofmann AW (1995) Nb-Ta-rich mantle amphiboles and micas: implications for subduction-related metasomatic trace element fractionations. Earth Planet Sci Lett 131 : 341-356

Irving AJ (1978) A review of experimental studies of crystal/liquid trace element partitioning. Geochim Cosmochim Acta 42 : 743-770

Irving AJ, Price RC (1981) Geochemistry and evolution of lherzolite-bearing phonolitic lavas from Nigeria, Australia, East Germany and New Zealand. Geochim Cosmochim Acta 45 : 1309-1320

Jackson SE, Longerich HP, Dunning GR, Fryer BJ (1992) The application of laser-ablation microprobe - inductively coupled plasma - mass spectrometry (LAM-ICP-MS) to *in situ* trace-element determinations in minerals. Can Mineral 30 : 1049-1064

Jakobsson S, Holloway JR (1986) Crystal-liquid experiments in the presence of a C-O-H fluid buffered by graphite+iron+wüstite: experimental method and near liquidus relations in basanite. J Volcanol Geotherm Res 29 : 265-291

Jarvis KE, Williams JG (1993) Laser ablation inductively coupled plasma mass spectrometry (LA-ICP-MS): a rapid technique for the direct, quantitative determination of major, trace and rare-earth elements in geological samples. Chem Geol 106 : 251-262

Jarvis KE, Gray AL, Houk RS (1992) Handbook of inductively coupled plasma mass spectrometry. Blackie, Glasgow, UK

Jenner GA, Longerich HP, Jackson SE, Fryer BJ (1990) ICP-MS - a powerful tool for high-precision trace-element analysis in earth sciences: evidence from analysis of selected U.S.G.S. reference samples. Chem Geol 83 : 133-148

Jenner GA, Foley SF, Jackson SE, Green TH, Fryer BJ, Longerich HP (1993) Determination of partition coefficients for trace elements in high pressure-temperature experimental run products by laser ablation microprobe-inductively coupled plasma-mass spectrometry. Geochim Cosmochim Acta 57 : 5099-5103

Jensen BB (1973) Patterns of trace element partitioning. Geochim Cosmochim Acta 37 : 2227-2242

Jones JH (1988) Partitioning of Mg and Fe between olivine and liquids of lunar compositions: the role of composition, pressure and Ti speciation. In: Lunar and Planet Sci XIX:561-562 (abstr)

Jones JH (1995) Experimental trace element partitioning. In: Rock physics and phase relations, a handbook of physical constants (Ahrens TJ ed), Am Geophys Union (Washington DC), 3 : 73-104

Jenkins DM, Sherriff BL, Cramer J, Xu Z (1997) Al, Si, and Mg occupancies in tetrahedrally and octahedrally coordinated sites in synthetic aluminous tremolite. Am Mineral 82 : 280-290

Jensen BB (1973) Patterns of trace element partitioning. Geochim Cosmochim Acta 37 : 2227-2242

Jones KW, Gordon BM, Hanson AL, Hastings JB, Howells MR, Kraner HW, Chen JR (1984) Application of synchrotron radiation to elemental analysis. Nucl Instrum Methods Phys Res B3 : 225-231

Kawamoto T, Hirose K (1994) Au-Pd sample containers for melting experiments on iron and water bearing systems. Eur J Mineral 6 : 381-385

Kennedy AK, Lofgren GE, Wasserburg GJ (1993) An experimental study of trace element partitioning between olivine, orthopyroxene and melt in chondrules: equilibrium values and kinetic effects. Earth Planet Sci Lett 115 : 177-195

Kesson S, Price RC (1972) The major and trace element chemistry of kaersutite and its bearing on the petrogenesis of alkaline rocks. Contrib Mineral Petrol 35 : 119-124

Klein M, Stosch H-G, Seck HA (1997) Partitioning of high field-strength and rare-earth elements between amphibole and quartz-dioritic to tonalitic melts: an experimental study. Chem Geol 138 : 257-271

Kohn SC, Schofield PF (1994) The importance of melt composition in controlling trace-element behaviour: an experimental study of Mn and Zn partitioning between forsterite and silicate melts. Chem Geol 117 : 73-87

Kress VC, Carmichael ISE (1991) The compressibility of silicate liquids containing Fe_2O_3 and the effect of composition, temperature, oxygen fugacity and pressure on their redox states. Contrib Mineral Petrol 108 : 82-92

Lagache M, Dujon SC (1987) Distribution of strontium between plagioclase and 1 molar aqueous chloride solutions at 600°C, 1.5 kbar and 750°C, 2 kbar. Bull Minéral 110 : 551-561

Lang S, Francis D, Ludden J, Frederiksen A, Bostock M (1998) Xenolith evidence for lithospheric melting above anomalously hot mantle under the Northern Canadian Cordillera. Contrib Mineral Petrol 131 : 39-53

LaTourrette TZ, Burnett DS (1992) Experimental determination of U and Th partitioning between clinopyroxene and natural and synthetic basaltic liquid. Earth Planet Sci Lett 110 : 227-244

LaTourrette TZ, Hervig RL, Holloway JR (1995) Trace element partitioning between amphibole, phlogopite, and basanite melt. Earth Planet Sci Lett 135 : 13-30

Leake BE, Woolley AR, Arps CES, Birch WD, Gilbert MC, Grice JD, Hawthorne FC, Kato A, Kisch HJ, Krivovichev VG, Linthout K, Laird J, Mandarino JA, Maresch WV, Nickel EH, Rock NMS, Schumacher JC, Smith DC, Stephenson NCN, Ungaretti L, Whittaker EJW, Youzhi G (1997) Nomenclature of amphiboles: report of the subcommittee on amphiboles of the international mineralogical association, commission on new minerals and mineral names. Can Mineral 35 : 219-246

Lemarchand F, Villemant B, Calas G (1987) Trace element distribution coefficients in alkaline series. Geochim Cosmochim Acta 51 : 1071-1081

Liotard J-M, Boivin P, Cantagrel J-M, Dupuy C (1983) Mégacristaux d'amphibole et basaltes alcalins associés. Probèmes de leurs relations pétrogénétiques et géochimiques. Bull Minéral 106 : 451-464

Liu C-Q, Masuda A, Shimizu H, Takahashi K, Xie G-H (1992) Evidence for pressure dependence of the peak position in the REE mineral / melt partition patterns of clinopyroxene. Geochim Cosmochim Acta 56 : 1523-1530

Longerich HP, Jenner GA, Fryer BJ, Jackson SE (1990) Inductively coupled plasma - mass spectrometric analysis of geological samples: a critical evaluation based on case studies. Chem Geol 83 : 105-118

Lu F-Q, Smith JV, Sutton SR, Rivers ML, Davis AM (1989) Synchrotron x-ray fluorescence analysis of rock-forming minerals. 1. Comparison with other techniques. 2. White-beam energy-dispersive procedure for feldspars. Chem Geol 75 : 123-143

Mattioli GS, Baker MB, Rutter MJ, Stolper EM (1989) Upper mantle oxygen fugacity and its relationship to metasomatism. J Geol 97 : 521-536

McCallum IS, Charette MP (1978) Zr and Nb partition coefficients: Implications for the genesis of mare basalts, KREEP and sea floor basalts. Geochim Cosmochim Acta 42 : 859-869.

McKay GA (1989) Partitioning of rare earth elements between major silicate minerals and basaltic melts. In: Geochemistry and mineralogy of rare earth elements (Lipin BR, McKay GA eds). Mineral Soc Am (Washington DC), Rev Mineral 21: 45-77

Merril RB, Wyllie PJ (1975) Kaersutite and kaersutite eclogite from Kakanui, New Zealand - water-excess and water-deficient melting to 30 kilobars. Geol Soc Am Bull 86 : 555-570

Middlemost EAK (1975) The basalt clan. Earth Sci Rev 11 : 337-364

Mitchell RH (1995) Kimberlites, Orangeites, and related rocks. Plenum Press, New York, N.Y.

Miyashiro A (1978) Nature of alkalic volcanic rock series. Contrib Mineral Petrol 66 : 91-104

Moenke-Blankenburg L (1989) Laser microanalysis. In: Chemical analysis 105 (Winefordner JD ed). Wiley-Interscience, New York (NY)

Möller P (1988) The dependence of partition coefficients on differences of ionic volumes in crystal-melt systems. Contrib Mineral Petrol 99 : 62-69

Morimoto N (1989) Nomenclature of pyroxenes. Can Mineral 27 : 143-156

Morse SA (1982) Kiglapait geochemistry: V. Strontium. Geochim Cosmochim Acta 46 : 223-234

Morse SA (1991) Partitioning of strontium between plagioclase and melt: A comment. Geochim Cosmochim Acta 55 : 1735-1737

Mysen BO (1976) Rare earth partitioning between crystals and liquid in the upper mantle. Carnegie Inst Wash Yearbook 75 : 656-659

Mysen BO (1978a) Experimental determination of nickel partition coefficients between liquid, pargasite, and garnet peridotite minerals and concentration limits of behavior according to Henry's law at high pressure and temperature. Am J Sci 278 : 217-243

Mysen BO (1978b) Experimental determination of rare earth element partitioning between hydrous silicate melt, amphibole and garnet peridotite minerals at upper mantle pressures and temperatures. Geochim Cosmochim Acta 42 : 1253-1263

Mysen BO (1988) Structure and properties of silicate melts. Elsevier, Amsterdam : 354 p

Mysen BO, Boettcher AL (1975) Melting of a hydrous mantle: II. Geochemistry of crystals and liquids formed by anatexis of mantle peridotite at high pressures and high temperatures as a function of controlled activities of water, hydrogen, and carbon dioxide. J Petrol 16 : 549-593

Nagasawa H (1966) Trace element partition coefficient in ionic crystals. Science 152 : 767-769

Nagasawa H (1973) Rare-earth distribution alkali rocks from Oki-Dogo Island, Japan. Contrib Mineral Petrol 39 : 301-308

Navrotsky A (1978) Thermodynamics of element partitioning: (1) systematics of transition metals in crystalline and molten silicates and (2) defect chemistry and "the Henry's law problem". Geochim Cosmochim Acta 42 : 887-902

Nicholls IA, Harris KL (1980) Experimental rare earth element partition coefficients for garnet, clinopyroxene and amphibole coexisting with andesitic and basaltic liquids. Geochim Cosmochim Acta 44 : 287-308

Oba T, Yagi K, Hariya Y (1982) Stability relation of kaersutite, reinvestigated on natural and synthetic samples. In: XIIIth General meeting I.M.A., Varne, Bulgaria:282 (abstr.)

Oberti R, Ungaretti L, Cannillo E, Hawthorne FC (1992) The behavior of Ti in amphiboles : I. four- and six-coordinate Ti in richterite. Eur J Mineral 4 : 425-439

Oberti R, Hawthorne FC, Ungaretti L, Cannillo E (1995) $^{[6]}$Al disorder in amphiboles from mantle peridotites. Can Mineral 33 : 867-878

Oberti R, Hawthorne FC, Raudsepp M (1997) The behaviour of Mn in amphiboles: Mn in synthetic fluor-edenite and synthetic fluor-pargasite. Eur. J. Mineral. 9:115-122

Onuma N, Higuchi H, Wakita H, Nagasawa H (1968) Trace element partition between two pyroxenes and the host lava. Earth Planet Sci Lett 5 : 47-51

O'Reilly SY, Griffin WL (1988) Mantle metasomatism beneath western Victoria, Australia: I. Metasomatic processes in Cr-diopside lherzolites. Geochim Cosmochim Acta 52 : 433-447

O'Reilly SY, Griffin WL, Ryan CG (1991) Residence of trace elements in metasomatized spinel lherzolite xenoliths: a proton-microprobe study. Contrib Mineral Petrol 109 : 98-113

Oxburgh ER (1964) Petrological evidence for the presence of amphibole in the upper mantle and its petrogenetic and geophysical implications. Mineral Mag 101 : 1-19

Papike JJ (1987) Chemistry of the rock-forming silicates: ortho, ring, and single-chain structures. Rev Geophys 25 : 1483-1526

Paris E, Mottana A, Della Ventura G, Robert J-L (1993) Titanium valence and coordination in synthetic richterite - Ti-richterite amphiboles. A synchrotron-radiation XAS study. Eur J Mineral 5 : 455-464

Pearce NJG, William TP, Abell I, Duller GAT, Fuge (1992) Mineral microanalysis by laser ablation inductively coupled plasma mass spectrometry. J Anal At Spectrom 7 : 53-57

Perkins WT, Pearce NJG, Jeffries TE (1993) Laser ablation inductively coupled plasma mass spectrometry: a new technique for the determination of trace and ultra-trace elements in silicates. Geochim Cosmochim Acta 57 : 475-482

Philpotts JA (1978) The law of constant rejection. Geochim Cosmochim Acta 42 : 909-920

Philpotts JA, Schnetzler CC (1970) Phenocryst-matrix partition coefficients for K, Rb, Sr and Ba, with applications to anorthosite and basalt genesis. Geochim Cosmochim Acta 34 : 307-322

Popp RK, Bryndzia LT (1992) Statistical analysis of Fe^{3+}, Ti, and OH in kaersutite from alkalic igneous rocks and mafic mantle xenoliths. Am Mineral 77 : 1250-1257

Popp RK, Virgo D, Phillips MW (1995) H deficiency in kaersutitic amphiboles: experimental verification. Am Mineral 80 : 1347-1350

Purton JA, Allan NL, Blundy JD, Wasserman EA (1996) Isovalent trace element partitioning between minerals and melts: A computer simulation study. Geochim Cosmochim Acta 60 : 4977-4987

Purton JA, Allan NL, Blundy JD (1997) Calculated solution energies of heterovalent cations in forsterite and diopside: Implications for trace element partitioning. Geochim Cosmochim Acta 61 : 3927-3936

Righter K, Carmichael ISE (1993) Mega-xenocrysts in alkali olivine basalts: fragments of disrupted mantle assemblages. Am Mineral 78 : 1230-1245

Robert J-L, Della Ventura G, Raudsepp M, Hawthorne FC (1993) Rietveld structure refinement of synthetic strontium-rich potassium-richterites. Eur J Mineral 5 : 199-206

Robinson P, Spear FS, Schumacher JC, Laird J, Klein C, Evans BW, Doolan BL (1982) Phase relations of metamorphic amphiboles: natural occurence and theory. In: Amphiboles: petrology and experimental phase relations, Veblen DR, Ribbe PH (eds), Rev Mineral 9B : 1-227

Robinson K, Gibbs GV, Ribbe PH, Hall MR (1973) Cation distribution in three hornblendes. Am J Sci 273A : 522-535

Roeder PL, Emslie RF (1970) Olivine-liquid equilibrium. Contrib Mineral Petrol 29 : 275-289

Schmidt KH, Bottazzi P, Vannucci R, Mengel K, Foley SF (1996) Trace element partitioning between phlogopite and leucite-lamproite melt. In: VM Goldschmidt Conference, J Conf Abstr 1(1) : 75

Schreiber HD, Balazs GB, Shaffer AP, Jamison PL (1982) Iron metal production in silicate melts through the direct reduction of Fe(II) by Ti(III), Cr(II), and Eu(II). Geochim Cosmochim Acta 46 : 1891-1901

Schumacher JC (1997) Appendix 2. The estimation of the proportion of ferric iron in the electron-microprobe analysis of amphiboles. Can Mineral 35 : 238-246

Shannon RD (1976) Revised effective ionic radii in oxides and fluorides. Acta Crystallogr, Sect A, 32 : 751-767

Shaw DM (1970) Trace element fractionation during anatexis. Geochim Cosmochim Acta 34 : 237-243

Shaw CSJ, Penczak (1996) Barium- and titanium-rich biotite and phlogopite from the western and eastern gabbro, Coldwell alkaline complex, northwestern Ontario. Can Mineral 34 : 967-975

Sisson TW, Grove TL (1993) Experimental investigations of the role of H_2O in calc-alkaline differentiation and subduction zone magmatism. Contrib Mineral Petrol 113 : 143-166

Skulski T, Minarik W, Watson EB (1994) High-pressure experimental trace-element partitioning between clinopyroxene and basaltic melts. Chem Geol 117 : 127-147

Sun S-S, Hanson GN (1976) Rare earth element evidence for differentiation of McMurdo Volcanics, Ross Island, Antartica. Contrib Mineral Petrol 54 : 139-155

Sutton SR, Rivers ML, Smith JV (1986) Synchrotron X-ray fluorescence: diffraction interference. Anal Chem 58 : 2167-2171

Sutton SR, Delaney JS, Smith JV, Prinz M (1987) Copper and nickel partitioning in iron meteorites. Geochim Cosmochim Acta 51 : 2653-2662

Sweeney RJ, Green DH, Sie SH (1992) Trace and minor element partitioning between garnet and amphibole and carbonatitic melt. Earth Planet Sci Lett 113 : 1-14

Thompson RH (1974) Some high pressure pyroxenes. Min Mag 39 : 768-787

Ulmer P (1989) The dependence of the Fe^{2+}-Mg cation-partitioning between olivine and basaltic liquid on pressure, temperature and composition, an experimental study to 30 kbars. Contrib Mineral Petrol 101 : 261-273

Vannucci R, Piccardo GB, Rivalenti G, Zanetti A, Rampone E, Ottolini L, Oberti R, Mazzucchelli M, Bottazzi P (1995) Origin of LREE-depleted amphiboles in the subcontinental mantle. Geochim Cosmochim Acta 59 : 1763-1771

Varne R (1970) Hornblende lherzolite and the upper mantle. Contrib Mineral Petrol 27 :45-51

Wagner C, Velde D (1986) The mineralogy of K-richterite-bearing lamproites. Am Mineral 71 : 17-37

Wallace ME, Green DH (1991) The effect of bulk rock composition on the stability of amphibole in the upper mantle: implications for solidus positions and mantle metasomatism. Mineral Petrol 44 : 1-19

Wallace RC (1977) Anorthoclase-calcite rodding within a kaersutite xenocryst from the Kakanui mineral breccia, New Zealand. Am Mineral 62 : 1038-1041

Wass SY, Roger NW (1980) Mantle metasomatism - precursor to continental alkaline volcanism. Geochim Cosmochim Acta 44 : 1811-1823

Watson EB (1977) Partitioning of manganese between forsterite and silicate liquid. Geochim Cosmochim Acta 41 : 1363-1374

Watson EB (1985) Henry's law behavior in simple systems and in magmas: criteria for discerning concentration-dependent partition coefficients in nature. Geochim Cosmochim Acta 49 : 917-923

Watson EB, Ryerson FJ (1986) Partitioning of zirconium between clinopyroxene and magmatic liquids of intermediate composition. Geochim Cosmochim Acta 50 : 2523-2526

Watson EB, Othman DB, Luck J-M, Hofmann AW (1987) Partitioning of U, Pb, Cs, Yb, Hf, Re and Os between chromian diopsidic pyroxene and haplobasaltic liquid. Chem Geol 62 : 191-208

White AJR, Chappell BW, Jakeš P (1972) Coexisting clinopyroxene, garnet and amphibole from an "eclogite", Kakanui, New Zealand. Contrib Mineral Petrol 34 : 185-191

Williams JG, Jarvis KE (1993) Preliminary assessment of laser ablation inductively coupled plasma mass spectrometry for quantitative multi-element determination in silicates. J Anal At Spectrom 8 : 25-34

Wilkinson JFG, Le Maître RW (1987) Upper mantle amphiboles and micas and TiO_2, K_2O, and P_2O_5 abundances and 100 $Mg/(Mg+Fe^{2+})$ ratios of common basalts and andesites: implications for modal mantle metasomatism and undepleted mantle compositions. J Petrol 28 : 37-73

Wilshire HG, Trask NJ (1971) Structural and textural relationships of amphibole and phlogopite in peridotite inclusions, Dish Hill, California. Am Mineral 56 : 240-255

Wilshire HG, Calk LC, Schwarzman EC (1971) Kaersutite - a product of reaction between pargasite and basanite at Dish Hill, California. Earth Planet Sci Lett 10 : 281-284

Wood BJ, Blundy JD (1997) A predictive model for rare earth element partitioning between clinopyroxene and anhydrous silicate melt. Contrib Mineral Petrol 129 : 166-181

Wood BJ, Virgo D (1989) Upper mantle oxidation state: ferric iron contents of lherzolite spinels by ^{57}Fe Mössbauer spectroscopy and resultant oxygen fugacities. Geochim Cosmochim Acta 53 : 1277-1291

Yoder HS Jr, Tilley CE (1962) Origin of basalt magmas: an experimental study of natural and synthetic rock systems. J Petrol 3 : 342-532

Zanetti A, Vannucci R, Bottazzi P, Oberti R, Ottolini L (1994) Crystal-chemical variations in amphiboles close to a hornblendite vein: implications for models of mantle metasomatism. Mineral Mag 58A : 998-999

Zhang L, Ahsbahs H, Hafner SS, Kutoglu A (1997) Single-crystal compression and crystal structure of clinopyroxene up to 10 GPa. Am Mineral 82 : 245-258

Appendix 1

(abstracts and other publications)

Dalpé C. and Baker D.R. (1997a) Experimental investigation of the effect of titanium on partitioning of LILE, HFSE, and REE between calcic amphibole and basaltic melt. In: *EOS (Trans. Am. Geophys. Union)* **78**, (abstr).

Experimental Investigation of the Effect of Titanium on Partitioning of LILE, HFSE, and REE Between Calcic Amphibole and Basaltic Melt

C Dalpé and D R Baker (Dept. of Earth and Planetary Sciences, McGill University, 3450 University St., Montréal, Que. H3A 2A7, Canada; 514-398-7485; clauded@geosci.lan.mcgill.ca)

Calcic amphiboles observed in xenoliths (titanian pargasite and kaersutite) are distinctive by both their major element (in particular, Ti) and the trace element (i.e., REE) chemistry.

In order to investigate the role of titanium on partitioning between amphibole and basaltic melt, a series of experiments were performed using two sets of starting materials: pargasite + Ti-doped pargasitic glass and ol-norm. nephelinite + Ti-doped ol-norm. nephelinitic glass. These materials were run in a piston-cylinder apparatus using double capsules ($Ag_{50}Pd_{50}$ + graphite inner capsule; $\log fO_2$~NNO-2) with ~10 wt.% deionized water. The materials were totally melted at 1200°C and 1.5 GPa for 1 h, then isobarically cooled to run temperatures and held at those conditions for times between 24 to 200 h. Temperatures of experiments on natural and Ti-doped starting materials were similar (i.e., within 20 to 30°C). Run products consist of basanitic to nephelinitic quenched melt (18-71 mod.%), titanian pargasite to kaersutite (15-62 mod.%), phlogopite (0-9 mod.%), olivine (0-10 mod.%), and clinopyroxene (1-11 mod.%). Analyses of amphibole and quenched melt for major and minor elements were performed by EMPA and trace elements by LAM-ICP-MS.

Given the measured partition coefficients from the two sets of experiments and based upon one standard deviation from multiple analyses, we observed that as the $Ti^{4+}_{M(2)}$ content into the amphibole structure increased by a factor of 1.4 (pargasite materials) or 1.5 (ol-norm. nephelinite materials), D_{Ba} [*A* site], D_{La}, D_{Ce}, D_{Pr}, D_{Sr}, D_{Nd} [*M*(4) site], and D_{Ta}, D_{Zr} [*M*(2) site] increased by a factor of 1.2 to 3.0 for pargasite materials and 1.1 to 1.7 for the ol-norm. nephelinite materials. The calculated Young's modulus of the *M*(2) and *M*(4) lattice-sites (i.e., $E^{4+}_{M(2)}$ and $E^{3+}_{M(4)}$) based on partition coefficients from the natural and Ti-doped experiments decreases as the $Ti^{4+}_{M(2)}$ content in the amphibole increases. This behaviour indicates that the mechanical strain energy around a substitute, homovalent cation in the amphibole decreases as $Ti^{4+}_{M(2)}$ increases, which implies that partitioning becomes more favourable.

Dalpé C. and Baker D.R. (1997b) Evidence of pressure effects on LILE, HFSE and REE partitioning between calcic amphibole and basaltic liquid. In: *Abstract volume, GAC/MAC Annual Meeting, Ottawa'97* **22** (Ont., Can.), A-34 (abstr).

EVIDENCE OF PRESSURE EFFECTS ON LILE, HFSE AND REE PARTITIONING BETWEEN CALCIC AMPHIBOLE AND BASALTIC LIQUID

Dalpé, C., and Baker, D.R. (Earth and Planetary Sciences, McGill University, Montréal, Qc H3A 2A7, Canada; email: clauded@geosci.lan.mcgill.ca)

Calcic amphiboles such as pargasite and kaersutite are commonly found in various alkaline basaltic suites. It is important to determine whether a pressure variation of <= 1 GPa would significantly affect partition coefficients (*D's*), in which case the variations should be taken into account during modelling. Amphiboles accommodate LILE, HFSE and REE in three crystallographic sites. To investigate pressure effects on trace element partitioning a series of experiments were performed using two similar starting materials (pargasite and pargasitic glass) at two oxygen fugacities and pressures. These materials were run in a piston-cylinder apparatus using double capsules ($Ag_{50}Pd_{50}$ or $Au_{75}Pd_{25}$ + graphite inner capsule: NNO-2) or single capsules ($Au_{75}Pd_{25}$: NNO+1.7) with ≈10 wt% deionized water. The materials were totally melted at 1200°C, 1.5 or 2.5 GPa for 1 h, then cooled to temperatures and pressures of interest and held at those conditions for times between 24 and 100 h. Run products are quenched glass (18-65% mode), Ti-rich pargasite (8-62%), clinopyroxene (2-16%), phlogopite (3-10%), and olivine (0-8%). Analyses of Ti-rich pargasite and quenched glass for major elements were performed by EPMA and trace elements by LAM-ICP-MS. Given the measured partition coefficients and based upon Onuma's diagram, we infer that LILE's occupy the $^{X\text{-}XII}A$-site, REE's occupy the $^{VI\text{-}VIII}M4$-site, and HFSE's occupy the $^{VI}M1,2,3$-sites. Based on one standard deviation from multiple analyses, we observed that as pressure increased by 1.0 GPa at constant temperature and oxygen fugacity (1.5 to 2.5 GPa), D_{Rb} (*A*-site) increased by a factor of ≈2 while D_{Ti}, D_{Hf}, D_{Zr}, D_{Nb}, and D_{Ta} (*M1,2,3*-sites) decreased by a factor of ≈1/2. Such behaviour can be explained by the lattice-site Young's modulus ($\bar{E}$) where for the *A*-site, $\bar{E}_A$ decreases (partitioning becomes more favorable) while for the *M1,2,3*-sites, $\bar{E}_{M1,2,3}$ increases (partitioning becomes less favorable) as pressure increases. However, decreases in D_{REE} (*M4*-site) with pressure are greater for LREE's (La to Pr) than HREE's (Er to Lu), and this tendency seems to be enhanced in the high oxygen fugacity experiments. Based upon these observations, we calculate significant differences for Rb/HFSE partition coefficients formed by the same degree of melting but at different pressures.

Dalpé C. and Baker D.R. (1994a): Partition coefficients for rare-earth elements between calcic amphibole and Ti-rich basanitic glass at 1.5 GPa, 1100°C. *Mineral. Mag.* **58A**, 207-208 (abstr).

Partition coefficients for rare-earth elements between calcic amphibole and Ti-rich basanitic glass at 1.5 Gpa, 1100°C.

C. Dalpé *Department of Earth and Planetary Sciences, McGill University*
D.R. Baker *3450 University Street, Montreal, Quebec, H3A 2A7, Canada.*

Introduction

Partition coefficients, *D*'s, between crystals and melts are fundamental data necessary for the petrogenetic modelling of igneous rock suites. Experimental studies have been limited because of the difficulty of analyzing trace elements in the small crystals (100's of μm's at the largest) produced during experiments. Recently, the laser ablation ICP-MS (LA-ICP-MS) has been demonstrated to be an effective tool for the analysis of a large suite of trace elements at spacial resolutions on the order of 100 μm or less (Jenner et al., 1994). Using the LA-ICP-MS we have measured partition coefficients between pargasite and basanitic glasses synthesized from undoped rock powders at 1100°C and 1.5 GPa.

Techniques

Natural kaersutite megacrysts were ground and used as starting materials. Mixtures of this kaersutite powder + 10 wt% deionized water were enclosed in graphite capsules and then sealed inside $Ag_{50}Pd_{50}$ capsules. Experiments were performed in a piston-cylinder apparatus with a 1.91 cm diameter NaCl-pyrex assembly. Temperatures was measured with type D thermocouples and no corrections were applied for the effect of pressure on EMF. Experiments were performed by bringing the pressure and temperature of the assembly to 1.5 GPa, 1200°C for 1 h to totally melt the amphibole. Then samples were isobarically cooled at a rate of 10 °C/min to 1100 °C and that temperature maintained for 100 h before quenching. Experiments were inspected optically under oil and chips of quenched glass + crystals were mounted in epoxy for electron microprobe analysis of major and minor elements and for trace element analysis by LA-ICP-MS.

Results and discussion

Partitioning of selected trace elements between pargasite and quench basanitic glass were measured. The amphiboles are Ti-rich and have higher Mg#'s compared to other studies. The crystal chemistry of our pargasites shows the same amount of calcium in the M4-site ($^{VIII}Ca_{M4}$), but a higher proportion of titanium in the octahedral site ($^{VI}Ti_{M1,2,3}$=0.459 pfu) compared to other studies. The quenched glass contains 39 % SiO_2, 5.9 % TiO_2, 14.2 % Al_2O_3, 7.6 % FeO, 7.0 % MgO, 11 % CaO, 1.8 % Na_2O, 1.3 % K_2O, has an Mg# of 65, and contains 7 wt% normative Ne. Electron microprobe analysis and mapping of crystals demonstrated no zoning of crystals in major and

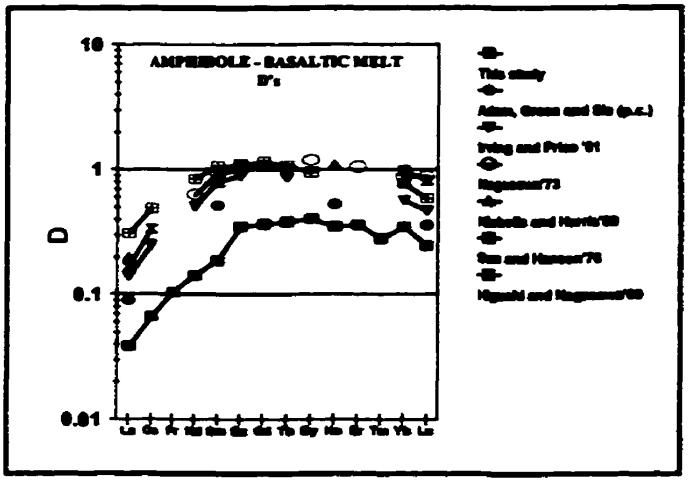

minor elements. Trace elements were measured with a laser ablation ICP-MS using a rastered grid. HFSE elements and light-to-middle REE's (La-Eu) in both crystals and quenched glass were analyzed with the laser in the "Free-Running" mode. This mode analysed a 50 x 150 x 80 (L x W x D) cubic micron volume of the sample and results less sample damage using a fixed point in the "Q-Switched" mode, but cannot be used to analyze elements with abundances below ≈1 ppm. Eu, HREE's, and Y in crystals and glass were analysed using the "Q-Switched" raster mode which analyzes a sample volume of 70 x 170 x 180 cubic microns. The greater intensity of the laser beam during "Q-Switched" analysis creates more sample damage than the "Free-Running" mode, but allows analysis of low-abundance trace elements. Concentrations of elements analyzed by both techniques (Eu and Y) are within error of each other. Using the rastered "Q-Switched" mode, concentrations down to approximately 0.2 ppm can be measured in our samples. The measured partition coefficients ($D^{\text{Ti-rich Pargasite/Ti-rich Melt}}$) are presented in Table 1 and displayed in Figure 1.

TABLE 1. Partition coefficients measured by Electron Microprobe and LA-ICP-MS for trace elements

Elem.	*D* value	S.D.	Replicates	Elem.	*D* value	S.D.	Replicates
Ti	0.717	0.028	15 glass, 21 mineral	La	0.039	0.005	5 glass, 5 mineral
K	1.360	0.780	"	Ce	0.067	0.002	"
Rb	0.220	0.043	5 glass, 5 mineral	Pr	0.105	0.007	"
Sr	0.376	0.005	"	Nd	0.142	0.007	"
Y	0.333	0.028	"	Sm	0.188	0.075	"
Zr	0.124	0.009	"	Eu	0.351	0.022	"
Nb	0.050	0.006	"	Gd	0.368	0.017	5 glass, 2 mineral
Ba	0.278	0.009	"	Tb	0.385	0.024	"
Hf	0.331	0.050	"	Dy	0.406	0.013	"
Ta	0.074	0.015	"	Ho	0.350	0.036	"
				Er	0.362	0.008	"
				Tm	0.281	0.030	"
				Yb	0.349	0.045	"
				Lu	0.246	0.032	"

The interesting feature of our results is that our *D* values for REE's are lower than previous

D values measured between natural pargasites and their host rocks (Irving and Price, 1981; Sun and Hanson, 1976; Nagasawa, 1973, Higuchi and Nagasawa, 1969), and lower than *D* values measured in earlier experimental studies (Adam J. pers. comm.; Nicholls and Harris, 1980). The rock (or melt) compositions from these earlier studies range from basinites to tholeiites and do not demonstrate any obvious effect of crystal or melt composition on the partition coefficients. Thus, despite the unique melt compositions formed during our experiments it is difficult to ascribe the low *D*'s of our study to differences in melt or crystal compositions. However, it may be possible that slight differences in composition (perhaps differences in $^{VI}Ti_{M1,2,3}$ or Fe^{3+} in the amphiboles?) may have a significant effect on the partition coefficients and explain the differences between the variety of measured REE partition coefficients.

References

Higuchi, H. and Nagasawa, H. (1969) Partition of trace elements between rock-forming minerals and the host volcanic rocks. *Earth Planet. Sci. Letters*, 7, 281-287.

Irving, A.J. and Price, R.C. (1981) Geochemistry and evolution of lherzolite-bearing phonolitic lavas from Nigeria, Australia, East Germany and New Zealand. *Geoch. Cosmoch. Acta*, 45, 1309-1320.

Jenner, G.A., Foley, S.F., Jackson, S.E., Green, T.H., Fryer, B.J. and Longerich, H.P. (1994) Determination of partition coefficients for trace elements in high pressure-temperature experimental run products by laser ablation microprobe-inductively coupled plasma-mass spectrometry (LAM-ICP-MS). *Geoch. Cosmoch. Acta*, 58, 5099-5103.

Nagasawa, H. (1973) Rare-earth distribution in alkali rocks from Oki-Dogo Island, Japan. *Contrib. Mineral. Petrol.*, 39, 301-308.

Nicholls, I.A. and Harris, K.L. (1980) Experimental rare earth element partition coefficients for garnet, clinopyroxene and amphibole coexisting with andesitic and basaltic liquids. *Geoch. Cosmoch. Acta*, 44, 287-308.

Sun, S.-S. and Hanson, G.N. (1976) Rare earth element evidence for differentiation of McMurdo volcanics, Ross Island, Antarctica. *Contrib. Mineral. Petrol.*, 54, 139-155.

Dalpé C. and Baker D.R. (1994b): Pargasite-basanitic melt partition coefficients determined by laser-ablation ICP-MS. *EOS (Trans. Am. Geophys. Union)* 75, 372 (abstr).

Pargasite-Basanitic Melt Partition Coefficients Determined by Laser-Ablation ICP-MS

C Dalpé and D R Baker (Department of Earth Sciences, McGill University, 3450 University, Montreal, QC H3A 2A7, Canada; 514-398-7485, CLAUDED@GEOSCI.LAN. MCGILL.CA)

Partition coefficients of HFSE (high field strength elements) and REE elements between partgasite and quench glass have been determined at natural concentration levels (0.07-100's of ppm in the amphibole) by LAM-ICP-MS. Natural pargasite was totally melt in graphite-lined $Ag_{50}Pd_{50}$ capsules in a piston-cylinder at 1.5 GPa, 1200 °C for 1 hour and then isobarically cooled to 1100 °C and held at those conditions for 100 h. Electron microprobe analysis and mapping of crystals demonstrated no zoning of crystals in major and minor elements. Our amphibole run products are Ti-rich and have higher Mg#'s compared to other studies. The quenched glass contains 39 wt% SiO_2, 6 wt% TiO_2, 3.4 wt% Na_2O+K_2O, Mg# 65, and 7 wt% normative Ne. Differences in partition coefficients between this study and previous ones are attributed to different compositions of crystals and melt studied.

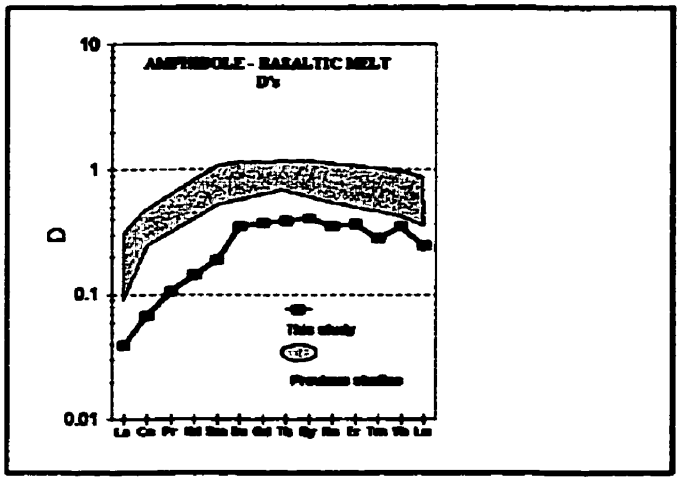

Dalpé C., Baker D.R. and Sutton S.R. (1993a): Investigation of secondary X-ray fluorescence during measurement on crystal-melt contact with synchrotron X-ray microprobe. In: *National Synchrotron Light Source Activity Report* **BNL52415**, B-223.

INVESTIGATION OF SECONDARY X-RAY FLUORESCENCE DURING MEASUREMENT ON CRYSTAL-MELT CONTACT WITH SYNCHROTRON X-RAY MICROPROBE

C. Dalpé, D.R. Baker (Department of Earth and Planetary Sciences, McGill University, 3450 University, Montréal, Que., Can., H3A 2A7; clauded@geosci.lan.mcgill.ca)
S.R. Sutton (Department of Geophysical Sciences and Center for Advanced Radiation Sources, The University of Chicago, Chicago, ILL. 60637, U.S.A.)

The partitioning of trace elements between calcic amphibole and quenched melt (conc. amph./conc. quench melt) has been determined with synchrotron x-ray fluorescence microprobe using established techniques (1). Recent measurements have investigated the role of masking one phase with lead tape (*i.e.*, calcic amphibole or quenched glass) during acquisition to avoid any secondary processes that will may affect measured partition coefficients (*e.g.*, secondary fluorescence; 2).

Measurements were performed on beamline X26A using Si(Li) energy-dispersive detector at 90° to the incident x-ray beam. Synchrotron ring characteristics were 2.584 GeV and the electron current between 202 and 101 mA. Specimens were excited with white light and the beam size was approximately 10 μm. A 170 μm aluminum filter was used on the detector to suppress the intense K energy fluorescence from the major elements in each phase.

We found that analyzing the same samples with or without lead masking complicated the determination of partition coefficients for Ga, Rb, and Sr. When the mask is used, this can be explained by similar energy levels between the L line of lead and the K line of the elements cited above (*e.g.*, Pb $L_l = 9.18$ keV, Ga $K_\alpha = 9.24$ keV). In fact, lead massking did not allow to discriminatre the effects of secondary x-ray fluorescence during analysis. We will investigate possible fluorescence with Mo-shield which lacks any *K* or *L* lines that overlap with those of elements that we wish to analyze.

References:

(1) Dalpé C., Baker D.R., and Sutton S.R. "Partition coefficient of Cr, Rb, Ga, Sr, Y, Nb, and Zr between pargasite and nephelinitic melt at 1.5 GPa", *EOS Trans. Supplement, AGU*, **73**, no. 43, (1992).
(2) McKay G.A. "Partitioning of rare earth elements between major silicate minerals and basaltic melts". In: Geochemistry and mineralogy of rare earth elements; Lipin B.R. and McKay G.A. (ed.), *Rev. Mineral.* **21**, 45-74, (1989).

(This research has been supported by the following grants: DOE DE#-FG02-92ER14244, NASA NAG9-106, NSF EAR89-15699, and NSERC OGP89662)

Dalpé C. and Baker D.R. (1993b): The importance of amphibole and mica in the generation of alkali basaltic suites. In: *Program and abstracts: GAC-MAC 1993 Joint Annual Meeting in Edmonton* (Alb., Can.), A-22 (abstr).

THE IMPORTANCE OF AMPHIBOLE AND MICA IN THE GENERATION OF ALKALI BASALTIC SUITES

Dalpé, C., and Baker, D.R., (Department of Earth and Planetary Sciences, McGill University, 3450 University, Montreal, Quebec H3A 2A7; clauded@geosci.lan.mcgill .ca)

Hydrous phases such as calcic amphibole and mica are commonly found in xenoliths hosted by alkali basalts. Previous experimental research shows that these hydrous phases are stable for a wide range of pressures and temperatures corresponding to upper mantle conditions. Their role in petrogenesis is not well understood, although clearly important in selected alkaline suites. To ascertain their importance we experimentally determined trace element partition coefficients between amphibole and phlogopite and hydrous nephelinitic melt at 1.5 GPa, 1100 °C. Mixtures of natural pargasite (or kaersutite) + water in graphite capsules sealed inside $Ag_{50}Pd_{50}$ outer capsules were totally melted at 1200 °C, 1.5 GPa for 1 h, then isobarically cooled to temperatures of 1100 °C for 1, 10, 20, and 100 h. Run products consisted of pargasite (TiO_2: 3.39 wt.%, Na_2O+K_2O: 3.9 wt.%, and Mg#: 0.71), phlogopite (TiO_2: 3.17 wt.%, Na_2O+K_2O: 7.85 wt.%, and Mg#: 0.77), olivine, and quenched glass of nephelinitic composition.

Based upon experiments of different time duration, constant partition coefficients (presumably equilibrium) are reached within 10 h. The measured partition coefficients at 1100 °C ($D^{Crystal/Melt}$ with 1 standard deviation) are:

	Na	K	Ti	Ga	Rb	Sr	Y	Nb	Zr
Pargasite	1.04	2.08	0.78	0.75	0.43	0.40	0.52	0.44	0.29
	±.11	±.66	±.03	±.24	±.16	±.05	±.09	±.24	±.11
Phlogopite	0.56	12.83	0.71	0.42	0.25	0.55	0.49	0.44	0.40
	±.14	±1.51	±.10	±.13	±.20	±.24	±.20	±.16	±.28

Based on these partition coefficients, we calculated significant differences between liquid compositions formed by small degrees of partial melting of amphibole-bearing or mica-bearing sources.

Dalpé C., Baker D.R. and Sutton S.R. (1992): Partition coefficient of Cr, Rb, Ga, Sr, Y, Nb, and Zr between pargasite and nephelinic melt at 1.5 GPa. *EOS (Trans. Am. Geophys. Union)* 73, 607 (abstr).

Partition Coefficient of Ti, Cr, Ga, Rb, Sr, Y, Nb, and Zr Between Pargasite and Nephelinitic Melt at 1.5 GPa.

C Dalpé and Don R Baker (Department of Earth and Planetary Sciences, McGill University, 3450 University, Montréal, QC H3A 2A7, Canada; 514-398-7485)
S R Sutton (Department of Applied Sciences, Brookhaven National Laboratory, Upton, NY 11973, USA; 516-282-2187)

Partitioning of trace elements between a nephelinitic melt with 10 wt.% water and high-titanium pargasite at 1.5 GPa and temperatures between 1075 and 1125 °C were determined. Mixtures of natural pargasite+water in graphite capsules sealed inside Pt or $Ag_{50}Pd_{50}$ capsules were totally melted at 1200 °C, 1.5 GPa for 1 h, then isobarically cooled to temperatures of interest and held at those conditions for times between 1 and 100 h. Run products consisted of pargasite (TiO_2: 3.4-5.0 wt.%, Na_2O+K_2O: 3.9-4.2 wt.%, and Al_2O_3: 14.8-16.1 wt.%), phlogopite, olivine (Fo_{86-91}) and quenched glass of nephelinitic composition (>10% normative ne, Mg#: 0.48-0.66, Na_2O+K_2O: 2.6-3.9 wt.%, and Cr > 2000 ppm).

Analysis of pargasite and quenched glass for major elements was performed by electron microprobe and for trace elements by x-ray fluorescence microprobe at Brookhaven National Laboratory. Beam sizes used in both instruments were approximately 10 μm; an aluminum filter was placed between the sample and the detector of the XRF and the counting times were 300 s.

Based upon experiments of 1, 10 and 100 h duration at 1100 °C, constant partition coefficients (presumably equilibrium) appear to be reached within 10 h. Replicated experiments with Pt and AgPd outer capsules demonstrate no significant differences in measured partition coefficients. The measured partition coefficicnets at 1100 °C ($D^{Pargasite/Melt}$ with 1 standard deviation) are: Ti: 0.73±0.25, Cr: 0.59±0.17, Ga: 0.58±0.11, Rb: 0.28±0.16, Sr: 0.43±0.17, Y: 0.54±0.14, Nb: 0.36±0.15, and Zr: 0.34±0.15.